Electromagnetics and Antenna Technology, Chapters 1, 2, 3

Alan J. Fenn

Senior Staff Member
Lincoln Laboratory
Massachusetts Institute of Technology
244 Wood Street
Lexington, MA 02420

January 12, 2017

This material is based upon work supported under Air Force Contract No. FA8721-05-C-0002 and/or FA8702-15-D-0001. Any opinions, findings, conclusions or recommendations expressed in this material are those of the author(s) and do not necessarily reflect the views of the U.S. Air Force.

Contents

1

Electromagnetics and Antenna Theory

1.1 Introduction

Electromagnetics [1–14] and antenna technology [15–29] are well developed and they have numerous practical applications. Radiofrequency (RF) electromagnetic waves can be produced by natural and manufactured processes. There are numerous antenna designs that can be considered for radar and communications applications depending on frequency band, type of platform and many other considerations to be discussed in this book. This book provides a detailed review of fundamental electromagnetics and antenna theory and development of practical implementations of antenna technology including phased arrays [30–47]. As part of the development of antenna theory, detailed discussions of transmission lines and antennas as a load impedance are provided. For some of the antennas described in this book, details of impedance matching between the antenna and transmission line are given based on well established methods.

An antenna is a transducer that can convert both an incident RF electromagnetic wave to a time-varying signal voltage (or waveform) on a transmission line and a time-varying signal voltage on a transmission line to a transmitted polarized electromagnetic wave [1–28] as depicted in Figure 1.1. An antenna can be characterized by a number of parameters including bandwidth, impedance, scattering parameters, gain, directivity, beamwidth, polarization, and sidelobes. A phased array antenna system [30–47] consists of two or more antenna elements that typically transmit or receive signals with a proper timing (phase relation) and amplitude relationship between the elements. Arrays operate with analog or digital beamforming either

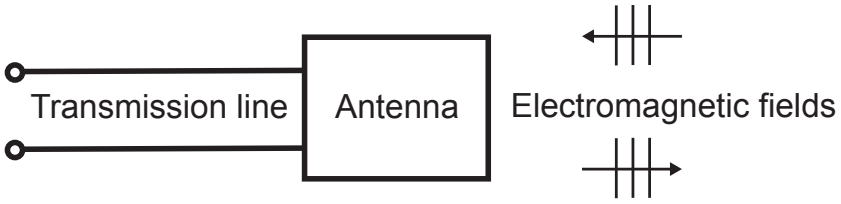

Figure 1.1 Simplified diagram showing a transmission line connected to an antenna that can transmit and receive electromagnetic fields.

nonadaptively or adaptively [48–61] such that the combination of the array elements provides desired radiation characteristics in particular directions over a band of frequencies.

Antennas have applications over a broad range of frequency bands, which have various designations. For example, frequency bands are defined by the International Telecommunications Union (ITU), which is a United Nations agency for information and communications technology. For example, as defined by the ITU, the high-frequency (HF) band extends from 3 MHz to 30 MHz, very high-frequency (VHF) band extends from 30 MHz to 300 MHz, and the ultra-high-frequency (UHF) band covers the 300 MHz to 3 GHz frequency range. The ITU super-high-frequency (SHF) band covers the range 3 to 30 GHz, and the extremely high-frequency (EHF) band covers 30 to 300 GHz. Frequency bands are also defined by the Institute for Electronic and Electrical Engineers (IEEE). The IEEE definitions of the HF and VHF bands are the same as the ITU definition, that is, 3 to 30 MHz and 30 to 300 MHz, respectively. The IEEE definition of UHF is from 300 MHz to 1 GHz, L band is from 1 to 2 GHz, S band is from 2 to 4 GHz, C band is from 4 to 8 GHz, X band is from 8 to 12 GHz, Ku band is from 12 to 18 GHz, K band is from 18 to 26.5 GHz, and Ka band is from 26.5 to 40 GHz. The broad term radiofrequency (RF or Rf) is typically used for frequencies in the range of 3 kHz to 300 GHz. The term microwave is typically used for frequencies in the range of 300 MHz to 30 GHz. The term millimeter wave is used for frequencies in the range of 30 GHz to 300 GHz.

An antenna and the surrounding structures, in general, can consist of electrically conducting materials, dielectric materials, magnetic materials, and absorbing components, arranged in such a way as to provide desired transmission and reception of electromagnetic fields over a specified bandwidth. An antenna typically has the same transmit and receive characteristics except when active electronics such as power amplifiers and low-noise amplifiers are included in the antenna design. In the general development of a phased array

antenna, the following topics often are important considerations as listed in Table 1.2.

Table 1.1
Some important topics in electromagnetics and antenna technology

Antenna types
Transmission lines
Reflection coefficient, input impedance
Impedance matching
Maxwell's equations
Electromagnetic simulations
Materials (conductivity, permittivity, permeability)
Bandwidth
Polarization
Radiation patterns, directivity, gain
Near field, far field
Resonant antennas
Electrically small antennas
Finite, infinite arrays
Periodic, random arrays, sparse arrays
Linear, planar, conformal arrays
Array mutual coupling
Beamforming
Grating lobes, Blind spots
Interference, Low sidelobes, Adaptive nulling
Direction finding
Subarrays, Phase centers
Electronic scanning
Passive electronically scanned array (PESA)
Active electronically scanned array (AESA)
Transmit/Receive modules
Phase shifters, time delays
High-power amplifiers, low noise amplifiers
Array design, fabrication, measurements
Array calibration
Radomes
Radar cross-section control
Field testing

In developing antenna technology, a number of detailed design parameters as well as testing methods need to be considered as listed below:

- Antenna system design and testing
  - RF radiation parameters
    - Field of view, scan sector, bandwidth (in-band, out-of-band), polarization, gain, half-power beamwidth, sidelobe level, front-to-back ratio, null depth, reflection coefficient, noise figure, effective isotropic radiated power
  - RF components
    - Antenna radiating elements
    - Beamformer: feed cables, transmission lines, connectors, combiners, amplifiers, filters, couplers, circulators, switches, attenuators, phase shifters, time-delay units

Table 1.2
Some common antenna types

Arrays (phased, broadside, endfire, lens, reflect)
Biconical (symmetric, asymmetric, solid surface, wire frame)
Dielectric rod
Dipole (linear, folded, vee, ultrawideband)
Discone (solid, wire frame)
Helix [axial mode (endfire), normal mode (broadside)]
Horn (pyramidal, conical, corrugated)
Lens (dielectric)
Log periodic
Long wire
Loop (circular, square)
Monocone (solid surface, wire frame)
Monopole (wire, sleeve, top loaded, blade)
Notch (flared Vivaldi, stepped)
Parasitic (Yagi-Uda)
Patch (circular, rectangular, triangular, microstrip, suspended)
Reflectors (corner, parabolic, shaped, dual)
Slot
Spiral (planar: Archimedean, equiangular; conical)
Subreflectors (parabolic, elliptical, hyperbola, shaped)
Waveguide (open-ended: rectangular, circular)

- Mechanical parameters
  - Antenna volume and mass budget, antenna durability/survivability, fabrication technique(s) and materials, ground plane and support structure
- Ground-based testing
  - Anechoic chamber measurements (far-field [rectangular chamber, tapered chamber, compact range], near-field [planar, cylindrical, spherical])
  - Thermal chamber, vacuum chamber measurements
  - Outdoor field testing
- Flight testing (airborne, spaceborne)
  - In-flight radiation patterns and calibration

The rest of this chapter is organized as follows. Section 1.2 reviews transmission line theory as it relates to antennas and provides various definitions for bandwidth. In Section 1.3, the generation of electromagnetic radiation and Maxwell's equations are described. Since the goal of electromagnetic analysis often is to compute the radiation pattern of antennas, in Section 1.4, a derivation of the fields radiated by current sources is given. Boundary conditions for the relations between the field quantities at the interface between two arbitrary media are derived in Section 1.5. Section 1.6 describes the wave equation and the complex propagation constant of electromagnetic waves in conducting media. In Section 1.7, a derivation of the electromagnetic wave energy flow and Poynting vector is given. Section 1.8 considers the derivation of near-field and far-field expressions for Hertzian (short) dipole and small loop antennas. In Section 1.10, discussion of polarization of electromagnetic waves and receive antennas is given. The topics of bandwidth and antenna quality factor are discussed in Section 1.11. Section 1.12 discusses the topics of antenna radiation pattern directivity and gain, with examples. Section 1.13 has a summary.

1.2 Some Basics: Transmission Lines and Antennas as a Load

1.2.1 Introduction

As depicted earlier in Figure 1.1 at some point an antenna will be connected to a transmission line. As far as transmission line analysis [62] is concerned, the antenna behaves effectively as a frequency-dependent complex load impedance. In order to provide efficient transfer of microwave signal between the transmission line and an arbitrary load, an impedance matching network

is often used as depicted in Figure 1.2. Similarly, an impedance matching network can be inserted at a position along the transmission line to improve the antenna performance in terms of the efficiency in transmitting and receiving microwave signals as depicted in Figure 1.3. The impedance matching network can take on a number of forms including ladder networks of low-loss inductors and capacitors, stub tuners, line transformers, amplifiers, and other circuits.

1.2.2 Transmission line impedance

A radiofrequency or microwave transmission line typically can be coaxial, microstrip, twin-lead, or a general wave-guiding structure. A fundamental frequency-dependent quantity is referred to as the antenna input impedance $Z_A(f)$ which is a complex quantity with units of ohms defined at the terminals of the antenna at frequency f with units of cycles per second. Let $V(f)$ be the complex voltage drop in volts across the terminals of the antenna and let $I(f)$ be the complex electric current in amperes flowing through the terminals of the antenna, then the antenna complex input impedance is equal to the ratio of the terminal voltage to current as

$$Z_A(f) = \frac{V(f)}{I(f)} = R_A(f) + jX_A(f) \tag{1.1}$$

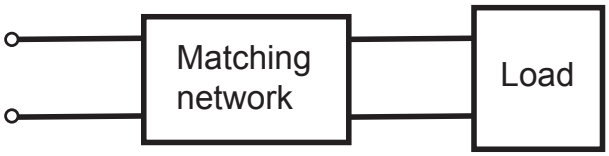

Figure 1.2 Simplified diagram showing a matching circuit connected to a load which can be an antenna.

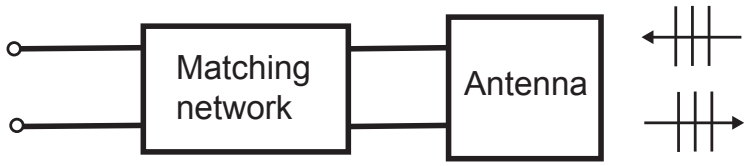

Figure 1.3 Simplified diagram showing a matching network connected to an antenna that receives and transmit electromagnetic fields.

where R_A in the input resistance (real part), j is the imaginary number, and X_A is the input reactance (imaginary part) of the antenna input impedance, respectively. Note: if the antenna is located in a phased array of antennas, then the antenna input impedance is also scan angle dependent as will be considered in Chapter 2. The antenna complex input admittance Y_A with units of Siemens is simply the inverse of the input impedance as

$$Y_A(f) = \frac{1}{Z_A} = G_A(f) + jB_A(f) \tag{1.2}$$

where G_A in the input conductance (real part) and B_A is the input susceptance (imaginary part) of the antenna input admittance, respectively. Note that it is common to also define antenna parameters in terms of the radian frequency (denoted ω) as

$$\omega = 2\pi f \tag{1.3}$$

with units of radians per second.

Consider now the general case of a transmission line connected to an antenna represented by the complex load impedance Z_L as shown in Figure 1.4. The transmission line can, in general, be lossy and will be

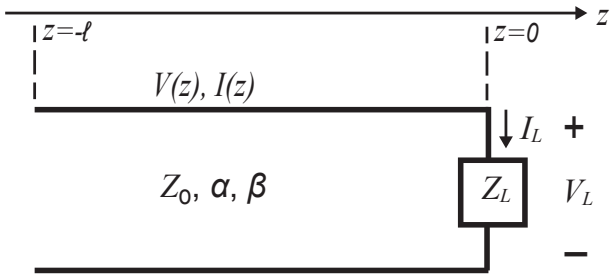

Figure 1.4 Simplified diagram showing a transmission line connected to a frequency-dependent complex load impedance.

described by the characteristic impedance Z_o, attenuation constant α, and phase constant β. The complex propagation constant (denoted γ) is expressed in terms of the attenuation constant and phase constant as

$$\gamma = \alpha + j\beta \tag{1.4}$$

Assume that an RF source has generated voltage $V(z)$ and current $I(z)$ waves along the transmission line. We seek to quantify the voltage and current at any point z along the transmission line. The voltage and current waves on a lossy

transmission line can be expressed in terms of waves traveling in the plus z and minus z directions as

$$V(z) = V_o^+ e^{-\gamma z} + V_o^- e^{-\gamma z} \tag{1.5}$$

$$I(z) = I_o^+ e^{-\gamma z} + I_o^- e^{-\gamma z} \tag{1.6}$$

Assume now that the transmission line is lossless (zero attenuation versus distance), that is, $\alpha = 0$ so that $\gamma = j\beta$, where $\beta = 2\pi/\lambda$, where λ is the wavelength for the transmission line. For the lossless transmission line $V(z)$ and $I(z)$ become

$$V(z) = V_o^+ e^{-j\beta z} + V_o^- e^{-j\beta z} \tag{1.7}$$

$$I(z) = I_o^+ e^{-j\beta z} + I_o^- e^{-j\beta z} \tag{1.8}$$

The characteristic impedance of the transmission line is computed from the ratio of the voltage and current waves in the positive and negative traveling wave directions as

$$Z_o = \frac{V_o^+}{I_o^+} = \frac{-V_o^-}{I_o^-} \tag{1.9}$$

which yields

$$I_o^+ = \frac{V_o^+}{Z_o} \tag{1.10}$$

$$I_o^- = \frac{-V_o^-}{Z_o} \tag{1.11}$$

Note that the minus sign for the negative traveling current wave is required due to the opposing vector orientation of the negative traveling current with respect to the vector orientation of the positive traveling current. Using Equations (1.10) and (1.11), the current wave $I(z)$ in Equation (1.8) can be expressed now as

$$I(z) = \frac{V_o^+}{Z_o} e^{-j\beta z} + \frac{-V_o^-}{Z_o} e^{-j\beta z} \tag{1.12}$$

Taking the ratio of the voltage wave given by Equation (1.5) and the current wave given by Equation (1.12) at the load position ($z = 0$) yields

$$Z_L = \frac{V_L(0)}{I_L(0)} = \frac{V_o^+ + V_o^-}{V_o^+ - V_o^-} Z_o \tag{1.13}$$

Solving for V_o^- yields

$$V_o^- = \frac{Z_L - Z_o}{Z_L + Z_o} V_o^+ \tag{1.14}$$

The complex voltage reflection coefficient Γ is defined as the ratio of the voltage wave reflected from the load to the voltage wave incident at the load, that is,

$$\Gamma = \frac{V_o^-}{V_o^+} = \frac{Z_L - Z_o}{Z_L + Z_o} \tag{1.15}$$

The voltage transmission coefficient T_v is defined as the voltage across the load divided by the incident voltage as

$$T_v = \frac{V_o^+ + V_o^-}{V_o^+} = 1 + \frac{V_o^-}{V_o^+} = 1 + \Gamma \tag{1.16}$$

Now the average incident and reflected powers are given by

$$P^+ = \frac{1}{2}|V_o^+|^2/Z_o \tag{1.17}$$

$$P^- = \frac{1}{2}|V_o^-|^2/Z_o \tag{1.18}$$

The average power actually delivered to the load (same as the average power accepted by the load or the average power actually transmitted by a lossless antenna) is equal to the difference between the average incident power and the average reflected power, that is,

$$P_L = P^+ - P^- = \frac{1}{2}|V_o^+|^2/Z_o - \frac{1}{2}|V_o^-|^2/Z_o \tag{1.19}$$

Now dividing the average power delivered to the load by the average incident power, which is referred to here as the transmission mismatch efficiency $\eta_{\text{transmission mismatch}}$, yields

$$P_L/P^+ = \eta_{\text{transmission mismatch}} = \frac{|V_o^+|^2/Z_o - |V_o^-|^2/Z_o}{|V_o^+|^2/Z_o} \tag{1.20}$$

which reduces to

$$\eta_{\text{transmission mismatch}} = 1 - \frac{|V_o^-|^2}{|V_o^+|^2} = 1 - |\Gamma|^2 \tag{1.21}$$

The parameter $\eta_{\text{transmission mismatch}}$ can be described as the mismatch efficiency (with values ranging from 0 to 1) in transferring power from the transmission line to the load or antenna, and it represents either power loss or gain loss, depending on its use. The antenna mismatch loss (ML) or realized gain

loss due to mismatch between the antenna load and the transmission line in decibels (dB) is quantifed as

$$\text{ML}_{\text{dB}} = 10\log_{10}\eta_{\text{transmission mismatch}} \tag{1.22}$$

Using Equation (1.15) in Equations (1.7) and (1.8) it follows that

$$V(z) = V_o^+(e^{-j\beta z} + \Gamma e^{j\beta z}) \tag{1.23}$$

$$I(z) = \frac{V_o^+}{Z_o}(e^{-j\beta z} - \Gamma e^{j\beta z}) \tag{1.24}$$

It can be shown that the maximum and minimum voltages on the transmission line are expressed as

$$V_{\text{max}} = |V_o^+|(1 + |\Gamma|) \tag{1.25}$$

$$V_{\text{min}} = |V_o^+|(1 - |\Gamma|) \tag{1.26}$$

The voltage standing wave ratio (VSWR) is defined as

$$\text{VSWR} = \frac{V_{\text{max}}}{V_{\text{min}}} = \frac{1 + |\Gamma|}{1 - |\Gamma|} \tag{1.27}$$

Solving Equation (1.27) for the magnitude of the reflection coefficient yields

$$|\Gamma| = \frac{\text{VSWR} - 1}{\text{VSWR} + 1} \tag{1.28}$$

Next, using Equations (1.23) and (1.24), the input impedance Z_{in} at any point along the transmission line is now expressed as

$$Z_{\text{in}}(-l) = \frac{V(-l)}{I(-l)} = \frac{V_o^+(e^{j\beta l} + \Gamma e^{-j\beta l})}{V_o^+(e^{j\beta l} - \Gamma e^{-j\beta l})}Z_o = \frac{1 + \Gamma e^{-j2\beta l}}{1 - \Gamma e^{-j2\beta l}}Z_o \tag{1.29}$$

Subsituting Equation (1.15) in Equation (1.29) yields after simplification

$$Z_{\text{in}}(-l) = Z_o\frac{Z_L + jZ_o\tan\beta l}{Z_o + jZ_L\tan\beta l} \tag{1.30}$$

In the general case with frequency dependence, if an antenna with complex input impedance Z_A is connected to a transmission line with characteristic impedance Z_o, then the antenna's frequency-dependent complex reflection coefficient Γ_A is given by

$$\Gamma_A(f) = \frac{Z_A(f) - Z_o(f)}{Z_A(f) + Z_o(f)} \tag{1.31}$$

It should be noted that the characteristic impedance of a coaxial transmission line or microstrip line is frequency independent, whereas in a rectangular or circular waveguide the characteristic impedance is frequency dependent. In this book, we concentrate primarily on antennas that are connected to a coaxial transmission line.

Impedance matching is a critical technique that is used to improve the performance of antennas. Figure 2 shows the situation in which a two-port matching network is connected at a position along the transmission that is connected to the antenna. To reduce impedance mismatch effects between the transmission line and the antenna, the parameters of the matching device can be adjusted so that the reflection coefficient magnitude is minimized. A significant amount of impedance matching theory has been developed by prior researchers. In this book, some general theory of impedance matching theory is given as well as specific applied examples for narrowband and wideband antennas.

1.2.3 Smith chart theory

In this book, impedance data are presented either in the form of a rectangular plot with the horizontal axis the real part of the impedance and the vertical axis the imaginary part of the impedance, or as in a Smith chart [63 – 66] as is described in this section. In a Smith chart, the impedance data are typically normalized by the charateristic impedance of a transmission line. A derivation of the Smith chart equations is now given.

The derivation starts by normalizing the right-hand side of the voltage reflection coefficient Equation (1.15) by Z_o with the result

$$\Gamma = \frac{z_L - 1}{z_L + 1} \tag{1.32}$$

where $z_L = Z_L/Z_o$ is the normalized impedance. Now solving Equation (1.32) for z_L yields

$$z_L = \frac{1 + \Gamma}{1 - \Gamma} \tag{1.33}$$

Expressing the normalized load impedance and the reflection cofficient in terms of real and imaginary components as $z_L = r_L + jx_L$ and $\Gamma = \Gamma_r + j\Gamma_i$ Equation (1.33) becomes

$$z_L = r_L + jx_L = \frac{1 + \Gamma}{1 - \Gamma} = \frac{(1 + \Gamma_r) + j\Gamma_i}{(1 - \Gamma_r) - j\Gamma_i} \tag{1.34}$$

Now, multiplying the top and bottom of the right-hand side of Equation (1.34) by the complex conjugate of the denominator, and then simplifying and

equating real and imaginary components with r_L and x_L yields

$$r_L = \frac{(1-\Gamma_r^2)-\Gamma_i^2}{(1-\Gamma_r)^2+\Gamma_i^2} \tag{1.35}$$

$$x_L = \frac{2\Gamma_i}{(1-\Gamma_r)^2+\Gamma_i^2} \tag{1.36}$$

By rearranging terms and factoring, Equations (1.35) and (1.36) can be put into the standard form for constant resistance circles as

$$\left(\Gamma_r - \frac{r_L}{r_L+1}\right)^2 + \Gamma_i^2 = \left(\frac{1}{r_L+1}\right)^2 \tag{1.37}$$

which is centered at

$$\Gamma_r = \frac{r_L}{r_L+1} \qquad \Gamma_i = 0 \tag{1.38}$$

and has radius

$$\frac{1}{r_L+1} \tag{1.39}$$

and for constant reactance circles as

$$(\Gamma_r - 1)^2 + \left(\Gamma_i - \frac{1}{x_L}\right)^2 = \left(\frac{1}{x_L}\right)^2 \tag{1.40}$$

which is centered at

$$\Gamma_r = 1 \qquad \Gamma_i = \frac{1}{x_L} \tag{1.41}$$

and has radius

$$\frac{1}{x_L} \tag{1.42}$$

Similarly, in a Smith chart, the admittance data are typically normalized by the charateristic admittance of a transmission line. The derivation starts by normalizing the right-hand side of Equation (1.15) by Z_o and then using $z_L = 1/y_L$ with the result

$$\Gamma = \frac{z_L - 1}{z_L + 1} = \frac{1/y_L - 1}{1/y_L + 1} = \frac{1 - y_L}{1 + y_L} \tag{1.43}$$

where y_L is the normalized impedance. Now solving Equation (1.43) for y_L yields

$$y_L = \frac{1-\Gamma}{1+\Gamma} \tag{1.44}$$

Expressing the normalized load impedance and the reflection cofficient in terms of real and imaginary components as $y_L = g_L + jb_L$ and $\Gamma = \Gamma_r + j\Gamma_i$ Equation (1.44) becomes

$$y_L = g_L + jb_L = \frac{1-\Gamma}{1+\Gamma} = \frac{(1-\Gamma_r) - j\Gamma_i}{(1+\Gamma_r) + j\Gamma_i} \tag{1.45}$$

Now, multiplying the top and bottom of the right-hand side of Equation (1.45) by the complex conjugate of the denominator, and then simplifying and equating real and imaginary components with g_L and b_L yields

$$g_L = \frac{(1-\Gamma_r^2) - \Gamma_i^2}{(1+\Gamma_r)^2 + \Gamma_i^2} \tag{1.46}$$

$$b_L = -\frac{2\Gamma_i}{(1-\Gamma_r)^2 + \Gamma_i^2} \tag{1.47}$$

By rearranging terms and factoring, Equations (1.47) and (1.35) can be put into the standard form for constant conductance circles as

$$\left(\Gamma_r + \frac{g_L}{g_L+1}\right)^2 + \Gamma_i^2 = \left(\frac{1}{g_L+1}\right)^2 \tag{1.48}$$

which is centered at

$$\Gamma_r = -\frac{g_L}{g_L+1} \qquad \Gamma_i = 0 \tag{1.49}$$

and has radius

$$\frac{1}{g_L+1} \tag{1.50}$$

and for constant susceptance circles as

$$(\Gamma_r+1)^2 + \left(\Gamma_i + \frac{1}{b_L}\right)^2 = \left(\frac{1}{b_L}\right)^2 \tag{1.51}$$

which is centered at

$$\Gamma_r = -1 \qquad \Gamma_i = -\frac{1}{b_L} \tag{1.52}$$

and has radius

$$\frac{1}{b_L} \tag{1.53}$$

A standard Smith chart normalized by the characteristic impedance or characteristic admitttance of the transmission line is shown in Figure 1.5. This type of Smith chart is referred to here as a Z-type Smith Chart. The same Z-type of Smith chart is repeated in Figure 1.6, but now with

constant resistance ($r = 0.3, 1, 2$) and positive constant reactance ($x = 1, 1.8, 3$) circles highlighted. Figure 1.7 shows a standard normalized Smith chart (Z-type) with VSWR circles 1.5, 2, and 3 highlighted. As mentioned, the standard Z-type Smith chart can be used to analyze impedance and admittance data. When impedance values are plotted in a Z-type Smith chart, the corresponding admittance values are positioned 180° away from the impedance values on a constant VSWR circle. An alternate method for working with admittance values, is to physically rotate the Smith chart by 180°. A 180° rotated Smith chart normalized by the characteristic impedance or characteristic admitttance of the transmission line is shown in Figure 1.8. This type of Smith chart is referred to here as a Y-type Smith Chart (some authors [72] refer to this type of Smith Chart presentation as an overlay), because the chart is used directly with the admittance circles. The same Y-type Smith chart is repeated in Figure 1.9, but now with constant conductance ($g = 0.3, 1, 2$) and constant susceptance ($b = 1, 1.8, 3$) circles highlighted. Note: The MATLAB RF Toolbox (www.mathworks.com) provides Smith charts of the following type: Z-type, Y-type, ZY-type (Z is the primary chart with Y the overlay), and YZ-type (Y is the primary chart with Z the overlay).

1.2.4 Impedance Matching Circuit Elements

Impedance matching [67–75] is an important part of antenna technology, as it can be used to improve the transmit and receive characteristics of antennas over a bandwidth of interest. To improve the impedance match of an antenna to a transmission line of characteristic impedance Z_o, it is common to use one or more inductors and/or capacitors in series or in parallel with the antenna. These circuit elements are placed as close to the antenna terminals as possible to reduce dispersive effects and allow improved impedance matching over a given bandwidth. Let L be the inductance (typically in nH) of an inductor and let C be the capacitance (typically in pF) of a capacitor. Let Z_A be the antenna input impedance. It follows then that

- A series inductor provides an impedance equal to $j\omega L$ and a series capacitor provides an impedance equal to $1/(j\omega C)$.
- A parallel inductor provides an admittance equal to $1/(j\omega L)$ and a parallel capacitor provides an admittance equal to $j\omega C$.

Figure (1.10) summarizes the input impedance Z_{in} for these four circuit types with either a single inductor or single capacitor in series or parallel to the antenna (load) impedance Z_A. The corresponding Smith charts in Figure (1.11) show the effect of tuning to a perfect match ($|\Gamma| = 0$) at a single frequency with these four circuit types.

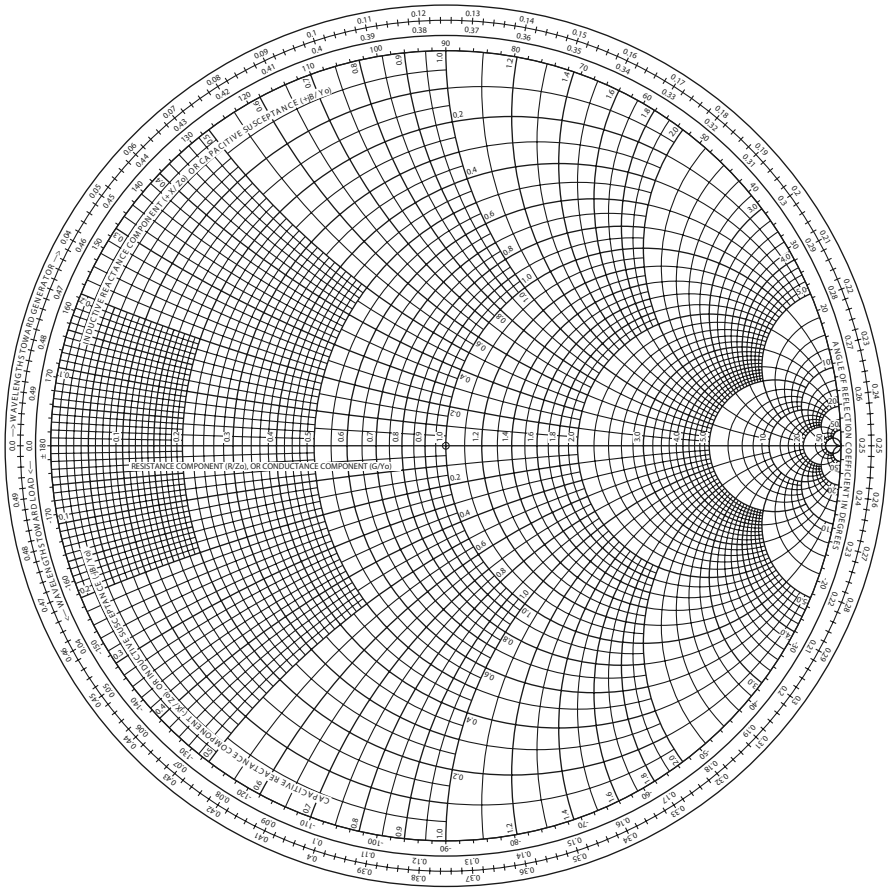

Figure 1.5 Standard Smith chart (Z-type) normalized by the characteristic impedance or characteristic admitttance of the transmission line. Copyright: IEEE [106]

- With a series inductor, the impedance rotates clockwise along circles of constant resistance on the impedance (Z-type) Smith Chart (Figure (1.11a)).
- With a series capacitor, the impedance rotates counter-clockwise along circles of constant resistance on the impedance (Z-type) Smith Chart (Figure (1.11b)).
- With a parallel inductor, the admittance rotates counter-clockwise along circles of constant conductance on the admittance (Y-type) Smith Chart (Figure (1.11c)).
- With a parallel capacitor, the admittance rotates clockwise along

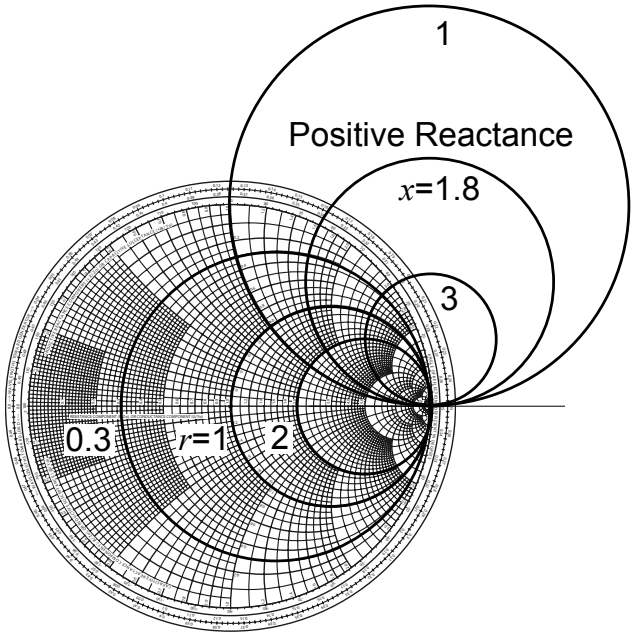

Figure 1.6 Standard normalized Smith chart (Z-type) with a few positive constant resistance ($r = 0.3, 1, 2$) and positive constant reactance ($x = 1, 1.8, 3$) circles highlighted.

circles of constant conductance on the admittance (Y-type) Smith Chart (Figure (1.11d)).

In Figure (1.12), the effect of two-stage tuning to a perfect match ($|\Gamma| = 0$) at a single frequency with four series/parallel circuit types is shown. In these four examples, since the first element is in series and the second element is in parallel with the antenna load, first a Z-type Smith chart rotation on a constant resistance circle is implemented which is then followed by a Y-type Smith chart rotation on the $g = 1$ constant conductance circle. The input admittance equation is indicated in each of the diagrams in Figure 1.12.

- With an initial series inductor L, the impedance rotates clockwise along a circle of constant resistance on the impedance (Z-type) Smith Chart. The rotation stops when the impedance reaches the point indicated by a prime $'$ on the $g = 1$ constant conductance circle. Then with a parallel capacitor C and switching to the Y-type Smith chart overlay the admittance rotates clockwise on the $g = 1$ circle to reach the center of the Smith chart for a perfect match (Figure (1.12a)).

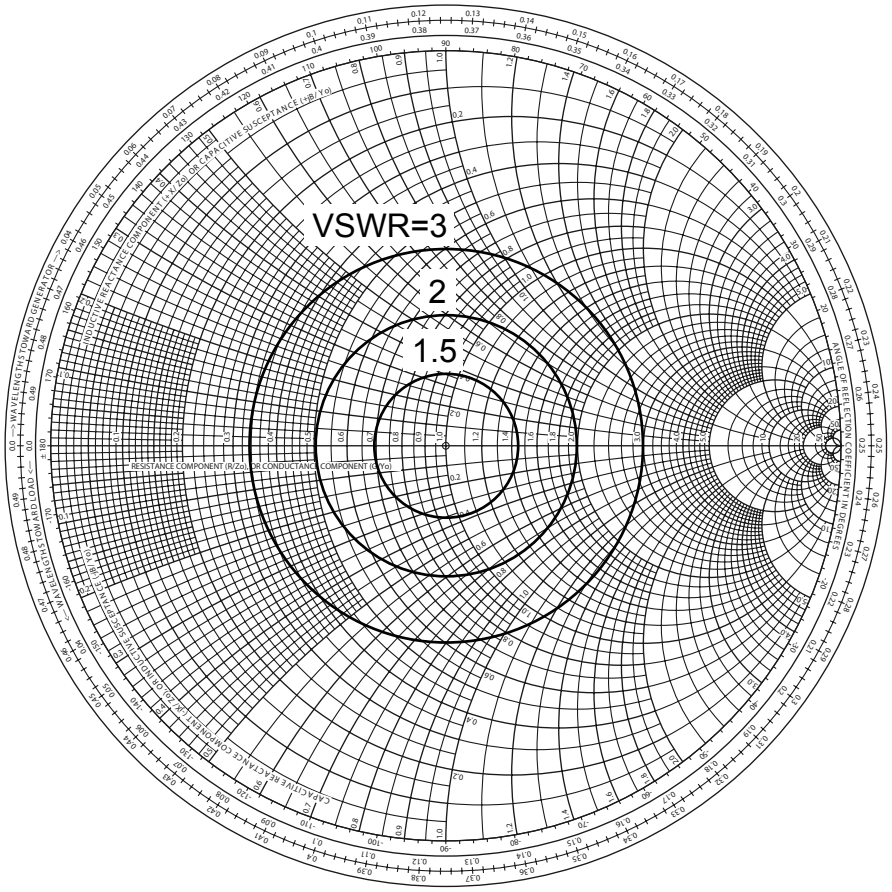

Figure 1.7 Standard normalized Smith chart (Z-type) with VSWR circles 1.5, 2, and 3 highlighted.

- With an initial series capacitor C, the impedance rotates counterclockwise along a circle of constant resistance on the impedance (Z-type) Smith Chart. The rotation stops when the impedance reaches the point indicated by a prime $'$ on the $g = 1$ constant conductance circle. Then with a parallel inductor L and switching to the Y-type Smith chart overlay the admittance rotates counterclockwise on the $g = 1$ circle to reach the center of the Smith chart for a perfect match (Figure (1.12b)).
- With an initial series inductor L_2, the impedance rotates clockwise along a circle of constant resistance on the impedance (Z-type) Smith Chart. The rotation stops when the impedance reaches the point

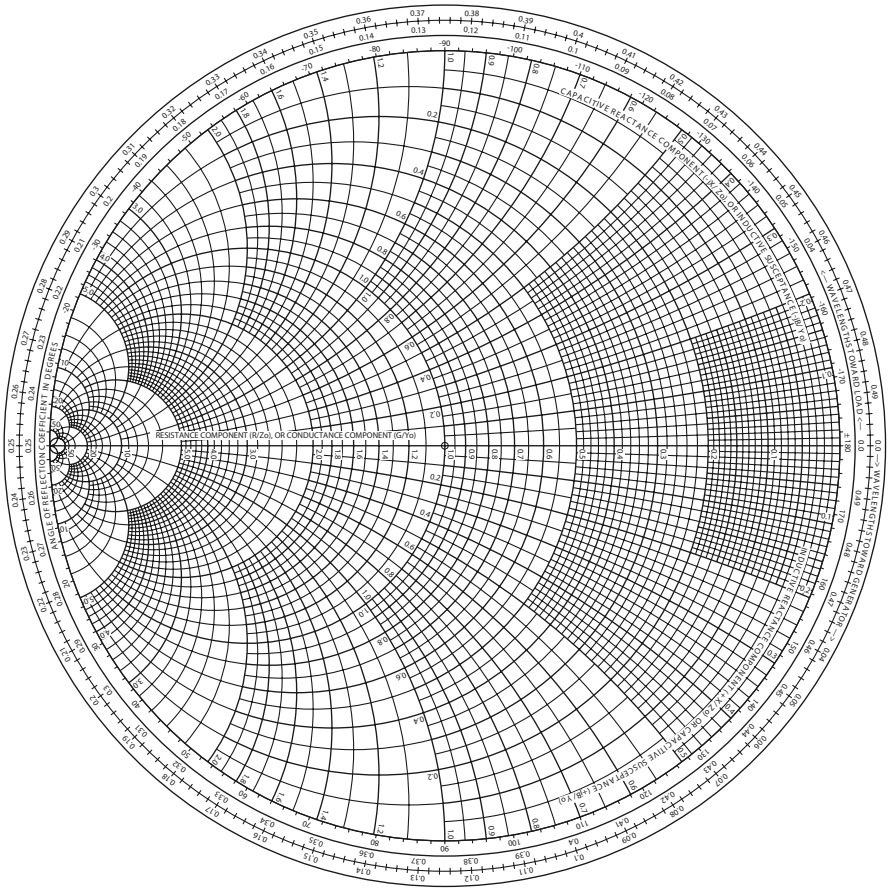

Figure 1.8 180° rotated Smith chart (Y-type) normalized by the characteristic impedance or characteristic admitttance of the transmission line.

indicated by a prime $'$ on the $g = 1$ constant conductance circle. Then with a parallel inductor L_1 and switching to the Y-type Smith chart overlay the admittance rotates counterclockwise on the $g = 1$ circle to reach the center of the Smith chart for a perfect match (Figure (1.12c)).

- With an initial series capacitor C_2, the impedance rotates counterclockwise along a circle of constant resistance on the impedance (Z-type) Smith Chart. The rotation stops when the impedance reaches the point indicated by a prime $'$ on the $g = 1$ constant conductance circle. Then with a parallel capacitor C_1 and switching to the Y-type Smith chart overlay the admittance rotates clockwise on the $g = 1$

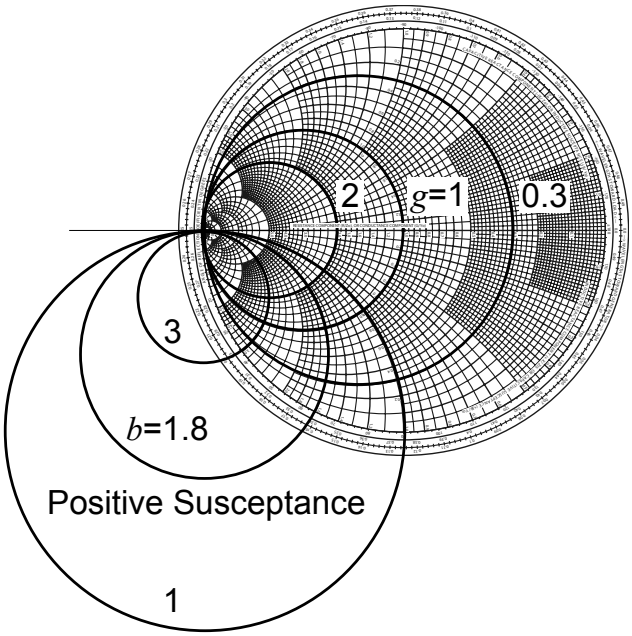

Figure 1.9 180° rotated normalized Smith chart (Y-type) with a few positive constant conductance ($g = 0.3, 1, 2$) and constant susceptance ($b = 1, 1.8, 3$) circles highlighted.

circle to reach the center of the Smith chart for a perfect match (Figure (1.12d)).

In Figure (1.13), the effect of two-stage tuning (with so-called L-sections) to a perfect match ($|\Gamma| = 0$) at a single frequency with four parallel/series circuit types is shown. In these four examples, since the first element is in parallel and the second element is in series with the antenna load, first a Y-type Smith chart rotation on a constant conductance circle is implemented which is then followed by a Z-type Smith chart rotation on the $r = 1$ constant resistance circle. The input impedance equation is indicated in each of the diagrams in Figure 1.13.

- With an initial parallel inductor L, the impedance rotates counter-clockwise along a circle of constant conductance on the admittance (Y-type) Smith Chart. The rotation stops when the admittance reaches the point indicated by a prime $'$ on the $r = 1$ constant resistance circle. Then with a series capacitor C and switching to the Z-type Smith chart overlay the impedance rotates counterclockwise on the

$r = 1$ circle to reach the center of the Smith chart for a perfect match (Figure (1.13a)).

- With an initial parallel capacitor C, the admittance rotates clockwise along a circle of constant conductance on the admittance (Y-type) Smith Chart. The rotation stops when the admittance reaches the point indicated by a prime $'$ on the $r = 1$ constant resistance circle. Then with a series inductor L and switching to the Z-type Smith chart overlay the impedance rotates clockwise on the $r = 1$ circle to reach the center of the Smith chart for a perfect match (Figure (1.13b)).
- With an initial parallel inductor L_2, the admittance rotates counterclockwise along a circle of constant admittance on the admittance (Y-type) Smith Chart. The rotation stops when the admittance reaches the point indicated by a prime $'$ on the $r = 1$ constant resistance circle. Then with a series inductor L_1 and switching to the Z-type Smith chart overlay the impedance rotates clockwise on the $r = 1$ circle to reach the center of the Smith chart for a perfect match (Figure (1.13c)).
- With an initial parallel capacitor C_2, the admittance rotates clockwise along a circle of constant conductance on the admittance (Y-type) Smith Chart. The rotation stops when the admittance reaches the point indicated by a prime $'$ on the $r = 1$ constant resistance circle. Then with a series capacitor C_1 and switching to the Z-type Smith chart overlay the impedance rotates counterclockwise on the $r = 1$ circle to reach the center of the Smith chart for a perfect match (Figure (1.13d)).

The examples shown in Figures 1.10 to 1.13 are ideal cases where a perfect impedance match ($|\Gamma = 0|$) is achieved at a single frequency. For practical antennas (loads) operating over a band of frequencies, a perfect match is not feasible. Instead, the antenna impedance match will provide a maximum allowed reflection coefficient magnitude or equivalently a maximum allowed voltage standing wave ratio (VSWR) over the desired frequency band. Impedance matching over a band of frequencies can be achieved for example with L-section networks, pi networks, T networks, and ladder networks consisting of multiple L, pi, and/or T networks, short-circuit and open-circuit stub tuners, and line transformers. Specific examples are given in later chapters. Impedance matching can be achieved using graphical methods manually on a Smith chart, or by commercial software that perform circuit synthesis and optimization such as the MATLAB RF Toolbox (www.mathworks.com) or Optenni Lab (www.optenni.com). For simple L-section networks, the values of the inductor(s) and/or capacitor(s) can be computed in closed form by first deriving the input impedance equation for

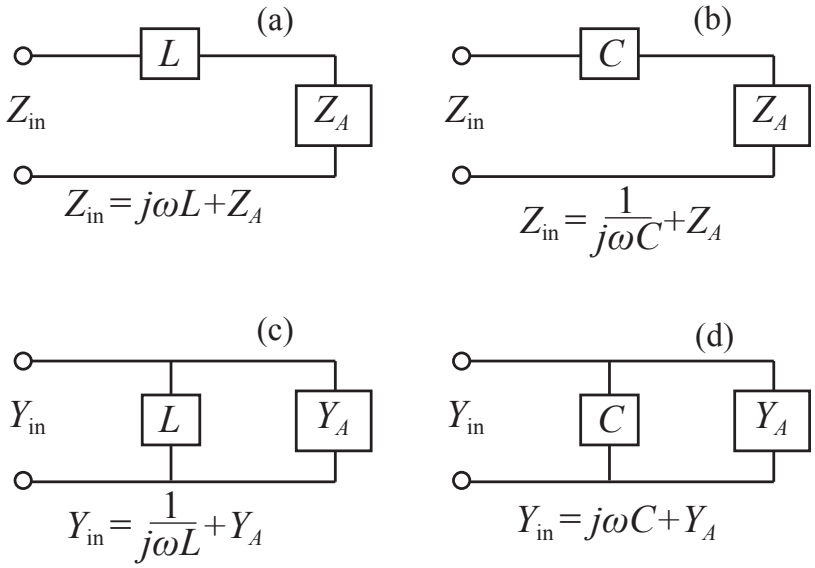

Figure 1.10 Four single element circuit types for impedance matching an antenna with input impedance Z_A or input admittance Y_A. (a) Series inductor, (b) Series capacitor, (c) Parallel inductor, and (d) Parallel capacitor.

the particular L-section network. Next, the real part of the input impedance is set equal to the characteristic impedance of the transmission line, and the imaginary part is set to zero. The resulting equation is then rearranged and separated into real and imaginary terms which gives two simultaneous equations. These two simultaneous equations are then solved for the values of the two reactive circuit components. In practice, for implementation of impedance matching with measurements and analysis of RF circuits, it is necessary to consider S-parameters as discussed in the next section.

1.2.5 S-parameters

S-parameters, or scattering parameters [62, 76–79] are commonly used to quantify the reflection and transmission of voltage and current waves in networks or antennas. In general, the S-parameters are quantified for an N-port system as an $N \times N$ complex matrix. A network analyzer is typically used in measuring S-parameters versus frequency. Consider Figure 1.14 which shows a transmission line with a two-port network. Voltage waves a_1 and a_2 are incident on ports 1 and 2, respectively. Similarly, voltage waves b_1 and b_2 are reflected from ports 1 and 2, respectively. In this case, the S-matrix or

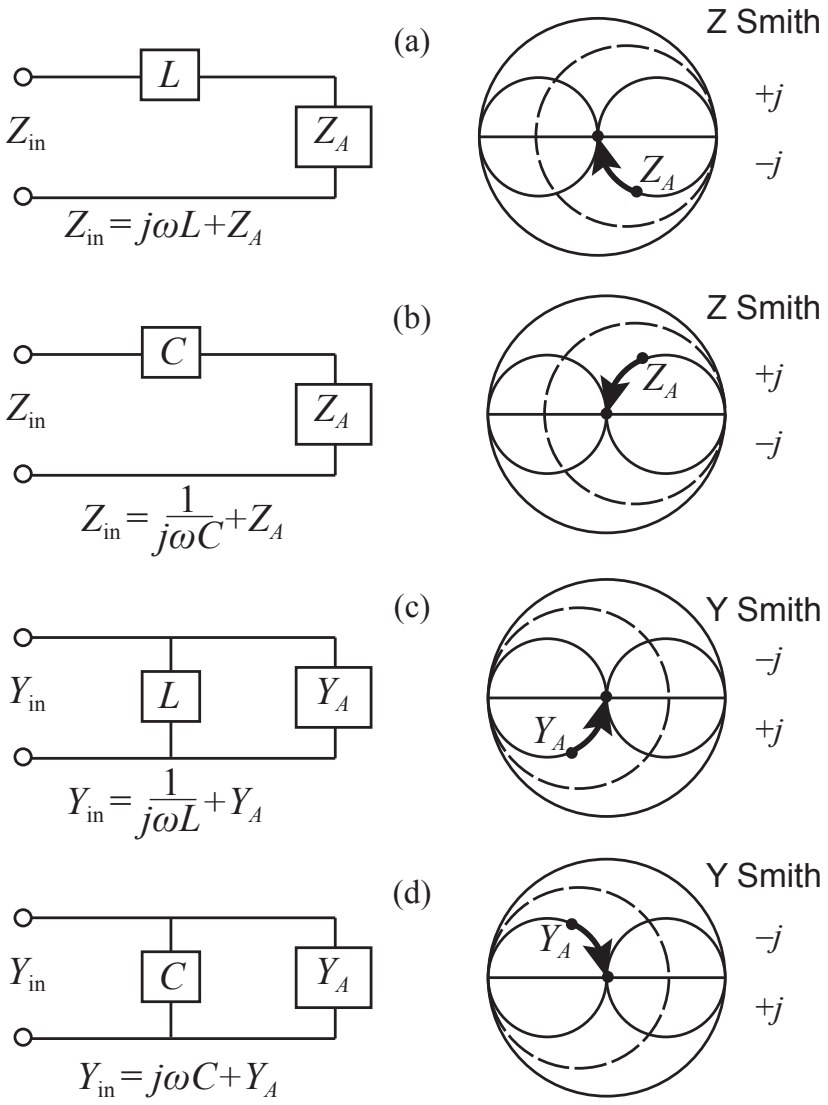

Figure 1.11 Series L or C circuits with corresponding Z and Y Smith chart diagrams. (a) Series inductor, (b) Series capacitor, (c) Parallel inductor, and (d) Parallel capacitor.

scattering matrix is a 2 x 2 complex matrix that is expressed as

$$\boldsymbol{S} = \begin{bmatrix} S_{11} & S_{12} \\ S_{21} & S_{22} \end{bmatrix}. \tag{1.54}$$

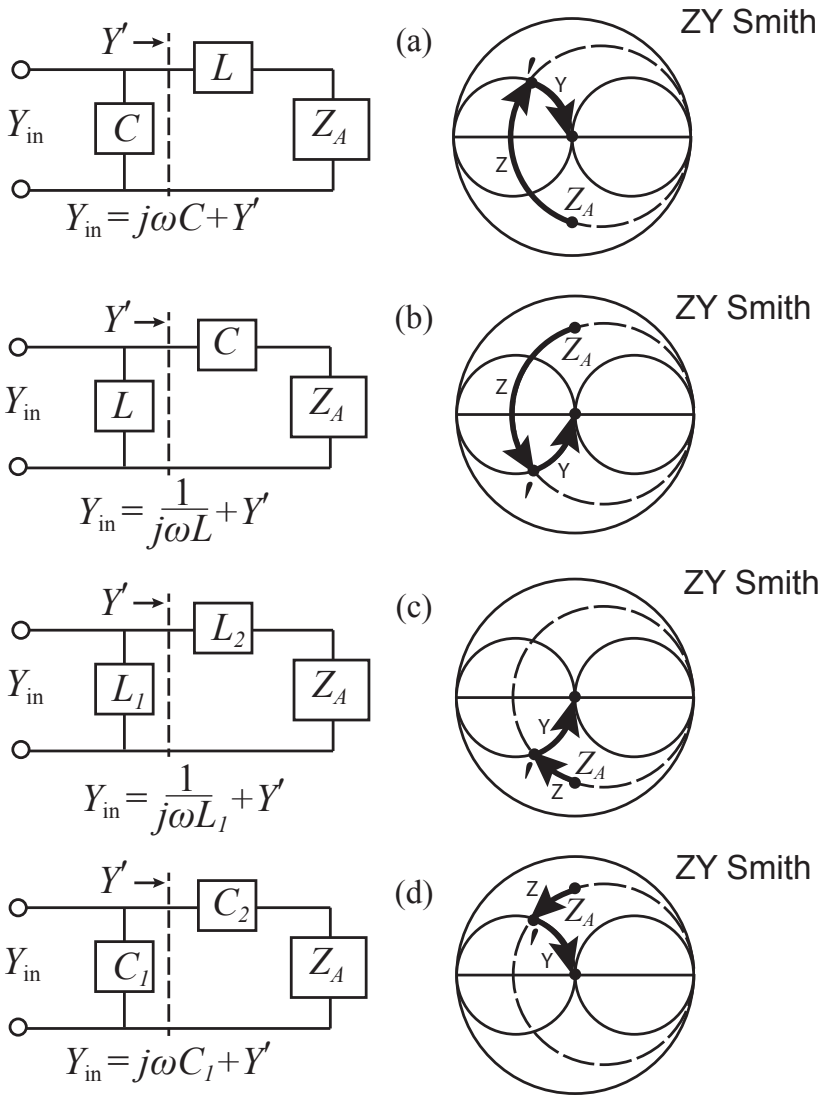

Figure 1.12 Series/parallel L-section matching circuits with corresponding Smith chart diagrams in Z then Y overlay format. The initial matching element is in series with the antenna load impedance Z_A. (a) Series inductor followed by parallel capacitor, (b) Series capacitor followed by parallel inductor, (c) Series inductor followed by parallel inductor, and (d) Series capacitor follwed by parallel capacitor.

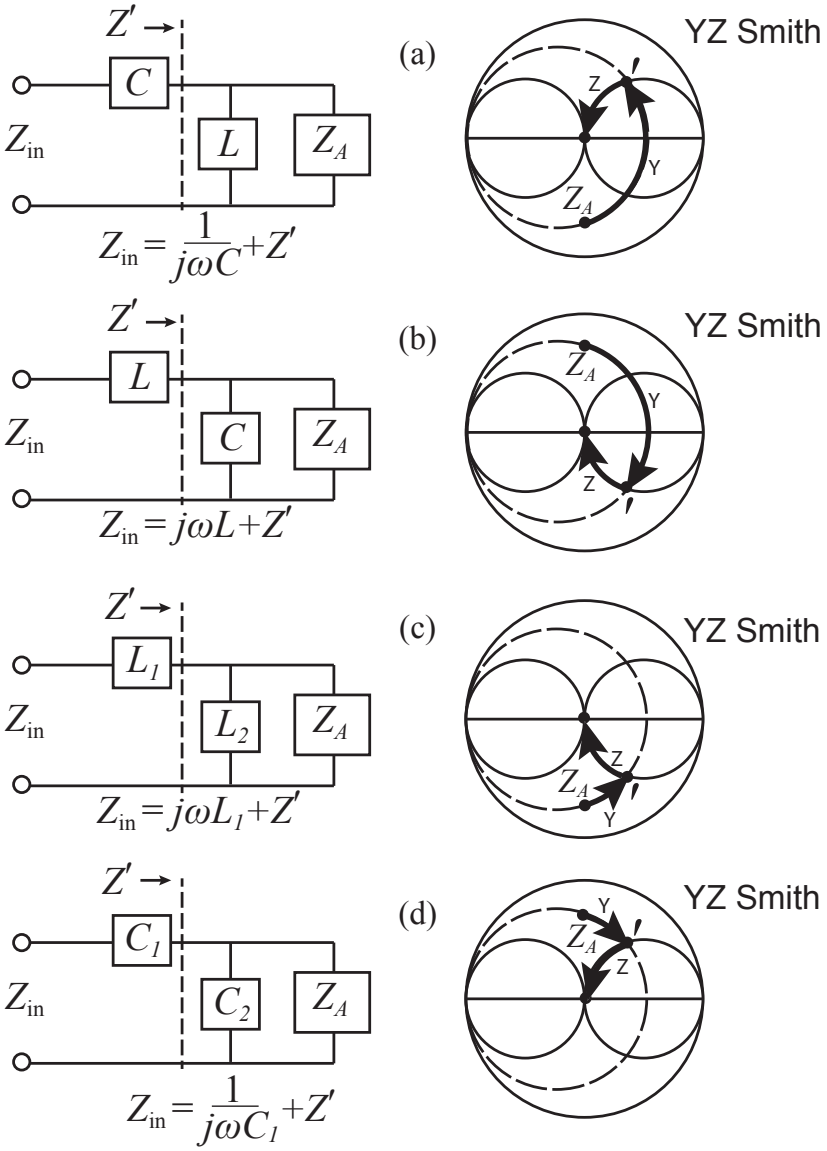

Figure 1.13 Parallel/series L-section matching circuits with corresponding Smith chart diagrams in Y then Z overlay format. The initial matching element is in parallel with the antenna load impedance Z_A. (a) Parallel inductor followed by series capacitor, (b) Parallel capacitor followed by series inductor, (c) Parallel inductor followed by series inductor, and (d) Parallel capacitor followed by series capacitor.

where the S-parameters are related to the voltage waves as

$$b_1 = S_{11}a_1 + S_{12}a_2 \tag{1.55}$$

$$b_2 = S_{21}a_1 + S_{22}a_2 \tag{1.56}$$

Now when $a_2 = 0$ it follows that $S_{11} = b_1/a_1$, and $S_{21} = b_2/a_1$, and when $a_1 = 0$ it follows that $S_{12} = b_1/a_2$, and $S_{22} = b_2/a_2$. In the case of a two-port network, the scattering matrix $\boldsymbol{S}$ provides a relation between the reflected wave parameters at the two ports and the incident wave paramters at the two port. Figure 1.15 shows a signal flow diagram for the scattering matrix S.

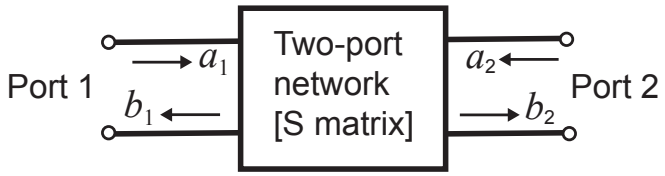

Figure 1.14 Two-port network quantified by the scattering matrix $\boldsymbol{S}$.

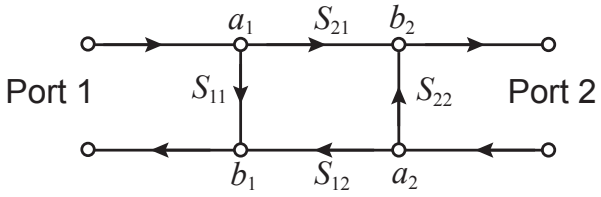

Figure 1.15 Signal flow diagram for the scattering matrix $\boldsymbol{S}$.

Refer now to the previous Figure 1.3, where the matching network is quantified by the scattering matrix S and the antenna (load) is quantified by the reflection coefficient Γ_L. Figure 1.16 shows a signal flow diagram for the scattering matrix matching network where the load impedance characterized by reflection coefficient Γ_L has been added. We want to determine the input reflection coefficient $\Gamma_{\text{in}} = b_1/a_1$. It is observed that two signal paths contribute to the voltage wave at node b_2. At node b_2 the load reflection coefficient acts as a feedback signal equal to $S_{22}\Gamma_L$ Thus, the flow diagram in Figure 1.16 can be reduced to the equivalent flow diagram shown in Figure 1.17 and it follows that

$$b_2 = a_1 S_{21} + b_2 S_{22}\Gamma_L \tag{1.57}$$

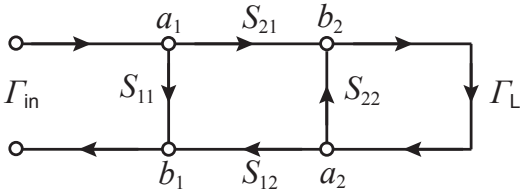

Figure 1.16 Signal flow diagram for the scattering matrix $\boldsymbol{S}$ with load characterized by reflection coefficient Γ_L.

and solving for b_2 yields

$$b_2 = a_1 \frac{S_{21}}{1 - S_{22}\Gamma_L} \tag{1.58}$$

It follows then that the flow diagram in Figure 1.17 can be reduced finally to Figure 1.18. It immediately follows that the input reflection can expressed as

$$\Gamma_{in} = \frac{b_1}{a_1} = S_{11} + \frac{S_{12}S_{21}\Gamma_L}{1 - S_{22}\Gamma_L} \tag{1.59}$$

S-parameters are very useful when only a single network is utilized in

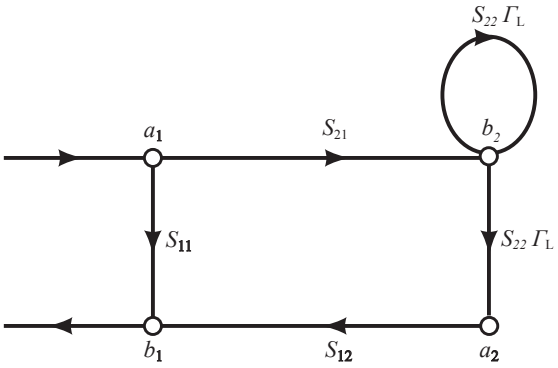

Figure 1.17 Signal flow diagram for the scattering matrix S with the load reflection coefficient included as a feedback loop at node b_2.

matching a transmission line to a load. In the case where casecaded networks are involved, it is necessary to convert the S-parameters to T-chain scattering parameters as discussed in the next section.

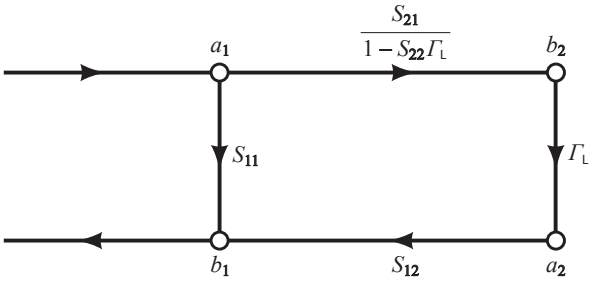

Figure 1.18 Final signal flow diagram for the scattering matrix $\boldsymbol{S}$ combined with the load impedance characterized by the reflection coefficient Γ.

1.2.6 T-Chain Scattering Matrices for Cascaded Networks

T-chain (transfer) scattering matrices [77 – 79] can be used when multiple networks are cascaded. A block diagram of a single T-chain scattering matrix is depicted in Figure (1.19). The T-chain scattering matrix $\boldsymbol{T}$ provides a relation between the incident and reflected waves (a_1 and b_1, respectively) of the input port to the incident and reflected waves (a_2 and b_2, respectively) of the output port. Figure (1.20) shows a block diagram where two T matrices ($\boldsymbol{T}^A$ and $\boldsymbol{T}^B$) are cascaded.

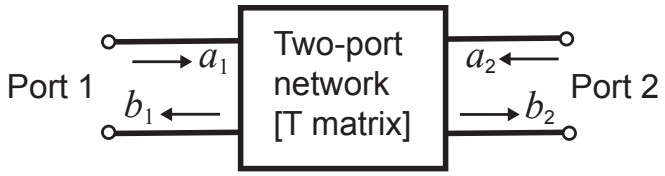

Figure 1.19 Block diagram for a T-chain scattering matrix.

The T-chain scattering matrix is related to the voltage wave parameters as

$$a_1 = T_{11}b_2 + T_{12}a_2 \tag{1.60}$$

$$b_1 = T_{21}b_2 + T_{22}a_2 \tag{1.61}$$

The T-chain scattering matrix parameters can be determined from the S parameters as follows. In the case where $a_2 = 0$ it follows from Equations (1.55), (1.56), and (1.60) that

$$T_{11} = \frac{1}{S_{21}} \tag{1.62}$$

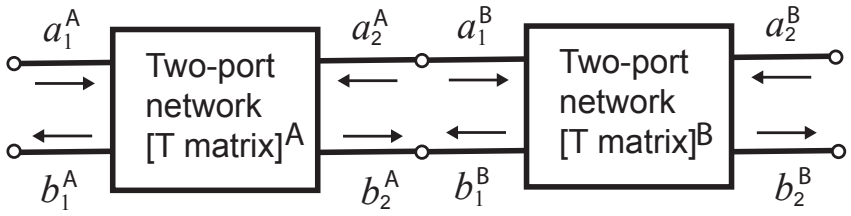

Figure 1.20 Block diagram for cascaded T-chain scattering matrices.

$$T_{21} = \frac{S_{11}}{S_{21}} \tag{1.63}$$

When $a_1 = 0$ it follows from Equation (1.56) and (1.61) that

$$T_{12} = -\frac{S_{22}}{S_{21}} \tag{1.64}$$

$$T_{22} = \frac{S_{12}S_{21} - S_{11}S_{22}}{S_{21}} \tag{1.65}$$

Similarly, the S parameters can be determined from the T-chain scattering parameters as

$$S_{11} = \frac{T_{21}}{T_{11}} \tag{1.66}$$

$$S_{21} = \frac{1}{T_{11}} \tag{1.67}$$

$$S_{12} = \frac{T_{11}T_{22} - T_{12}T_{21}}{T_{11}} \tag{1.68}$$

$$S_{22} = -\frac{T_{12}}{T_{11}} \tag{1.69}$$

Referring now to Figure (1.20) the T-matrices $\boldsymbol{T}^A$ and $\boldsymbol{T}^B$ are expressed in terms of voltage waves as

$$\begin{bmatrix} a_1^A \\ b_1^A \end{bmatrix} = \begin{bmatrix} T_{11}^A & T_{12}^A \\ T_{21}^A & T_{22}^A \end{bmatrix} \begin{bmatrix} b_2^A \\ a_2^A \end{bmatrix} \tag{1.70}$$

$$\begin{bmatrix} a_1^B \\ b_1^B \end{bmatrix} = \begin{bmatrix} T_{11}^B & T_{12}^B \\ T_{21}^B & T_{22}^B \end{bmatrix} \begin{bmatrix} b_2^B \\ a_2^B \end{bmatrix} \tag{1.71}$$

but since

$$\begin{bmatrix} b_2^A \\ a_2^A \end{bmatrix} = \begin{bmatrix} a_1^B \\ b_1^B \end{bmatrix} \tag{1.72}$$

it follows that the cascaded T-chain matrices can be expressed as

$$\begin{bmatrix} a_1^A \\ b_1^A \end{bmatrix} = \begin{bmatrix} T_{11}^A & T_{12}^A \\ T_{21}^A & T_{22}^A \end{bmatrix} \begin{bmatrix} T_{11}^B & T_{12}^B \\ T_{21}^B & T_{22}^B \end{bmatrix} \begin{bmatrix} b_2^B \\ a_2^B \end{bmatrix} \tag{1.73}$$

Thus, the cascaded T-matrix product is given by

$$\boldsymbol{T}^C = \boldsymbol{T}^A \boldsymbol{T}^B \tag{1.74}$$

Once the cascaded T-matrix product $\boldsymbol{T}^C$ has been computed, the S-parameters for the cascaded network can then be determined by Equations (1.66) to (1.69).

1.3 Electromagnetic Radiation: Maxwell's Equations

This section begins with a brief discussion of accelerated charges, time-varying currents, and photons, with the goal of providing a fundamental understanding of the mechanisms of electromagnetic radiation as described mathematically by Maxwell's equations.

Electromagnetic waves are known to be generated by accelerated electron charges or, equivalently, by time-varying currents [1-14]. For example, the time-varying vector current density $\boldsymbol{J}(t)$ with units of amperes/m^2 at a particular cross section of an electrically conducting antenna can be expressed in terms of the volume electric charge density ρ (coulombs/m^3) and the velocity $\boldsymbol{v}(t)$ (m/s) of the charge as

$$\boldsymbol{J}(t) = \rho \boldsymbol{v}(t). \tag{1.75}$$

Thus, the electric current density has units of coulombs per m^2 per second. In Equation (1.75), the local charge density is related to the electron charge (denoted as q_e) times the number of electrons (N_e) accelerated through the local cross section of the antenna, that is,

$$\rho = q_e N_e. \tag{1.76}$$

Taking the derivative of $\boldsymbol{J}(t)$ with respect to time yields

$$\frac{d\boldsymbol{J}(t)}{dt} = \rho\frac{d\boldsymbol{v}(t)}{dt} = \rho\boldsymbol{a}(t) \tag{1.77}$$

where $d\boldsymbol{v}(t)/dt = \boldsymbol{a}(t)$ is the acceleration of the charge with units of m/s^2. Thus, the units of the time derivative of the current density are coulombs per meters squared per second per second, and, as will be shown, radiation occurs when the time derivative of the current density $\boldsymbol{J}$ is nonzero and equivalently when the charge acceleration $\boldsymbol{a}$ is nonzero. The time derivative of the current density and acceleration of charge are of interest in explaining the source of the electromagnetic radiation for antenna systems.

A complete characterization of electromagnetic fields can be determined by means of Maxwell's equations. However, in the process of generating electromagnetic waves, an intermediate process, referred to in the literature as photon emission, occurs and ultimately produces the electromagnetic wave. A photon can be described as a discrete packet of electromagnetic radiation that includes X rays, visible light, and microwaves. The term ionizing radiation refers to radiation that has enough energy to knock electrons out of atoms and includes X rays, protons, heavy ions, and neutrons that are generated by accelerators. Nonionizing radiation includes visible light, ultraviolet (UV) radiation, infrared (IR) radiation, and microwaves. In the case of an antenna receiving an electromagnetic wave, photon absorption and scattering occur with some probability that produces accelerated charges or, equivalently, time-varying currents on the antenna. Here, a brief discussion of the generation and reception of photons and electromagnetic waves is given. A complete mathematical treatment of photon emission and photon absorption is beyond the scope of this book, and the reader is referred to other sources mentioned in the paragraphs below. One situation in which photon/electron interaction is important is in determining the effect of electromagnetic waves on human tissues as a potential safety issue. When the electromagnetic wave frequency is sufficiently high, as is the case for X-ray radiation, the energy in the electromagnetic photons is large enough to break the atom-electron bond and knock out electrons causing damage to the DNA of tissue. Low-level (nonthermal) microwave energy does not contain sufficient photon energy to knock out electrons from tissue, but if the power density is sufficiently high and is applied for a sufficient time interval, it is capable of heating and damaging tissues [96, 97]. The interaction of microwave energy and a wide range of dielectric materials has been investigated in the literature [98].

For RF transmission, when a time-varying signal voltage (e.g., a sinusoidal or pulsed waveform) on a transmission line is applied across the terminals of an antenna, electrons (negatively charged particles) distributed

across the metallic lattice portion of the antenna experience a time-varying vector force, and they accelerate and generate a time-varying electric current. An electron has a negative electric charge equal to $q_e = -1.602 \times 10^{-19}$ coulombs and a rest mass of $m_{oe} = 9.109 \times 10^{-31}$ kg. The RF-induced acceleration of the electrons alters their vector momentum and energy state, which with some probability gives rise to the emission of RF photons, which can be described in a dual nature as particles or waves with zero rest mass ($m_{op} = 0$) and zero electric charge ($q_p = 0$), as described by Cohen-Tannoudji [100, 101]. Each photon has an energy level E (equal to the change in energy level between the excited state and the ground state of an electron) as computed by

$$E = hf \tag{1.78}$$

where $h = 6.626 \times 10^{-34}$J-s is Planck's constant and f is the frequency in cycles per second or Hertz (Hz). For example, the energy of a single microwave photon packet at 300 MHz is computed and rounded as

$$E = (6.626 \times 10^{-34}\text{J-s})(300 \times 10^{6}\text{s}^{-1}) = 2 \times 10^{-25}\text{J}. \tag{1.79}$$

Suppose an antenna is radiating 1 watt or 1 joule per second of microwave power, then the number of 300 MHz microwave photons generated per second is computed as

$$N_{\text{photons per second}} = \frac{1\text{J/s}}{2 \times 10^{-25}\text{J/photon}} = 5 \times 10^{24}. \tag{1.80}$$

Microwave photons are polarized according to the design of the antenna, which can be linear, circular, or elliptically polarized. In free space, RF photons travel at the speed of light, and they have an energy-momentum vector $\boldsymbol{p}$ with amplitude equal to

$$p = \frac{h}{\lambda} = \frac{hf}{c} \tag{1.81}$$

where $\lambda = c/f$ is the wavelength of the photon in free space. It should be noted that the energy-momentum vector $\boldsymbol{p}$ has units of J-s/m.

As microwave power is continuously pumped into the antenna terminals, RF photons are continuously generated and radiated outward from the transmitting antenna. When a sufficient amount and spatial distribution of photons are generated from the radiating antenna, a propagating wavefront, described by an electromagnetic field, is created. Electromagnetic fields (and photons) are characterized by Maxwell's equations, and these fields travel at the speed of light in vacuum and slower than the speed of light in a dielectric medium.

The characteristics of the electromagnetic-field wavefront, such as the spatial distribution of amplitude and phase, signal bandwidth, power density, and polarization, depend on the design of the antenna and the characteristics of the transmitting source. The radiating field will produce a force on any electrical charges that it may encounter. The total time-varying electromagnetic force vector $\boldsymbol{F}(\boldsymbol{r},t)$ at vector position $\boldsymbol{r}$ and time t applied to an electric charge q is given by the Lorentz force equation as described by Jackson [102, p. 3]:

$$\boldsymbol{F}(\boldsymbol{r},t) = q\boldsymbol{E}(\boldsymbol{r},t) + q\boldsymbol{v}(\boldsymbol{r},t)\times\boldsymbol{B}(\boldsymbol{r},t) \tag{1.82}$$

where q is the charge of the particle (in this case an electron), $\boldsymbol{E}$ is the electric-field vector, $\boldsymbol{v}$ is the vector velocity of the charged particle, $\boldsymbol{B}$ is the magnetic flux density, and the symbol $\times$ means vector cross product. Such charges will exist, for example, as electrons in a distant metallic receive antenna for communications or within a metallic or other scattering target in a radar application.

For RF signal reception, when a time-varying electromagnetic field is incident on a metallic antenna, the electrons in the metal experience a time-varying force, as computed by the Lorentz force equation, which accelerates them according to the classical equation

$$\boldsymbol{F}(t) = m\boldsymbol{a}(t) \tag{1.83}$$

or

$$\boldsymbol{a}(t) = \frac{\boldsymbol{F}(t)}{m} \tag{1.84}$$

where $\boldsymbol{a}(t)$ is the acceleration as a function of time and m is the mass of the particle. Equivalently, the photon particles in the incident electromagnetic field are absorbed with some probability by the electrons in the metal, altering the electron momentum and causing acceleration of the electrons. (The interaction of the moving, drifting electrons in the metal is a complex process, but here we only care about the net effect.) For low velocities ($v << c$), using Equation (1.82), the force on the electrons in the metal can be approximated by $\boldsymbol{F}(t) = q\boldsymbol{E}(t)$, and in the case of a sinusoidally varying electric field from Equation (1.84), the force and charge acceleration are time varying in a sinusoidal fashion as well.

The acceleration of the negatively charged electrons induces a time-varying electric current in the metallic antenna, which produces a signal voltage across the antenna terminals connected to the transmission line that is connected to a receiver. The time variation of the electric current in the receive antenna tends to be matched to the time variation of the incident field, depending on the design of the antenna.

The remainder of this section describes the mathematical foundation of Maxwell's equations for computation of electromagnetic fields of antennas. In computing electromagnetic fields, the fundamental photon/electron interaction is not used, but rather the current distribution induced on the antenna or scatterer is the required source of the fields.

To quantify the propagation of an electromagnetic wave from or to an antenna, it is useful to review certain fundamental equations that govern the field characteristics. Assume an isotropic medium that is characterized by a permittivity, denoted ϵ, and a permeability μ. As described in many textbooks on electromagnetic theory, electromagnetic fields can be analyzed by Maxwell's equations [1–14, 102, 103], which provide the relationships between electric and magnetic fields, electric charge, and electric current. Depending on the application, Maxwell's equations can take on many different forms, including differential, integral, source driven, and source free, and take account of many different types of materials both isotropic and anisotropic. An overview of the development of Maxwell's equations is given [4, pp. 45–55]. In time-dependent differential form in the general case for antennas in isotropic media, Maxwell's equations follow from Faraday's law, Ampere's circuital law, Gauss's law for electric fields, and Gauss's law for magnetic fields, respectively, as given by the following curl (denoted $\boldsymbol{\nabla}\times$) and divergence (denoted $\boldsymbol{\nabla}\cdot$) equations:

$$\boldsymbol{\nabla}\times\boldsymbol{E} = -\boldsymbol{M} - \frac{\partial \boldsymbol{B}}{\partial t} \tag{1.85}$$

$$\boldsymbol{\nabla}\times\boldsymbol{H} = \boldsymbol{J} + \frac{\partial \boldsymbol{D}}{\partial t} \tag{1.86}$$

$$\boldsymbol{\nabla}\cdot\boldsymbol{D} = \rho \tag{1.87}$$

$$\boldsymbol{\nabla}\cdot\boldsymbol{B} = \rho_m \tag{1.88}$$

where $\boldsymbol{E} = \boldsymbol{E}(\boldsymbol{r}, t)$ is the vector electric field with units of volts/meter, $\boldsymbol{H} = \boldsymbol{H}(\boldsymbol{r}, t)$ is the vector magnetic field with units of amperes/meter, $\boldsymbol{J} = \boldsymbol{J}(\boldsymbol{r}, t)$ is the electric current density with units of amperes/m^2, $\boldsymbol{M} = \boldsymbol{M}(\boldsymbol{r}, t)$ is the equivalent magnetic current density with units of volts/m^2, ρ is the volume electric charge density with units of coulombs/m^3, and ρ_m is the equivalent volume magnetic charge density with units of webers/m^3, which is usually taken to be zero since magnetic monopoles (charges) have not been observed to date. Bold lettering or bold symbols are used here to represent vectors or vector operations. Bold lettering with an overbar is used to refer to a dyadic (tensor rank two) quantity. Vector and dyadic analyses presented here make use of the theoretical work developed by prior researchers such as summarized by Tai [109 – 112]. In Equation (1.86), the term $\partial \boldsymbol{D}/\partial t$

was introduced as a displacement current density by Maxwell. The previous Maxwell equations take into account the general properties of the linear isotropic material, radiating sources, and fields, all of which can have both spatial and time dependence. The inclusion (for mathematical convenience) of the equivalent magnetic current density $\boldsymbol{M}$ and equivalent volume magnetic charge density ρ_m allows for analysis of aperture fields and other general electromagnetics problems requiring these equivalent quantities. In the prior form of the Maxwell's equations, the time dependence of the electromagnetic fields is arbitrary. For arbitrary antenna geometries, this time-dependent form of the Maxwell equations can be solved via numerical methods such as the finite difference time domain technique. An overview of computational methods for solving Maxwell's equations for the electromagnetic fields is given for example in [2]. For the case in which the material properties are linear, isotropic, and nondispersive, the following constitutive relations hold:

$$\boldsymbol{D}(\boldsymbol{r},t) = \epsilon \boldsymbol{E}(\boldsymbol{r},t) \tag{1.89}$$

where $\boldsymbol{D}$ is the vector electric flux density with units of coulombs/m^2, and ϵ is the permittivity of the material

$$\boldsymbol{B}(\boldsymbol{r},t) = \mu \boldsymbol{H}(\boldsymbol{r},t) \tag{1.90}$$

where $\boldsymbol{B}$ is the vector magnetic flux density with units of webers/m^2, and μ is the permeability of the material. Equations (1.89) and (1.90) are referred to as the constitutive relations, and in this isotropic case, $\boldsymbol{D}$ is parallel to $\boldsymbol{E}$ and $\boldsymbol{B}$ is parallel to $\boldsymbol{H}$. In general, the material properties ϵ and μ are frequency dependent.

In the case in which the material is anisotropic, the constitutive relations are expressed in terms of the material dyadic (tensor) quantities $\overline{\boldsymbol{\epsilon}}$ and $\overline{\boldsymbol{\mu}}$ to convert the vector fields to vector flux densities as

$$\boldsymbol{D}(\boldsymbol{r},t) = \overline{\boldsymbol{\epsilon}} \cdot \boldsymbol{E}(\boldsymbol{r},t) \tag{1.91}$$

$$\boldsymbol{B}(\boldsymbol{r},t) = \overline{\boldsymbol{\mu}} \cdot \boldsymbol{H}(\boldsymbol{r},t) \tag{1.92}$$

where the overbar is used to indicate a dyadic quantity (refer to Section 1.6 for a detailed discussion of dyadics), and the symbol $\cdot$ means dot product. For the anisotropic case, the vector directions of the vector flux densities $\boldsymbol{D}$ and $\boldsymbol{B}$ can be different from the vector directions of the vector fields $\boldsymbol{E}$ and $\boldsymbol{H}$, respectively.

In spherical coordinates, with $\boldsymbol{A} = A_r\hat{\boldsymbol{r}} + A_\theta\hat{\boldsymbol{\theta}} + A_\phi\hat{\boldsymbol{\phi}}$, the curl operation $\boldsymbol{\nabla}\times\boldsymbol{A}$ is given in terms of the unit vectors $\hat{\boldsymbol{r}}, \hat{\boldsymbol{\theta}}, \hat{\boldsymbol{\phi}}$ in convenient

determinant form as

$$\boldsymbol{\nabla}\times\boldsymbol{A} = \frac{1}{r^2\sin\theta}\begin{vmatrix} \hat{\boldsymbol{r}} & r\hat{\boldsymbol{\theta}} & r\sin\theta\hat{\boldsymbol{\phi}} \\ \frac{\partial}{\partial r} & \frac{\partial}{\partial\theta} & \frac{\partial}{\partial\phi} \\ A_r & rA_\theta & r\sin\theta A_\phi \end{vmatrix}. \tag{1.93}$$

Performing the determinant operation in Equation (1.93), the curl operation in expanded form is then given by

$$\begin{aligned}\boldsymbol{\nabla}\times\boldsymbol{A} \quad = \quad & \frac{\hat{\boldsymbol{r}}}{r\sin\theta}\left[\frac{\partial}{\partial\theta}(A_\phi\sin\theta) - \frac{\partial A_\theta}{\partial\phi}\right] + \frac{\hat{\boldsymbol{\theta}}}{r}\left[\frac{1}{\sin\theta}\frac{\partial A_r}{\partial\phi} - \frac{\partial}{\partial r}(rA_\phi)\right] \\ & + \frac{\hat{\boldsymbol{\phi}}}{r}\left[\frac{\partial}{\partial r}(rA_\theta) - \frac{\partial A_r}{\partial\theta}\right].\end{aligned} \tag{1.94}$$

The divergence operation $\boldsymbol{\nabla}\cdot\boldsymbol{A}$ is given by

$$\boldsymbol{\nabla}\cdot\boldsymbol{A} = \frac{1}{r^2}\frac{\partial}{\partial r}(r^2A_r) + \frac{1}{r\sin\theta}\frac{\partial}{\partial\theta}(A_\theta\sin\theta) + \frac{1}{r\sin\theta}\frac{\partial}{\partial\phi}(A_\phi). \tag{1.95}$$

Additionally, note that the vector cross product in spherical coordinates is given by

$$\boldsymbol{A}\times\boldsymbol{B} = \begin{bmatrix} \hat{\boldsymbol{r}} & \hat{\boldsymbol{\theta}} & \hat{\boldsymbol{\phi}} \\ A_r & A_\theta & A_\phi \\ B_r & B_\theta & B_\phi \end{bmatrix}. \tag{1.96}$$

Substituting Equations (1.89) and (1.90) into Equations (1.85) and (1.86), respectively, yields an alternate representation of Maxwell's equations:

$$\boldsymbol{\nabla}\times\boldsymbol{E} = -\boldsymbol{M} - \mu\frac{\partial\boldsymbol{H}}{\partial t} \tag{1.97}$$

$$\boldsymbol{\nabla}\times\boldsymbol{H} = \boldsymbol{J} + \epsilon\frac{\partial\boldsymbol{E}}{\partial t} \tag{1.98}$$

$$\boldsymbol{\nabla}\cdot\boldsymbol{D} = \rho \tag{1.99}$$

$$\boldsymbol{\nabla}\cdot\boldsymbol{B} = \rho_m. \tag{1.100}$$

An equation for expressing the continuity of electrical charge can be derived by taking the divergence of Maxwell's curl equation for the magnetic field, ($\boldsymbol{\nabla}\cdot\boldsymbol{\nabla}\times\boldsymbol{H}$), and applying Gauss's law for electric fields (Equation (1.99)), and using the property that the divergence of the curl of any vector is zero, with the result

$$\boldsymbol{\nabla}\cdot\boldsymbol{J}(\boldsymbol{r},t) = -\frac{\partial\rho(\boldsymbol{r},t)}{\partial t}. \tag{1.101}$$

The continuity equation given by Equation (1.101) indicates that the divergence of the electric current density $\boldsymbol{J}$ depends on the time rate of change of the charge density. Similarly, an equation for expressing the continuity of equivalent magnetic charge can be derived by taking the divergence of Maxwell's curl equation for the electric field, applying Gauss's law for magnetic fields, and using the property that the divergence of the curl of any vector is zero, with the result

$$\boldsymbol{\nabla}\cdot\boldsymbol{M}(\boldsymbol{r},t) = -\frac{\partial \rho_m(\boldsymbol{r},t)}{\partial t}. \tag{1.102}$$

The continuity equation given by Equation (1.102) indicates that the divergence of the equivalent magnetic current density $\boldsymbol{M}$ depends on the time rate of change of the equivalent magnetic charge density ρ_m.

The electric current density $\boldsymbol{J}$ in Equation (1.98) can be composed of a source current $\boldsymbol{J}_{\text{source}}$ and a conduction current $\boldsymbol{J}_c$ as

$$\boldsymbol{J} = \boldsymbol{J}_{\text{source}} + \boldsymbol{J}_c. \tag{1.103}$$

For a conducting medium with electrical conductivity σ having units of siemens/meter (amperes per volt-meter), the conducting current density $\boldsymbol{J}_c$ and electric field $\boldsymbol{E}$ are related as

$$\boldsymbol{J}_c = \sigma \boldsymbol{E}, \tag{1.104}$$

which is Ohm's law for conducting current density. Note that electrical conductivity is equal to the reciprocal of electrical resistivity. In free space, it should be noted that $\sigma = 0$.

Similarly, the equivalent magnetic current density $\boldsymbol{M}$ in Equation (1.97) can be composed of an equivalent magnetic source current $\boldsymbol{M}_{\text{source}}$ and an equivalent magnetic conduction current expressed as

$$\boldsymbol{M}_c = \sigma_m \boldsymbol{H} \tag{1.105}$$

where σ_m is the magnetic conductivity that has units of ohms per meter.

Thus, in the case of a lossy dielectric material, the electric current density can be expressed as

$$\boldsymbol{J} = \boldsymbol{J}_{\text{source}} + \sigma \boldsymbol{E}. \tag{1.106}$$

Similarly, in the case of a lossy magnetic material, the magnetic current density can be written as

$$\boldsymbol{M} = \boldsymbol{M}_{\text{source}} + \sigma_m \boldsymbol{H}. \tag{1.107}$$

In summary, the source currents $\boldsymbol{J}_{\text{source}}$ and $\boldsymbol{M}_{\text{source}}$ produce the electromagnetic fields, which then induce a corresponding conduction current density.

Substituting Equations (1.106) and (1.107) into Maxwell's curl equations given by Equations (1.97) and (1.98) yields an alternate form of Maxwell's equations as

$$\boldsymbol{\nabla}\times\boldsymbol{E} = -\boldsymbol{M}_{\text{source}} - \sigma_m\boldsymbol{H} - \mu\frac{\partial\boldsymbol{H}}{\partial t} \tag{1.108}$$

$$\boldsymbol{\nabla}\times\boldsymbol{H} = \boldsymbol{J}_{\text{source}} + \sigma\boldsymbol{E} + \epsilon\frac{\partial\boldsymbol{E}}{\partial t} \tag{1.109}$$

$$\boldsymbol{\nabla}\cdot\boldsymbol{D} = \rho \tag{1.110}$$

$$\boldsymbol{\nabla}\cdot\boldsymbol{B} = \rho_m. \tag{1.111}$$

The instantaneous electric and magnetic fields, as a function of spatial position (x, y, z) or position vector $(\boldsymbol{r})$ and time t, are real functions, and for the time-harmonic case, they are sinusoidal (or cosinusoidal) and can be expressed as

$$\boldsymbol{E}(\boldsymbol{r}, t) = |\boldsymbol{E}(\boldsymbol{r})|\cos(\omega t + \psi(r)) = |\boldsymbol{E}(\boldsymbol{r})|\cos(\omega t - kr) \tag{1.112}$$

$$\boldsymbol{H}(\boldsymbol{r}, t) = |\boldsymbol{H}(\boldsymbol{r})|\cos(\omega t + \psi(r)) = |\boldsymbol{H}(\boldsymbol{r})|\cos(\omega t - kr) \tag{1.113}$$

where $\psi(r) = -kr$ is the spatial phase variation of the electric and magnetic fields, with $k = 2\pi/\lambda = \omega\sqrt{\mu\epsilon}$ the wavenumber, and $\omega = 2\pi f$ is the radian frequency, where f is the frequency. The time-harmonic fields can be extended to most waveforms by utilizing standard Fourier transform techniques. Equivalently, the instantaneous electric and magnetic fields can be written in a more convenient exponential form in terms of the non-time-varying complex electric and magnetic fields $\boldsymbol{E}(\boldsymbol{r})$ and $\boldsymbol{H}(\boldsymbol{r})$ as

$$\boldsymbol{E}(\boldsymbol{r}, t) = \text{Re}[\boldsymbol{E}(\boldsymbol{r})e^{j\omega t}] \tag{1.114}$$

$$\boldsymbol{H}(\boldsymbol{r}, t) = \text{Re}[\boldsymbol{H}(\boldsymbol{r})e^{j\omega t}] \tag{1.115}$$

where $\text{Re}[\cdot]$ indicates the real part. Note that the $e^{j\omega t}$ convention used here throughout is common to the electrical engineering convention; however, in cases for which the $e^{-i\omega t}$ convention would be used, the equations presented here can be converted by simply interchanging $j\omega t$ with $-i\omega t$. Similarly, the instantaneous electric current density $\boldsymbol{J}$ and equivalent magnetic current density $\boldsymbol{M}$ can be written as

$$\boldsymbol{J}(\boldsymbol{r}, t) = \text{Re}[\boldsymbol{J}(\boldsymbol{r})e^{j\omega t}] \tag{1.116}$$

$$\boldsymbol{M}(\boldsymbol{r},t) = \text{Re}[\boldsymbol{M}(\boldsymbol{r})e^{j\omega t}]. \tag{1.117}$$

The time-dependent fields can also be expressed in terms of the magnitude and phase of the fields as

$$\boldsymbol{E}(\boldsymbol{r},t) = \text{Re}[|\boldsymbol{E}(\boldsymbol{r})|e^{j(\omega t+\psi(r))}] \tag{1.118}$$

$$\boldsymbol{H}(\boldsymbol{r},t) = \text{Re}[|\boldsymbol{H}(\boldsymbol{r})|e^{j(\omega t+\psi(r))}]. \tag{1.119}$$

If the Re[·] operation in Equations (1.118) and (1.119) is dropped and the $e^{j\omega t}$ factor is suppressed, then the following phasor designations for the electric and magnetic fields can also be used:

$$\boldsymbol{E}(\boldsymbol{r}) = |\boldsymbol{E}(\boldsymbol{r})|e^{j\psi(r)} \tag{1.120}$$

$$\boldsymbol{H}(\boldsymbol{r}) = |\boldsymbol{H}(\boldsymbol{r})|e^{j\psi(r)}. \tag{1.121}$$

In Equations (1.120) and (1.121), the magnitudes $|\boldsymbol{E}(\boldsymbol{r})|$ and $|\boldsymbol{H}(\boldsymbol{r})|$ represent the envelope of the electric and magnetic fields, respectively.

In an electrically conducting medium, the electric flux density $\boldsymbol{D}$ is given by

$$\boldsymbol{D}(\boldsymbol{r},t) = \epsilon'\boldsymbol{E}(\boldsymbol{r},t) \tag{1.122}$$

where ϵ' is the real part of the complex permittivity of the medium. Similarly, in a magnetically conducting medium, the magnetic flux density $\boldsymbol{B}$ is given by

$$\boldsymbol{B}(\boldsymbol{r},t) = \mu'\boldsymbol{H}(\boldsymbol{r},t) \tag{1.123}$$

where μ' is the real part of the complex permeability of the medium.

With the prior relations, it is now possible to convert Maxwell's equations to a time-harmonic form as follows. This form of the Maxwell equations is particularly amenable to solution via numerical methods such as the method of moments. Substituting Equations (1.114), (1.115), (1.122), (1.123), and (1.116) into Equations (1.97) and (1.98) yields

$$\boldsymbol{\nabla}\times\text{Re}[\boldsymbol{E}(\boldsymbol{r})e^{j\omega t}] = -\text{Re}[\boldsymbol{M}(\boldsymbol{r})e^{j\omega t}] - \frac{\partial}{\partial t}\text{Re}[\mu'\boldsymbol{H}(\boldsymbol{r})e^{j\omega t}] \tag{1.124}$$

$$\boldsymbol{\nabla}\times\text{Re}[\boldsymbol{H}(\boldsymbol{r})e^{j\omega t}] = \text{Re}[\boldsymbol{J}(\boldsymbol{r})e^{j\omega t}] + \frac{\partial}{\partial t}\text{Re}[\epsilon'\boldsymbol{E}(\boldsymbol{r})e^{j\omega t}] \tag{1.125}$$

and computing the partial derivatives, and noting that the real operation commutes with the partial derivative operation, yields

$$\text{Re}\boldsymbol{\nabla}\times[\boldsymbol{E}(\boldsymbol{r})e^{j\omega t}] = -\text{Re}[\boldsymbol{M}(\boldsymbol{r})e^{j\omega t}] - \text{Re}[j\omega\mu'\boldsymbol{H}(\boldsymbol{r})e^{j\omega t}] \tag{1.126}$$

$$\text{Re}\boldsymbol{\nabla}\times[\boldsymbol{H}(\boldsymbol{r})e^{j\omega t}] = \text{Re}[\boldsymbol{J}(\boldsymbol{r})e^{j\omega t}] + \text{Re}[j\omega\epsilon'\boldsymbol{E}(\boldsymbol{r})e^{j\omega t}]. \tag{1.127}$$

The previous two equations can be simplified by dropping the real (Re) operation and suppressing the exponential function $e^{j\omega t}$ that are common to all terms, with the result for Maxwell's equations in time-harmonic (frequency domain) form

$$\boldsymbol{\nabla}\times\boldsymbol{E} = -\boldsymbol{M} - j\omega\mu'\boldsymbol{H} \tag{1.128}$$

$$\boldsymbol{\nabla}\times\boldsymbol{H} = \boldsymbol{J} + j\omega\epsilon'\boldsymbol{E} \tag{1.129}$$

$$\boldsymbol{\nabla}\cdot\boldsymbol{D} = \rho \tag{1.130}$$

$$\boldsymbol{\nabla}\cdot\boldsymbol{B} = \rho_m. \tag{1.131}$$

In the prior Maxwell's equations, the real part of the complex permeability can be expressed as

$$\mu' = \mu'_r\mu_o \tag{1.132}$$

where μ'_r is the relative permeability and μ_o is the permeability of free space. The real part of the complex permittivity is expressed as

$$\epsilon' = \epsilon'_r\epsilon_o \tag{1.133}$$

where ϵ'_r is the dielectric constant (relative permittivity) and ϵ_o is the permittivity of free space. In free space, the speed of light c (also the speed of electromagnetic wave propagation) is related to ϵ_o and μ_o as

$$c = \frac{1}{\sqrt{\mu_o\epsilon_o}} \tag{1.134}$$

and has a measured value of approximately 2.99792458×10^8 m/s $\approx 3.0 \times 10^8$ m/s. The value of ϵ_o can be measured by an experiment involving Coulomb's force law for two charges separated by a distance [4, p. 61]. The established value for the permittivity of free space is $\epsilon_o = \frac{1}{36\pi} \times 10^{-9} = 8.8542 \times 10^{-12}$ farads/meter (farads have units of amperes-seconds/volts). The established value for the permeability of free space is $\mu_o = 4\pi \times 10^{-7} = 1.257 \times 10^{-6}$ henries/meter (henries have units of volts-seconds/ampere).

To determine the speed of electromagnetic wave propagation, consider now Equations (1.112) and (1.113) and follow a constant phase point along the electromagnetic wavefront. Then taking the derivative with respect to time of the argument of the cosine function set equal to a constant yields

$$\frac{d}{dt}(\omega t - kr) = \omega - k\frac{dr}{dt} = 0 \tag{1.135}$$

or in free space

$$\frac{dr}{dt} = \frac{\omega}{k} = \frac{\omega}{\omega\sqrt{\mu_o \epsilon_o}} = c, \tag{1.136}$$

which shows that the time-harmonic electromagnetic fields travel at the speed of light.

For an electrically conducting medium, the electrical conducting current density $\boldsymbol{J}_c$ and electric field $\boldsymbol{E}$ are related by Equation (1.104). When a source $\boldsymbol{J}_{\text{source}}$ is present, substituting Equations (1.103) and (1.104) into Equation (1.129) yields

$$\boldsymbol{\nabla} \times \boldsymbol{H} = \boldsymbol{J}_{\text{source}} + (\sigma + j\omega\epsilon')\boldsymbol{E}. \tag{1.137}$$

In Equation (1.137), the quantity $(\sigma + j\omega\epsilon')$ can be expressed as a complex electrical conductivity σ_c as

$$\sigma + j\omega\epsilon' = \sigma' + j\sigma'' = \sigma_c \tag{1.138}$$

where it is observed that the real part of σ_c is $\sigma' = \sigma$ and the imaginary part is $\sigma'' = \omega\epsilon'$.

The electrical conductivity σ of the dielectric medium can be expressed in terms of the imaginary component (denoted ϵ'') of the complex permittivity as

$$\sigma = \omega\epsilon'' = \omega\epsilon_o\epsilon_r'' \tag{1.139}$$

where ϵ_r'' is the relative imaginary component of the complex permittivity. Thus, using Equations (1.133) and (1.139), it follows that Equation (1.137) can be expressed as

$$\boldsymbol{\nabla} \times \boldsymbol{H} = \boldsymbol{J}_{\text{source}} + (j\omega\epsilon_o\epsilon_r' + \omega\epsilon_o\epsilon_r'')\boldsymbol{E}, \tag{1.140}$$

which can be written in an alternate form (by factoring the quantity $j\omega\epsilon_o$) as

$$\boldsymbol{\nabla} \times \boldsymbol{H} = \boldsymbol{J}_{\text{source}} + j\omega\epsilon_o(\epsilon_r' - j\epsilon_r'')\boldsymbol{E}. \tag{1.141}$$

In Equation (1.141), the complex permittivity of the conducting medium can be expressed in terms of real and imaginary components as

$$\epsilon_c = \epsilon' - j\epsilon'' = \epsilon_o(\epsilon_r' - j\epsilon_r''). \tag{1.142}$$

Similarly, the complex permeability can be defined in terms of real and imaginary components as

$$\mu_c = \mu' - j\mu'' = \mu_o(\mu_r' - j\mu_r''). \tag{1.143}$$

Thus, Equation (1.141) can be written in a simplified form in terms of the complex permittivity given by Equation (1.142) as

$$\boldsymbol{\nabla}\times\boldsymbol{H} = \boldsymbol{J}_{\text{source}} + j\omega\epsilon_c\boldsymbol{E}. \tag{1.144}$$

By using the above mathematical development and a similar development for equivalent magnetic current, an explicit representation of Maxwell's equations in time-harmonic (frequency domain) form can be written in terms of source currents as

$$\boldsymbol{\nabla}\times\boldsymbol{E} = -\boldsymbol{M}_{\text{source}} - j\omega\mu_c\boldsymbol{H} \tag{1.145}$$

$$\boldsymbol{\nabla}\times\boldsymbol{H} = \boldsymbol{J}_{\text{source}} + j\omega\epsilon_c\boldsymbol{E} \tag{1.146}$$

$$\boldsymbol{\nabla}\cdot\boldsymbol{D} = \rho \tag{1.147}$$

$$\boldsymbol{\nabla}\cdot\boldsymbol{B} = \rho_m. \tag{1.148}$$

In the above form of Maxwell's equations, the electric conduction current has effectively been folded into the complex permittivity quantity.

By comparing the Maxwell curl of $\boldsymbol{H}$ equations given by Equations (1.137) and (1.146), the following relations can be determined:

$$j\omega\epsilon_c = \sigma + j\omega\epsilon' \tag{1.149}$$

and solving for ϵ_c yields

$$\epsilon_c = \epsilon' - j\frac{\sigma}{\omega} = \epsilon' - j\epsilon''. \tag{1.150}$$

Thus,

$$\epsilon'' = \frac{\sigma}{\omega} \tag{1.151}$$

and it follows from Equation (1.142) that

$$\epsilon_c = \epsilon_o(\epsilon_r' - j\frac{\sigma}{\omega\epsilon_o}), \tag{1.152}$$

which can be rewritten as

$$\epsilon_c = \epsilon_o\epsilon_r'(1 - j\frac{\sigma}{\omega\epsilon_o\epsilon_r'}) \tag{1.153}$$

or as

$$\epsilon_c = \epsilon_o\epsilon_r'(1 - j\frac{\sigma}{\omega\epsilon'}). \tag{1.154}$$

Next, defining the loss tangent as

$$\tan\delta = \frac{\sigma}{\omega\epsilon'}, \tag{1.155}$$

the complex permittivity can be expressed as

$$\epsilon_c = \epsilon_o\epsilon_r'(1 - j\tan\delta). \tag{1.156}$$

1.4 Fields from Time-Varying Electric and Magnetic Current Sources

In this section, Maxwell's equations (described in the previous section) are used to formulate the radiated electromagnetic fields from time-varying electric and magnetic current sources. A detailed derivation is given for the case of electric current sources, and the result is simply stated for magnetic current sources.

Maxwell's equations as given by Equations (1.97–1.100) can be expressed in the time domain in terms of the current densities $\boldsymbol{J}$ and $\boldsymbol{M}$ as

$$\boldsymbol{\nabla}\times\boldsymbol{E}(\boldsymbol{r},t) = -\boldsymbol{M}(\boldsymbol{r},t) - \mu\frac{\partial\boldsymbol{H}(\boldsymbol{r},t)}{\partial t} \tag{1.157}$$

$$\boldsymbol{\nabla}\times\boldsymbol{H}(\boldsymbol{r},t) = \boldsymbol{J}(\boldsymbol{r},t) + \epsilon\frac{\partial\boldsymbol{E}(\boldsymbol{r},t)}{\partial t} \tag{1.158}$$

$$\boldsymbol{\nabla}\cdot\boldsymbol{D}(\boldsymbol{r},t) = \rho \tag{1.159}$$

$$\boldsymbol{\nabla}\cdot\boldsymbol{B}(\boldsymbol{r},t) = \rho_m. \tag{1.160}$$

It was mentioned at the start of the previous section that the source of electromagnetic radiation is the time-varying current, which is equal to the acceleration of charges. To demonstrate this fact, the following derivation can be made by using Maxwell's curl equations and a vector identity. Starting with the curl of Maxwell's curl of $\boldsymbol{E}$ equation with the equivalent magnetic current source equal to zero, that is, $\boldsymbol{M}_{\text{source}} = 0$ and the equivalent magnetic charge equal to zero ($\rho_m = 0$), and assuming free space, that is, $\mu = \mu_o$, $\epsilon = \epsilon_o$, $\sigma = 0$, and $\boldsymbol{J}_c = 0$ so $\boldsymbol{J} = \boldsymbol{J}_{\text{source}}$,

$$\boldsymbol{\nabla}\times\boldsymbol{\nabla}\times\boldsymbol{E} = -\mu_o\frac{\partial}{\partial t}\boldsymbol{\nabla}\times\boldsymbol{H} \tag{1.161}$$

and substituting Maxwell's curl of $\boldsymbol{H}$ equation expressed as

$$\boldsymbol{\nabla}\times\boldsymbol{H} = \boldsymbol{J} + \epsilon_o\frac{\partial\boldsymbol{E}}{\partial t} \tag{1.162}$$

yields

$$\boldsymbol{\nabla}\times\boldsymbol{\nabla}\times\boldsymbol{E} - \mu_o\epsilon_o\frac{\partial^2\boldsymbol{E}}{\partial t^2} = -\mu_o\frac{\partial}{\partial t}\boldsymbol{J}. \tag{1.163}$$

Now use the vector identity

$$\boldsymbol{\nabla}\times\boldsymbol{\nabla}\times\boldsymbol{E} = \boldsymbol{\nabla}(\boldsymbol{\nabla}\cdot\boldsymbol{E}) - \boldsymbol{\nabla}^2\boldsymbol{E} \tag{1.164}$$

where

$$\boldsymbol{\nabla}^2 = \boldsymbol{\nabla}\cdot\boldsymbol{\nabla} \tag{1.165}$$

is the Laplacian operator, such that Equation (1.163) becomes

$$\boldsymbol{\nabla}(\boldsymbol{\nabla}\cdot\boldsymbol{E}) - \boldsymbol{\nabla}^2\boldsymbol{E} - \mu_o\epsilon_o\frac{\partial^2\boldsymbol{E}}{\partial t^2} = -\mu_o\frac{\partial}{\partial t}\boldsymbol{J}. \tag{1.166}$$

It should be noted that the quantity $\boldsymbol{\nabla}^2\boldsymbol{E} = \boldsymbol{\nabla}\cdot\boldsymbol{\nabla}\boldsymbol{E}$ yields a vector. The quantity $\boldsymbol{\nabla}\boldsymbol{E}$ yields a dyadic (tensor of order two), and then taking the divergence of the dyadic yields a vector. The left-hand side of Equation (1.166) contains expressions involving the electric field $\boldsymbol{E}$ and the right-hand side is a function of the derivative of the time-varying current density $\boldsymbol{J}$. Thus, Equation (1.166) is inhomogeneous and it explicitly shows that the time derivative of the electric current density $\boldsymbol{J}(t)$ is a source of electromagnetic radiation. Substituting Equation (1.77) in Equation (1.166) yields

$$\boldsymbol{\nabla}(\boldsymbol{\nabla}\cdot\boldsymbol{E}) - \boldsymbol{\nabla}^2\boldsymbol{E} - \mu_o\epsilon_o\frac{\partial^2\boldsymbol{E}}{\partial t^2} = -\mu_o\rho\boldsymbol{a}, \tag{1.167}$$

which explicitly shows that the charge ρ with acceleration $\boldsymbol{a}$ is a source of electromagnetic radiation, as desired. Furthermore, in free space, using Equation (1.134) in Equation (1.167) yields the following inhomogeneous equation in terms of the speed of light with the accelerated charge as the driving function for the operations on the electric field:

$$\boldsymbol{\nabla}(\boldsymbol{\nabla}\cdot\boldsymbol{E}) - \boldsymbol{\nabla}^2\boldsymbol{E} - \frac{1}{c^2}\frac{\partial^2\boldsymbol{E}}{\partial t^2} = -\mu_o\rho\boldsymbol{a}. \tag{1.168}$$

When both $\rho = 0$ and $\boldsymbol{J} = 0$, that is, there are no local sources, Equations (1.166) to (1.168) reduce to the homogeneous wave equation form as

$$\boldsymbol{\nabla}^2\boldsymbol{E} - \frac{1}{c^2}\frac{\partial^2\boldsymbol{E}}{\partial t^2} = 0, \tag{1.169}$$

and similarly it can be shown that

$$\boldsymbol{\nabla}^2\boldsymbol{H} - \frac{1}{c^2}\frac{\partial^2\boldsymbol{H}}{\partial t^2} = 0. \tag{1.170}$$

Equations (1.169) and (1.170) indicate that in free space the electromagnetic field exists and is self-sustaining and propagating at the speed of light in the absence of local driving sources.

While Equations (1.166) to (1.168) indicate a source of the electromagnetic radiation, to compute the electromagnetic fields from the electric current

density $\boldsymbol{J}$ for a practical antenna, it is necessary to determine an expression for $\boldsymbol{E}$ in terms of $\boldsymbol{J}$.

Consider now, in the frequency domain, the derivation of the electromagnetic fields caused by an electric current source $\boldsymbol{J}$ radiating in an infinite space described by the complex parameters $\mu = \mu_c$ and $\epsilon = \epsilon_c$ (note: although represented here as scalar quantities, μ and ϵ can also be dyadic [tensor] quantities). There are two ways to arrive at the desired expression for $\boldsymbol{E}$ in terms of a volume integral involving $\boldsymbol{J}$. One way starts with the traditional magnetic vector potential approach, as derived in the time-harmonic form [2], and with this approach, the scalar Green's function for isotropic media is used. The other approach is to use the dyadic Green's function approach as described by Tai [109] and Kong [3]. The Green's function characterizes the response to a point source and essentially allows the current density distribution to be integrated in such a way as to determine the electromagnetic field distribution in the surrounding space. Both approaches using the scalar Green's function and the dyadic Green's function are described, respectively, in the next two sections.

1.4.1 Magnetic Vector Potential and the Scalar Green's Function

Starting with the Maxwell divergence equation for the time-harmonic magnetic field (Equation [1.131]) with the equivalent magnetic charge density equal to zero yields

$$\boldsymbol{\nabla}\cdot\boldsymbol{B} = \boldsymbol{\nabla}\cdot\mu\boldsymbol{H} = 0, \tag{1.171}$$

that is,

$$\boldsymbol{\nabla}\cdot\boldsymbol{H} = 0. \tag{1.172}$$

Since the divergence of the vector magnetic field is zero, the vector magnetic field has only circulation and is called a solenoidal field, which can be expressed in terms of the curl of another function by a vector identity. Now, define the magnetic flux density $\boldsymbol{B}$ in terms of the curl of a magnetic vector potential function $\boldsymbol{A}$ as

$$\boldsymbol{B} = \mu\boldsymbol{H} = \boldsymbol{\nabla}\times\boldsymbol{A}. \tag{1.173}$$

Thus, the magnetic field $\boldsymbol{H}$ in terms of $\boldsymbol{A}$ is just

$$\boldsymbol{H} = \frac{1}{\mu}\boldsymbol{\nabla}\times\boldsymbol{A}. \tag{1.174}$$

Substituting this result in Maxwell's curl of $\boldsymbol{E}$ Equation (1.128) yields

$$\boldsymbol{\nabla}\times\boldsymbol{E} = -j\omega\mu\boldsymbol{H} = -j\omega\boldsymbol{\nabla}\times\boldsymbol{A}, \tag{1.175}$$

which can be rewritten as

$$\boldsymbol{\nabla}\times[\boldsymbol{E}+j\omega\boldsymbol{A}]=0. \tag{1.176}$$

Making use of the general vector identity

$$\boldsymbol{\nabla}\times\boldsymbol{\nabla}\Phi=0 \tag{1.177}$$

where Φ is defined as the electric scalar potential, allows Equation (1.176) to be written as

$$\boldsymbol{\nabla}\times[\boldsymbol{E}+j\omega\boldsymbol{A}]=-\boldsymbol{\nabla}\times\boldsymbol{\nabla}\Phi \tag{1.178}$$

or as

$$\boldsymbol{E}+j\omega\boldsymbol{A}=-\boldsymbol{\nabla}\Phi, \tag{1.179}$$

and solving for $\boldsymbol{E}$ as

$$\boldsymbol{E}=-j\omega\boldsymbol{A}-\boldsymbol{\nabla}\Phi. \tag{1.180}$$

Now use the vector identity

$$\boldsymbol{\nabla}\times\boldsymbol{\nabla}\times\boldsymbol{A}=\boldsymbol{\nabla}(\boldsymbol{\nabla}\cdot\boldsymbol{A})-\boldsymbol{\nabla}^2\boldsymbol{A} \tag{1.181}$$

such that from Equation (1.173)

$$\boldsymbol{\nabla}\times(\mu\boldsymbol{H})=\boldsymbol{\nabla}(\boldsymbol{\nabla}\cdot\boldsymbol{A})-\boldsymbol{\nabla}^2\boldsymbol{A} \tag{1.182}$$

and for a homogeneous medium

$$\mu\boldsymbol{\nabla}\times\boldsymbol{H}=\boldsymbol{\nabla}(\boldsymbol{\nabla}\cdot\boldsymbol{A})-\boldsymbol{\nabla}^2\boldsymbol{A}. \tag{1.183}$$

Now using the Maxwell curl equation for the magnetic field, that is,

$$\boldsymbol{\nabla}\times\boldsymbol{H}=\boldsymbol{J}+j\omega\epsilon\boldsymbol{E}, \tag{1.184}$$

Equation (1.183) can now be written as

$$\mu\boldsymbol{J}+j\omega\mu\epsilon\boldsymbol{E}=\boldsymbol{\nabla}(\boldsymbol{\nabla}\cdot\boldsymbol{A})-\boldsymbol{\nabla}^2\boldsymbol{A}. \tag{1.185}$$

Substituting Equation (1.180) in Equation (1.185) yields

$$\boldsymbol{\nabla}^2\boldsymbol{A}+\omega^2\mu\epsilon\boldsymbol{A}=-\mu\boldsymbol{J}+\boldsymbol{\nabla}(\boldsymbol{\nabla}\cdot\boldsymbol{A}+j\omega\mu\epsilon\Phi). \tag{1.186}$$

Next, applying the divergence operation on the electric field vector in Equation (1.180) as $\boldsymbol{\nabla}\cdot\boldsymbol{E}$ and using Maxwell's equation $\boldsymbol{\nabla}\cdot\boldsymbol{E}=\rho/\epsilon$ yields

$$\boldsymbol{\nabla}^2\Phi+j\omega\boldsymbol{\nabla}\cdot\boldsymbol{A}=-\rho/\epsilon. \tag{1.187}$$

In order to uncouple, simplify, and produce a wave-equation form of Equations (1.186) and (1.187), the Lorenz condition [102, p. 240] can be invoked, that is,

$$\boldsymbol{\nabla}\cdot\boldsymbol{A} = -j\omega\mu\epsilon\Phi. \tag{1.188}$$

It should be noted that the Lorenz condition is consistent with the conservation of electric current and charge density as in the continuity equation from Equation (1.101) expressed in time-harmonic form as (see the discussion following Equation [1.201])

$$\boldsymbol{\nabla}\cdot\boldsymbol{J} = -j\omega\mu\rho. \tag{1.189}$$

Substituting the Lorenz condition (Equation [1.188]) in Equation (1.186) yields

$$\boldsymbol{\nabla}^2\boldsymbol{A}(\boldsymbol{r}) + \omega^2\mu\epsilon\boldsymbol{A}(\boldsymbol{r}) = -\mu\boldsymbol{J}(\boldsymbol{r}), \tag{1.190}$$

which is an inhomogeneous vector wave equation. Similarly, it follows that substituting Equation (1.188) in Equation (1.187) yields

$$\boldsymbol{\nabla}^2\Phi + \omega^2\mu\epsilon\Phi = -\rho/\epsilon, \tag{1.191}$$

which is an inhomogeneous scalar wave equation. Again by using the Lorenz condition given by Equation (1.188), Equation (1.180) becomes

$$\boldsymbol{E} = -j\omega\boldsymbol{A} - \frac{j}{\omega\mu\epsilon}\boldsymbol{\nabla}(\boldsymbol{\nabla}\cdot\boldsymbol{A}). \tag{1.192}$$

Equation (1.192) is an exact relation between the vector electric field $\boldsymbol{E}$ and the magnetic vector potential $\boldsymbol{A}$ and applies in the near field and far field of a radiating source. Thus, to determine the vector electric field $\boldsymbol{E}$, it is necessary to determine the magnetic vector potential $\boldsymbol{A}$.

Consider now Figure 1.6, which shows the coordinate system for a radiating source and field observation point. To solve the inhomogeneous equation given by Equation (1.190), the Green's function method is used [113]. Let L_{op} be a linear differential operator such that

$$L_{\text{op}}y(x) = f(x). \tag{1.193}$$

It is desired to determine the Green's function $G(x, x')$ that is given by the solution to

$$L_{\text{op}}G(x, x') = \delta(x - x') \tag{1.194}$$

where δ is the delta function with $\delta(0) = 1$ and δ is equal to zero otherwise, and boundary conditions must be satisfied. A solution for $y(x)$ is then

$$y(x) = \int G(x, x')f(x')\,dx', \tag{1.195}$$

which follows since

$$L_{\text{op}}y(x) = \int L_{\text{op}}G(x,x')f(x')\,dx' = \int \delta(x-x')f(x')\,dx' = f(x) \tag{1.196}$$

where it is noted that $\delta(x-x')$ acts as a sampling function and L_{op} was moved inside the integral since this operator depends only on unprimed coordinates. Assume that the vector electric current source $\boldsymbol{J}$ is a function of the primed coordinates (x', y', z') and the position vector $\boldsymbol{R} = \boldsymbol{r} - \boldsymbol{r}'$ is a function of the observation position (x, y, z) and the source coordinates. Then it follows from Equation (1.195), which applies to each vector component in homogeneous space solution of Equation (1.190) is

$$\boldsymbol{A}(\boldsymbol{r}) = \mu \int_V \boldsymbol{J}(\boldsymbol{r}') \frac{e^{-jk|\boldsymbol{r}-\boldsymbol{r}'|}}{4\pi|\boldsymbol{r}-\boldsymbol{r}'|}\,dv' \tag{1.197}$$

where

$$k = \omega\sqrt{\mu\epsilon} \tag{1.198}$$

is the wavenumber. Thus, in homogeneous space, the magnetic vector potential $\boldsymbol{A}$ is collinear with the source current $\boldsymbol{J}$, which allows the use of the scalar Green's function method to solve Equation (1.190). The magnetic vector potential is also commonly expressed as

$$\boldsymbol{A}(\boldsymbol{r}) = \mu \int_V \boldsymbol{J}(\boldsymbol{r}')g(\boldsymbol{r},\boldsymbol{r}')\,dv'. \tag{1.199}$$

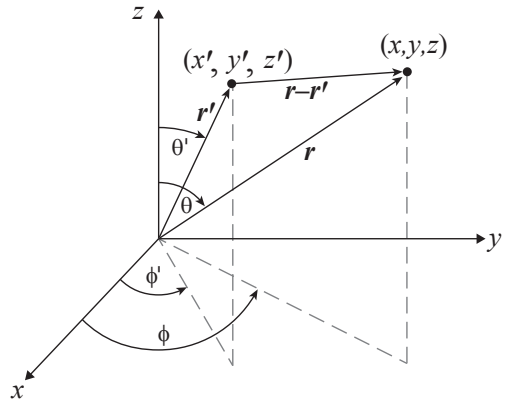

Figure 1.21 Coordinate system for radiating source at $\boldsymbol{r}'$ and field observation point at $\boldsymbol{r}$.

In Equation (1.199), the quantity

$$g(\boldsymbol{r},\boldsymbol{r}') = \frac{e^{-jk|\boldsymbol{r}-\boldsymbol{r}'|}}{4\pi|\boldsymbol{r}-\boldsymbol{r}'|} \tag{1.200}$$

is referred to as the scalar Green's function solution to the vector wave equation (Equation [1.190]), which is derived later in section 1.6.2 (starting with Equation [1.311]). By solving Equation (1.191) using the Green's function method, it can be shown that the electric scalar potential Φ is given by

$$\Phi(\boldsymbol{r}) = \frac{1}{\epsilon}\int_V \rho(\boldsymbol{r}')g(\boldsymbol{r},\boldsymbol{r}')\,dv'. \tag{1.201}$$

Note that by substituting Equations (1.199) and (1.201) into the Lorenz condition given by Equation (1.188), it is clear that the continuity equation (Equation [1.189]) is satisfied when multiplied by the scalar Green's function and integrated over a volume.

Using equation(1.197), Equation (1.192) can be written as

$$\boldsymbol{E} = -j\omega\mu\int_V \boldsymbol{J}(\boldsymbol{r}')g(\boldsymbol{r},\boldsymbol{r}')\,dv' - \frac{j}{\omega\epsilon}\boldsymbol{\nabla}\left[\boldsymbol{\nabla}\cdot\int_V \boldsymbol{J}(\boldsymbol{r}')g(\boldsymbol{r},\boldsymbol{r}')\,dv'\right] \tag{1.202}$$

or as

$$\boldsymbol{E} = -j\omega\mu\int_V \boldsymbol{J}(\boldsymbol{r}')\frac{e^{-jk|\boldsymbol{r}-\boldsymbol{r}'|}}{4\pi|\boldsymbol{r}-\boldsymbol{r}'|}\,dv' - \frac{j}{\omega\epsilon}\boldsymbol{\nabla}\left[\boldsymbol{\nabla}\cdot\int_V \boldsymbol{J}(\boldsymbol{r}')\frac{e^{-jk|\boldsymbol{r}-\boldsymbol{r}'|}}{4\pi|\boldsymbol{r}-\boldsymbol{r}'|}\,dv'\right], \tag{1.203}$$

which can be reduced to the following integral form

$$\boldsymbol{E} = -j\omega\mu\left[\int_V \boldsymbol{J}(\boldsymbol{r}')\frac{e^{-jk|\boldsymbol{r}-\boldsymbol{r}'|}}{4\pi|\boldsymbol{r}-\boldsymbol{r}'|}\,dv' + \frac{1}{k^2}\boldsymbol{\nabla}\left[\boldsymbol{\nabla}\cdot\int_V \boldsymbol{J}(\boldsymbol{r}')\frac{e^{-jk|\boldsymbol{r}-\boldsymbol{r}'|}}{4\pi|\boldsymbol{r}-\boldsymbol{r}'|}\,dv'\right]\right] \tag{1.204}$$

where $k^2 = \omega^2\mu\epsilon$. Equation (1.204) can be expressed in a simplified form by using a dyadic notation (discussed in Section 1.6.2) with $\overline{\boldsymbol{I}}$ the identity dyadic (refer to Equation [1.242]):

$$\boldsymbol{E}(\boldsymbol{r}) = -j\omega\mu[\overline{\boldsymbol{I}} + \frac{1}{k^2}\boldsymbol{\nabla}\boldsymbol{\nabla}]\cdot\int_V \boldsymbol{J}(\boldsymbol{r}')\frac{e^{-jk|\boldsymbol{r}-\boldsymbol{r}'|}}{4\pi|\boldsymbol{r}-\boldsymbol{r}'|}\,dv', \tag{1.205}$$

which is a general form of the electric field caused by an electric current source $\boldsymbol{J}$.

A similar wave equation can be derived in terms of the electric vector potential $\boldsymbol{F}$ and the magnetic current density $\boldsymbol{M}$ as

$$\boldsymbol{\nabla}^2\boldsymbol{F} + \omega^2\mu\epsilon\boldsymbol{F} = -\epsilon\boldsymbol{M} \tag{1.206}$$

and for the magnetic field $\boldsymbol{H}$ in terms of $\boldsymbol{F}$ as

$$\boldsymbol{H} = -j\omega\boldsymbol{F} - \frac{j}{\omega\mu\epsilon}\boldsymbol{\nabla}(\boldsymbol{\nabla}\cdot\boldsymbol{F}). \tag{1.207}$$

The solution for $\boldsymbol{F}$ in terms of $\boldsymbol{M}$ is given by

$$\boldsymbol{F}(\boldsymbol{r}) = \epsilon\int_V \boldsymbol{M}(\boldsymbol{r}')\frac{e^{-jk|\boldsymbol{r}-\boldsymbol{r}'|}}{4\pi|\boldsymbol{r}-\boldsymbol{r}'|}\,dv'. \tag{1.208}$$

The fields radiated by an antenna are in general spherical waves. In the far field, the spherical waves more closely resemble planar (plane) waves. The far-field range distance R from an antenna is typically computed as

$$R = 2D^2/\lambda \tag{1.209}$$

where D is the antenna diameter and λ is the wavelength. In the far field, using spherical coordinates, it can be shown (see Equation [1.279]) that only the first term in Equation (1.192) involving the $\hat{\boldsymbol{\theta}}$ and $\hat{\boldsymbol{\phi}}$ components is significant; thus,

$$\boldsymbol{E}_{\text{FF}} = -j\omega\left(A_\theta\hat{\boldsymbol{\theta}} + A_\phi\hat{\boldsymbol{\phi}}\right). \tag{1.210}$$

In the far zone in spherical coordinates, the radial component of the electric and magnetic fields is zero, and the far-zone magnetic field can be computed from the electric field in free space as (see Equation [1.281])

$$\boldsymbol{H}_{\text{FF}} = \frac{\hat{\boldsymbol{r}}\times\boldsymbol{E}_{\text{FF}}}{\eta_o} \tag{1.211}$$

where η_o is the wave impedance of free space as given by

$$\eta_o = \sqrt{\frac{\mu_o}{\epsilon_o}}. \tag{1.212}$$

Similarly, it can be shown that the far-zone magnetic field $\boldsymbol{H}_{\text{FF}}$ can be computed from the electric vector potential $\boldsymbol{F}$, for example, in spherical coordinates, as

$$\boldsymbol{H}_{\text{FF}} = -j\omega\left(F_\theta\hat{\boldsymbol{\theta}} + F_\phi\hat{\boldsymbol{\phi}}\right) \tag{1.213}$$

from which the far-zone electric field can be computed as

$$\boldsymbol{E}_{\text{FF}} = -\eta_o\hat{\boldsymbol{r}}\times\boldsymbol{H}_{\text{FF}}. \tag{1.214}$$

Once the current density and field quantities have been determined, to convert between frequency and time domains, the Fourier transform pairs can be applied, for example, for $\boldsymbol{J}$ and $\boldsymbol{E}$, as

$$\boldsymbol{J}(r,\omega) = \int_{-\infty}^{\infty} \boldsymbol{J}(r,t)e^{-j\omega t}dt \tag{1.215}$$

$$\boldsymbol{J}(r,t) = \frac{1}{2\pi}\int_{-\infty}^{\infty} \boldsymbol{J}(r,\omega)e^{j\omega t}d\omega \tag{1.216}$$

$$\boldsymbol{E}(r,\omega) = \int_{-\infty}^{\infty} \boldsymbol{E}(r,t)e^{-j\omega t}dt \tag{1.217}$$

$$\boldsymbol{E}(r,t) = \frac{1}{2\pi}\int_{-\infty}^{\infty} \boldsymbol{E}(r,\omega)e^{j\omega t}d\omega. \tag{1.218}$$

1.4.2 Dyadic Green's Function

It was mentioned earlier in Section 1.6.1 that a direct dyadic relationship between the source current and electric field can be determined. To see this fact, Equations (1.192) and (1.197) can be combined and re-expressed by using a dyadic notation as was given in Equation (1.205). In this section, the dyadic Green's function is derived. Some background on vector and dyadic relations is necessary to derive the desired expression. Given two vectors, $\boldsymbol{U}$ and $\boldsymbol{V}$, their dot product is expressed as $\boldsymbol{U}\cdot\boldsymbol{V}$, which is also referred to as an inner product. The inner product is equal to the product of a row vector $\boldsymbol{U}^T$ ($\boldsymbol{U}$ transpose) and a column vector $\boldsymbol{V}$, which yields a scalar. Thus, $\boldsymbol{U}\cdot\boldsymbol{V}$ = $\boldsymbol{U}^T\boldsymbol{V}$ is a scalar quantity. The dyadic $\overline{\boldsymbol{D}} = \boldsymbol{U}\boldsymbol{V}$ is an outer product of two vectors and is the product of a column vector and a row vector, that is, $\boldsymbol{U}\boldsymbol{V}$ is interpreted as $\boldsymbol{U}\boldsymbol{V}^T$. Thus, $\overline{\boldsymbol{D}}\cdot\boldsymbol{C} = \boldsymbol{U}\boldsymbol{V}\cdot\boldsymbol{C} = \boldsymbol{U}(\boldsymbol{V}^T\boldsymbol{C})$, that is, a vector weighted by a scalar. Let the unit vectors in a given coordinate system, such as Cartesian, cylindrical, or spherical, be expressed as $\hat{\boldsymbol{e}_1}$, $\hat{\boldsymbol{e}_2}$, $\hat{\boldsymbol{e}_3}$. Now, let the two vectors $\boldsymbol{U}$ and $\boldsymbol{V}$ be represented in terms of the unit vectors as

$$\boldsymbol{U} = U_1\hat{\boldsymbol{e}_1} + U_2\hat{\boldsymbol{e}_2} + U_3\hat{\boldsymbol{e}_3} \tag{1.219}$$

$$\boldsymbol{V} = V_1\hat{\boldsymbol{e}_1} + V_2\hat{\boldsymbol{e}_2} + V_3\hat{\boldsymbol{e}_3}, \tag{1.220}$$

which can also be written as the column vectors

$$\boldsymbol{U} = \begin{bmatrix} U_1 \\ U_2 \\ U_3 \end{bmatrix} \tag{1.221}$$

$$\boldsymbol{V} = \begin{bmatrix} V_1 \\ V_2 \\ V_3 \end{bmatrix}. \tag{1.222}$$

The dyadic matrix $\overline{\boldsymbol{D}} = \boldsymbol{UV}$ is formed as

$$\overline{\boldsymbol{D}} = \boldsymbol{UV}^T = \begin{bmatrix} U_1 \\ U_2 \\ U_3 \end{bmatrix} \begin{bmatrix} V_1 & V_2 & V_3 \end{bmatrix} = \begin{bmatrix} U_1V_1 & U_1V_2 & U_1V_3 \\ U_2V_1 & U_2V_2 & U_2V_3 \\ U_3V_1 & U_3V_2 & U_3V_3 \end{bmatrix}. \tag{1.223}$$

The dyadic $\overline{\boldsymbol{D}} = \boldsymbol{UV}^T$ can be expressed in terms of the unit vectors as

$$\overline{\boldsymbol{D}} = \sum_i \sum_j U_i V_j \hat{\boldsymbol{e}}_i \hat{\boldsymbol{e}}_j \tag{1.224}$$

and the summation can be expanded as

$$\begin{aligned} \overline{\boldsymbol{D}} = \boldsymbol{UV}^T \quad = \quad & U_1V_1\hat{\boldsymbol{e}}_1\hat{\boldsymbol{e}}_1 + U_1V_2\hat{\boldsymbol{e}}_1\hat{\boldsymbol{e}}_2 + U_1V_3\hat{\boldsymbol{e}}_1\hat{\boldsymbol{e}}_3 \\ & + U_2V_1\hat{\boldsymbol{e}}_2\hat{\boldsymbol{e}}_1 + U_2V_2\hat{\boldsymbol{e}}_2\hat{\boldsymbol{e}}_2 + U_2V_3\hat{\boldsymbol{e}}_2\hat{\boldsymbol{e}}_3 \\ & + U_3V_1\hat{\boldsymbol{e}}_3\hat{\boldsymbol{e}}_1 + U_3V_2\hat{\boldsymbol{e}}_3\hat{\boldsymbol{e}}_2 + U_3V_3\hat{\boldsymbol{e}}_3\hat{\boldsymbol{e}}_3. \end{aligned} \tag{1.225}$$

The product of a dyadic $\overline{\boldsymbol{D}}$ and a vector $\boldsymbol{A}$ yields another vector $\boldsymbol{X}$, that is,

$$\overline{\boldsymbol{D}} \cdot \boldsymbol{A} = \boldsymbol{X}. \tag{1.226}$$

Now the dyadic $\overline{\boldsymbol{D}}$ can be written in matrix form as

$$\overline{\boldsymbol{D}} = \begin{bmatrix} D_{11} & D_{12} & D_{13} \\ D_{21} & D_{22} & D_{23} \\ D_{31} & D_{32} & D_{33} \end{bmatrix}. \tag{1.227}$$

For the vectors $\boldsymbol{U}$ and $\boldsymbol{V}$ discussed earlier, in Equation (1.227), the dyadic matrix elements (dyads) D_{ij} are equal to U_iV_j. In general, the dyadic $\overline{\boldsymbol{D}}$ can be expressed in terms of the unit vectors as

$$\overline{\boldsymbol{D}} = \sum_i \sum_j D_{ij} \hat{\boldsymbol{e}}_i \hat{\boldsymbol{e}}_j. \tag{1.228}$$

The vector $\boldsymbol{A}$ above can be written as a column matrix as

$$\boldsymbol{A} = \begin{bmatrix} A_1 \\ A_2 \\ A_3 \end{bmatrix} \tag{1.229}$$

and it can also be written in terms of the unit vectors as

$$\boldsymbol{A} = \sum_k A_k \hat{\boldsymbol{e}}_k. \tag{1.230}$$

It follows then that

$$\overline{\boldsymbol{D}}\cdot\boldsymbol{A} = \left[\sum_i \sum_j D_{ij}\hat{\boldsymbol{e}}_i\hat{\boldsymbol{e}}_j\right]\cdot\left[\sum_k A_k\hat{\boldsymbol{e}}_k\right] \tag{1.231}$$

or

$$\overline{\boldsymbol{D}}\cdot\boldsymbol{A} = \sum_i \sum_j \sum_k D_{ij}A_k\left[\hat{\boldsymbol{e}}_i\hat{\boldsymbol{e}}_j\cdot\hat{\boldsymbol{e}}_k\right] \tag{1.232}$$

$$\overline{\boldsymbol{D}}\cdot\boldsymbol{A} = \sum_i \sum_j \sum_k D_{ij}A_k\left[\hat{\boldsymbol{e}}_i\delta_{jk}\right] \tag{1.233}$$

where δ_{jk} is the Kronecker delta function, that is, $\delta_{jk} = 0$, if $j \neq k$ and $\delta_{jk} = 1$, if $j = k$. It follows then that

$$\overline{\boldsymbol{D}}\cdot\boldsymbol{A} = \sum_i \hat{\boldsymbol{e}}_i\left[\sum_j D_{ij}A_j\right], \tag{1.234}$$

which can be expressed as

$$\begin{aligned}\overline{\boldsymbol{D}}\cdot\boldsymbol{A} \;=\;& \hat{\boldsymbol{e}}_1(D_{11}A_1 + D_{12}A_2 + D_{13}A_3)\\ &+\hat{\boldsymbol{e}}_2(D_{21}A_1 + D_{22}A_2 + D_{23}A_3)\\ &+\hat{\boldsymbol{e}}_3(D_{31}A_1 + D_{32}A_2 + D_{33}A_3).\end{aligned} \tag{1.235}$$

For the spherical coordinate geometry under consideration, with coordinate variables r, θ, ϕ, the unit vectors are $\hat{\boldsymbol{e}}_1 = \hat{\boldsymbol{r}}$, $\hat{\boldsymbol{e}}_2 = \hat{\boldsymbol{\theta}}$, $\hat{\boldsymbol{e}}_3 = \hat{\boldsymbol{\phi}}$. The metric coefficients in the spherical coordinate system are $1, r, r\sin\theta$. The mixed dyadic/vector calculus needed to solve electromagnetic problems is clearly more involved than vector calculus. In some cases, it is necessary to differentiate the unit vectors, for example, in spherical coordinates, where the nonzero partial derivatives are given by $\partial\hat{\boldsymbol{r}}/\partial\theta = \hat{\boldsymbol{\theta}}$, $\partial\hat{\boldsymbol{r}}/\partial\phi = \sin\theta\hat{\boldsymbol{\phi}}$, $\partial\hat{\boldsymbol{\theta}}/\partial\theta = -\hat{\boldsymbol{r}}$, $\partial\hat{\boldsymbol{\theta}}/\partial\phi = \cos\theta\hat{\boldsymbol{\phi}}$, and $\partial\hat{\boldsymbol{\phi}}/\partial\phi = -\sin\theta\hat{\boldsymbol{r}} - \cos\theta\hat{\boldsymbol{\theta}}$, and the partial derivatives equal to zero are $\partial\hat{\boldsymbol{r}}/\partial r = \partial\hat{\boldsymbol{\theta}}/\partial r = \partial\hat{\boldsymbol{\phi}}/\partial r = \partial\hat{\boldsymbol{\phi}}/\partial\theta = 0$. These unit vector derivatives are readily derived by differentiating the spherical unit vectors in terms of the rectangular unit vector components as expressed as

$$\hat{\boldsymbol{r}} = \hat{\boldsymbol{x}}\sin\theta\cos\phi + \hat{\boldsymbol{y}}\sin\theta\sin\phi + \hat{\boldsymbol{z}}\cos\theta \tag{1.236}$$

$$\hat{\boldsymbol{\theta}} = \hat{\boldsymbol{x}}\cos\theta\cos\phi + \hat{\boldsymbol{y}}\cos\theta\sin\phi - \hat{\boldsymbol{z}}\sin\theta \tag{1.237}$$

$$\hat{\boldsymbol{\phi}} = -\hat{\boldsymbol{x}}\sin\phi + \hat{\boldsymbol{y}}\cos\phi. \tag{1.238}$$

Furthermore, the rectangular unit vectors can be expressed in terms of the spherical unit vectors as

$$\hat{\boldsymbol{x}} = \hat{\boldsymbol{r}} \sin\theta \cos\phi + \hat{\boldsymbol{\theta}} \cos\theta \cos\phi - \hat{\boldsymbol{\phi}} \sin\phi \tag{1.239}$$

$$\hat{\boldsymbol{y}} = \hat{\boldsymbol{r}} \sin\theta \sin\phi + \hat{\boldsymbol{\theta}} \cos\theta \sin\phi + \hat{\boldsymbol{\phi}} \cos\phi \tag{1.240}$$

$$\hat{\boldsymbol{z}} = \hat{\boldsymbol{r}} \cos\theta - \hat{\boldsymbol{\theta}} \sin\theta. \tag{1.241}$$

The identity dyadic $\overline{\boldsymbol{I}}$ in spherical coordinates can be expressed in tensor summation form as

$$\overline{\boldsymbol{I}} = \hat{\boldsymbol{r}}\hat{\boldsymbol{r}} + \hat{\boldsymbol{\theta}}\hat{\boldsymbol{\theta}} + \hat{\boldsymbol{\phi}}\hat{\boldsymbol{\phi}} \tag{1.242}$$

or in matrix form as

$$\overline{\boldsymbol{I}} = \begin{bmatrix} 1 & 0 & 0 \\ 0 & 1 & 0 \\ 0 & 0 & 1 \end{bmatrix}. \tag{1.243}$$

The product of the identity dyadic $\overline{\boldsymbol{I}}$ and any vector, say $\boldsymbol{A}$, is just the vector $\boldsymbol{A}$, that is,

$$\overline{\boldsymbol{I}} \cdot \boldsymbol{A} = \boldsymbol{A} \cdot \overline{\boldsymbol{I}} = \boldsymbol{A}. \tag{1.244}$$

Next, it is observed that the quantity $\boldsymbol{\nabla}(\boldsymbol{\nabla} \cdot \boldsymbol{A})$ in Equation (1.192) is the gradient of the divergence of $\boldsymbol{A}$, which is a vector quantity. In spherical coordinates, the vector $\boldsymbol{A}$ is expressed as

$$\boldsymbol{A} = A_r \hat{\boldsymbol{r}} + A_\theta \hat{\boldsymbol{\theta}} + A_\phi \hat{\boldsymbol{\phi}}. \tag{1.245}$$

Furthermore, the del operator in spherical coordinates is expressed as

$$\boldsymbol{\nabla} = \hat{\boldsymbol{r}} \frac{\partial}{\partial r} + \hat{\boldsymbol{\theta}} \frac{1}{r} \frac{\partial}{\partial \theta} + \hat{\boldsymbol{\phi}} \frac{1}{r \sin\theta} \frac{\partial}{\partial \phi}. \tag{1.246}$$

Special care must be used in evaluating mixed vector/dyadic expressions involving the del differential operator $\boldsymbol{\nabla}$ [111]. From Tai [110], given an orthogonal coordinate system with unit vectors $\hat{\boldsymbol{e}_1}, \hat{\boldsymbol{e}_2}, \hat{\boldsymbol{e}_3}$, coordinate variables v_1, v_2, v_3, and metric coefficients h_1, h_2, h_3, the gradient, divergence, and curl differential operations for the vector function $\boldsymbol{A}$ are given by, respectively,

$$\boldsymbol{\nabla} \boldsymbol{A} = \sum_i \frac{\hat{\boldsymbol{e}_i}}{h_i} \frac{\partial \boldsymbol{A}}{\partial v_i} \tag{1.247}$$

$$\boldsymbol{\nabla} \cdot \boldsymbol{A} = \sum_i \frac{\hat{\boldsymbol{e}_i}}{h_i} \cdot \frac{\partial \boldsymbol{A}}{\partial v_i} \tag{1.248}$$

$$\boldsymbol{\nabla}\times\boldsymbol{A}=\sum_i \frac{\hat{\boldsymbol{e}_i}}{h_i}\times\frac{\partial \boldsymbol{A}}{\partial v_i}. \tag{1.249}$$

In spherical coordinates, the coordinate variables are $v_1=r, v_2=\theta, v_3=\phi$, the unit vectors are $\boldsymbol{e}_1=\hat{\boldsymbol{r}}, \boldsymbol{e}_2=\hat{\boldsymbol{\theta}}, \boldsymbol{e}_3=\hat{\boldsymbol{\phi}}$, and the metric coefficients are $h_1=1, h_2=r, h_3=r\sin\theta$.

It is worthwhile utilizing the del operator $\boldsymbol{\nabla}$ as follows. A dyadic such as $\boldsymbol{\nabla A}$ can be formed either as a summation by Equation (1.247) or by matrix operation as

$$\boldsymbol{\nabla A}=\boldsymbol{\nabla A}^T=\begin{bmatrix} (\hat{\boldsymbol{r}})\frac{\partial}{\partial r} \\ (\hat{\boldsymbol{\theta}})\frac{1}{r}\frac{\partial}{\partial\theta} \\ (\hat{\boldsymbol{\phi}})\frac{1}{r\sin\theta}\frac{\partial}{\partial\phi} \end{bmatrix}\begin{bmatrix} (\hat{\boldsymbol{r}})A_r & (\hat{\boldsymbol{\theta}})A_\theta & (\hat{\boldsymbol{\phi}})A_\phi \end{bmatrix}. \tag{1.250}$$

The nine terms of the tensor summation of Equation (1.250) are computed using the chain rule for the unit vectors. For example, the $\hat{\boldsymbol{r}}\hat{\boldsymbol{r}}$ dyad term is given by

$$(\boldsymbol{\nabla A})_{rr}=\hat{\boldsymbol{r}}[\hat{\boldsymbol{r}}\frac{\partial}{\partial r}A_r+A_r\frac{\partial\hat{\boldsymbol{r}}}{\partial r}] \tag{1.251}$$

and noting $\frac{\partial\hat{\boldsymbol{r}}}{\partial r}=0$. The remaining eight terms of Equation (1.250) are computed similarly, with the result expressed as the tensor summation

$$\begin{aligned}\boldsymbol{\nabla A} \quad = \quad & \tfrac{\partial A_r}{\partial r}\hat{\boldsymbol{r}}\hat{\boldsymbol{r}}+\tfrac{\partial A_\theta}{\partial r}\hat{\boldsymbol{r}}\hat{\boldsymbol{\theta}}+\tfrac{\partial A_\phi}{\partial r}\hat{\boldsymbol{r}}\hat{\boldsymbol{\phi}} \\ & +(\tfrac{1}{r}\tfrac{\partial A_r}{\partial\theta}-\tfrac{A_\theta}{r})\hat{\boldsymbol{\theta}}\hat{\boldsymbol{r}}+(\tfrac{1}{r}\tfrac{\partial A_\theta}{\partial\theta}+\tfrac{A_r}{r})\hat{\boldsymbol{\theta}}\hat{\boldsymbol{\theta}}+\tfrac{1}{r}\tfrac{\partial A_\phi}{\partial\theta}\hat{\boldsymbol{\theta}}\hat{\boldsymbol{\phi}} \\ & +(\tfrac{1}{r\sin\theta}\tfrac{\partial A_r}{\partial\phi}-\tfrac{A_\phi}{r})\hat{\boldsymbol{\phi}}\hat{\boldsymbol{r}}+(\tfrac{1}{r\sin\theta}\tfrac{\partial A_\theta}{\partial\phi}-\cot\theta\tfrac{A_\phi}{r})\hat{\boldsymbol{\phi}}\hat{\boldsymbol{\theta}} \\ & +(\tfrac{1}{r\sin\theta}\tfrac{\partial A_\phi}{\partial\phi}+\cot\theta\tfrac{A_\theta}{r}+\tfrac{A_r}{r})\hat{\boldsymbol{\phi}}\hat{\boldsymbol{\phi}}.\end{aligned} \tag{1.252}$$

Earlier it was stated (see Equation [1.205]) that the electric field caused by the source current density $\boldsymbol{J}$ is given by

$$\boldsymbol{E}(\boldsymbol{r})=-j\omega\mu[\bar{\boldsymbol{I}}+\frac{1}{k^2}\boldsymbol{\nabla\nabla}]\cdot\int_V \boldsymbol{J}(\boldsymbol{r}')\frac{e^{-jk|\boldsymbol{r}-\boldsymbol{r}'|}}{4\pi|\boldsymbol{r}-\boldsymbol{r}'|}\,dv' \tag{1.253}$$

and now it is desired to solve this equation under far-field conditions. Using the vector identity

$$(\boldsymbol{\nabla\nabla})\cdot\boldsymbol{A}=\boldsymbol{\nabla}(\boldsymbol{\nabla}\cdot\boldsymbol{A}), \tag{1.254}$$

it follows that the gradient of the divergence of a vector function $\boldsymbol{A}$ is [110, p. 126]

$$\boldsymbol{\nabla}(\boldsymbol{\nabla}\cdot\boldsymbol{A})=\sum_i\frac{\hat{\boldsymbol{e}_i}}{h_i}\frac{\partial}{\partial v_i}\sum_j\frac{\hat{\boldsymbol{e}_j}}{h_j}\cdot\frac{\partial\boldsymbol{A}}{\partial v_j}, \tag{1.255}$$

and then performing the partial derivative operation using the chain rule yields

$$\boldsymbol{\nabla}(\boldsymbol{\nabla}\cdot\boldsymbol{A}) = \sum_i \sum_j \frac{\hat{\boldsymbol{e}}_i}{h_i}\left[\frac{\partial}{\partial v_i}\left(\frac{\hat{\boldsymbol{e}}_j}{h_j}\right)\cdot\frac{\partial \boldsymbol{A}}{\partial v_j} + \frac{\hat{\boldsymbol{e}}_j}{h_j}\cdot\frac{\partial^2 \boldsymbol{A}}{\partial v_i \partial v_j}\right]. \tag{1.256}$$

Using the spherical coordinate parameters in Equation (1.256) yields for the $i = 1, j = 1$ term

$$\boldsymbol{\nabla}(\boldsymbol{\nabla}\cdot\boldsymbol{A})_{i=1,j=1} = \hat{\boldsymbol{r}}\left[\frac{\partial}{\partial r}(\hat{\boldsymbol{r}})\cdot\frac{\partial \boldsymbol{A}}{\partial r} + \hat{\boldsymbol{r}}\cdot\frac{\partial^2 \boldsymbol{A}}{\partial r^2}\right], \tag{1.257}$$

and since $\partial\hat{\boldsymbol{r}}/\partial r = 0$, it follows that

$$\boldsymbol{\nabla}(\boldsymbol{\nabla}\cdot\boldsymbol{A})_{i=1,j=1} = \hat{\boldsymbol{r}}\hat{\boldsymbol{r}}\cdot\frac{\partial^2 \boldsymbol{A}}{\partial r^2}. \tag{1.258}$$

Similarly, Equation (1.256) yields for the $i = 1$, $j = 2$ term

$$\boldsymbol{\nabla}(\boldsymbol{\nabla}\cdot\boldsymbol{A})_{i=1,j=2} = \hat{\boldsymbol{r}}\left[\frac{\partial}{\partial r}\left(\frac{\hat{\boldsymbol{\theta}}}{r}\right)\cdot\frac{\partial \boldsymbol{A}}{\partial \theta} + \frac{\hat{\boldsymbol{\theta}}}{r}\cdot\frac{\partial^2 \boldsymbol{A}}{\partial r \partial \theta}\right], \tag{1.259}$$

and since $\frac{\partial}{\partial r}(\hat{\boldsymbol{\theta}}/r) = -\hat{\boldsymbol{\theta}}/r^2$, it follows that

$$\boldsymbol{\nabla}(\boldsymbol{\nabla}\cdot\boldsymbol{A})_{i=1,j=2} = \hat{\boldsymbol{r}}\hat{\boldsymbol{\theta}}\left[-\frac{1}{r^2}\cdot\frac{\partial \boldsymbol{A}}{\partial \theta} + \frac{1}{r}\cdot\frac{\partial^2 \boldsymbol{A}}{\partial r \partial \theta}\right]. \tag{1.260}$$

Next, for the $i = 1$, $j = 3$ term,

$$\boldsymbol{\nabla}(\boldsymbol{\nabla}\cdot\boldsymbol{A})_{i=1,j=3} = \hat{\boldsymbol{r}}\hat{\boldsymbol{\phi}}\left[-\frac{1}{r^2\sin\theta}\cdot\frac{\partial \boldsymbol{A}}{\partial \phi} + \frac{1}{r\sin\theta}\cdot\frac{\partial^2 \boldsymbol{A}}{\partial r \partial \phi}\right]. \tag{1.261}$$

In solving for the far-zone radiation pattern function of an antenna, typically only a $1/r$ variation is retained with all other terms involving $1/r^2$, $1/r^3$ ignored. All of the remaining terms of $\boldsymbol{\nabla}(\boldsymbol{\nabla}\cdot\boldsymbol{A})_{i,j}$ for $i = 2, 3$ have higher-order dependence on inverse r and can be neglected. Thus, in the far field, the gradient of the divergence of the magnetic vector potential can be expressed as

$$\boldsymbol{\nabla}(\boldsymbol{\nabla}\cdot\boldsymbol{A})_{\text{FF}} = \hat{\boldsymbol{r}}\hat{\boldsymbol{r}}\cdot\frac{\partial^2 \boldsymbol{A}}{\partial r^2}. \tag{1.262}$$

The electric field given by Equation (1.192) can be written as

$$\boldsymbol{E} = -j\omega[\boldsymbol{A} + \frac{1}{k^2}\boldsymbol{\nabla}\left(\boldsymbol{\nabla}\cdot\boldsymbol{A}\right)] \tag{1.263}$$

where $k^2 = \omega^2\mu\epsilon$. Now, using Equation (1.262) in Equation (1.263) yields an expression for the far-zone vector electric field

$$\boldsymbol{E}_{\text{FF}} = -j\omega\left[\boldsymbol{A} + \frac{1}{k^2}\hat{\boldsymbol{r}}\hat{\boldsymbol{r}}\cdot\frac{\partial^2\boldsymbol{A}}{\partial r^2}\right]. \tag{1.264}$$

Repeating Equation (1.197) for the magnetic vector potential

$$\boldsymbol{A}(\boldsymbol{r}) = \mu\int_V \boldsymbol{J}(\boldsymbol{r}')\frac{e^{-jk|\boldsymbol{r}-\boldsymbol{r}'|}}{4\pi|\boldsymbol{r}-\boldsymbol{r}'|}\,dv' \tag{1.265}$$

and in computing the far field of a radiating source, Equation (1.265) can be simplified by approximating $|\boldsymbol{r}-\boldsymbol{r}'|$ in the exponential argument as

$$|\boldsymbol{r}-\boldsymbol{r}'| \approx r - \hat{\boldsymbol{r}}\cdot\boldsymbol{r}' \tag{1.266}$$

and using

$$kr >> 1 \tag{1.267}$$

such that the factor $|\boldsymbol{r}-\boldsymbol{r}'|$ in the denominator can be replaced by r. Thus, under far-field conditions, Equation (1.265) can be expressed as

$$\boldsymbol{A}_{\text{FF}} = \mu\frac{e^{-jkr}}{4\pi r}\int_V \boldsymbol{J}(\boldsymbol{r}')e^{jk\hat{\boldsymbol{r}}\cdot\boldsymbol{r}'}\,dv'. \tag{1.268}$$

Define a far-field vector current moment $\boldsymbol{f}(\theta,\phi)$ in spherical coordinates as the integral in Equation (1.268) as

$$\boldsymbol{f}(\theta,\phi) = f_r\hat{\boldsymbol{r}} + f_\theta\hat{\boldsymbol{\theta}} + f_\phi\hat{\boldsymbol{\phi}} = \int_V \boldsymbol{J}(\boldsymbol{r}')e^{jk\hat{\boldsymbol{r}}\cdot\boldsymbol{r}'}\,dv'. \tag{1.269}$$

Using Equation (1.269) in Equation (1.268) yields the far-field magnetic vector potential as

$$\boldsymbol{A}_{\text{FF}} = \mu\frac{e^{-jkr}}{4\pi r}\boldsymbol{f}(\theta,\phi). \tag{1.270}$$

Now, comparing Equations (1.263) and (1.264), the contribution of $\boldsymbol{\nabla}(\boldsymbol{\nabla}\cdot\boldsymbol{A})$ to the far-field vector electric field depends on the second partial derivative of the free-space Green's function. Performing the first partial derivative operation, it follows that

$$\frac{\partial}{\partial r}\left[\frac{e^{-jkr}}{4\pi r}\right] = -\frac{jke^{-jkr}}{4\pi r} - \frac{e^{-jkr}}{4\pi r^2}, \tag{1.271}$$

and then the second partial derivative is determined to be

$$\frac{\partial^2}{\partial r^2}\left[\frac{e^{-jkr}}{4\pi r}\right] = -k^2\frac{e^{-jkr}}{4\pi r} + 2jk\frac{e^{-jkr}}{4\pi r^2} + 2\frac{e^{-jkr}}{4\pi r^3} \tag{1.272}$$

and in the far field, the $1/r^2$ and $1/r^3$ terms go to zero compared to $1/r$, and thus only the $1/r$ term contributes to the far-zone electric field. Thus, in the far field,

$$\frac{\partial^2}{\partial r^2}\left[\frac{e^{-jkr}}{4\pi r}\right]_{\text{FF}} = -k^2\frac{e^{-jkr}}{4\pi r} \tag{1.273}$$

and it follows that

$$\frac{\partial^2 \boldsymbol{A}_{\text{FF}}}{\partial r^2} = \frac{\partial^2}{\partial r^2}\left[\mu\frac{e^{-jkr}}{4\pi r}\boldsymbol{f}(\theta,\phi)\right] = -\mu k^2\frac{e^{-jkr}}{4\pi r}\boldsymbol{f}(\theta,\phi). \tag{1.274}$$

Note: another derivative of the scalar Green's function, in this case divided by r, used subsequently in evaluating Equation (1.457), is given by

$$\frac{\partial}{\partial r}\left[\frac{e^{-jkr}}{4\pi r^2}\right] = -\frac{jke^{-jkr}}{4\pi r^2} - \frac{2e^{-jkr}}{4\pi r^3}. \tag{1.275}$$

Substituting Equations (1.270) and (1.274) in Equation (1.264) yields

$$\boldsymbol{E}_{\text{FF}} = -j\omega\left[\mu\frac{e^{-jkr}}{4\pi r}\boldsymbol{f}(\theta,\phi) - \mu\frac{e^{-jkr}}{4\pi r}\hat{\boldsymbol{r}}\hat{\boldsymbol{r}}\cdot\boldsymbol{f}(\theta,\phi)\right], \tag{1.276}$$

which can also be expressed in dyadic/vector notation as

$$\boldsymbol{E}_{\text{FF}} = -j\omega\mu\frac{e^{-jkr}}{4\pi r}(\overline{\boldsymbol{I}} - \hat{\boldsymbol{r}}\hat{\boldsymbol{r}})\cdot\boldsymbol{f}(\theta,\phi) \tag{1.277}$$

where

$$\overline{\boldsymbol{I}} - \hat{\boldsymbol{r}}\hat{\boldsymbol{r}} = \hat{\boldsymbol{\theta}}\hat{\boldsymbol{\theta}} + \hat{\boldsymbol{\phi}}\hat{\boldsymbol{\phi}}. \tag{1.278}$$

Now using Equations (1.278) and (1.235) and performing the dyadic/vector operations in Equation (1.277) yields the vector form of the desired expression for the far-zone electric field as

$$\boldsymbol{E}_{\text{FF}} = -j\omega\mu\frac{e^{-jkr}}{4\pi r}(\hat{\boldsymbol{\theta}}f_\theta + \hat{\boldsymbol{\phi}}f_\phi). \tag{1.279}$$

Noting that

$$\frac{1}{r}\frac{\partial}{\partial r}(r\boldsymbol{E}_{\text{FF}}) = -jk\boldsymbol{E}_{\text{FF}} \tag{1.280}$$

the far-zone magnetic field is then computed using the far-zone electric field (Equation [1.279]), the curl operation (1.94) and vector cross product (1.96) as

$$\boldsymbol{H}_{\text{FF}} = \frac{1}{-j\omega\mu}\boldsymbol{\nabla}\times\boldsymbol{E}_{\text{FF}}(\boldsymbol{r}) = \frac{k\hat{\boldsymbol{r}}}{\omega\mu}\times\boldsymbol{E}_{\text{FF}}(\boldsymbol{r}). \tag{1.281}$$

Performing the vector operation in Equation (1.281) yields

$$\boldsymbol{H}_{\text{FF}} = -jk\frac{e^{-jkr}}{4\pi r}(\hat{\boldsymbol{\phi}}f_\theta - \hat{\boldsymbol{\theta}}f_\phi). \tag{1.282}$$

Referring to Equation (1.399) and using Equations (1.279) and (1.281), the time-average Poynting's power density in the far zone is now computed as

$$< \boldsymbol{S} >= \frac{1}{2}\text{Re}\{\boldsymbol{E}\times\boldsymbol{H}^*\} = \hat{\boldsymbol{r}}\frac{1}{2}\sqrt{\frac{\mu}{\epsilon}}\left(\frac{k}{4\pi r}\right)^2(|f_\theta|^2 + |f_\phi|^2). \tag{1.283}$$

Return now to the general form of the electric field given by Equation (1.205) and express the electric field in terms of the scalar Green's function $g(\boldsymbol{r},\boldsymbol{r}')$ as

$$\boldsymbol{E}(\boldsymbol{r}) = -j\omega\mu[\overline{\boldsymbol{I}} + \frac{1}{k^2}\boldsymbol{\nabla}\boldsymbol{\nabla}]\cdot\int_V \boldsymbol{J}(\boldsymbol{r}')g(\boldsymbol{r},\boldsymbol{r}')\,dv'. \tag{1.284}$$

Now the bracketed terms in front of the integral depend only on the unprimed coordinates and can be moved inside the integral in Equation (1.284) and rearranging yields

$$\boldsymbol{E}(\boldsymbol{r}) = -j\omega\mu\int_V \left[[\overline{\boldsymbol{I}} + \frac{1}{k^2}\boldsymbol{\nabla}\boldsymbol{\nabla}]g(\boldsymbol{r},\boldsymbol{r}')\right]\cdot\boldsymbol{J}(\boldsymbol{r}')\,dv'. \tag{1.285}$$

It is assumed here that the observation point is outside the source volume. In cases where the observation point is within the source volume, additional integration terms must be taken into account [116]. The dyadic Green's function $\overline{\boldsymbol{G}}(\boldsymbol{r},\boldsymbol{r}')$ can now be expressed in terms of the scalar Green's function $g(\boldsymbol{r},\boldsymbol{r}')$ as

$$\overline{\boldsymbol{G}}(\boldsymbol{r},\boldsymbol{r}') = [\overline{\boldsymbol{I}} + \frac{1}{k^2}\boldsymbol{\nabla}\boldsymbol{\nabla}]g(\boldsymbol{r},\boldsymbol{r}'). \tag{1.286}$$

Thus, Equation (1.285) can be rewritten in the more compact dyadic Green's function representation as

$$\boldsymbol{E}(\boldsymbol{r}) = -j\omega\mu\int_V \overline{\boldsymbol{G}}(\boldsymbol{r},\boldsymbol{r}')\cdot\boldsymbol{J}(\boldsymbol{r}')\,dv'. \tag{1.287}$$

The dyadic and scalar Green's functions are now examined in more detail. Let us return now to the time-harmonic form of Maxwell's equations corresponding to Equations (1.145) and (1.146), that is,

$$\boldsymbol{\nabla}\times\boldsymbol{E}(\boldsymbol{r}) = -j\omega\mu\boldsymbol{H}(\boldsymbol{r}) - \boldsymbol{M}(\boldsymbol{r}) \tag{1.288}$$

$$\boldsymbol{\nabla}\times\boldsymbol{H}(\boldsymbol{r}) = j\omega\epsilon\boldsymbol{E}(\boldsymbol{r}) + \boldsymbol{J}(\boldsymbol{r}) \tag{1.289}$$

where μ and ϵ are assumed to be complex in general and the current densities $\boldsymbol{J}$ and $\boldsymbol{M}$ are source currents. Assuming that the equivalent magnetic current is zero, that is, $\boldsymbol{M} = 0$, $\boldsymbol{H}(\boldsymbol{r})$ can be eliminated from Equation (1.288) by taking the curl of the curl of $\boldsymbol{E}$ as

$$\boldsymbol{\nabla}\times\boldsymbol{\nabla}\times\boldsymbol{E}(\boldsymbol{r}) = -j\omega\mu\boldsymbol{\nabla}\times\boldsymbol{H}(\boldsymbol{r}) \tag{1.290}$$

and substituting Equation (1.289) yields

$$\boldsymbol{\nabla}\times\boldsymbol{\nabla}\times\boldsymbol{E}(\boldsymbol{r}) = -j\omega\mu j\omega\epsilon\boldsymbol{E}(\boldsymbol{r}) - j\omega\mu\boldsymbol{J}(\boldsymbol{r}) \tag{1.291}$$

and rearranging yields the following inhomogeneous wave equation for $\boldsymbol{E}(\boldsymbol{r})$, that is,

$$\boldsymbol{\nabla}\times\boldsymbol{\nabla}\times\boldsymbol{E}(\boldsymbol{r}) - k^2\boldsymbol{E}(\boldsymbol{r}) = -j\omega\mu\boldsymbol{J}(\boldsymbol{r}). \tag{1.292}$$

To solve Equation (1.292), the dyadic Green's function method can be used for an arbitrary response vector function $\boldsymbol{y}$ and source vector function $\boldsymbol{f}$ as follows.

Let L_{op} be a linear differential operator such that

$$L_{\text{op}}\boldsymbol{y}(\boldsymbol{r}) = \boldsymbol{f}(\boldsymbol{r}). \tag{1.293}$$

It is desired to determine the dyadic Green's function $\overline{\boldsymbol{G}}$ that is given by the solution to

$$L_{\text{op}}\overline{\boldsymbol{G}}(\boldsymbol{r},\boldsymbol{r}') = \overline{\boldsymbol{I}}\delta(\boldsymbol{r}-\boldsymbol{r}') \tag{1.294}$$

and boundary conditions must be satisfied. A solution for $\boldsymbol{y}(\boldsymbol{r})$ is then

$$\boldsymbol{y}(\boldsymbol{r}) = \int \overline{\boldsymbol{G}}(\boldsymbol{r},\boldsymbol{r}')\cdot\boldsymbol{f}(\boldsymbol{r}')dv'. \tag{1.295}$$

Next, from Equation (1.287), in terms of the complex permeability μ, the vector electric field can be expressed in terms of the dyadic Green's function as

$$\boldsymbol{E}(\boldsymbol{r}) = -j\omega\mu\int_V \overline{\boldsymbol{G}}(\boldsymbol{r},\boldsymbol{r}')\cdot\boldsymbol{J}(\boldsymbol{r}')\,dv' \tag{1.296}$$

where it should be noted that, in addition, any boundary conditions must be enforced. In Equation (1.292), it is desirable to express the source density in

terms of the primed coordinate system. One way to achieve this transformation from unprimed to primed coordinates is to make use of the three-dimensional delta function $\delta(\boldsymbol{r}-\boldsymbol{r}')$ as described by Kong [3, p. 496] as

$$\boldsymbol{J}(\boldsymbol{r}) = \int_V \delta(\boldsymbol{r}-\boldsymbol{r}')\overline{\boldsymbol{I}}\cdot\boldsymbol{J}(\boldsymbol{r}')dv'. \tag{1.297}$$

Substituting Equations (1.296) and (1.297) in Equation (1.292) yields

$$\begin{aligned}-j\omega\mu \int_V \boldsymbol{\nabla}\times\boldsymbol{\nabla}\times\overline{\boldsymbol{G}}(\boldsymbol{r},\boldsymbol{r}')\cdot\boldsymbol{J}(\boldsymbol{r}')\,dv' + j\omega\mu k^2 \int_V \overline{\boldsymbol{G}}(\boldsymbol{r},\boldsymbol{r}')\cdot\boldsymbol{J}(\boldsymbol{r}')\,dv' \\ = -j\omega\mu \int_V \delta(\boldsymbol{r}-\boldsymbol{r}')\overline{\boldsymbol{I}}\cdot\boldsymbol{J}(\boldsymbol{r}')dv'.\end{aligned} \tag{1.298}$$

Since the integral operation involving $\boldsymbol{J}(\boldsymbol{r}')$ appears in each term of Equation (1.298), it follows that the integral operation on $\boldsymbol{J}(\boldsymbol{r}')$ and the $j\omega\mu$ quantity can be eliminated, which gives

$$\boldsymbol{\nabla}\times\boldsymbol{\nabla}\times\overline{\boldsymbol{G}}(\boldsymbol{r},\boldsymbol{r}') - k^2\overline{\boldsymbol{G}}(\boldsymbol{r},\boldsymbol{r}') = \overline{\boldsymbol{I}}\delta(\boldsymbol{r}-\boldsymbol{r}'). \tag{1.299}$$

Substituting Equation (1.286) in Equation (1.299 yields

$$\boldsymbol{\nabla}\times\boldsymbol{\nabla}\times\left[\overline{\boldsymbol{I}} + \frac{1}{k^2}\boldsymbol{\nabla}\boldsymbol{\nabla}\right]g(\boldsymbol{r},\boldsymbol{r}') - k^2\left[\overline{\boldsymbol{I}} + \frac{1}{k^2}\boldsymbol{\nabla}\boldsymbol{\nabla}\right]g(\boldsymbol{r},\boldsymbol{r}') = \overline{\boldsymbol{I}}\delta(\boldsymbol{r}-\boldsymbol{r}'). \tag{1.300}$$

Now Equation (1.300) can be simplified by first observing that the curl of a gradient of an arbitrary vector is zero, that is,

$$\boldsymbol{\nabla}\times\boldsymbol{\nabla}\boldsymbol{V} = 0, \tag{1.301}$$

and recognizing that the gradient of the scalar Green's function $g(\boldsymbol{r},\boldsymbol{r}')$ is a vector, it follows that

$$\frac{1}{k^2}\boldsymbol{\nabla}\times\boldsymbol{\nabla}\times\boldsymbol{\nabla}\boldsymbol{\nabla}g(\boldsymbol{r},\boldsymbol{r}') = \frac{1}{k^2}\boldsymbol{\nabla}\times[\boldsymbol{\nabla}\times\boldsymbol{\nabla}(\boldsymbol{\nabla}g(\boldsymbol{r},\boldsymbol{r}'))] = 0. \tag{1.302}$$

Thus, Equation (1.300) reduces to

$$\boldsymbol{\nabla}\times\boldsymbol{\nabla}\times\overline{\boldsymbol{I}}g(\boldsymbol{r},\boldsymbol{r}') - k^2\left[\overline{\boldsymbol{I}} + \frac{1}{k^2}\boldsymbol{\nabla}\boldsymbol{\nabla}\right]g(\boldsymbol{r},\boldsymbol{r}') = \overline{\boldsymbol{I}}\delta(\boldsymbol{r}-\boldsymbol{r}'). \tag{1.303}$$

Next, using the dyadic identity

$$\boldsymbol{\nabla}\times\boldsymbol{\nabla}\times\overline{\boldsymbol{D}} = \boldsymbol{\nabla}(\boldsymbol{\nabla}\cdot\overline{\boldsymbol{D}}) - \boldsymbol{\nabla}^2\overline{\boldsymbol{D}}, \tag{1.304}$$

it follows that

$$\boldsymbol{\nabla}\times\boldsymbol{\nabla}\times\overline{\boldsymbol{I}}g = \boldsymbol{\nabla}(\boldsymbol{\nabla}\cdot\overline{\boldsymbol{I}}g) - \boldsymbol{\nabla}^2(\overline{\boldsymbol{I}}g); \tag{1.305}$$

but from the identity

$$\boldsymbol{\nabla}\cdot(\phi\overline{\boldsymbol{I}}) = \boldsymbol{\nabla}\phi \tag{1.306}$$

it follows that

$$\boldsymbol{\nabla}\cdot\overline{\boldsymbol{I}}g = \boldsymbol{\nabla}g. \tag{1.307}$$

Therefore,

$$\boldsymbol{\nabla}\times\boldsymbol{\nabla}\overline{\boldsymbol{I}}g = \boldsymbol{\nabla}\boldsymbol{\nabla}g - \overline{\boldsymbol{I}}\boldsymbol{\nabla}^2 g. \tag{1.308}$$

Substituting Equation (1.308) in Equation (1.303) yields

$$\boldsymbol{\nabla}\boldsymbol{\nabla}g(\boldsymbol{r},\boldsymbol{r}') - \overline{\boldsymbol{I}}\boldsymbol{\nabla}^2 g(\boldsymbol{r},\boldsymbol{r}') - k^2\left[\overline{\boldsymbol{I}} + \frac{1}{k^2}\boldsymbol{\nabla}\boldsymbol{\nabla}\right]g(\boldsymbol{r},\boldsymbol{r}') = \overline{\boldsymbol{I}}\delta(\boldsymbol{r}-\boldsymbol{r}'), \tag{1.309}$$

and canceling like terms yields the simplified inhomogeneous wave equation

$$\boldsymbol{\nabla}^2 g(\boldsymbol{r},\boldsymbol{r}') + k^2 g(\boldsymbol{r},\boldsymbol{r}') = -\delta(\boldsymbol{r}-\boldsymbol{r}'). \tag{1.310}$$

To determine the functional form of the scalar Green's function $g(\boldsymbol{r},\boldsymbol{r}')$ in Equation (1.310), it is necessary first to solve the homogeneous form of the equation and then invoke the boundary conditions in the inhomogeneous case. To simplify the solution for g, shift the source position to the origin, which means $\boldsymbol{r}' = 0$. Thus, Equation (1.310) can now be expressed as

$$\boldsymbol{\nabla}^2 g(\boldsymbol{r}) + k^2 g(\boldsymbol{r}) = -\delta(\boldsymbol{r}), \tag{1.311}$$

and it is observed that the solution for $g(\boldsymbol{r})$ is independent of the spherical coordinate angles θ and ϕ.

In spherical coordinates, the Laplacian of a scalar g that depends only on r can be expressed as [3, p. 18]

$$\boldsymbol{\nabla}^2 g(r) = \frac{1}{r^2}\frac{\partial}{\partial r}\left[r^2\frac{\partial g(r)}{\partial r}\right] = \frac{1}{r}\frac{\partial^2}{\partial r^2}(rg(r)). \tag{1.312}$$

Thus, Equation (1.311) can be rewritten as the inhomogeneous form

$$\frac{1}{r}\frac{d^2}{dr^2}(rg(\boldsymbol{r})) + k^2 g(\boldsymbol{r}) = -\delta(\boldsymbol{r}). \tag{1.313}$$

If the observation point is not at the origin, that is, $r \neq 0$, then Equation (1.313) reduces to the homogeneous differential equation

$$\frac{d^2}{dr^2}(rg(\boldsymbol{r})) + k^2 rg(\boldsymbol{r}) = 0. \tag{1.314}$$

The solution to the differential equation expressed by Equation (1.314) is an outgoing wave of the form

$$g(r) = C\frac{e^{-jkr}}{r}. \tag{1.315}$$

To determine the constant C in Equation (1.315), it is necessary to satisfy the boundary conditions at infinity and at the origin where the point source is located. In the limit as $r \to \infty$ in Equation (1.315) $g(r) \to 0$, which satifies the condition that the wave amplitude must attenuate to zero because of field spreading loss. To satisfy the boundary condition at the origin, it is necessary to integrate Equation (1.311) over an infinitesimal sphere of radius r_s centered at the origin and let the sphere radius tend to zero. Expressing the Laplacian operation on the scalar g as

$$\boldsymbol{\nabla}^2 g = \boldsymbol{\nabla}\cdot\boldsymbol{\nabla} g \tag{1.316}$$

and noting that the delta function acts as a sampling function, that is,

$$\int f(x)\delta(x - x_o)\, dx = f(x_o) \tag{1.317}$$

and substituting Equation (1.315) in Equation (1.311), the following integral equation can be written as

$$C\int_V \boldsymbol{\nabla}\cdot\left(\boldsymbol{\nabla}\frac{e^{-jkr}}{r}\right)dv + C\int_V k^2\frac{e^{-jkr}}{r}dv = -\int_V \delta(r)\, dv = -1. \tag{1.318}$$

Now, applying the divergence theorem

$$\int_V \boldsymbol{\nabla}\cdot\boldsymbol{A}\, dv = \oint_S \boldsymbol{A}\cdot\hat{\boldsymbol{n}}\, ds \tag{1.319}$$

to the first term in Equation (1.318) yields

$$C\int_V \boldsymbol{\nabla}\cdot\left(\boldsymbol{\nabla}\frac{e^{-jkr}}{r}\right)dv = C\oint_S \hat{\boldsymbol{n}}\cdot\hat{\boldsymbol{r}}\frac{\partial}{\partial r}\left(\frac{e^{-jkr}}{r}\right)ds. \tag{1.320}$$

The surface integral in Equation (1.320) is evaluated as follows. Noting that for the assumed spherical volume $\hat{\boldsymbol{n}} = \hat{\boldsymbol{r}}$ and $ds = r^2\sin\theta\, d\theta\, d\phi$, the surface integral in the first term of Equation (1.318) becomes

$$\begin{aligned}
\oint_S \tfrac{d}{dr}\left(\tfrac{e^{-jkr}}{r}\right)ds &= \int_0^{2\pi}\int_0^{\pi}\left[\tfrac{d}{dr}\left(\tfrac{e^{-jkr}}{r}\right)\right]r^2\sin\theta\, d\theta\, d\phi \\
&= \int_0^{2\pi}\int_0^{\pi}\left[\tfrac{e^{-jkr}(-jkr-1)}{r^2}\right]_{r=r_s}\sin\theta\, d\theta\, d\phi \\
&= \int_0^{2\pi}\int_0^{\pi}\left[e^{-jkr}(-jkr-1)\right]_{r=r_s\to 0}\sin\theta\, d\theta\, d\phi \\
&= \int_0^{2\pi}\int_0^{\pi}[-1]\sin\theta\, d\theta\, d\phi = -4\pi.
\end{aligned} \tag{1.321}$$

Now the integral in the second term in Equation (1.320) is evaluated as

$$\begin{aligned}\int_V k^2 \tfrac{e^{-jkr}}{r} dv &= k^2 \int_0^{r_s} \int_0^{2\pi} \int_0^{\pi} \tfrac{e^{-jkr}}{r} r^2 \sin\theta \, dr \, d\theta \, d\phi \\ &= 4\pi k^2 \int_0^{r_s \to 0} r e^{-jkr} dr \\ &= 4\pi k^2 \left[\tfrac{e^{-jkr}}{k^2}(-jkr - 1) \right]_0^{r_s \to 0} = 0.\end{aligned} \tag{1.322}$$

Substituting the results of Equations (1.321) and (1.322) in Equation (1.318), it follows that

$$C = \frac{1}{4\pi}, \tag{1.323}$$

and substituting the result for the constant in Equation (1.315) yields the scalar Green's function as a function of r

$$g(r) = \frac{e^{-jkr}}{4\pi r}. \tag{1.324}$$

Since the radius r in Equation (1.324) is the distance between the source and the observation point, it is possible to shift the source to the vector position $\boldsymbol{r}'$, and thus the transformed distance between the source and observation point becomes $|\boldsymbol{r} - \boldsymbol{r}'|$. Therefore, the general form of the scalar Green's function is given by

$$g(\boldsymbol{r}, \boldsymbol{r}') = \frac{e^{-jk|\boldsymbol{r}-\boldsymbol{r}'|}}{4\pi|\boldsymbol{r} - \boldsymbol{r}'|}. \tag{1.325}$$

Substituting Equation (1.325) in Equation (1.286) yields the dyadic Green's function in terms of the scalar Green's function as

$$\overline{\boldsymbol{G}}(\boldsymbol{r}, \boldsymbol{r}') = [\overline{\boldsymbol{I}} + \frac{1}{k^2} \boldsymbol{\nabla}\boldsymbol{\nabla}] \frac{e^{-jk|\boldsymbol{r}-\boldsymbol{r}'|}}{4\pi|\boldsymbol{r} - \boldsymbol{r}'|}. \tag{1.326}$$

The electric field is then determined by using Equation (1.326) in Equation (1.296).

1.5 Boundary Conditions

In determining the solution of electromagnetic fields for a general antenna or scattering problem, it is necessary to satisfy boundary conditions between different media for the tangential and normal field components. The boundary conditions depend on the type of media and also whether any charges or currents are present at the interface between the media. To derive the boundary conditions from Maxwell's equations, two vector identities are needed, namely the divergence theorem expressed as

$$\int_V \boldsymbol{\nabla} \cdot \boldsymbol{A} \, dv = \oint_S \boldsymbol{A} \cdot d\boldsymbol{s} \tag{1.327}$$

and Stokes' theorem expressed as

$$\int_S (\boldsymbol{\nabla} \times \boldsymbol{A}) \cdot d\boldsymbol{s} = \oint_C \boldsymbol{A} \cdot d\boldsymbol{l}. \tag{1.328}$$

To be completely general and allow for boundary conditions for antenna apertures, it is necessary to include the contribution from the fictitious magnetic current density $\boldsymbol{M}$ in Maxwell's curl of $\boldsymbol{E}$ equation as a mathematical convenience, that is,

$$\boldsymbol{\nabla} \times \boldsymbol{E} = -\boldsymbol{M} - \frac{\partial \boldsymbol{B}}{\partial t}. \tag{1.329}$$

Note, the magnetic current density has units of V/m^2.

The divergence theorem given by Equation (1.327) states that the volume integral of the divergence of $\boldsymbol{A}$ is equal to the outward flux of the vector field $\boldsymbol{A}$ through the surface S enclosing the volume V. Assuming that $\boldsymbol{A}$ and the curl of $\boldsymbol{A}$ are continuous, Stokes' theorem given by Equation (1.328) states that the curl of $\boldsymbol{A}$ over the open surface S bounded by C is equal to the circulation of $\boldsymbol{A}$ around the closed path C.

Consider now Figure 1.7, which shows two media separated by an interface surface that can be of arbitrary shape and can support surface charges ρ_s and surface currents $\boldsymbol{J}_s$ and $\boldsymbol{M}_s$. To determine the boundary conditions for the normal field components, consider Figure 1.8. From Maxwell's divergence of $\boldsymbol{D}$ equation and the divergence theorem, we can write

$$\int_V \boldsymbol{\nabla} \cdot \boldsymbol{D} dv = \oint_S \boldsymbol{A} \cdot d\boldsymbol{s} = \int_V \rho dv \tag{1.330}$$

where ρ is the volume charge density. In the limit where Δh approaches zero, only the top and bottom of the cylindrical box contribute, such that in vector notation,

$$\hat{\boldsymbol{n}} \cdot (\boldsymbol{D}_2 - \boldsymbol{D}_1) = \rho_s \tag{1.331}$$

where ρ_s is the surface charge density. Similarly, it can be shown that

$$\hat{\boldsymbol{n}} \cdot (\boldsymbol{B}_2 - \boldsymbol{B}_1) = 0. \tag{1.332}$$

Now, referring to Figure 1.9 from Maxwell's curl of $\boldsymbol{E}$ equation including the fictitious magnetic current density and Stokes' theorem, we can write

$$\int_S (\boldsymbol{\nabla} \times \boldsymbol{E}) \cdot d\boldsymbol{s} = \oint_C \boldsymbol{E} \cdot d\boldsymbol{l} = -\int_S \boldsymbol{M} \cdot d\boldsymbol{s} - \int_S \frac{\partial \boldsymbol{B}}{\partial t} \cdot d\boldsymbol{s}. \tag{1.333}$$

As Δh goes to zero, the term involving the integral of $\boldsymbol{B}$ goes to zero, and now in vector form, Equation (1.333) becomes

$$(\boldsymbol{E}_2 - \boldsymbol{E}_1) \times \hat{\boldsymbol{n}} = \boldsymbol{M}_s \tag{1.334}$$

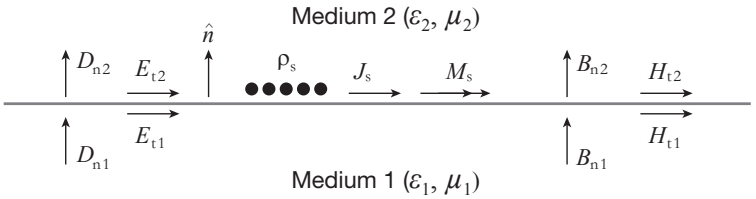

Figure 1.22 Electric charge, currents, and fields at a general interface between two media.

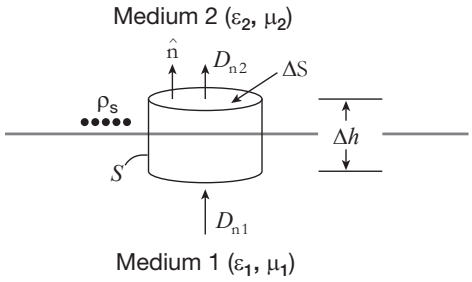

Figure 1.23 Electric charge and the normal components of electric flux density with a closed surface for evaluation of boundary conditions.

where $\boldsymbol{M}_s$ is the fictitious magnetic surface current. Similarly, it can be shown that

$$\hat{\boldsymbol{n}}\times(\boldsymbol{H}_2-\boldsymbol{H}_1)=\boldsymbol{J}_s. \tag{1.335}$$

From Equations (1.334) and (1.335) for general media in the absence of sources on the boundary (i.e., $\boldsymbol{J}_s=0$ and $\boldsymbol{M}_s=0$), the tangential components of $\boldsymbol{E}$ and $\boldsymbol{H}$ are continuous across the boundary. When medium 1 is a perfect electric conductor ($\sigma=\infty$), which means $\boldsymbol{E}_1=0$, from Equation (1.334), the tangential component of $\boldsymbol{E}_2$ must be zero at the perfect electric conductor.

1.6 Wave Equation for Conducting Media, Propagation Parameters

Consider Maxwell's equations given by Equations (1.145) and (1.146), but now in a source-free conducting region with $\boldsymbol{J}_{\text{source}}=0$ and $\boldsymbol{M}_{\text{source}}=0$, that is,

$$\boldsymbol{\nabla}\times\boldsymbol{E}=-j\omega\mu_c\boldsymbol{H} \tag{1.336}$$

$$\boldsymbol{\nabla}\times\boldsymbol{H}=j\omega\epsilon_c\boldsymbol{E} \tag{1.337}$$

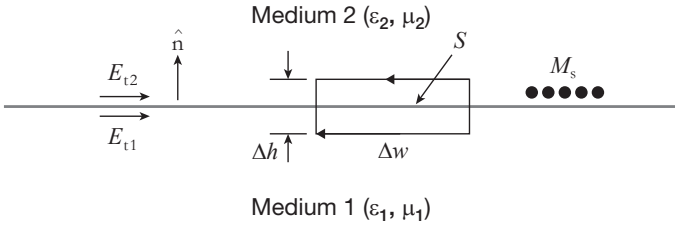

Figure 1.24 Magnetic current and tangential E fields with a closed contour for evaluation of boundary conditions.

$$\boldsymbol{\nabla}\cdot\boldsymbol{D} = 0 \tag{1.338}$$

$$\boldsymbol{\nabla}\cdot\boldsymbol{B} = 0. \tag{1.339}$$

Taking the curl of Equation (1.336) and substituting Equations (1.149) and (1.337) yields

$$\boldsymbol{\nabla}\times\boldsymbol{\nabla}\times\boldsymbol{E} = -j\omega\mu_c j\omega\epsilon_c\boldsymbol{E} = -j\omega\mu_c(\sigma + j\omega\epsilon')\boldsymbol{E} \tag{1.340}$$

or

$$\boldsymbol{\nabla}\times\boldsymbol{\nabla}\times\boldsymbol{E} = -j\omega\mu_c j\omega\epsilon_c\boldsymbol{E} = \omega^2\mu_c\epsilon_c\boldsymbol{E} \tag{1.341}$$

and defining the complex wavenumber k here as

$$k = \omega\sqrt{\mu_c\epsilon_c} \tag{1.342}$$

it follows that

$$\boldsymbol{\nabla}\times\boldsymbol{\nabla}\times\boldsymbol{E} = k^2\boldsymbol{E}. \tag{1.343}$$

By using the vector identity

$$\boldsymbol{\nabla}\times\boldsymbol{\nabla}\times\boldsymbol{E} = \boldsymbol{\nabla}(\boldsymbol{\nabla}\cdot\boldsymbol{E}) - \boldsymbol{\nabla}^2\boldsymbol{E} \tag{1.344}$$

and noting that the divergence of $\boldsymbol{E}$ is zero by Equation (1.338), it follows that

$$\boldsymbol{\nabla}^2\boldsymbol{E} + k^2\boldsymbol{E} = 0, \tag{1.345}$$

which is a form of the vector wave equation in complex media. A similar wave equation involving the vector magnetic field is given by

$$\boldsymbol{\nabla}^2\boldsymbol{H} + k^2\boldsymbol{H} = 0. \tag{1.346}$$

The vector wave equations expressed by Equations (1.345) and (1.346) are also commonly expressed as

$$\boldsymbol{\nabla}^2\boldsymbol{E} - \gamma^2\boldsymbol{E} = 0 \tag{1.347}$$

$$\boldsymbol{\nabla}^2\boldsymbol{H} - \gamma^2\boldsymbol{H} = 0 \tag{1.348}$$

where γ is the complex propagation constant. The above vector wave equations allow for spherical, cylindrical, and plane wave solutions.

For example, consider a $\hat{\boldsymbol{z}}$-polarized plane wave propagating in the $\hat{\boldsymbol{x}}$ direction as given by the linearly polarized electric field

$$\boldsymbol{E}(x) = e^{-\gamma x}\hat{\boldsymbol{z}}. \tag{1.349}$$

The plane-wave function given by Equation (1.349) is a solution of Equation (1.347), which can be verified by observing that the wave equation can be expressed in cartesian coordinates as

$$\nabla^2\boldsymbol{E} - \gamma^2\boldsymbol{E} = \frac{\partial^2\boldsymbol{E}}{\partial x^2} - \gamma^2\boldsymbol{E} = 0 \tag{1.350}$$

and then performing the partial derivative operation.

The relationship between the complex propagation constant γ and the complex wavenumber k is

$$\gamma = jk = j\omega\sqrt{\mu_c\epsilon_c}. \tag{1.351}$$

Thus,

$$\gamma^2 = -k^2 = -\omega^2\mu_c\epsilon_c. \tag{1.352}$$

By using Equation (1.340), it follows that

$$\gamma^2 = j\omega\mu_c(\sigma + j\omega\epsilon'). \tag{1.353}$$

Assume now an electrically conducting medium, and then it is readily shown that the propagation constant can be expressed as

$$\gamma = \pm\sqrt{j\omega\mu'(\sigma + j\omega\epsilon')} = \pm j\omega\sqrt{\mu'\epsilon'}\sqrt{1 - j\frac{\sigma}{\omega\epsilon'}}. \tag{1.354}$$

Again, the quantity (refer to Equation [1.355])

$$\frac{\sigma}{\omega\epsilon'} = \frac{\epsilon''}{\epsilon'} = \tan\delta \tag{1.355}$$

is referred to as the electric loss tangent or dissipation factor. Both σ and $\tan\delta$ are used in tables of dielectric characteristics of materials. It is common to express the complex propagation constant as

$$\gamma = \alpha + j\beta \tag{1.356}$$

where α is the attenuation constant in nepers/meter and β is the phase constant in radians/meter. Again, the complex wavenumber is expressed as

$$jk = \alpha + j\beta \tag{1.357}$$

and either way of analyzing the wave propagation provides the same results. The units of nepers/meter can be converted to decibels by multiplying by the factor 8.686. The units of radians/meter can be converted to degrees/meter by multiplying by the factor $180/\pi = 57.296$.

The constants α and β are found by setting Equation (1.354) equal to Equation (1.356) and then squaring both sides, equating the real and imaginary parts, and solving the pair of simultaneous equations, with the result

$$\alpha = \frac{\omega\sqrt{\mu'\epsilon'}}{\sqrt{2}}\left\{\sqrt{1+\left(\frac{\sigma}{\omega\epsilon'}\right)^2}-1\right\}^{1/2} \tag{1.358}$$

$$\beta = \frac{\omega\sqrt{\mu'\epsilon'}}{\sqrt{2}}\left\{\sqrt{1+\left(\frac{\sigma}{\omega\epsilon'}\right)^2}+1\right\}^{1/2}. \tag{1.359}$$

The wavelength λ in the lossy dielectric is then computed from the phase constant given by Equation (1.359) as

$$\lambda = \frac{2\pi}{\beta}. \tag{1.360}$$

The intrinsic wave impedance η is related to the ratio of the electric and magnetic fields and in lossy dielectric material is given by [8]

$$\eta = \sqrt{\frac{\mu}{\epsilon}} = \sqrt{\frac{j\omega\mu'}{\sigma+j\omega\epsilon'}} = \sqrt{\frac{\mu'}{\epsilon'}}\frac{1}{\sqrt{1-j\frac{\sigma}{\omega\epsilon'}}}. \tag{1.361}$$

In free space, the electrical conductivity σ is equal to zero, and it follows from Equation (1.361) that the free-space intrinsic wave impedance is

$$\eta_{\text{free space}} = \sqrt{\frac{\mu_o}{\epsilon_o}} = 120\pi = 376.99 \approx \ 377 \text{ ohms}. \tag{1.362}$$

In the general media case, in which both electric and magnetic loss are present, the constants α and β are determined from Equations (1.352) and (1.356) using Equations (1.142) and (1.143), by solving the simultaneous equations for the real and imaginary components with the result

$$\alpha = \frac{\omega\sqrt{\mu'\epsilon'}}{\sqrt{2}}\left\{\sqrt{\left(1+\tan^2\delta_e\right)\left(1+\tan^2\delta_m\right)}-\left(1-\tan\delta_e\tan\delta_m\right)\right\}^{1/2} \tag{1.363}$$

$$\beta = \frac{\omega\sqrt{\mu'\epsilon'}}{\sqrt{2}} \left\{ \sqrt{(1+\tan^2\delta_e)\,(1+\tan^2\delta_m)} + (1-\tan\delta_e\tan\delta_m) \right\}^{1/2} \tag{1.364}$$

where

$$\tan\delta_e = \frac{\epsilon''}{\epsilon'} = \frac{\sigma_e}{\omega\epsilon'} = \frac{\sigma_e}{\omega\epsilon_o\epsilon_r'} \tag{1.365}$$

and

$$\tan\delta_m = \frac{\mu''}{\mu'} = \frac{\sigma_m}{\omega\mu'} = \frac{\sigma_m}{\omega\mu_o\mu_r'} \tag{1.366}$$

are the electric and magnetic loss tangents, respectively. For general lossy media, the wave impedance is given by

$$\eta = \sqrt{\frac{\mu}{\epsilon}} = \sqrt{\frac{\mu' - j\mu''}{\epsilon' - j\epsilon''}} = \sqrt{\frac{\mu'}{\epsilon'}}\sqrt{\frac{1-j\tan\delta_m}{1-j\tan\delta_e}}. \tag{1.367}$$

Taking account of boundary conditions as described in Section 1.7, for normal angle of incidence of a plane wave, the reflection coefficient Γ for a uniform plane wave traveling in medium 1 and reflecting at the boundary of medium 2 is given by

$$\Gamma = \frac{\eta_2 - \eta_1}{\eta_2 + \eta_1}, \tag{1.368}$$

and the transmission coefficient T for a plane wave at normal incidence transmitted into medium 2 is given by

$$T = \frac{2\eta_2}{\eta_2 + \eta_1} \tag{1.369}$$

where η_1 is the impedance of medium 1 and η_2 is the impedance of medium 2. The more general cases of plane-wave incidence, including oblique incidence, polarization effects, and different media, are covered by Balanis [2, pp. 173–257].

It is convenient to have a simple equation for computing the wave propagation between any two points in the near field of an isolated transmitting antenna in conducting media. Consider a time-harmonic source radiating a spherical wave into an infinite homogeneous conducting medium. For an isotropic radiator and suppressing the $e^{j\omega t}$ time dependence where $\omega = 2\pi f$, the electric field as a function of range r can be expressed in phasor notation as a spherical wave

$$E(r) = E_o\frac{e^{-\gamma r}}{r} \tag{1.370}$$

where E_o is a constant and γ is the propagation constant given by Equation (1.354). For some cases in which the $1/r$ dependence can be ignored, a plane wavefront approximation to Equation (1.370) can be used. For example, a plane wavefront propagating along the x-axis can be expressed as

$$E(x) = E_o e^{-\gamma x}. \tag{1.371}$$

Equation (1.370) or Equation (1.371) can be used in a simplified ray-tracing analysis to compute the approximate electric field, generated by one or more transmitting antennas, at any point in a homogeneous lossy dielectric. If we let the electric field at the rectangular coordinates (x, y, z) due to the nth transmitting antenna in an array of N transmitting antennas be denoted as $E_n(x, y, z)$, then the total electric field of the transmitting array can be expressed as the following summation,

$$E_{\text{total}}(x, y, z) = \sum_{n=1}^{N} E_n(x, y, z). \tag{1.372}$$

For a transmitting point source at the origin, the amplitude of the electric field at range r_1 is given by

$$|E(r_1)| = E_o \frac{e^{-\alpha r_1}}{r_1} \tag{1.373}$$

and at range r_2 by

$$|E(r_2)| = E_o \frac{e^{-\alpha r_2}}{r_2}. \tag{1.374}$$

The total propagation loss between ranges r_1 and r_2 is found by taking the ratio of Equations (1.374) and (1.373) as

$$\frac{|E(r_2)|}{|E(r_1)|} = \frac{r_1}{r_2} e^{-\alpha(r_2 - r_1)}. \tag{1.375}$$

The field attenuation A_α in decibels from range r_1 to range r_2 caused by the lossy dielectric is simply

$$A_\alpha = 20 \log_{10}(e^{-\alpha(r_2 - r_1)}). \tag{1.376}$$

If we let $d = r_2 - r_1$, the above equation can be written in a convenient form as

$$A_\alpha = 20 \log_{10}(e^{-\alpha d}), \tag{1.377}$$

which is the relative field attenuation as a function of distance d into a lossy dielectric or transmission loss of a plane wave in decibels per meter. The

attenuation constant α has units of nepers per unit length or typically in the literature of nepers per meter (Np/m), where neper is dimensionless. If d is one meter and $\alpha = 1$ Np/m, then the field strength in decibels is $20\log_{10}(e^{-1}) = 20\log_{10}|0.368| = -8.686$ dB. Thus, the attenuation in decibels per meter is 8.686 times the attenuation constant in nepers per meter. If the attenuation constant is expressed in nepers/cm, then to convert to attenuation in decibels per cm, the multiplying factor remains 8.686. Similarly, the $1/r$ attenuation loss A_r in decibels is

$$A_r = 20\log_{10}\frac{r_1}{r_2}. \tag{1.378}$$

1.7 Electromagnetic Energy Flow

To demonstrate that an electromagnetic field can transfer electromagnetic energy into an electrically conducting volume (e.g., soil as in a ground-penetrating radar application), consider the following application of Maxwell's curl equations in the time domain in a source-free region where $\boldsymbol{J}_{\text{source}} = 0$ and $\boldsymbol{M}_{\text{source}} = 0$. Starting with the curl of the instantaneous magnetic field as in Equation (1.86), substitute Equations (1.104) and (1.122) with the result

$$\boldsymbol{\nabla}\times\boldsymbol{H}(\boldsymbol{r},t) = \sigma\boldsymbol{E} + \epsilon'\frac{\partial\boldsymbol{E}}{\partial t}. \tag{1.379}$$

Next, the curl of the instantaneous electric field from Equation (1.85) is given by

$$\boldsymbol{\nabla}\times\boldsymbol{E}(\boldsymbol{r},t) = -\mu'\frac{\partial\boldsymbol{H}}{\partial t}. \tag{1.380}$$

Fundamentally, it is desired to derive a power-flow expression for the electric and magnetic fields. The electric field has units of volts/meter and the magnetic field has units of amperes/meter. The product of volts/meter and amperes/meter produces watts/meter^2, which is power density. There are two possibilities for manipulating the electric and magnetic field expressions to produce a relation for power density, either a dot product or a cross product of the two field quantities. To produce a meaningful relation here, the cross product is the desired vector operation on the electric and magnetic field vectors. A vector identity will also be needed to convert to the desired field relation. Of the available general vector identities, the one that applies here is

$$\boldsymbol{\nabla}\cdot(\boldsymbol{A}\times\boldsymbol{B}) = \boldsymbol{B}\cdot(\boldsymbol{\nabla}\times\boldsymbol{A}) - \boldsymbol{A}\cdot(\boldsymbol{\nabla}\times\boldsymbol{B}). \tag{1.381}$$

On the basis of the vector identity in Equation (1.381), it is observed that the desired mathematical manipulations are to dot the electric field into the curl of the magnetic field and to dot the magnetic field into the curl of the electric

field. Once these manipulations are done, the desired cross product between $\boldsymbol{E}$ and $\boldsymbol{H}$ will appear. Thus, from Equations (1.379), (1.380), and (1.381) and by using $\boldsymbol{J}\cdot\boldsymbol{E} = \boldsymbol{E}\cdot\boldsymbol{J}$, it follows that

$$\boldsymbol{E}\cdot(\boldsymbol{\nabla}\times\boldsymbol{H}) = \boldsymbol{J}\cdot\boldsymbol{E} + \boldsymbol{E}\cdot\epsilon'\frac{\partial\boldsymbol{E}}{\partial t} = \boldsymbol{J}\cdot\boldsymbol{E} + \frac{1}{2}\epsilon'\frac{\partial E^2}{\partial t} \tag{1.382}$$

and

$$\boldsymbol{H}\cdot(\boldsymbol{\nabla}\times\boldsymbol{E}) = -\boldsymbol{H}\cdot\mu'\frac{\partial\boldsymbol{H}}{\partial t} = -\frac{1}{2}\mu'\frac{\partial H^2}{\partial t}. \tag{1.383}$$

Simplifying and subtracting Equation (1.382) from Equation (1.383) yields

$$\boldsymbol{E}\cdot(\boldsymbol{\nabla}\times\boldsymbol{H}) - \boldsymbol{H}\cdot(\boldsymbol{\nabla}\times\boldsymbol{E}) = \boldsymbol{J}\cdot\boldsymbol{E} + \frac{1}{2}\epsilon'\frac{\partial E^2}{\partial t} + \frac{1}{2}\mu'\frac{\partial H^2}{\partial t} \tag{1.384}$$

or applying the vector identity Equation (1.381) in Equation (1.384) yields

$$\boldsymbol{\nabla}\cdot(\boldsymbol{E}\times\boldsymbol{H}) = -\boldsymbol{J}\cdot\boldsymbol{E} - \frac{1}{2}\epsilon'\frac{\partial E^2}{\partial t} - \frac{1}{2}\mu'\frac{\partial H^2}{\partial t} \tag{1.385}$$

and now integrating over a volume of media

$$\int_V \boldsymbol{\nabla}\cdot(\boldsymbol{E}\times\boldsymbol{H})dv = -\int_V \boldsymbol{J}\cdot\boldsymbol{E}dv - \frac{\partial}{\partial t}\int_V [\frac{1}{2}\epsilon' E^2 + \frac{1}{2}\mu' H^2]dv. \tag{1.386}$$

The divergence theorem for any vector $\boldsymbol{A}$ for a closed surface S enclosing volume V is given by

$$\int_V \boldsymbol{\nabla}\cdot\boldsymbol{A}dv = \oint_S \boldsymbol{A}\cdot\hat{\boldsymbol{n}}ds \tag{1.387}$$

where dv is the elemental volume and ds is the elemental area perpendicular to the outward unit normal $\hat{\boldsymbol{n}}$. Thus, applying Equation (1.387) to the left-hand side of Equation (1.386) yields

$$\int_V \boldsymbol{\nabla}\cdot(\boldsymbol{E}\times\boldsymbol{H})dv = \oint_S (\boldsymbol{E}\times\boldsymbol{H})\cdot\hat{\boldsymbol{n}}ds. \tag{1.388}$$

Finally, Equation (1.386) reduces to

$$\oint_S (\boldsymbol{E}\times\boldsymbol{H})\cdot\hat{\boldsymbol{n}}ds = -\int_V \boldsymbol{J}\cdot\boldsymbol{E}dv - \frac{\partial}{\partial t}\int_V [\frac{1}{2}\epsilon' E^2 + \frac{1}{2}\mu' H^2]dv. \tag{1.389}$$

The term on the left side of Equation (1.389) represents the net inward flux of the vector

$$\boldsymbol{P}(\boldsymbol{r},t) = \boldsymbol{E}(\boldsymbol{r},t)\times\boldsymbol{H}(\boldsymbol{r},t). \tag{1.390}$$

In Equations (1.389) and (1.390), the vector quantity $\boldsymbol{P}(\boldsymbol{r},t) = \boldsymbol{E}(\boldsymbol{r},t)\times\boldsymbol{H}(\boldsymbol{r},t)$ is known as the instantaneous Poynting vector (due to J.H. Poynting [104]) and can be interpreted as the instantaneous power-flow density in watts/meter^2 at each observation point $(\boldsymbol{r})$ on the surface S, or equivalently the power delivered to the volume V by external electromagnetic sources. Equation (1.389) is referred to as the integral form of Poynting's theorem and describes conservation of energy for electromagnetic waves. From Equation (1.104), it follows that

$$\boldsymbol{J}\cdot\boldsymbol{E} = \sigma\boldsymbol{E}\cdot\boldsymbol{E} = \sigma|\boldsymbol{E}|^2 \tag{1.391}$$

where the dot product of the real vector $\boldsymbol{E}$ with itself is just the magnitude of $\boldsymbol{E}$ squared. The first integral term on the right side of Equation (1.389) involving $\boldsymbol{J}\cdot\boldsymbol{E} = \sigma|E|^2$ represents the instantaneous ohmic losses within the volume enclosed by the surface S. The integral in the second term on the right side of Equation (1.389) is the total energy (with units of watt-seconds = joules), due to electric and magnetic fields, stored within the volume V.

To understand the electromagnetic field energy transfer to conductive media such as lossy dielectrics, it is necessary to determine the time-average power delivered to and dissipated within the volume. The time-average Poynting vector or time-average power density given by Equation (1.389) is computed over one period T as

$$\boldsymbol{P}_{\text{ave}}(\boldsymbol{r}) = \frac{1}{T}\int_0^T \boldsymbol{E}(\boldsymbol{r},t)\times\boldsymbol{H}(\boldsymbol{r},t)\,dt \tag{1.392}$$

where the period is equal to

$$T = 2\pi/\omega. \tag{1.393}$$

Substituting the exponential forms given by Equations (1.114) and (1.115) into Equation (1.392) yields

$$\boldsymbol{P}_{\text{ave}}(\boldsymbol{r}) = \frac{1}{T}\int_0^T \Big[\text{Re}[\boldsymbol{E}(\boldsymbol{r})e^{j\omega t}]\times\text{Re}[\boldsymbol{H}(\boldsymbol{r})e^{j\omega t}]\Big]\,dt. \tag{1.394}$$

Making use of the relation

$$\text{Re}[\boldsymbol{A}B] = \frac{1}{2}[\boldsymbol{A}B + \boldsymbol{A}^*B^*], \tag{1.395}$$

it follows that

$$\text{Re}[\boldsymbol{E}(\boldsymbol{r})e^{j\omega t}]\times\text{Re}[\boldsymbol{H}(\boldsymbol{r})e^{j\omega t}] = \frac{1}{2}[\boldsymbol{E}e^{j\omega t} + \boldsymbol{E}^*e^{-j\omega t}]\times\frac{1}{2}[\boldsymbol{H}e^{j\omega t} + \boldsymbol{H}^*e^{-j\omega t}]. \tag{1.396}$$

Expanding Equation (1.396) and using the relation (with * denoting conjugate)

$$\mathrm{Re}[\boldsymbol{E}\times\boldsymbol{H}^*] = \frac{1}{2}[\boldsymbol{E}\times\boldsymbol{H}^* + \boldsymbol{E}^*\times\boldsymbol{H}] \tag{1.397}$$

it can be shown that Equation (1.394) reduces to

$$\boldsymbol{P}_{\text{ave}} = \frac{1}{T}\int_0^{\frac{2\pi}{\omega}} \left[\frac{1}{2}\mathrm{Re}[\boldsymbol{E}\times\boldsymbol{H}^*] + \frac{1}{4}\boldsymbol{E}\times\boldsymbol{H}e^{j2\omega t} + \frac{1}{4}\boldsymbol{E}^*\times\boldsymbol{H}^*e^{-j2\omega t}\right] dt. \tag{1.398}$$

It can be shown, by integration, that Equation (1.398) reduces to

$$\boldsymbol{P}_{\text{ave}}(\boldsymbol{r}) = \frac{1}{2}\mathrm{Re}[\boldsymbol{E}\times\boldsymbol{H}^*], \tag{1.399}$$

which is the desired expression for the time-average power density of the electromagnetic field, or the time-average Poynting's vector, which has units of watts/meter^2.

As an example, for the case of a plane wave propagating in a conducting medium, the electric field is given by

$$\boldsymbol{E}(\boldsymbol{r}) = \eta\,\hat{\boldsymbol{n}}\times\boldsymbol{H}(\boldsymbol{r}) \tag{1.400}$$

and the magnetic field is given by

$$\boldsymbol{H}(\boldsymbol{r}) = \hat{\boldsymbol{n}}\times\boldsymbol{E}(\boldsymbol{r})/\eta \tag{1.401}$$

and thus, by substituting Equation (1.401) in Equation (1.399), it follows from a vector identity that the time-average Poynting vector for a plane wave is equal to

$$\boldsymbol{P}_{\text{ave}}(\boldsymbol{r}) = \hat{\boldsymbol{n}}\frac{1}{2}|\boldsymbol{E}(\boldsymbol{r})|^2/\eta \tag{1.402}$$

where $\hat{\boldsymbol{n}}$ is the direction of propagation.

Next, it is desired to quantify the average power deposition in a lossy dielectric because this quantity is needed to determine the absorption of electromagnetic energy in any dielectric materials that the antenna might be constructed from, or in the case in which the antenna is radiating in the presence of such lossy materials. Referring to Equation (1.389), for the first term on the right-hand side, the time-average power dissipation per unit volume is computed over one period T as

$$P_d(\boldsymbol{r}) = \frac{1}{T}\int_0^T \boldsymbol{J}(\boldsymbol{r},t)\cdot\boldsymbol{E}(\boldsymbol{r},t)dt. \tag{1.403}$$

Substituting Equations (1.114) and (1.116) into Equation (1.403) yields

$$P_d(\boldsymbol{r}) = \frac{1}{T}\int_0^T \left[\text{Re}[\boldsymbol{J}(\boldsymbol{r})e^{j\omega t}]\cdot\text{Re}[\boldsymbol{E}(\boldsymbol{r})e^{j\omega t}]\right] dt. \tag{1.404}$$

Making use of the relation given in Equation (1.395), it follows that

$$\text{Re}[\boldsymbol{J}(\boldsymbol{r})e^{j\omega t}]\cdot\text{Re}[\boldsymbol{E}(\boldsymbol{r})e^{j\omega t}] = \frac{1}{2}[\boldsymbol{J}e^{j\omega t} + \boldsymbol{J}^* e^{-j\omega t}]\cdot\frac{1}{2}[\boldsymbol{E}e^{j\omega t} + \boldsymbol{E}^* e^{-j\omega t}]. \tag{1.405}$$

Using Equation (1.405) in Equation (1.404) and observing that the current density $\boldsymbol{J}$ and electric field $\boldsymbol{E}$ are in phasor form, it follows that

$$\boldsymbol{J}\cdot\boldsymbol{E}^* = \sigma\boldsymbol{E}\cdot\boldsymbol{E}^* = \sigma|\boldsymbol{E}|^2 \tag{1.406}$$

$$\boldsymbol{J}^*\cdot\boldsymbol{E} = \sigma\boldsymbol{E}^*\cdot\boldsymbol{E} = \sigma|\boldsymbol{E}|^2 \tag{1.407}$$

and it can be shown that

$$P_d = \frac{1}{T}\int_0^{T=\frac{2\pi}{\omega}} \left[\frac{1}{2}\sigma|\boldsymbol{E}|^2 + \frac{1}{4}\boldsymbol{J}\cdot\boldsymbol{E}e^{j2\omega t} + \frac{1}{4}\boldsymbol{J}^*\cdot\boldsymbol{E}^* e^{-j2\omega t}\right] dt. \tag{1.408}$$

It also can be shown that Equation (1.408) reduces to

$$P_d(\boldsymbol{r}) = P_{\text{ave dissipated}} = \frac{1}{2}\sigma|\boldsymbol{E}(\boldsymbol{r})|^2, \tag{1.409}$$

which is the desired expression for the time-average power dissipation per unit volume of the lossy dielectric, which has units of watts/m^3.

The specific absorption rate (SAR) [114] in the dielectric is the power dissipated or absorbed per unit mass (W/kg) of the medium (lossy dielectric), so from Equation (1.409), it follows that

$$\text{SAR}(\boldsymbol{r}) = \frac{P_d(\boldsymbol{r})}{\rho} = \frac{\sigma}{2\rho}|\boldsymbol{E}(\boldsymbol{r})|^2 \tag{1.410}$$

where ρ is the density of the medium in kg/m^3. To estimate the initial linear temperature rise ΔT versus time interval Δt in a lossy dielectric that is characterized by the specific heat c_d with units of kJ/(kg-°C), the following calculation can be made:

$$\Delta T = \frac{\text{SAR}\,\Delta t}{c_d} \tag{1.411}$$

where in Equation (1.411), it has been assumed that any thermal conduction or thermal boundary conditions have been ignored.

1.8 Fields of Short Electric and Magnetic Dipoles

1.8.1 Introduction

Arbitrarily shaped antennas can be considered to be composed of the superposition of a number of short electric dipoles and/or magnetic dipoles (electric loops) as depicted in Figure 1.10.

The closed-form expressions for the near-zone electromagnetic fields in free space resulting from an electrically short (Hertzian) dipole of length l with current I_e along the z axis are given by [10]

$$E_r^{\text{dipole}}(r,\theta) = \frac{I_e l e^{j(\omega t-\beta r)}}{2\pi\epsilon_o}\cos\theta\left(\frac{1}{cr^2}+\frac{1}{j\omega r^3}\right) \tag{1.412}$$

$$E_\theta^{\text{dipole}}(r,\theta) = \frac{I_e l e^{j(\omega t-\beta r)}}{4\pi\epsilon_o}\sin\theta\left(\frac{j\omega}{c^2 r}+\frac{1}{cr^2}+\frac{1}{j\omega r^3}\right) \tag{1.413}$$

$$H_\phi^{\text{dipole}}(r,\theta) = \frac{I_e l e^{j(\omega t-\beta r)}}{4\pi}\sin\theta\left(\frac{j\omega}{cr}+\frac{1}{r^2}\right). \tag{1.414}$$

Similarly, the near-zone electromagnetic fields for an electrically small loop or short (small) magnetic dipole of length l with current I_m along the z axis are given by

$$H_r^{\text{loop}}(r,\theta) = \frac{I_m l e^{j(\omega t-\beta r)}}{2\pi\mu_o}\cos\theta\left(\frac{1}{cr^2}+\frac{1}{j\omega r^3}\right) \tag{1.415}$$

$$H_\theta^{\text{loop}}(r,\theta) = \frac{I_m l e^{j(\omega t-\beta r)}}{4\pi\mu_o}\sin\theta\left(\frac{j\omega}{c^2 r}+\frac{1}{cr^2}+\frac{1}{j\omega r^3}\right) \tag{1.416}$$

$$E_\phi^{\text{loop}}(r,\theta) = \frac{I_m l e^{j(\omega t-\beta r)}}{4\pi}\sin\theta\left(\frac{j\omega}{cr}+\frac{1}{r^2}\right). \tag{1.417}$$

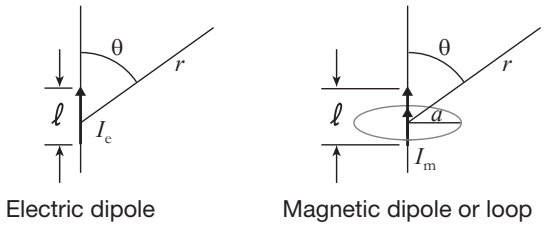

Figure 1.25 Geometry for short electrical dipole with length l and current I_e and short magnetic dipole with length l and current I_m (small electric current loop with radius a).

In the far field, the terms involving $1/r^2$ and $1/r^3$ can be neglected relative to the $1/r$ term. Thus, the only significant far-field radiating components of the short vertical electric dipole are E_θ and H_ϕ. For the small horizontal loop antenna (short vertical magnetic dipole), the only significant far-field radiating components are E_ϕ and H_θ. In each case, in the far field, it can be shown that the ratio of the electric to magnetic field amplitude is equal to the impedance of free space. That is,

$$\frac{E}{H} = \eta_o. \tag{1.418}$$

To derive the near-zone fields stated above, there are two approaches. One approach is to compute the magnetic vector potential $\boldsymbol{A}$ from the source current $\boldsymbol{J}$, and then the magnetic field $\boldsymbol{H}$ can be computed. The electric field $\boldsymbol{E}$ is then obtained from the magnetic field $\boldsymbol{H}$ by using Maxwell's curl equation. The other approach is to compute the electric field directly from the source current $\boldsymbol{J}$. Both approaches are discussed below.

In the first approach, the magnetic vector potential is needed and is given by Equation (1.197), which is repeated below for general isotropic media:

$$\boldsymbol{A}(\boldsymbol{r}) = \mu \int_V \boldsymbol{J}(\boldsymbol{r}') \frac{e^{-jk|\boldsymbol{r}-\boldsymbol{r}'|}}{4\pi|\boldsymbol{r}-\boldsymbol{r}'|}\, dv'. \tag{1.419}$$

Repeating Equation (1.174), the magnetic field $\boldsymbol{H}$ in terms of $\boldsymbol{A}$ is given by

$$\boldsymbol{H} = \frac{1}{\mu} \boldsymbol{\nabla} \times \boldsymbol{A}. \tag{1.420}$$

1.8.2 Derivation of Fields for $\hat{z}$ Hertzian Dipole

In the case of a $\hat{\boldsymbol{z}}$ Hertzian dipole, let the electric current density be given by

$$\boldsymbol{J}(\boldsymbol{r}') = \hat{\boldsymbol{z}} I_e l \delta(r') \tag{1.421}$$

where the delta function $\delta(r')$ is equal to unity when $r' = 0$ and is equal to zero elsewhere. Substituting Equation (1.421) in Equation (1.419) yields

$$\boldsymbol{A}(r) = \hat{\boldsymbol{z}} \frac{\mu I_e l}{4\pi} \frac{e^{-jkr}}{r}. \tag{1.422}$$

To reduce the above equation, use the standard conversion from rectangular components to spherical components,

$$\begin{bmatrix} A_r \\ A_\theta \\ A_\phi \end{bmatrix} = \begin{bmatrix} \sin\theta\cos\phi & \sin\theta\sin\phi & \cos\theta \\ \cos\theta\cos\phi & \cos\theta\sin\phi & -\sin\theta \\ -\sin\phi & \cos\phi & 0 \end{bmatrix} \begin{bmatrix} A_x \\ A_y \\ A_z \end{bmatrix}. \tag{1.423}$$

If the x and y components of $\boldsymbol{A}$ are zero, the transformation reduces to

$$A_r = A_z \cos\theta \tag{1.424}$$

$$A_\theta = -A_z \sin\theta \tag{1.425}$$

and note that the A_ϕ component is zero. Thus, from Equations (1.422), (1.424), and (1.425), it follows that

$$A_r = \mu I_e l \frac{e^{-jkr}}{4\pi r} \cos\theta \tag{1.426}$$

$$A_\theta = -\mu I_e l \frac{e^{-jkr}}{4\pi r} \sin\theta \tag{1.427}$$

$$A_\phi = 0. \tag{1.428}$$

Since the A_ϕ component is zero and the ϕ variation of A_r and A_θ is zero for a z-directed current, referring to Equation (1.93), the magnetic field $\boldsymbol{H}$ in spherical coordinates is reduced to

$$\boldsymbol{H} = \frac{1}{\mu}\boldsymbol{\nabla}\times\boldsymbol{A} = \hat{\boldsymbol{\phi}}\frac{1}{\mu r}\left[\frac{\partial}{\partial r}(rA_\theta) - \frac{\partial A_r}{\partial \theta}\right]. \tag{1.429}$$

Performing the partial derivatives in Equation (1.429) yields the only nonzero magnetic-field component

$$H_\phi = jkI_e l \sin\theta \left[1 + \frac{1}{jkr}\right]\frac{e^{-jkr}}{4\pi r}. \tag{1.430}$$

In general, the Maxwell curl equation for the magnetic field in time-harmonic form is Equation (1.146), which is repeated here as

$$\boldsymbol{\nabla}\times\boldsymbol{H} = \boldsymbol{J}_{\text{source}} + j\omega\epsilon_c\boldsymbol{E}, \tag{1.431}$$

and when the magnetic field is computed at a point removed from the source, the magnetic field expression is reduced to

$$\boldsymbol{\nabla}\times\boldsymbol{H} = j\omega\epsilon\boldsymbol{E} \tag{1.432}$$

where it is now assumed that the complex permittivity is denoted by ϵ. Furthermore, using Equations (1.192) and (1.432), the electric field as a function of the vector distance $\boldsymbol{r}$ from the source can be computed from either the magnetic vector potential $\boldsymbol{A}$ or magnetic field $\boldsymbol{H}$ as expressed below:

$$\boldsymbol{E}(\boldsymbol{r}) = -j\omega\boldsymbol{A} - \frac{j}{\omega\mu\epsilon}\boldsymbol{\nabla}(\boldsymbol{\nabla}\cdot\boldsymbol{A}) = \frac{1}{j\omega\epsilon}\boldsymbol{\nabla}\times\boldsymbol{H}. \tag{1.433}$$

Substituting either Equations (1.426) and (1.427) or Equation (1.430) into (1.433) yields

$$E_r(r,\theta) = 2\eta I_e l \cos\theta \left[\frac{1}{r} + \frac{1}{jkr^2}\right] \frac{e^{-jkr}}{4\pi r} \tag{1.434}$$

$$E_\theta(r,\theta) = j\eta k I_e l \sin\theta \left[1 + \frac{1}{jkr} - \frac{1}{(kr)^2}\right] \frac{e^{-jkr}}{4\pi r} \tag{1.435}$$

$$E_\phi = 0. \tag{1.436}$$

The same near fields are computed for the $\hat{\boldsymbol{z}}$ Hertzian dipole using the dyadic Green's function approach described below. With this approach, the electric field is computed directly, from which computation the magnetic field can be computed using Maxwell's $\boldsymbol{\nabla}\times\boldsymbol{E}$ equation. Repeating Equation (1.205),

$$\boldsymbol{E}(\boldsymbol{r}) = -j\omega\mu[\overline{\boldsymbol{I}} + \frac{1}{k^2}\boldsymbol{\nabla}\boldsymbol{\nabla}]\cdot\int_V \boldsymbol{J}(\boldsymbol{r}')\frac{e^{-jk|\boldsymbol{r}-\boldsymbol{r}'|}}{4\pi|\boldsymbol{r}-\boldsymbol{r}'|}\,dv' \tag{1.437}$$

and substituting Equation (1.421) in Equation (1.437) yields

$$\boldsymbol{E}(\boldsymbol{r}) = -j\omega\mu[\overline{\boldsymbol{I}} + \frac{1}{k^2}\boldsymbol{\nabla}\boldsymbol{\nabla}]\cdot\hat{\boldsymbol{z}} I_e l \frac{e^{-jkr}}{4\pi r} \tag{1.438}$$

or using spherical components (refer to Equation [1.241]) for $\hat{\boldsymbol{z}}$ as

$$\boldsymbol{E}(\boldsymbol{r}) = -j\omega\mu[\overline{\boldsymbol{I}} + \frac{1}{k^2}\boldsymbol{\nabla}\boldsymbol{\nabla}]\cdot\left[\left[\hat{\boldsymbol{r}} I_e l\cos\theta - \hat{\boldsymbol{\theta}} I_e l \sin\theta\right]\frac{e^{-jkr}}{4\pi r}\right] \tag{1.439}$$

and then define

$$\boldsymbol{V} = \left[\hat{\boldsymbol{r}} I_e l\cos\theta - \hat{\boldsymbol{\theta}} I_e l \sin\theta\right]\frac{e^{-jkr}}{4\pi r} = \hat{\boldsymbol{r}} V_r + \hat{\boldsymbol{\theta}} V_\theta. \tag{1.440}$$

Next, use the following identity

$$(\boldsymbol{\nabla}\boldsymbol{\nabla})\cdot\boldsymbol{V} = \boldsymbol{\nabla}(\boldsymbol{\nabla}\cdot\boldsymbol{V}) \tag{1.441}$$

and it follows that Equation (1.439) becomes

$$\boldsymbol{E}(\boldsymbol{r}) = -j\omega\mu[\hat{\boldsymbol{r}} V_r + \hat{\boldsymbol{\theta}} V_\theta] - j\omega\mu\frac{1}{k^2}\boldsymbol{\nabla}\left[\boldsymbol{\nabla}\cdot\left[\hat{\boldsymbol{r}} V_r + \hat{\boldsymbol{\theta}} V_\theta\right]\right]. \tag{1.442}$$

Carrying out the vector operations in Equation (1.442) using Equation (1.256) yields the E-field components given previously in Equations (1.434), (1.435), and (1.436), which the reader can verify.

1.8.3 Derivation of Fields for an Arbitrarily Polarized Hertzian Dipole

The electric field produced by a source current density $\boldsymbol{J}$ with arbitrary polarization unit vector $\hat{\boldsymbol{p}}$ in infinite homogeneous space can be determined as follows [3, p. 506]. Assume a Hertzian dipole with vector electric current $\boldsymbol{I}_e l$ located at the origin, that is,

$$\boldsymbol{J}(\boldsymbol{r}') = \boldsymbol{I}_e l \delta(\boldsymbol{r}') \tag{1.443}$$

where

$$\boldsymbol{I}_e l = \hat{\boldsymbol{p}} I_e l \tag{1.444}$$

and I_e is the magnitude of the current. Repeating Equation (1.205)

$$\boldsymbol{E}(\boldsymbol{r}) = -j\omega\mu[\overline{\boldsymbol{I}} + \frac{1}{k^2}\boldsymbol{\nabla}\boldsymbol{\nabla}]\cdot \int_V \boldsymbol{J}(\boldsymbol{r}')\frac{e^{-jk|\boldsymbol{r}-\boldsymbol{r}'|}}{4\pi|\boldsymbol{r}-\boldsymbol{r}'|}\, dv' \tag{1.445}$$

and substituting in Equation (1.443) yields

$$\boldsymbol{E}(\boldsymbol{r}) = -j\omega\mu[\overline{\boldsymbol{I}} + \frac{1}{k^2}\boldsymbol{\nabla}\boldsymbol{\nabla}]\cdot \boldsymbol{I}_e l \frac{e^{-jkr}}{4\pi r}. \tag{1.446}$$

Using the vector identity given by Equation (1.441) and

$$\boldsymbol{\nabla}\cdot\psi\boldsymbol{A} = \psi(\boldsymbol{\nabla}\cdot\boldsymbol{A}) + \boldsymbol{A}\cdot(\boldsymbol{\nabla}\psi) \tag{1.447}$$

and from Equation (1.95), it is observed that

$$\boldsymbol{\nabla}\cdot\boldsymbol{I}_e l = 0, \tag{1.448}$$

and it follows that

$$\boldsymbol{\nabla}\boldsymbol{\nabla}\cdot\boldsymbol{I}_e l\frac{e^{-jkr}}{4\pi r} = \boldsymbol{\nabla}\left[\frac{e^{-jkr}}{4\pi r}(\boldsymbol{\nabla}\cdot\boldsymbol{I}_e l) + \boldsymbol{I}_e l\cdot\left(\boldsymbol{\nabla}\frac{e^{-jkr}}{4\pi r}\right)\right] = \boldsymbol{\nabla}\left[\boldsymbol{I}_e l\cdot\left(\boldsymbol{\nabla}\frac{e^{-jkr}}{4\pi r}\right)\right]. \tag{1.449}$$

Next, use the vector identity

$$\boldsymbol{\nabla}(\boldsymbol{A}\cdot\boldsymbol{B}) = (\boldsymbol{A}\cdot\boldsymbol{\nabla})\boldsymbol{B} + (\boldsymbol{B}\cdot\boldsymbol{\nabla})\boldsymbol{A} + \boldsymbol{A}\times(\boldsymbol{\nabla}\times\boldsymbol{B}) + \boldsymbol{B}\times(\boldsymbol{\nabla}\times\boldsymbol{A}). \tag{1.450}$$

Letting $\boldsymbol{A} = \boldsymbol{I}_e l$ and $\boldsymbol{B} = \boldsymbol{\nabla}(e^{-jkr}/4\pi r)$ and using the vector identity

$$\boldsymbol{\nabla}\times(\boldsymbol{\nabla}\psi) = 0 \tag{1.451}$$

and noting that $\boldsymbol{\nabla} \boldsymbol{I}_e l = 0$ and $\boldsymbol{\nabla} \times \boldsymbol{I}_e l = 0$, it follows that the rightmost side of Equation (1.449) reduces to

$$\boldsymbol{\nabla} \left[\boldsymbol{I}_e l \cdot \left(\boldsymbol{\nabla} \frac{e^{-jkr}}{4\pi r} \right) \right] = (\boldsymbol{I}_e l \cdot \boldsymbol{\nabla}) \boldsymbol{\nabla} \frac{e^{-jkr}}{4\pi r}. \tag{1.452}$$

Now the gradient operation in Equation (1.452) is evaluated to be

$$\boldsymbol{\nabla} \left(\frac{e^{-jkr}}{4\pi r} \right) = \hat{\boldsymbol{r}} \frac{\partial}{\partial r} \left(\frac{e^{-jkr}}{4\pi r} \right) = \hat{\boldsymbol{r}} \left(-jk - \frac{1}{r} \right) \frac{e^{-jkr}}{4\pi r}. \tag{1.453}$$

Next, using Equation (1.453) in the right-hand side of Equation (1.452) yields

$$(\boldsymbol{I}_e l \cdot \boldsymbol{\nabla}) \boldsymbol{\nabla} \frac{e^{-jkr}}{4\pi r} = \boldsymbol{I}_e l \cdot \boldsymbol{\nabla} \boldsymbol{\nabla} \frac{e^{-jkr}}{4\pi r} = \boldsymbol{I}_e l \cdot \left(\boldsymbol{\nabla} \hat{\boldsymbol{r}} \left(-jk - \frac{1}{r} \right) \frac{e^{-jkr}}{4\pi r} \right). \tag{1.454}$$

To perform the gradient operation on the right-hand side of Equation (1.454), it is observed that

$$\boldsymbol{\nabla} (\hat{\boldsymbol{r}} \psi(r)) = \hat{\boldsymbol{r}} \boldsymbol{\nabla} \psi(r) + \psi(r) \boldsymbol{\nabla} \hat{\boldsymbol{r}}. \tag{1.455}$$

Now let

$$\psi(r) = \left(-jk - \frac{1}{r} \right) \frac{e^{-jkr}}{4\pi r} \tag{1.456}$$

and compute the gradient of $\psi(r)$ as

$$\boldsymbol{\nabla} \psi(r) = \boldsymbol{\nabla} \left[\left(-jk - \frac{1}{r} \right) \frac{e^{-jkr}}{4\pi r} \right] = \hat{\boldsymbol{r}} \left[-k^2 + \frac{2jk}{r} + \frac{2}{r^2} \right] \frac{e^{-jkr}}{4\pi r}. \tag{1.457}$$

Using Equation (1.252) and the unit vector derivatives given below Equation (1.235), it follows that

$$\boldsymbol{\nabla} \hat{\boldsymbol{r}} = \frac{1}{r} \hat{\boldsymbol{\theta}} \hat{\boldsymbol{\theta}} + \frac{1}{r} \hat{\boldsymbol{\phi}} \hat{\boldsymbol{\phi}}. \tag{1.458}$$

Using the results of Equations (1.455), (1.456), (1.457), and (1.458), it follows that the dyadic operation in Equation (1.454) is evaluated as

$$\boldsymbol{\nabla} \boldsymbol{\nabla} \frac{e^{-jkr}}{4\pi r} = \hat{\boldsymbol{r}} \hat{\boldsymbol{r}} \left[-k^2 + \frac{2jk}{r} + \frac{2}{r^2} \right] \frac{e^{-jkr}}{4\pi r} + \left[\hat{\boldsymbol{\theta}} \hat{\boldsymbol{\theta}} + \hat{\boldsymbol{\phi}} \hat{\boldsymbol{\phi}} \right] \left[-\frac{jk}{r} - \frac{1}{r^2} \right] \frac{e^{-jkr}}{4\pi r}. \tag{1.459}$$

Note: substituting Equation (1.459) in Equation (1.326) yields the explicit dyadic Green's function for a point source at the origin as

$$\overline{\boldsymbol{G}}(\boldsymbol{r}) = \hat{\boldsymbol{r}}\hat{\boldsymbol{r}}\left[\frac{2j}{kr} + \frac{2}{k^2r^2}\right]\frac{e^{-jkr}}{4\pi r} + \left[\hat{\boldsymbol{\theta}}\hat{\boldsymbol{\theta}} + \hat{\boldsymbol{\phi}}\hat{\boldsymbol{\phi}}\right]\left[1 - \frac{j}{kr} - \frac{1}{k^2r^2}\right]\frac{e^{-jkr}}{4\pi r}. \tag{1.460}$$

Using Equations (1.459), (1.449), and (1.242) in Equation (1.446) yields the near-zone electric field for an arbitrary polarized Hertzian dipole at the origin as

$$\boldsymbol{E}(\boldsymbol{r}) = -j\omega\mu\frac{e^{-jkr}}{4\pi r}\left[\left[1 - \frac{j}{kr} - \frac{1}{k^2r^2}\right]\boldsymbol{I}_e l + \hat{\boldsymbol{r}}\left(\hat{\boldsymbol{r}}\cdot\boldsymbol{I}_e l\right)\left[-1 + \frac{3j}{kr} + \frac{3}{k^2r^2}\right]\right]. \tag{1.461}$$

The near-zone magnetic field is then determined from Maxwell's curl of $\boldsymbol{E}$ equation as

$$\boldsymbol{H}(\boldsymbol{r}) = -\frac{1}{j\omega\mu}\boldsymbol{\nabla}\times\boldsymbol{E}(\boldsymbol{r}) = \boldsymbol{\nabla}\times\left[\overline{\boldsymbol{I}} + \frac{1}{k^2}\boldsymbol{\nabla}\boldsymbol{\nabla}\right]\cdot\boldsymbol{I}_e l\frac{e^{-jkr}}{4\pi r} = \boldsymbol{\nabla}\times\boldsymbol{I}_e l\frac{e^{-jkr}}{4\pi r} \tag{1.462}$$

which follows from the identity that the curl of the gradient of any scalar is equal to zero (Equation [1.451]). To solve Equation (1.462), the following vector identity is used:

$$\boldsymbol{\nabla}\times(\Psi\boldsymbol{A}) = \Psi\boldsymbol{\nabla}\times\boldsymbol{A} - \boldsymbol{A}\times\boldsymbol{\nabla}\Psi. \tag{1.463}$$

Noting that

$$\boldsymbol{\nabla}\times\boldsymbol{I}_e = 0 \tag{1.464}$$

and using Equation (1.453), it follows that the near-zone magnetic field for an arbitrary polarized Hertzian dipole is expressed as

$$\boldsymbol{H}(\boldsymbol{r}) = \boldsymbol{\nabla}\times\boldsymbol{I}_e l\frac{e^{-jkr}}{4\pi r} = -\hat{\boldsymbol{r}}\times\boldsymbol{I}_e ljk\left[1 - \frac{j}{kr}\right]\frac{e^{-jkr}}{4\pi r}. \tag{1.465}$$

To compute the time-average power density of the electromagnetic field generated by the arbitrary polarized dipole, first substitute Equations (1.461) and (1.465) into the bracketed expression in Equation (1.399) using complex power density denoted $\boldsymbol{P}_c = \boldsymbol{E}\times\boldsymbol{H}^*$ with the result

$$\boldsymbol{P}_c = \eta\left[\frac{k}{4\pi r}\right]^2\left\{\hat{\boldsymbol{r}}(Il)^2\left(1 - \frac{j}{k^3r^3}\right) - \hat{\boldsymbol{r}}(\hat{\boldsymbol{r}}\cdot\boldsymbol{I}l)^2\left[1 - \frac{2j}{kr} - \frac{3j}{k^3r^3}\right] - (\hat{\boldsymbol{r}}\cdot\boldsymbol{I}l)\boldsymbol{I}l\left[\frac{2j}{kr} + \frac{2j}{k^3r^3}\right]\right\} \tag{1.466}$$

from which it follows that the time-average power density of the arbitrary dipole is

$$\boldsymbol{P}_{\text{ave}}^{\text{dipole}}(\boldsymbol{r}) = \frac{1}{2}\text{Re}[\boldsymbol{E}\times\boldsymbol{H}^*] = \frac{1}{2}\text{Re}[\boldsymbol{P}_c] = \eta\left[\frac{k}{4\pi r}\right]^2\left[\hat{\boldsymbol{r}}(Il)^2 - \hat{\boldsymbol{r}}(\hat{\boldsymbol{r}}\cdot\boldsymbol{I}l)^2\right]. \tag{1.467}$$

In the case of a z-directed dipole, referring to Equations (1.475) to (1.478), it can be shown that the complex power density is

$$\boldsymbol{P}_c^{\text{z-dipole}} = \eta\left[\frac{kIl}{4\pi r}\right]^2 \left\{\hat{\boldsymbol{r}}\left[1+\left(\frac{j}{kr}\right)^3\right]\sin^2\theta + \hat{\boldsymbol{\theta}}\left[\left(\frac{j}{kr}\right)-\left(\frac{j}{kr}\right)^3\right]\sin 2\theta\right\} \tag{1.468}$$

from which it follows that the time-average power density of the z-directed dipole is

$$\boldsymbol{P}_{\text{ave}}^{\text{z-dipole}}(\boldsymbol{r}) = \frac{1}{2}\text{Re}[\boldsymbol{E}\times\boldsymbol{H}^*] = \frac{1}{2}\text{Re}[\boldsymbol{P}_c] = \hat{\boldsymbol{r}}\frac{\eta}{2}\left[\frac{kIl}{4\pi r}\right]^2 \sin^2\theta. \tag{1.469}$$

1.8.4 Duality and Fields for Hertzian Loop and Dipole Antennas

In the case of a Hertzian loop antenna with radius a centered at the origin (Figure 1.10), the electric and magnetic fields can be readily found from the Hertzian electric dipole antenna fields by utilizing the duality principle. For a small circular loop of radius a that has area $A = \pi a^2$, the magnetic dipole moment $m = IA = I\pi a^2$, which has units of amperes meters squared. The vector magnetic dipole moment can be expressed as $\boldsymbol{m} = m\hat{\boldsymbol{p}}$, where $\hat{\boldsymbol{p}}$ is the polarization unit vector for the magnetic dipole moment, which is perpendicular to the plane of the loop. In terms of the electric current I flowing in the small current loop, the vector magnetic dipole moment is expressed as

$$\boldsymbol{m} = IA\hat{\boldsymbol{p}}. \tag{1.470}$$

The relevant duality relationships with the following replacement of quantities have been described by Kong [3, pp. 510, 511], that is, $\boldsymbol{E} \to \boldsymbol{H}$, $\boldsymbol{H} \to -\boldsymbol{E}$, $\mu \to \epsilon$, $\epsilon \to \mu$, $k \to k$, $\eta \to 1/\eta$, $\boldsymbol{D} \to \boldsymbol{B}$, $\boldsymbol{B} \to -\boldsymbol{D}$, and $\boldsymbol{I}_e l \to j\omega\mu\boldsymbol{m}$, $j\omega\mu\boldsymbol{m} \to -\boldsymbol{I}_e l$. Summarizing the near-zone fields of the Hertzian electric dipole (referred to as dipole), we have from Equations (1.461) and (1.465)

$$\boldsymbol{E}_{\text{dipole}}(\boldsymbol{r}) = -j\omega\mu\frac{e^{-jkr}}{4\pi r}\left\{\left[1-\frac{j}{kr}-\frac{1}{k^2r^2}\right]\boldsymbol{I}_e l + \hat{\boldsymbol{r}}\,(\hat{\boldsymbol{r}}\cdot\boldsymbol{I}_e l)\left[-1+\frac{3j}{kr}+\frac{3}{k^2r^2}\right]\right\} \tag{1.471}$$

$$\boldsymbol{H}_{\text{dipole}}(\boldsymbol{r}) = -\hat{\boldsymbol{r}}\times\boldsymbol{I}_e l jk\left[1-\frac{j}{kr}\right]\frac{e^{-jkr}}{4\pi r}. \tag{1.472}$$

Using the above duality relationships, the fields for the Hertzian magnetic dipole (referred to as electric current loop) are found to be

$$\boldsymbol{H}_{\text{loop}}(\boldsymbol{r}) = k^2\frac{e^{-jkr}}{4\pi r}\left\{\left[1-\frac{j}{kr}-\frac{1}{k^2r^2}\right]\boldsymbol{m} + \hat{\boldsymbol{r}}\,(\hat{\boldsymbol{r}}\cdot\boldsymbol{m})\left[-1+\frac{3j}{kr}+\frac{3}{k^2r^2}\right]\right\} \tag{1.473}$$

$$\boldsymbol{E}_{\text{loop}}(\boldsymbol{r}) = -\hat{\boldsymbol{r}}\times\boldsymbol{m}\omega\mu k\left[1-\frac{j}{kr}\right]\frac{e^{-jkr}}{4\pi r}. \tag{1.474}$$

From Equations (1.471) and (1.472), the near-field components for a z-directed dipole are determined to be

$$H_{\phi}^{\text{NF, z-dipole}}(r,\theta) = jkI_el\sin\theta\left[1+\frac{1}{jkr}\right]\frac{e^{-jkr}}{4\pi r} \tag{1.475}$$

$$E_{r}^{\text{NF, z-dipole}}(r,\theta) = 2\eta I_el\cos\theta\left[\frac{1}{r}+\frac{1}{jkr^2}\right]\frac{e^{-jkr}}{4\pi r} \tag{1.476}$$

$$E_{\theta}^{\text{NF, z-dipole}}(r,\theta) = j\eta kI_el\sin\theta\left[1+\frac{1}{jkr}-\frac{1}{(kr)^2}\right]\frac{e^{-jkr}}{4\pi r} \tag{1.477}$$

$$E_{\phi}^{\text{NF, z-dipole}} = 0, \tag{1.478}$$

which are the same as Equations (1.430), (1.434), (1.435), and (1.436), respectively. The corresponding near-zone fields for a z-directed loop can be determined by applying the duality relationships $\boldsymbol{E}\rightarrow\boldsymbol{H}$, $\boldsymbol{H}\rightarrow-\boldsymbol{E}$, $\mu\rightarrow\epsilon$, $\epsilon\rightarrow\mu$, $k\rightarrow k$, $\eta\rightarrow 1/\eta$, and $I_el\rightarrow j\omega\mu m = j\omega\mu IA$, to the fields of the z-directed Hertzian dipole given by Equations (1.475), (1.476), (1.477), and (1.478), and noting that

$$\eta = \omega\mu/k, \tag{1.479}$$

leads to the simplified results as

$$E_{\phi}^{\text{NF, z-loop}}(r,\theta) = \eta IA\sin\theta\left[k^2-\frac{jk}{r}\right]\frac{e^{-jkr}}{4\pi r} \tag{1.480}$$

$$H_{r}^{\text{NF, z-loop}}(r,\theta) = 2IA\cos\theta\left[\frac{jk}{r}+\frac{1}{r^2}\right]\frac{e^{-jkr}}{4\pi r} \tag{1.481}$$

$$H_{\theta}^{\text{NF, z-loop}}(r,\theta) = IA\sin\theta\left[-k^2+\frac{jk}{r}+\frac{1}{r^2}\right]\frac{e^{-jkr}}{4\pi r} \tag{1.482}$$

$$H_{\phi}^{\text{NF, z-loop}} = 0. \tag{1.483}$$

1.9 Far-Zone Fields of Arbitrary Dipoles and Loops

1.9.1 Introduction

The far-zone fields can be computed by ignoring the higher-order terms $1/r^2$ and $1/r^3$ as mentioned earlier. Thus, in the far field for arbitrary Hertzian dipole current orientation, Equations (1.471) and (1.472) reduce to

$$\boldsymbol{E}_{\text{dipole}}^{FF}(\boldsymbol{r}) = -j\omega\mu\frac{e^{-jkr}}{4\pi r}\left[\boldsymbol{I}_el-\hat{\boldsymbol{r}}\left(\hat{\boldsymbol{r}}\cdot\boldsymbol{I}_el\right)\right] \tag{1.484}$$

$$\boldsymbol{H}^{FF}_{\text{dipole}}(\boldsymbol{r}) = -\hat{\boldsymbol{r}}\times\boldsymbol{I}_e l j k \frac{e^{-jkr}}{4\pi r}. \tag{1.485}$$

Similarly, using Equations (1.473), and (1.474), the far-zone fields for the arbitrary Hertzian magnetic dipole (referred to as electric current loop) are found to be

$$\boldsymbol{H}^{FF}_{\text{loop}}(\boldsymbol{r}) = k^2 \frac{e^{-jkr}}{4\pi r}\left[\boldsymbol{m} - \hat{\boldsymbol{r}}\,(\hat{\boldsymbol{r}}\cdot\boldsymbol{m})\right] \tag{1.486}$$

$$\boldsymbol{E}^{FF}_{\text{loop}}(\boldsymbol{r}) = -\hat{\boldsymbol{r}}\times\boldsymbol{m}\omega\mu k \frac{e^{-jkr}}{4\pi r}. \tag{1.487}$$

For a particular vector current polarization, Equations (1.239) to (1.241) would be used in evaluating the field components.

1.9.2 Far-Zone Fields for $\hat{z}$ Oriented Dipoles and Loops

For example, when the electric dipole moment has only a z orientation, that is, $\boldsymbol{I}_e l = \hat{\boldsymbol{z}} I_e l$, and referring to Equation (1.241) $\hat{\boldsymbol{z}} = \hat{\boldsymbol{r}}\cos\theta - \hat{\boldsymbol{\theta}}\sin\theta$, Equations (1.484) and (1.485) reduce to the far-field results

$$\boldsymbol{E}^{FF}_{\text{z-dipole}}(\boldsymbol{r}) = \hat{\boldsymbol{\theta}} j\omega\mu I_e l \frac{e^{-jkr}}{4\pi r}\sin\theta \tag{1.488}$$

$$\boldsymbol{H}^{FF}_{\text{z-dipole}}(\boldsymbol{r}) = \hat{\boldsymbol{\phi}} I_e l j k \frac{e^{-jkr}}{4\pi r}\sin\theta. \tag{1.489}$$

The far-zone fields for the Hertzian magnetic dipole (electric current loop) oriented with the axis in the z direction, that is, $\boldsymbol{m} = m\hat{\boldsymbol{z}}$, where $m = IA$, are found from Equations (1.488) and(1.489) using the duality relations given in the previous section, and noting $\hat{\boldsymbol{\phi}}\times\hat{\boldsymbol{\theta}} = -\hat{\boldsymbol{r}}$, to be

$$\boldsymbol{H}^{FF}_{\text{z-loop}}(\boldsymbol{r}) = -\hat{\boldsymbol{\theta}} k^2 I A \frac{e^{-jkr}}{4\pi r}\sin\theta \tag{1.490}$$

$$\boldsymbol{E}^{FF}_{\text{z-loop}}(\boldsymbol{r}) = \hat{\boldsymbol{\phi}} I A \omega\mu k \frac{e^{-jkr}}{4\pi r}\sin\theta. \tag{1.491}$$

As discussed earlier, by taking the ratio of the magnitudes of the electric field and magnetic fields, it is readily shown that the far-zone fields of the dipole and loop in free space satisfy $|E|/|H| = \eta_o$, where η_o is the impedance of free space. In the case of a multiturn small loop antenna with N turns, the field expressions given in this section are generalized by simply replacing the quantity IA with NIA such that the vector magnetic dipole moment is now given by

$$\boldsymbol{m} = NIA\hat{\boldsymbol{p}}. \tag{1.492}$$

Consider now an example of the near-zone electric field dependence with range distance from a z directed Hertzian dipole antenna. For an observation point in the xy-plane, using Equation (1.477) it can be shown that the magnitude of the z component of the electric field is proportional to

$$|E_z(r)| \propto \sqrt{\left[\frac{1}{r} - \frac{1}{k^2 r^3}\right]^2 + \left[\frac{1}{kr^2}\right]^2} \tag{1.493}$$

Assume that the radiating frequency is 300 MHz, so that the wavelength is $\lambda = 1$m and the corresponding wavenumber is $k = 2\pi$ radians/m. The normalized electric-field magnitude (envelope) versus near-field range distance is shown in Figure (1.26). From Equation (1.112), the time variation of the

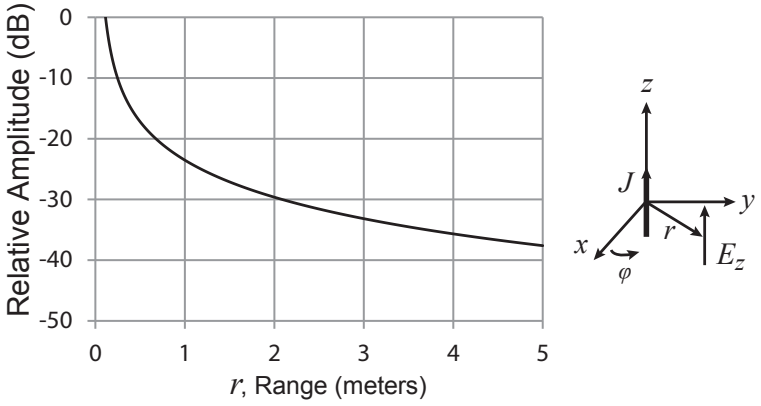

Figure 1.26 Normalized electric-field magnitude (envelope) versus near-field range distance for a z-polarized Hertzian dipole antenna radiating at 300 MHz.

electric field is given by

$$\boldsymbol{E}(\boldsymbol{r}, t) = |\boldsymbol{E}(\boldsymbol{r})| \cos(\omega t - kr) \tag{1.494}$$

and taking snapshots of just the cosine factor at fixed instants in time, say $t = 0$, $t = 1$ns with $k = 2\pi$ radians/m, Figure (1.27) shows that the wave moves to the right at the speed of light (0.3m per nanosecond). The wavelength 1m is observed between two consecutive positive (or negative) peaks. Now, taking a snapshot of the electric-field amplitude at $t = 0$, from Equation (1.494), the spatial variation of the electric field is given by

$$\boldsymbol{E}(\boldsymbol{r}, 0) = |\boldsymbol{E}(\boldsymbol{r})| \cos(kr) \tag{1.495}$$

and Figure (1.28) shows the decrease in the amplitude of the peaks and troughs as the range increases. Next, the magnitude in dB of the instantaneous E-

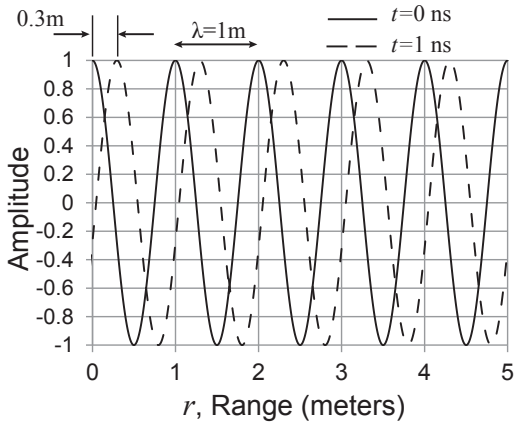

Figure 1.27 Instantaneous electric-field amplitude (ignoring the envelope factor) versus near-field range distance for a z-polarized Hertzian dipole antenna radiating at 300 MHz.

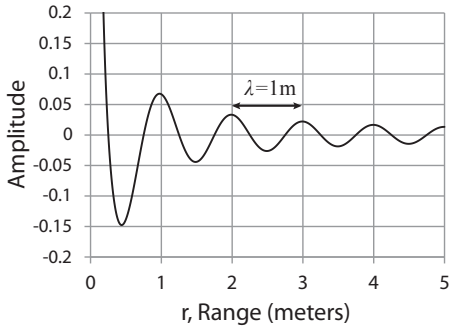

Figure 1.28 Instantaneous electric-field amplitude (including the envelope factor) $|E_z(r)|\cos(kr)$ versus near-field range distance for a z-polarized Hertzian dipole antenna radiating at 300 MHz.

field at $t = 0$ versus range distance is shown in Figure (1.29) Finally, the instantaneous phase versus range distance is shown in Figure (1.30), and the phase is observed to rotate through 360 degrees every 1m (one wavelength in this case) distance.

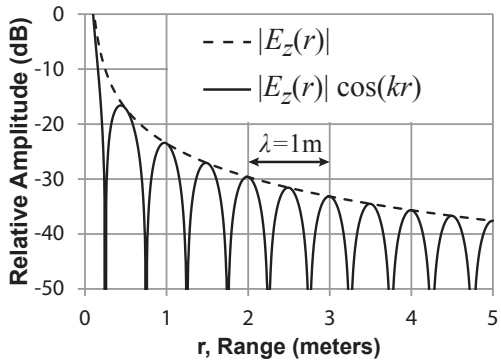

Figure 1.29 Comparison of the electric-field envelope (dashed curve) and instantaneous electric-field magnitude (solid curve) in dB (including the envelope factor) versus near-field range distance for a z-polarized Hertzian dipole antenna radiating at 300 MHz.

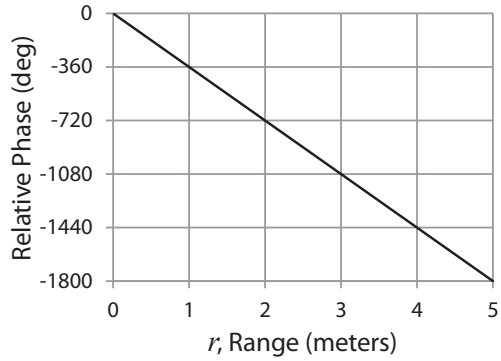

Figure 1.30 Electric-field phase versus near-field range distance for a z-polarized Hertzian dipole antenna radiating at 300 MHz.

1.9.3 Far-Zone Fields for $\hat{x}$ Oriented Dipoles and Loops

When the electric dipole moment has only an x orientation, that is, $\boldsymbol{I}_e l = \hat{\boldsymbol{x}} I_e l$, and referring to Equation (1.239) then Equation (1.485) reduces to

$$\boldsymbol{H}^{FF}_{\text{x-dipole}}(\boldsymbol{r}) = -\left[\hat{\boldsymbol{\theta}}\sin\phi + \hat{\boldsymbol{\phi}}\cos\theta\cos\phi\right] jkI_e l\frac{e^{-jkr}}{4\pi r}. \tag{1.496}$$

Then, applying Equation (1.400), $\hat{\boldsymbol{\phi}} \times \hat{\boldsymbol{r}} = \hat{\boldsymbol{\theta}}$, and $\hat{\boldsymbol{\theta}} \times \hat{\boldsymbol{r}} = -\hat{\boldsymbol{\phi}}$ yields

$$\boldsymbol{E}^{FF}_{\text{x-dipole}}(\boldsymbol{r}) = \left[-\hat{\boldsymbol{\theta}} \cos\theta \cos\phi + \hat{\boldsymbol{\phi}} \sin\phi\right] jkI_e l\eta \frac{e^{-jkr}}{4\pi r}. \tag{1.497}$$

By applying duality, the loop fields are given by

$$\boldsymbol{H}^{FF}_{\text{x-loop}}(\boldsymbol{r}) = \left[\hat{\boldsymbol{\theta}} \cos\theta \cos\phi - \hat{\boldsymbol{\phi}} \sin\phi\right] k^2 IA \frac{e^{-jkr}}{4\pi r}. \tag{1.498}$$

$$\boldsymbol{E}^{FF}_{\text{x-loop}}(\boldsymbol{r}) = -\left[\hat{\boldsymbol{\theta}} \sin\phi + \hat{\boldsymbol{\phi}} \cos\theta \cos\phi\right] \eta k^2 IA \frac{e^{-jkr}}{4\pi r}. \tag{1.499}$$

1.9.4 Far-Zone Fields for $\hat{y}$ Oriented Dipoles and Loops

When the electric dipole moment has only a y orientation, that is, $\boldsymbol{I}_e l = \hat{\boldsymbol{y}} I_e l$, and referring to Equation (1.240) then Equation (1.485) reduces to

$$\boldsymbol{H}^{FF}_{\text{y-dipole}}(\boldsymbol{r}) = \left[\hat{\boldsymbol{\theta}} \cos\phi - \hat{\boldsymbol{\phi}} \cos\theta \sin\phi\right] jkI_e l \frac{e^{-jkr}}{4\pi r}. \tag{1.500}$$

Then, applying Equation (1.400), $\hat{\boldsymbol{\phi}} \times \hat{\boldsymbol{r}} = \hat{\boldsymbol{\theta}}$, and $\hat{\boldsymbol{\theta}} \times \hat{\boldsymbol{r}} = -\hat{\boldsymbol{\phi}}$ yields

$$\boldsymbol{E}^{FF}_{\text{y-dipole}}(\boldsymbol{r}) = -\left[\hat{\boldsymbol{\theta}} \cos\theta \sin\phi + \hat{\boldsymbol{\phi}} \cos\phi\right] jk\eta I_e l\eta \frac{e^{-jkr}}{4\pi r}. \tag{1.501}$$

By applying duality, the loop fields are given by

$$\boldsymbol{H}^{FF}_{\text{y-loop}}(\boldsymbol{r}) = \left[\hat{\boldsymbol{\theta}} \cos\theta \sin\phi + \hat{\boldsymbol{\phi}} \cos\phi\right] k^2 IA \frac{e^{-jkr}}{4\pi r}. \tag{1.502}$$

$$\boldsymbol{E}^{FF}_{\text{y-loop}}(\boldsymbol{r}) = \left[\hat{\boldsymbol{\theta}} \cos\phi - \hat{\boldsymbol{\phi}} \cos\theta \sin\phi\right] \eta k^2 IA \frac{e^{-jkr}}{4\pi r}. \tag{1.503}$$

1.9.5 Image Theory for Electric and Magnetic Dipole Antennas

Image theory can be used to compute the fields caused by an electric dipole or a magnetic dipole (electric current loop) over a perfect electric conductor as depicted in Figure 1.15. The sign of the image can be determined by using the exact electric field expresssions (as given in the previous section) for the electric dipole and magnetic dipole and by enforcing boundary conditions that the total tangential electric field be zero at the surface of the perfect electric conductor. A horizontal electric dipole will have a negative image, whereas a horizontal magnetic dipole will have a positive image. Additionally, a vertical

electric dipole has a positive image, whereas a vertical magnetic dipole has a negative image. For these cases, the dipole over a perfect electric conductor is replaced by the equivalent situation of the original dipole and the dipole image with the perfect electric conductor removed. Thus, the electromagetic fields above the perfect electric conductor can be computed by analyzing a two-element array with the proper phasing, as described for general arrays in the next chapter.

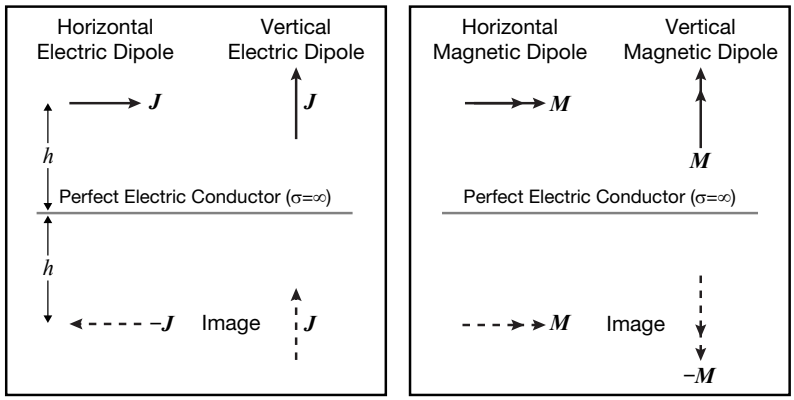

Figure 1.31 Image theory applied to electric and magnetic dipoles.

1.10 Electromagnetic Wave Polarization and Receive Antennas

1.10.1 Wave Polarization Theory

In this section, a brief discussion of electromagnetic wave polarization in the context of antennas is given based on standard IEEE definitions and electrical engineering notation [106]. The polarization of an electromagnetic wave is defined, with the antenna transmitting by the movement of the tip of the electric field vector as a function of time at a fixed position in space. When the E-field tip follows a straight line, the wave is linearly polarized. When the tip follows a circle, the wave is said to be circularly polarized. In the general case, the tip of the electric field will follow the shape of an ellipse. Two orthogonal electric field components can be superimposed to form the total electric field vector. The polarization state of the total electric field depends on the amplitude and phase relations of these orthogonal field components.

Consider Figure 1.16, which shows examples of linear, circular, and elliptical polarizations. In this figure, the wave is viewed as approaching along

the positive z axis at $z = 0$. To characterize the polarization state of a general

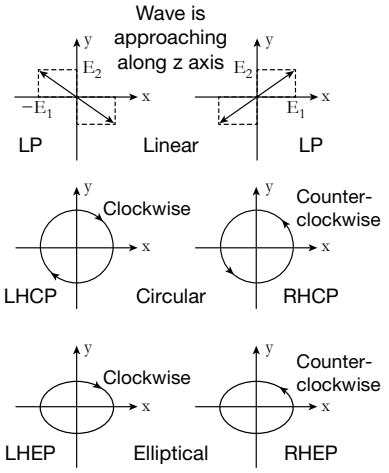

Figure 1.32 Depiction of linear, circular, and elliptical polarizations.

electromagnetic wave propagating along the positive z axis as depicted now in Figure 1.17, we can write the complex electric field in terms of the complex x component E_x, complex y component E_y, E-field amplitude E_1 in the x direction and E_2 in the y direction in phasor form as

$$\boldsymbol{E}(z) = E_x\hat{\boldsymbol{x}} + E_y\hat{\boldsymbol{y}} = E_1 e^{-jkz}\hat{\boldsymbol{x}} + E_2 e^{-jkz} e^{j\delta_p}\hat{\boldsymbol{y}}, \tag{1.504}$$

where δ_p is the relative phase shift between the two electric-field components. Equation (1.510) can now be written in instantaneous form as

$$\boldsymbol{E}(z,t) = \mathrm{Re}[E_1 e^{j(\omega t - kz)}\hat{\boldsymbol{x}}] + \mathrm{Re}[E_2 e^{j(\omega t - kz + \delta_p)}\hat{\boldsymbol{y}}]. \tag{1.505}$$

In Equation (1.505), expressing the exponentials in terms of cosines and sines and taking the real part yields

$$\boldsymbol{E}(z,t) = E_x\hat{\boldsymbol{x}} + E_y\hat{\boldsymbol{y}} = E_1\cos(\omega t - kz)\hat{\boldsymbol{x}} + E_2\cos(\omega t - kz + \delta_p)\hat{\boldsymbol{y}}. \tag{1.506}$$

Note that in Equation (1.506), the magnitudes $E_x = E_1\cos(\omega t - kz)$ and $E_y = E_2\cos(\omega t - kz + \delta_p)$ follow the tip of the electric-field vector as a function of time and spatial position. For the case when $z = 0$, Equation (1.506) reduces to

$$\boldsymbol{E}(t) = E_x\hat{\boldsymbol{x}} + E_y\hat{\boldsymbol{y}} = E_1\cos(\omega t)\hat{\boldsymbol{x}} + E_2\cos(\omega t + \delta_p)\hat{\boldsymbol{y}}. \tag{1.507}$$

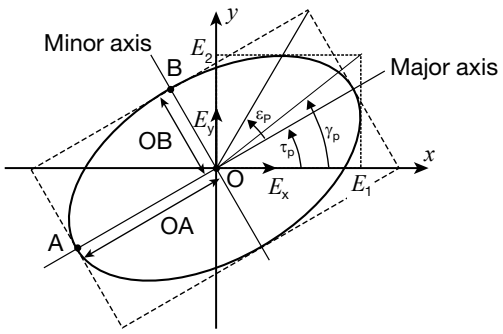

Figure 1.33 Depiction of the general tilted polarization ellipse.

Referring to Figure 1.17, the angle γ_p is expressed in terms of E_1 and E_2 as

$$\gamma_p = \tan^{-1} \frac{E_2}{E_1}. \tag{1.508}$$

In Equation (1.508) we note that E_1 and E_2 are peak values and thus $0^\circ \leq \gamma_p \leq 90^\circ$. Furthermore, note that

$$|\boldsymbol{E}| = \boldsymbol{E}\cdot\boldsymbol{E}^* = |E_x|^2 + |E_y|^2 = |E_1|^2 + |E_2|^2. \tag{1.509}$$

At $z = 0$, Equation (1.510) reduces to

$$\boldsymbol{E}(z=0) = E_x\hat{\boldsymbol{x}} + E_y\hat{\boldsymbol{y}} = E_1\hat{\boldsymbol{x}} + E_2 e^{j\delta_p}\hat{\boldsymbol{y}}, \tag{1.510}$$

Further, note that the amplitudes $E_1 = |\boldsymbol{E}|\cos\gamma_p$ and $E_2 = |\boldsymbol{E}|\sin\gamma_p$, and then the electric field unit vector can be expressed as

$$\hat{\boldsymbol{e}} = \frac{\boldsymbol{E}}{|\boldsymbol{E}|} = \frac{E_1}{|\boldsymbol{E}|}\hat{\boldsymbol{x}} + \frac{E_2}{|\boldsymbol{E}|}\hat{\boldsymbol{y}} \tag{1.511}$$

which reduces to

$$\hat{\boldsymbol{e}} = \cos\gamma_p\hat{\boldsymbol{x}} + \sin\gamma_p e^{j\delta_p}\hat{\boldsymbol{y}}. \tag{1.512}$$

For the case with $z = 0$, it is observed that Equation (1.510) can also be expressed as

$$\boldsymbol{E}(\gamma_p, \delta_p) = \sqrt{E_1^2 + E_2^2}(\cos\gamma_p\hat{\boldsymbol{x}} + \sin\gamma_p e^{j\delta_p}\hat{\boldsymbol{y}}) = |\boldsymbol{E}|\hat{\boldsymbol{e}}. \tag{1.513}$$

In Equation (1.513), $\hat{\boldsymbol{e}}$ is the complex unit vector polarization state of the electromagnetic wave.

It is worth noting that the more general case of spherical coordinates for a plane wave propagating in the radial direction r can be expressed as

$$\boldsymbol{E}(r) = E_\theta \hat{\boldsymbol{\theta}} + E_\phi \hat{\boldsymbol{\phi}} = E_1 e^{-jkr} \hat{\boldsymbol{\theta}} + E_2 e^{-jkr} e^{j\delta_p} \hat{\boldsymbol{\phi}}, \tag{1.514}$$

For the case with $r = 0$, it is observed that Equation (1.514) can be expressed as

$$\boldsymbol{E}(\gamma_p, \delta_p) = \sqrt{E_1^2 + E_2^2}(\cos\gamma_p \hat{\boldsymbol{\theta}} + \sin\gamma_p e^{j\delta_p} \hat{\boldsymbol{\phi}}) = |\boldsymbol{E}|\hat{\boldsymbol{e}}. \tag{1.515}$$

Now for an incident plane wave propagating in the negative radial direction, note that the cross product of the unit vectors for theta and phi gives

$$\hat{\boldsymbol{\theta}} \times \hat{\boldsymbol{\phi}} = -\hat{\boldsymbol{r}} \tag{1.516}$$

If we compare $\hat{\boldsymbol{\phi}}$ with $\hat{\boldsymbol{x}}$ and $\hat{\boldsymbol{\theta}}$ with $\hat{\boldsymbol{y}}$ in Figure 1.33 and with Equation (1.512) then it follows that the incident wave electric-field unit vector $\hat{\boldsymbol{e}}^{\text{inc}}$ or incident polarization unit vector $\hat{\boldsymbol{p}}^{\text{inc}}$ in spherical coordinates is given by

$$\hat{\boldsymbol{e}}^{\text{inc}} = \hat{\boldsymbol{p}}^{\text{inc}} = \frac{E_\theta}{|\boldsymbol{E}|}\hat{\boldsymbol{\theta}} + \frac{E_\phi}{|\boldsymbol{E}|}\hat{\boldsymbol{\phi}} = \sin\gamma_p e^{j\delta_p}\hat{\boldsymbol{\theta}} + \cos\gamma_p \hat{\boldsymbol{\phi}}. \tag{1.517}$$

Referring now to the upper left diagram of Figure 1.16, the wave shown is slanted to the left, and it is linearly polarized. In contrast, in the upper right diagram of Figure 1.16, the linearly polarized wave is slanted to the right. For circularly polarized (CP) waves, the amplitude of the two orthogonal electric field components will be equal, that is, $E_1 = E_2$, and the relative phase will be $\delta_p = \pm 90^\circ$. By the IEEE definition, for a left-hand CP wave approaching, the relative phase will be $\delta_p = 90^\circ$ and the tip of the electric field vector will rotate clockwise as in the middle-left diagram in Figure 1.16. For a right-hand CP wave approaching, $\delta_p = -90^\circ$, and the tip will rotate counter-clockwise as in the middle-right diagram in Figure 1.16.

For elliptically polarized (EP) waves, the amplitudes E_1 and E_2 will not be equal. If the relative phase is $\delta_p = 90^\circ$, then the wave will be left-hand elliptically polarized (LHEP) with the major axis along the x-axis (lower left diagram in Figure 1.16). If the relative phase is $\delta_p = -90^\circ$, then the wave will be right-hand elliptically polarized (RHEP) with the major axis also along the x-axis (lower right diagram in Figure 1.16). For general elliptically polarized waves, the relative phase δ_p will vary over $\pm 180^\circ$. The elliptical polarization will be right-handed for $-180^\circ < \delta_p < 0$ and will be left-handed for $0 < \delta_p < 180^\circ$.

For the general case of an elliptically polarized wave [106], the polarization ellipse major axis will tilt away at the angle τ_p from the x axis

as depicted in Figure 1.17. In Figure 1.17, the ratio of the major axis to the minor axis is defined as the axial ratio (AR), that is,

$$\text{AR} = \pm\frac{\text{OA}}{\text{OB}}. \tag{1.518}$$

The sign of the axial ratio is positive for right-hand polarization and negative for left-hand polarization [106, p. 38]. The magnitude of the axial ratio varies from 1 to infinity, that is, $1 \leq |\text{AR}| \leq \infty$. The polarization ellipticity angle, denoted ϵ_p, is expressed as

$$\epsilon_p = \cot^{-1}(-\text{AR}). \tag{1.519}$$

In decibels, the axial ratio is expressed as

$$\text{AR}_{\text{dB}} = 20\log_{10}|\text{AR}|. \tag{1.520}$$

The polarization state of a general electromagnetic wave can be completely specified by either the pair of angles (ϵ_p, τ_p) or (γ_p, δ_p). The transformation of the angles (ϵ_p, τ_p) to (γ_p, δ_p) is given by

$$\gamma_p = \frac{1}{2}\cos^{-1}(\cos 2\epsilon_p \cos 2\tau_p) \tag{1.521}$$

$$\delta_p = \tan^{-1}\frac{\tan 2\epsilon_p}{\sin 2\tau_p}. \tag{1.522}$$

In Equation (1.522), the angle $2\tau_p$ represents longitude and $2\epsilon_p$ represents latitude for a point on a sphere known as the Poincaré sphere [106].

Consider now the polarization efficiency (or antenna-wave coupling) between transmit and receive linearly polarized antennas as depicted in Figure 1.18. The transmit antenna produces the incident linear polarization denoted $\hat{\boldsymbol{p}}_{\text{inc}}$.

The polarization efficiency η_p is expressed as the magnitude squared of the dot product of the unit vectors for the incident linear polarization and complex conjugate of the receiving antenna's unit vector polarization defined under transmitting conditions (denoted $\hat{\boldsymbol{p}}_{\text{a}}$), that is,

$$\eta_p = |\hat{\boldsymbol{p}}_{\text{inc}} \cdot \hat{\boldsymbol{p}}_{\text{a}}^*|^2 = \cos^2\psi \tag{1.523}$$

where ψ is the projected angle between the associated transmit and receive linear-polarized antenna unit vectors, and the complex conjugate is required to take account of the relative coordinate systems for the incident field and the receive antenna (the propagation directions are opposite). That is, the

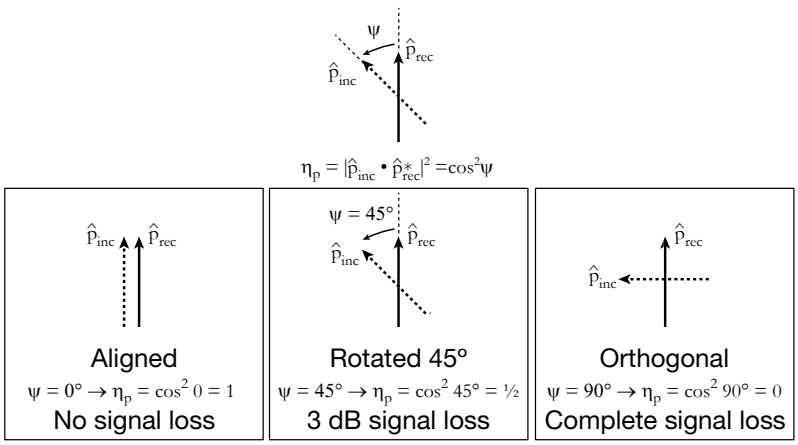

Figure 1.34 Depiction of polarization efficiency for an incident wave and a receive antenna.

polarization of the receive antenna $\hat{\boldsymbol{p}}_{\text{rec}}$ is the complex conjugate of the receive antenna's polarization when used to transmit

$$\hat{\boldsymbol{p}}_{\text{rec}} = \hat{\boldsymbol{p}}^*_{\text{a}} \tag{1.524}$$

When two linearly polarized antennas are polarization aligned (co-polarized), as in the left diagram in Figure 1.14, the angle ψ is zero, the polarization efficiency is 100% ($\eta_p = 1$), and there is no signal loss. When the antennas are rotated 45° with respect to each other (middle diagram in Figure 1.14), the polarization efficiency is 0.5, and there is a 3 dB signal loss. For the case in which the linear polarized antennas are orthogonal (right diagram in Figure 1.14), there is complete signal loss. For the case where a circularly polarized wave is incident on a linearly polarized antenna, the signal loss is 3 dB. More general cases of polarization efficiency between antennas with circular and elliptical polarizations are considered by Stutzman [106]. It should be mentioned here that, in general, electromagnetic waves can consist of completely and partially polarized waves. To quantify the general polarization case, Stokes parameters (I, Q, U, V) are used [106, p. 43].

It is useful to determine the open-circuit terminal voltage (denoted V) induced when an electric field impinges on a receiving antenna. By using a Thévinen equivalent circuit, the open-circuit induced voltage can then be used as a generator together with the antenna input impedance $Z_A = R_A + jX_A$ to determine the current I flowing through a load impedance $Z_L = R_L + jX_L$ at a receiver. That is,

$$I = \frac{V}{Z_A + Z_L}. \tag{1.525}$$

Note that the real part of the antenna input impedance is equal to the antenna radiation resistance (denoted R_r), that is, $R_A = R_r$. The time-average power P_L delivered to the receiver, in terms of the resistive component R_L of the receiver load impedance, is given by

$$P_L = \frac{1}{2}|I|^2 R_L = \frac{1}{2}|V|^2 \frac{R_L}{|Z_A + Z_L|^2} \tag{1.526}$$

and the complex voltage across the receiver load is given by

$$V_{\text{rec}} = V \frac{Z_L}{Z_A + Z_L}. \tag{1.527}$$

Utilizing the generalized antenna vector effective height ($\boldsymbol{h}$), which has units of meters, the induced open-circuit voltage across the terminals of an antenna is given by

$$V = \boldsymbol{E}_{\text{inc}} \cdot \boldsymbol{h}^* \tag{1.528}$$

where

$$\boldsymbol{h} = h\hat{\boldsymbol{p}}_{\text{a}} \tag{1.529}$$

and where h is the magnitude of the vector effective height. Now express the incident electric field $\boldsymbol{E}_{\text{inc}}$ with magnitiude E_o, phase ψ_o, with polarization $\hat{\boldsymbol{p}}_{\text{inc}}$ as

$$\boldsymbol{E}_{\text{inc}} = E_o e^{\psi_o} \hat{\boldsymbol{p}}_{\text{inc}}. \tag{1.530}$$

A few examples of the induced open-circuit voltage given by Equation (1.528) will now be considered.

Assume 45° slant-left and 45° slant-right linearly-polarized short dipoles oriented in the yz-plane such that

$$\hat{\boldsymbol{p}}_{\text{slant left}} = \frac{-\hat{\boldsymbol{y}} + \hat{\boldsymbol{z}}}{\sqrt{2}} \tag{1.531}$$

$$\hat{\boldsymbol{p}}_{\text{slant right}} = \frac{\hat{\boldsymbol{y}} + \hat{\boldsymbol{z}}}{\sqrt{2}} \tag{1.532}$$

Assume plane wave incidence with vertical polarization at the arbitrary position (x, y, z) as

$$\boldsymbol{E}^v_{\text{inc}} = \hat{\boldsymbol{\theta}} E^i_\theta(x, y, z) \tag{1.533}$$

or horizontal polarization as

$$\boldsymbol{E}^h_{\text{inc}} = \hat{\boldsymbol{\phi}} E^i_\phi(x, y, z) \tag{1.534}$$

Substituting Equations (1.531), (1.532), (1.533), and (1.534) in Equation (1.528) yields

$$V^v_{\text{slant left}} = E^i_\theta(x,y,z)\hat{\boldsymbol{\theta}} \cdot \left[\frac{-\hat{\boldsymbol{y}} + \hat{\boldsymbol{z}}}{\sqrt{2}}\right] \tag{1.535}$$

$$V^v_{\text{slant right}} = E^i_\theta(x,y,z)\hat{\boldsymbol{\theta}} \cdot \left[\frac{\hat{\boldsymbol{y}} + \hat{\boldsymbol{z}}}{\sqrt{2}}\right] \tag{1.536}$$

$$V^h_{\text{slant left}} = E^i_\phi(x,y,z)\hat{\boldsymbol{\phi}} \cdot \left[\frac{-\hat{\boldsymbol{y}} + \hat{\boldsymbol{z}}}{\sqrt{2}}\right] \tag{1.537}$$

$$V^h_{\text{slant right}} = E^i_\phi(x,y,z)\hat{\boldsymbol{\phi}} \cdot \left[\frac{\hat{\boldsymbol{y}} + \hat{\boldsymbol{z}}}{\sqrt{2}}\right] \tag{1.538}$$

From Equations (1.237) and (1.238) and referring to Figure 2.4 it follows for source incidence angles $\theta = \theta^i$ and $\phi = \phi^i$ that

$$\hat{\boldsymbol{\theta}}\cdot\hat{\boldsymbol{y}} = \cos\theta^i \sin\phi^i \tag{1.539}$$

$$\hat{\boldsymbol{\theta}}\cdot\hat{\boldsymbol{z}} = -\sin\theta^i \tag{1.540}$$

$$\hat{\boldsymbol{\phi}}\cdot\hat{\boldsymbol{y}} = \cos\phi^i \tag{1.541}$$

$$\hat{\boldsymbol{\phi}}\cdot\hat{\boldsymbol{z}} = 0 \tag{1.542}$$

It follows then that

$$V^v_{\text{slant left}} = -E^i_\theta(x,y,z)\left[\frac{\cos\theta^i \sin\phi^i + \sin\theta^i}{\sqrt{2}}\right] \tag{1.543}$$

$$V^v_{\text{slant right}} = -E^i_\theta(x,y,z)\left[\frac{\cos\theta^i \sin\phi^i - \sin\theta^i}{\sqrt{2}}\right] \tag{1.544}$$

$$V^h_{\text{slant left}} = -E^i_\phi(x,y,z)\frac{\cos\phi^i}{\sqrt{2}} \tag{1.545}$$

$$V^h_{\text{slant right}} = E^i_\phi(x,y,z)\frac{\cos\phi^i}{\sqrt{2}} \tag{1.546}$$

For plane-wave incidence with wavenumber $k = 2\pi/\lambda$ at an arbitrary nth position (x_n, y_n, z_n), the electric field has a constant amplitude and a phase that varies as

$$\Psi^i = k\sin\theta^i(x_n\cos\phi^i + y_n\sin\phi^i) + kz_n\cos\theta^i \tag{1.547}$$

and the complex electric field is then

$$E^i(k, x_n, y_n, z_n, \theta^i, \phi^i) = e^{jk[\sin\theta^i(x_n\cos\phi^i + y_n\sin\phi^i) + z_n\cos\theta^i]} \tag{1.548}$$

It follows from Equations (1.523) and (1.528) that

$$|V| = E_o h |\hat{\boldsymbol{p}}_{\text{inc}} \cdot \hat{\boldsymbol{p}}_{\text{a}}^*| = E_o h \sqrt{\eta_p}. \tag{1.549}$$

Substituting Equation (1.549) in Equation (1.526) yields

$$P_L = \frac{1}{2}|V|^2 \frac{R_L}{|Z_A + Z_L|^2} = \frac{1}{2} E_o^2 h^2 \eta_p \frac{R_L}{|Z_A + Z_L|^2}. \tag{1.550}$$

In the case where the receive antenna is connected to a conjugate-matched load impedance ($Z_L = R_A - jX_A$), it follows from Equation (1.550) that the time-average power transferred to the resistive part (R_A) of the receiver load is given by

$$P_{\text{L}} = \frac{1}{2}\frac{|V|^2}{4R_A} = \frac{1}{8R_A} E_o^2 h^2 \eta_p. \tag{1.551}$$

Now the magnitude of the time-average power density (denoted S) incident on an antenna in free space is given by

$$S = \frac{1}{2}\frac{E_o^2}{\eta_o} \tag{1.552}$$

where η_o is the impedance of free space. Next, in terms of effective receive aperture (denoted A_{eff}), the time-average received power at the conjugate-matched load can be expressed as

$$P_{\text{L}} = \eta_p S A_{\text{eff}} = \eta_p \frac{1}{2}\frac{E_o^2}{\eta_o} A_{\text{eff}}. \tag{1.553}$$

Now, setting Equation (1.551) equal to Equation (1.553) yields

$$h = 2\sqrt{\frac{R_A}{\eta_o} A_{\text{eff}}} \tag{1.554}$$

which is a general expression for the effective height of an antenna assuming a conjugate matched load. Solving Equation (1.554) for the effective aperture gives

$$A_{\text{eff}} = \frac{h^2 \eta_o}{4R_A}. \tag{1.555}$$

Note, in the literature, the electric antenna factor (denoted AF_e) with units of 1/m is often used to convert the incident electric field magnitude (E_o) to received voltage magnitude, that is,

$$|V| = \frac{E_o}{\text{AF}_e}, \tag{1.556}$$

and it follows that the electric antenna factor and effective antenna height are related as

$$\text{AF}_e = \frac{1}{h}. \tag{1.557}$$

Additionally, in the literature, the magnetic antenna factor (denoted AF_m) with units of 1/m is often used to convert the incident magnetic field magnitude (H_o) to received voltage magnitude, that is,

$$|V| = \frac{H_o}{\text{AF}_m}, \tag{1.558}$$

and it follows that the magnetic antenna factor and magnetic effective antenna height are related as

$$\text{AF}_m = \frac{1}{h_m}. \tag{1.559}$$

To quantify the maximum effective area given by Equation (1.555), it is necessary to determine the radiation resistance R_r, or equivalently the input resistance R_A, for the antenna of interest, as discussed below for the short dipole and small loop antenna. Since an antenna can be treated as a load, the radiation resistance can be determined by quantifying the time-average radiated power (denoted P_{ave}) or equivalently the time-average power delivered to the antenna, and using the relation

$$P_{\text{rad}} = \frac{1}{2} I_o^2 R_r \tag{1.560}$$

and solving for R_r as

$$R_r = \frac{2P_{\text{rad}}}{I_o^2}. \tag{1.561}$$

Now the time-average radiated power can be found by integrating the time-average power density over the volume surrounding the antenna as the range distance tends to infinity, that is,

$$P_{\text{rad}} = \int_0^{2\pi} \int_0^{\pi} \hat{\boldsymbol{r}} \cdot \frac{1}{2} \text{Re}[\boldsymbol{E} \times \boldsymbol{H}^*] r^2 \sin\theta d\theta d\phi. \tag{1.562}$$

Repeating the general far-field Equations (1.279) and (1.282), we have

$$\boldsymbol{E}_{\text{FF}} = -j\omega\mu\frac{e^{-jkr}}{4\pi r}(\hat{\boldsymbol{\theta}} f_\theta + \hat{\boldsymbol{\phi}} f_\phi) \tag{1.563}$$

$$\boldsymbol{H}_{\text{FF}} = -jk\frac{e^{-jkr}}{4\pi r}(\hat{\boldsymbol{\phi}} f_\theta - \hat{\boldsymbol{\theta}} f_\phi). \tag{1.564}$$

To compute the far-zone electric ($\boldsymbol{E}_{\text{FF}}$) and magnetic ($\boldsymbol{H}_{\text{FF}}$) fields, it is necessary to determine the vector current moment $\boldsymbol{f}(\theta, \phi)$ for the antenna of interest.

1.10.2 Short Dipole Receive Characteristics

For an electrically short dipole with total length l in free space, the current distribution has a triangular shape [121]. The maximum effective height is determined by integrating the current over the dipole physical length divided by the terminal current I_o [1, p. 31], and for symmetrical currents,

$$h = \frac{1}{I_o}\int_{-\frac{l}{2}}^{\frac{l}{2}} I(z')dz' = \frac{2}{I_o}\int_0^{\frac{l}{2}} I(z')dz'. \tag{1.565}$$

A triangular current distribution is a good approximation for short dipoles of total length l, that is,

$$I(z') = \frac{2I_o}{l}\left[\frac{l}{2} - |z'|\right]. \tag{1.566}$$

Substituting Equation (1.566) in Equation (1.565) and integrating, the effective height is found to be equal to one-half the physical length of the short dipole with triangular current, that is,

$$h_{\text{dipole}} = \frac{1}{2}l. \tag{1.567}$$

Thus, the open-circuit voltage induced in a short dipole is determined by substituting Equation (1.567) into Equation (1.549) with the result (ignoring the radiation pattern)

$$|V_{\text{dipole}}| = \frac{1}{2}E_o l\sqrt{\eta_p}. \tag{1.568}$$

For the short dipole, the far-zone electric and magnetic fields can be determined from the vector current moment given by Equation (1.269), and using Equation (1.566) for the triangular current distribution, it follows that

$$\boldsymbol{J}(\boldsymbol{r}') = \hat{\boldsymbol{z}} I(z')\delta(x')\delta(y') = \hat{\boldsymbol{z}}\frac{2I_o}{l}\left[\frac{l}{2} - |z'|\right]\delta(x')\delta(y'). \tag{1.569}$$

Now, using Equations (1.236) and (1.241), it follows from Equation (1.269) that for the triangular current distribution that the vector current moment is

$$\boldsymbol{f}(\theta,\phi) = \int_V \boldsymbol{J}(\boldsymbol{r}')e^{jk\hat{\boldsymbol{r}}\cdot\boldsymbol{r}'}\,dv' = -\hat{\boldsymbol{\theta}}\frac{2I_o}{l}\sin\theta\int_{-\frac{l}{2}}^{\frac{l}{2}}\left[\frac{l}{2}-|z'|\right]e^{jkz'\cos\theta}dz' \tag{1.570}$$

where the only nonradial component in this case is the $\hat{\boldsymbol{\theta}}$ component. For an electrically short dipole, the phase term in Equation (1.570) can be ignored, and thus the vector current moment for the triangular current distribution is determined to be

$$f_\theta(\theta) = -\frac{l}{2}I_o\sin\theta. \tag{1.571}$$

Using the above expressions given by Equations (1.562), (2.33), (1.564), and (1.571) the radiated power is now determined as

$$P_{\text{rad}} = 2\pi\left[\frac{\eta k^2}{(4\pi)^2}\right]\frac{1}{2}\int_0^\pi |f_\theta|^2\sin\theta d\theta = \pi\left[\frac{120\pi k^2}{(4\pi)^2}\right]\frac{l^2I_o^2}{4}\int_0^\pi \sin^3\theta d\theta \tag{1.572}$$

and noting that

$$\int_0^\pi \sin^3\theta d\theta = \frac{4}{3}, \tag{1.573}$$

it follows that the power radiated in watts is

$$P_{\text{rad}}^{\text{dipole, triangular current}} = \frac{5}{2}(kl)^2I_o^2. \tag{1.574}$$

Thus, the radiation resistance of a short dipole with triangular current distribution is

$$R_r^{\text{dipole, triangular current}} = \frac{2P_{\text{rad}}}{I_o^2} = 5(kl)^2. \tag{1.575}$$

Substituting Equations (1.567) and (1.575) in Equation (1.555) yields the effective area of a short dipole with triangular current as

$$A_{\text{eff}}^{\text{dipole, triangular current}} = \frac{h^2\eta_o}{4R_A} = \frac{\frac{l^2}{4}120\pi}{4\cdot 5(kl)^2} = \frac{3\lambda^2}{8\pi} \approx \frac{\lambda^2}{8}. \tag{1.576}$$

1.10.3 Small Current Loop Receive Characteristics

Consider now an N-turn loop antenna of arbitrary shape with physical area A illuminated by a uniform magnetic flux density with magnitude $B_o = \mu_o H_o$, where μ_o is the permeability of free space and H_o is the magnitude

of the magnetic field. The magnitude of the open-circuit voltage is readily determined, according to the time rate of change of magnetic flux density through the loop, using Faraday's law in time-harmonic form as

$$|V_{\text{loop}}| = |-j\omega ANB_o\sqrt{\eta_p}| = \omega AN\mu_o H_o\sqrt{\eta_p}. \tag{1.577}$$

For a plane wave, $H_o = E_o/\eta_o$, where η_o is the impedance of free space, and noting $\omega\mu_o/\eta_o = k = 2\pi/\lambda$, it follows that the open-circuit voltage of the loop is

$$|V_{\text{loop}}| = AN\frac{\omega\mu_o}{\eta_o}E_o\sqrt{\eta_p} = ANkE_o\sqrt{\eta_p} \tag{1.578}$$

and so setting Equation (1.578) equal to Equation (1.549), the maximum effective height of an N-turn loop antenna with physical area A is

$$h_{\text{loop}} = ANk. \tag{1.579}$$

In the case of an N-turn small loop antenna with uniform current, from Equations (1.490) and (1.491), the far-zone fields are

$$\boldsymbol{H}^{FF}_{\text{z-loop, N turns}}(\boldsymbol{r}) = -\hat{\boldsymbol{\theta}}k^2NIA\frac{e^{-jkr}}{4\pi r}\sin\theta \tag{1.580}$$

$$\boldsymbol{E}^{FF}_{\text{z-loop, N turns}}(\boldsymbol{r}) = \hat{\boldsymbol{\phi}}NIA\omega\mu k\frac{e^{-jkr}}{4\pi r}\sin\theta. \tag{1.581}$$

Substituting Equations (6.11) and (6.12) in Equation (1.562) and evaluating the integral yields the radiated power

$$P_{\text{rad}}^{\text{loop, uniform current}} = 10(k^2NA)^2I_o^2. \tag{1.582}$$

Thus, the radiation resistance of an N-turn loop antenna with uniform current distribution and physical area A is

$$R_r^{\text{loop, uniform current}} = \frac{2P_{\text{rad}}}{I_o^2} = 20(k^2NA)^2. \tag{1.583}$$

Substituting Equations (1.589) and (1.583) in Equation (1.555) yields the effective area of an N-turn small loop antenna with uniform current as

$$A_{\text{eff}}^{\text{loop, uniform current}} = \frac{h^2\eta_o}{4R_A} = \frac{(ANk)^2120\pi}{4\cdot 20(k^2NA)^2} = \frac{3\lambda^2}{8\pi} \approx \frac{\lambda^2}{8}, \tag{1.584}$$

and this result is identical to the result obtained for the short dipole (see Equation (1.576).

1.10.4 Ferrite-Loaded Small Current Loop Receive Characteristics

Consider now a ferrite-loaded N-turn loop antenna [20]with physical area A illuminated by a uniform magnetic flux density with magnitude $B_o = \mu_o H_o$, where μ_o is the permeability of free space and H_o is the magnitude of the magnetic field in free space. The N-turn loop is assumed to be wound around a uniform ferrite core with relative intrinsic permeability of the unbounded ferrite material denoted as $\mu_{ri\text{ ferrite core}}$. The relative effective permeability of the ferrite core is denoted as $\mu_{re\text{ ferrite core}}$, which is related to $\mu_{ri\text{ ferrite core}}$ as

$$\mu_{re\text{ ferrite core}} = \frac{\mu_{ri\text{ ferrite core}}}{1 + D(\mu_{ri\text{ ferrite core}} - 1)} \tag{1.585}$$

where D is the static demagnetization factor. The static demagnetization factor is geometry dependent, and for an ellipsoidal core with length L and radius a (where $L >> a$), D is given by

$$D = \left(\frac{2a}{L}\right)^2 \left[\ln\left(\frac{L}{a}\right) - 1\right] \tag{1.586}$$

The presence of the ferrite material increases the amplitude of the incident magnetic field and open-circuit voltage linearly by the relative effective permeability of the ferrite core as [20]

$$H_{o\text{ ferrite core}} = \mu_{re\text{ ferrite core}} H_o \tag{1.587}$$

and from Equation (1.578)

$$\left|V_{\text{loop}}\right| = ANk\mu_{re\text{ ferrite core}} E_o \sqrt{\eta_p} \tag{1.588}$$

and so setting Equation (1.588) equal to Equation (1.549), the maximum effective height of an N-turn ferrite loop antenna with physical area A is

$$h_{\text{loop}} = ANk\mu_{re\text{ ferrite core}}. \tag{1.589}$$

The radiation resistance of an N-turn ferrite-loaded loop antenna, with uniform current distribution and physical area A, increases by the square of the relative effective permeability of the ferrite and is given by

$$R_r^{\text{ferrite loop, uniform current}} = \frac{2P_{\text{rad}}}{I_o^2} = 20(k^2 NA)^2 \mu_{re\text{ ferrite core}}^2 \tag{1.590}$$

or in terms of loop circumference C using $A = C^2/(4\pi)$ as

$$R_r^{\text{ferrite loop, uniform current}} = 20\pi^2 \left(\frac{C}{\lambda}\right)^4 N^2 \mu_{re\text{ ferrite core}}^2. \tag{1.591}$$

1.11 Bandwidth and Quality Factor

1.11.1 Introduction

Bandwidth (B) is defined as the difference between the highest f_2 and lowest f_1 operating frequencies, that is,

$$B = f_2 - f_1 = \Delta f. \tag{1.592}$$

The terms highest and lowest operating frequencies usually refer to the radar or communications system meeting some desired performance metric, such as radiation pattern, gain, beamwidth, sidelobe level, reflection coefficient or VSWR, transmit power level, sensitivity, and so on. In specifying a bandwidth value, sometimes the -3 dB point is used, and sometimes a different level, say the -10 dB point, is used; hence, it is important to define what is meant by bandwidth. Fractional bandwidth (FBW) is defined as the ratio of the bandwidth to the arithmetic mean center frequency f_c, that is,

$$\text{FBW} = \frac{f_2 - f_1}{f_c} = \frac{\Delta f}{f_c}. \tag{1.593}$$

The percent bandwidth (PBW) is computed as

$$\text{PBW} = \text{FBW} \times 100\% = \frac{\Delta f}{f_c} \times 100\%. \tag{1.594}$$

The ratio bandwidth (RBW) is defined as the ratio of the highest operating frequency to the lowest operating frequency, or

$$\text{RBW} = \frac{f_2}{f_1}. \tag{1.595}$$

Antennas that have ultrawideband (or wideband) characteristics have numerous applications [80–93]. To quantify the bandwidth, consider an ultrawideband system that requires an antenna to operate from 30 to 3000 MHz. It follows that the bandwidth $B = 2700$ MHz, the FBW = $(3000 - 30)/1515 = 1.96$, the PBW = 196%, and the RBW = 3000 / 30 = 100. In the limit as the bandwidth grows linearly, the FBW approaches 2, the PBW approaches 200%, and the RBW grows linearly. Each of the bandwidth definitions are useful and are applied as appropriate to the desired application.

Bandwidth is important in radar systems requiring fine range resolution. The time t it takes for an electromagnetic wave to travel a range distance r between two points in free space is fundamentally related to the speed of light c (measured value $c = 2.99792458 \times 10^8$ m/s $\approx 3.0 \times 10^8$ m/s) as

$$t = \frac{r}{c}. \tag{1.596}$$

The wavelength of an electromagnetic wave in free space is expressed as

$$\lambda = \frac{c}{f} \tag{1.597}$$

where f is the frequency of the wave. In a radar system application, the range resolution Δr in free space is given in terms of the radar pulse width τ as [47]

$$\Delta r = \frac{c\tau}{2}. \tag{1.598}$$

Since the bandwidth of the radar pulse is inversely proportional to the pulse width, that is,

$$B = \frac{1}{\tau} \tag{1.599}$$

it follows that the range resolution can also be expressed as

$$\Delta r = \frac{c}{2B}. \tag{1.600}$$

For example, a 1 μs pulse width has a bandwidth of 1 MHz; thus, the range resolution is computed from Equation (1.600) to be 150 m. Similarly, a 10 ns pulse width has a bandwidth of 100 MHz, which corresponds to a range resolution of 1.5 m. In the case of an ultrawideband pulse with a bandwidth on the order of gigahertz, the range resolution is on the order of centimeters and Equation (1.600) can be written conveniently as

$$\Delta r_{\text{cm}} = \frac{30}{2B_{\text{GHz}}}. \tag{1.601}$$

Thus, a radar with a pulse width of 1 ns, which has a bandwidth of 1 GHz, will have a range resolution of

$$\Delta r = \frac{30 \text{ cm}}{2} = 15 \text{ cm} \approx 6 \text{ inches}. \tag{1.602}$$

The terms ultrawideband[80-93] or wideband are used to refer to an antenna that covers a large frequency range. As there is no standard definition for ultrawideband antennas, we simply define that an ultrawideband antenna will have a PBW typically 25% or more or a RBW of 1.25 or more as described in the 2007 IEEE Standard for Ultrawideband Radar Definitions [80]. Over this bandwidth, the antenna will have desired radiation characteristics and will not have any significant amplitude degradation for the application of interest.

Ultrawideband array performance requirements are highly dependent on the application [81]. For example, in a receive-only application with a strong

signal, it might only be necessary to provide an antenna with a reflection coefficient on the order of -6 dB or better with sufficient pattern gain to close the link, but for a transmit application, the reflection coefficient requirement might be on the order of -10 dB or better to avoid significant reflected signal toward the transmitter and significant loss in effective isotropic radiated power. For ground-penetrating radar or impulse radar applications [81, 82], since targets are at very close range (1 to 2 m), it is important to design the ultrawideband antenna with sufficient resistive attenuation to avoid signal ringing effects [83–85].

The above definitions of bandwidth do not take into account the size of the antenna aperture, which affects the time delay for transmitted and received signals. For a transmitted or incident wavefront with either a pulsed, noise, or other wideband spectrum, the phased array design and analysis must take into account the time delay as will be described in the next chapter. The next section quantifies bandwidth in terms of the antenna input impedance and quality factor Q.

1.11.2 Derivation of Q Factor from Input Impedance

The impedance bandwidth for an allowed value of VSWR of an antenna can be computed from a quantity known as the quality factor that depends on the reactance and radian frequency derivatives of the resistance and reactance. The so-called quality factor (denoted $Q(\omega)$ for an antenna tuned to have zero reactance at the radian frequency ω is defined for example by Yaghjian and Best [99] as

$$Q(\omega) = \frac{\omega |W(\omega)|}{P_A(\omega)} \tag{1.603}$$

where $W(\omega)$ is the internal energy and P_A is the total power accepted by the antenna. Assume that the antenna has an input impedance expressed as

$$Z_A(\omega) = R_A(\omega) + jX_A(\omega) \tag{1.604}$$

where $R_A(\omega)$ and $X_A(\omega)$ are the antenna input resistance and input reactance, respectively. Tuning can be achieved at radian frequency ω_o with a series reactance, denoted X_s, for either a series inductor L_s or series capacitor C_s to make the total reactance of an antenna equal to zero at a radian frequency ω_o. That is, the total reactance of the antenna plus series reactance is expressed as,

$$X_T(\omega) = X_A(\omega) + X_s(\omega) \tag{1.605}$$

where

$$X_s(\omega) = \begin{cases} \omega L_s & \text{if } X(\omega_o) < 0 \\ -\frac{1}{\omega C_s} & \text{if } X(\omega_o) > 0 \end{cases} \tag{1.606}$$

Yaghjian and Best assume that after the antenna has been tuned at frequency ω_o, then the antenna is connected to a transmission line with characteristic impedance equal to the antenna's tuned input resistance (denoted R_o). Taking the derivative of $X_T(\omega)$ with respect to radian frequency yields

$$\frac{dX_T(\omega)}{d\omega} = \begin{cases} \frac{dX_A(\omega)}{d\omega} + L_s & \text{if } X(\omega_o) < 0 \\ \frac{dX_A(\omega)}{d\omega} + \frac{1}{\omega^2 C_s} & \text{if } X(\omega_o) > 0 \end{cases} \tag{1.607}$$

which can be written in simplifed form as

$$\frac{dX_T(\omega)}{d\omega} = \frac{dX_A(\omega)}{d\omega} + \frac{|X(\omega)|}{\omega} \tag{1.608}$$

Now, the power accepted by the antenna is given by

$$P_A(\omega) = \frac{1}{2}\text{Re}[V_o(\omega) I_o^*(\omega)] \tag{1.609}$$

where * means complex conjugate. The power accepted by the antenna is also expressed as the sum of the radiated power and any power lost due to the material of the antenna as

$$P_A(\omega) = P_{\text{radiated}}(\omega) + P_{\text{loss}}(\omega) \tag{1.610}$$

The radiated power is quantified by

$$P_{\text{radiated}}(\omega) = \frac{1}{2}|I_o(\omega)|^2 R_r(\omega) \tag{1.611}$$

where $R_r(\omega)$ is defined as the radiation resistance. The power loss due to any lossy material of the antenna is determined as

$$P_{\text{loss}}(\omega) = \frac{1}{2}|I_o(\omega)|^2 R_{\text{loss}}(\omega) \tag{1.612}$$

where R_{loss} is defined as the loss resistance. Then, applying Maxwell's equations in a lengthy derivation by Yaghjian and Best [99, Equation 96], an accurate approximate expression for the antenna quality factor (denoted by the authors as Q_z) is given by

$$Q_Z = \frac{\omega}{2R(\omega)}\sqrt{\left[\frac{dR(\omega)}{d\omega}\right]^2 + \left[\frac{dX(\omega)}{d\omega} + \left|\frac{X(\omega)}{\omega}\right|\right]^2} \tag{1.613}$$

Furthermore, Yaghjian and Best have shown that another accurate approximate quality factor Q_B is expressed in terms of allowed VSWR and fractional bandwidth (FBW) as

$$Q_B = \frac{\text{VSWR-1}}{\text{FBW}\sqrt{\text{VSWR}}} \tag{1.614}$$

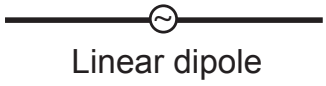

Figure 1.35 Center-fed linear dipole antenna.

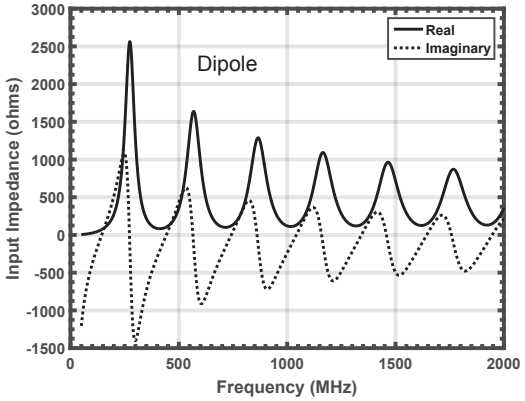

Figure 1.36 Moment method simulated input impedance versus frequency (50 MHz to 2000 MHz) for a linear dipole with overall length 1 meter and wire diameter 1 mm.

Yaghjian and Best have shown that the approximate relations given by Q_z and Q_B are in very good agreement with the exact calculation of Q, that is $Q_z = Q_B = Q$ for engineering purposes, thus, solving for the fractional bandwidth in terms of Q and allowed VSWR yields

$$\text{FBW} = \frac{f_2 - f_1}{f_c} = \frac{\text{VSWR-1}}{Q\sqrt{\text{VSWR}}} \tag{1.615}$$

1.11.3 Example: Q Factor for a Dipole Antenna

As in the paper by Yaghjian and Best [99], consider now an electromagnetic simulation of a center-fed linear dipole antenna (Figure 1.35) having total wire length 1m with a 1 mm wire diameter. This simulation is performed here using the commercial FEKO software [117] with a method of moments solver – the moment method technique is described in the next chapter. Figure 1.36 shows the simulated complex input impedance (real and imaginary components) over the frequency band 50 MHz to 2000 MHz. This antenna is one wavelength long at 300 MHz and is thus one-half wavelength long at 150 MHz. Resonance

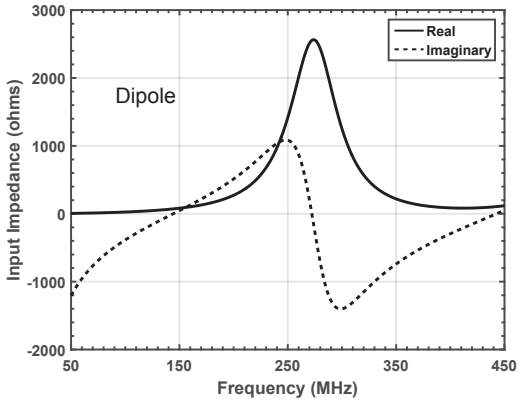

Figure 1.37 Moment method simulated input impedance versus frequency (50 MHz to 450 MHz) for a linear dipole with overall length 1 meter and wire diameter 1 mm.

occurs at 13 frequencies where the imaginary component is zero. The first resonance occurs at 144 MHz, which can be seen more clearly in Figure 1.37, and this resonance is referred to as a natural resonance where the slope of the imaginary component is positive. The second resonance occurs at 272 MHz where the slope of the imaginary component is negative and this type of resonance is referred to as antiresonant. At each frequency where the natural resonance with positive slope in the imaginary component occurs, the corresponding real (resistive) component is low (starting at 72 ohms at the first natural resonance and increasing gradually to about 200 ohms at high frequencies). At each frequency where the antiresonance with negative slope in the imaginary component occurs, the corresponding real (resistive) component is very high (starting at about 2500 ohms at the first anti-resonance and reducing gradually to about 1000 ohms for the antiresonance just below 1500 MHz . Taking 72 ohms as the reference impedance, the magnitude of the reflection coefficient in dB is plotted versus frequency in Figure 1.38. The reflection coefficient has a minimum at approximately 144 MHz. Since the reflection coefficient magnitude is very low, the corresponding VSWR at 144 MHz is approximately equal to 1 (Figure 1.39). Figure 1.40 shows the quality factor Q_Z computed using Equation (1.613) over the band 50 MHz to 450 MHz. The derivatives for the column vectors of real and imaginary impedances in Equation (1.613) were computed by utilizing the MATLAB™ difference function [diff()]. Using percent bandwidth PBW equal to $100 \times$ FBW, Figure 1.41 shows the percent bandwidth achieved by Equation (1.615) assuming allowed VSWR values equal to 1.5, 2, and 3. The peak value of

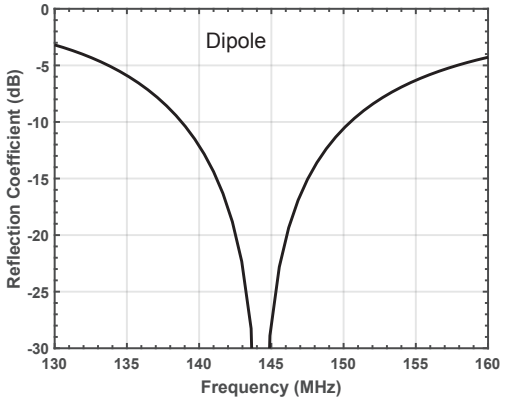

Figure 1.38 Moment method simulated reflection coefficient versus frequency (130 MHz to 160 MHz) for a linear dipole with overall length 1 meter and wire diameter 1 mm. The reference impedance is 72 ohms

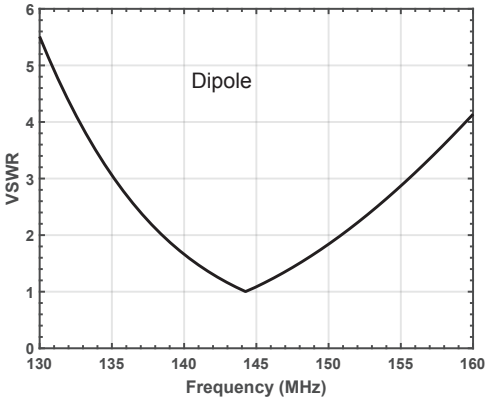

Figure 1.39 Moment method simulated VSWR versus frequency (130 MHz to 160 MHz) for a linear dipole with overall length 1 meter and wire diameter 1 mm. The reference impedance is 72 ohms.

PBW occurs near the first antiresonance, where the corresponding resistive component of input impedance is very high. If we assume that the antenna would be driven with a transmission line with a low characteristic impedance, say 72 ohms, then the frequency at the first natural resonance would be used as the center frequency. We can now compare the percent bandwidth observed in the method of moments simulated VSWR versus frequency plot in Figure 1.39 with the percent bandwidth computed using Equation (1.615). The results are

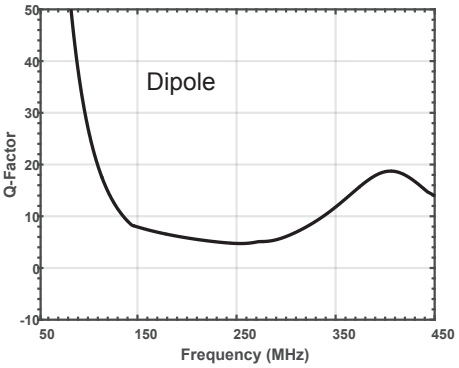

Figure 1.40 Quality factor Q_Z calculated from moment method simulated input impedance versus frequency (50 MHz to 450 MHz) for a linear dipole with overall length 1 meter and wire diameter 1 mm.

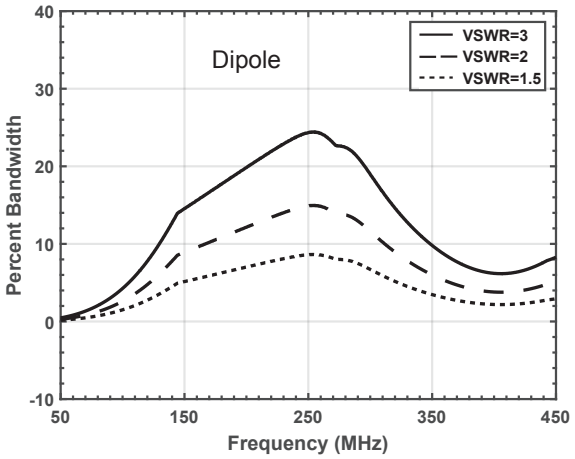

Figure 1.41 Calculated percent bandwidth based on quality factor Q_Z and assumed values of VSWR (1.5, 2, and 3) versus operating frequency (50 MHz to 450 MHz) for a linear dipole with overall length 1 meter and wire diameter 1 mm. The quality factor was calculated from the moment method simulated input impedance.

tabulated in Table 1.2 and good agreement between the bandwidth calculated from the simulated input impedance data using Equation (1.613) and directly from the reflection coefficient.

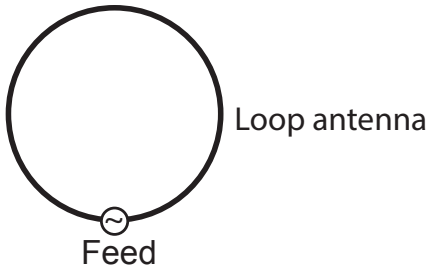

Figure 1.42 Circular loop antenna with single feed point.

1.11.4 Example: Q Factor for a Circular Loop Antenna

Consider now an electromagnetic simulation of a circular loop antenna with a single feed point as shown in Figure 1.42. The loop antenna is assumed to have a circumference equal to 1m and has a 1 mm wire diameter as in the article by Yaghjian and Best [99]. Again, the simulation is performed here using the commercial FEKO software with a method of moments solver. Figure 1.43 shows the simulated complex input impedance up to 2 GHz. Similar to the dipole, resonance occurs at 13 frequencies where the imaginary component is zero. The first resonance occurs at 144 MHz, which can be seen more clearly in the expanded scale plot in Figure 1.44, but unlike the dipole this first resonance is an antiresonance where the slope of the imaginary component is negative. The second resonance occurs at 317 MHz and it is a natural resonance where the slope of the imaginary component is positive. At each frequency where the natural resonance occurs, the corresponding real (resistive) component is low (starting at 140 ohms at the first natural resonance and increasing gradually to about 266 ohms at the high frequencies

Table 1.3
Comparison of quality factor computed from Equation (1.613) and from the method of moments simulation for a 1m linear wire dipole with 1 mm wire diameter operating at a 144 MHz center frequency.

	Percent Bandwidth for Wire Dipole	
Allowed VSWR	Q_Z, Eq. (1.613)	FEKO (Method of Moments)
1.5	4.9%	4.9%
2.0	8.5%	9.0%
3.0	14.0%	14.6%

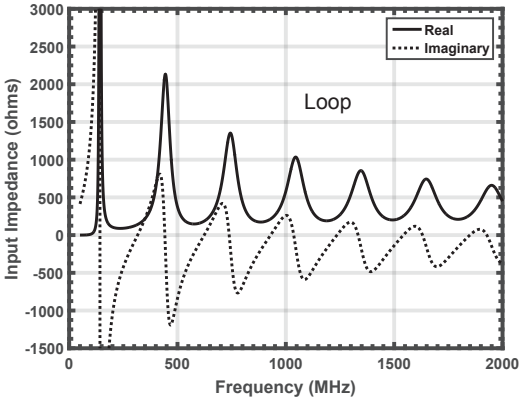

Figure 1.43 Moment method simulated input impedance versus frequency (50 MHz to 2000 MHz) for a circular wire loop antenna with circumference 1 meter and wire diameter 1 mm.

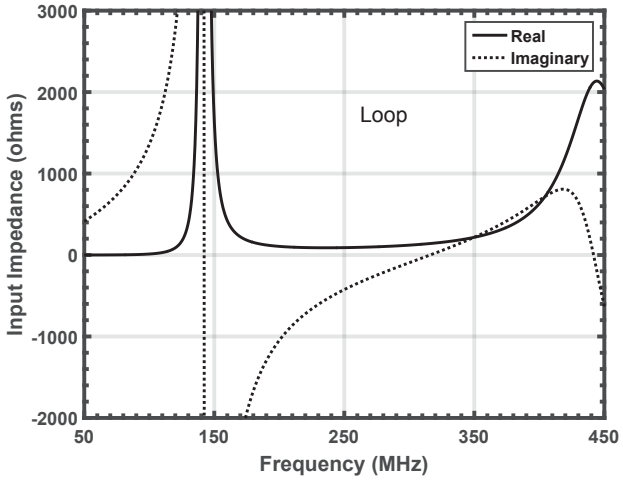

Figure 1.44 Moment method simulated input impedance versus frequency (50 MHz to 450 MHz) for a circular wire loop antenna with circumference 1 meter and wire diameter 1 mm.

shown). At each frequency where the antiresonance occurs, the corresponding real (resistive) component is very high (starting on the order of 40,000 ohms at the first anti-resonance and reducing quickly down to the range of about 500 to 1000 ohms for the antiresonances below 2000 MHz. Assume now that the loop antenna is driven with a transmission line with a characteristic

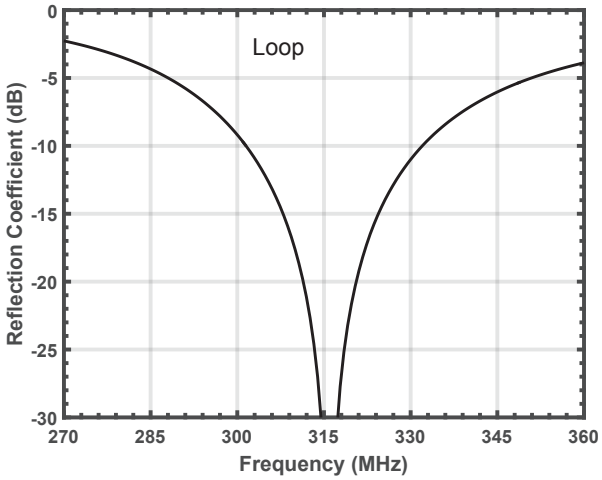

Figure 1.45 Moment method simulated reflection coefficient versus frequency (270 MHz to 360 MHz) for a circular wire loop antenna with circumference 1 meter and wire diameter 1 mm. The reference impedance is 140 ohms

impedance equal to 140 ohms corresponding to the input resistance at the first natural resonance. Taking 140 ohms as the reference impedance, the magnitude of the reflection coefficient in dB is plotted versus frequency in Figure 1.45. The reflection coefficient has a minimum at approximately 317 MHz. The corresponding VSWR is shown in Figure 1.46. Figure 1.47 shows the quality factor Q_Z computed using Equation (1.613) over the band 50 MHz to 450 MHz. Figure 1.48 shows the percent bandwidth achieved by Equation (1.615) assuming allowed VSWR values equal to 1.5, 2, and 3. For this loop antenna, the peak value of PBW occurs near the first natural resonance. The percent bandwidth observed in the method of moments simulated VSWR versus frequency plot in Figure 1.46 with the percent bandwidth computed using Equation (1.615). The results are tabulated in Table 1.3 and good agreement between the bandwidth calculated from the simulated input impedance data using Equation (1.613) and directly from the reflection coefficient.

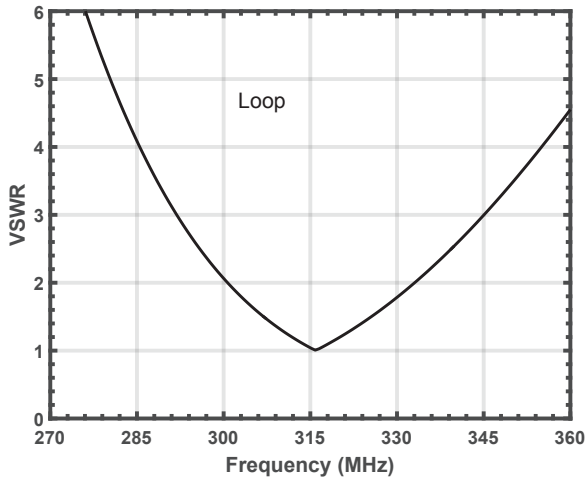

Figure 1.46 Moment method simulated VSWR versus frequency (270 MHz to 360 MHz) for a circular wire loop antenna with circumference 1 meter and wire diameter 1 mm. The reference impedance is 140 ohms.

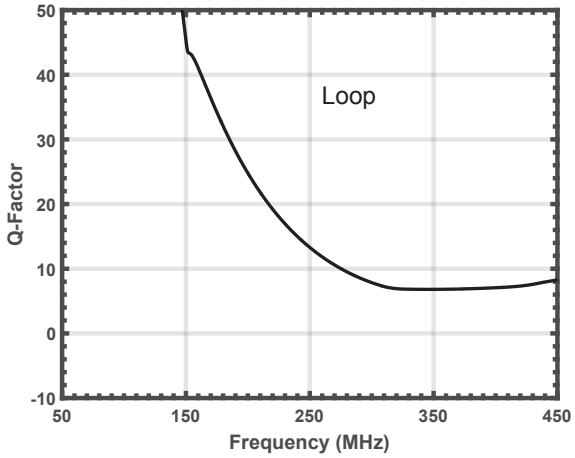

Figure 1.47 Quality factor Q_Z calculated from moment method simulated input impedance versus frequency (50 MHz to 450 MHz) for a circular wire loop antenna with circumference 1 meter and wire diameter 1 mm.

1.12 Antenna Directivity

The radiation intensity of an antenna can be computed from the antenna radiation pattern, denoted $P(\theta, \phi)$, as

$$U(\theta, \phi) = |P(\theta, \phi)|^2 = P(\theta, \phi)P^*(\theta, \phi) \tag{1.616}$$

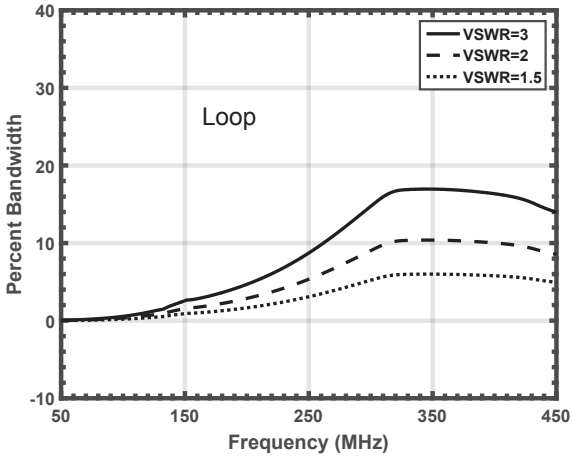

Figure 1.48 Calculated percent bandwidth based on quality factor Q_Z and assumed values of VSWR (1.5, 2, and 3) versus operating frequency (50 MHz to 450 MHz) for a circular wire loop antenna with circumference 1 meter and wire diameter 1 mm. The quality factor was calculated from the moment method simulated input impedance.

where * denotes conjugate. The directivity of an antenna is a function of the radiation intensity normalized by the average radiation intensity as

$$D(\theta,\phi) = \frac{U(\theta,\phi)}{U_{\text{ave}}} \tag{1.617}$$

where

$$U_{\text{ave}} = \frac{1}{4\pi}\int_{\theta=0}^{\pi}\int_{\phi=0}^{2\pi} U(\theta,\phi)\sin\theta d\theta d\phi. \tag{1.618}$$

Table 1.4
Comparison of quality factor computed from Equation (1.613) and from the method of moments simulation for a circular wire loop antenna with 1m circumference and 1 mm wire diameter operating at a 317 MHz center frequency.

	Percent Bandwidth for Wire Loop	
Allowed VSWR	Q_Z, Eq. (1.613)	FEKO (Method of Moments)
1.5	6.0%	6.0%
2.0	10.3%	10.4%
3.0	16.9%	17.7%

The antenna directivity, $D(\theta, \phi)$, relative to an isotropic radiator, depends only on the shape of the radiation pattern of the antenna and does not depend on power delivered to the antenna. The antenna directivity in decibels relative to an isotropic radiator (dBi) is computed by evaluating $10 \log_{10} D(\theta, \phi)$.

1.12.1 Hertzian Dipole or Electrically Small Loop Directivity Pattern

Consider now the far-field radiation pattern of a z-directed Hertzian (electrically short) dipole antenna (refer to Figure 1.25), which has a θ electric field component that varies in observation angle only as $\sin\theta$ according to Equation (1.488). Now for the Hertzian dipole, since $U(\theta) = |\sin\theta|^2$, it follows from Equation (1.618) that $U_{\text{ave}} = \frac{2}{3}$. Substituting this value of average radiation intensity into Equation (1.617), it follows that the angular dependence of the Hertzian dipole directivity is expressed as

$$D(\theta) = \frac{3}{2}|\sin\theta|^2 \tag{1.619}$$

The electrically-short dipole normalized 3D radiation pattern in decibels is shown in Figure 1.49, and it is observed that the pattern is a figure of revolution about the z axis, with a null along the z axis. From Equation (1.619) the half-power (-3 dB) beamwidth is 90°. A polar diagram of the absolute

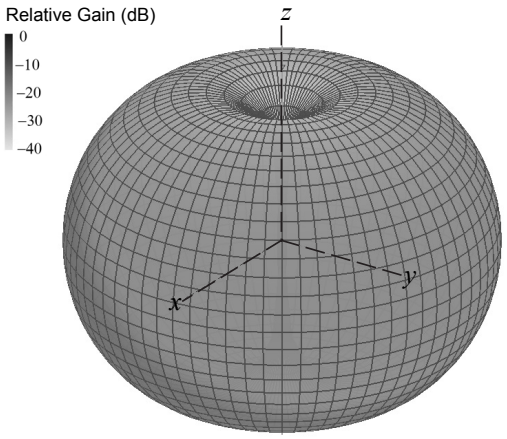

Figure 1.49 3D radiation pattern for a z-directed Hertzian dipole in free space.

directivity pattern (θ component) as a function of θ is shown in Figure 1.50, where the peak directivity of 1.76 dBi is observed to occur at $\theta = 90°$. An electrically small loop antenna (Figure 1.25) has the same $\sin\theta$ angular

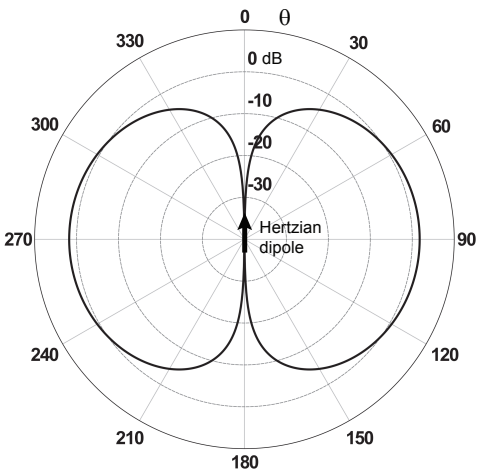

Figure 1.50 Polar directivity pattern D_θ for a z-directed Hertzian dipole antenna.

dependence, so it has the same 3D radiation pattern and the polar directivity patterns as in Figures 1.49 and 1.50, respectively.

1.12.2 Crossed Hertzian Dipoles (Turnstile Antenna) Directivity Pattern

Crossed dipole antennas have a number of applications including operation for independent dual linear polarization, circular polarization, and nearly omnidirectional coverage with horizontal polarization depending on the phase relation between the dipoles. Consider the crossed Hertzian (short) dipoles in the xy-plane in free space as shown in Figure 1.51. As an example of

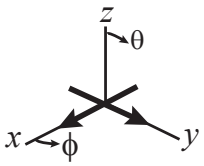

Figure 1.51 Crossed Hertzian (short) dipole antennas in free space.

circular polarization on transmit, let the y-polarized dipole be transmitting with a -90° phase shift with respect to the x-polarized dipole. This antenna configuration is referred to as a turnstile antenna [118]. By the right-hand rule, this quadrature phase relation between the two dipoles generates peak RHCP gain at $\theta = 0^\circ$ and peak LHCP gain at $\theta = 180^\circ$. Figure 1.52 shows a

polar diagram of the moment method simulated circularly polarized elevation radiation patterns for these crossed-dipole antennas in free space. These

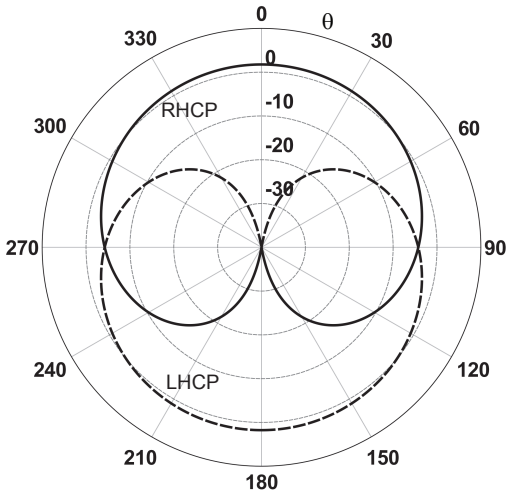

Figure 1.52 Simulated circularly polarized elevation radiation patterns for crossed-dipole antennas phased for RHCP in the upper hemisphere.

radiation patterns are a figure of revolution about the z axis. For example, the LHCP directivity pattern in three dimensions is shown in Figure 1.53. Peak RHCP directivity 1.76 dBi and half-power beamwidth 131° occurs in the forward hemisphere at $\theta = 0°$. Figure 1.54 shows a polar diagram of the corresponding linearly polarized elevation radiation patterns, and again these patterns are a figure of revolution. The $\hat{\phi}$ polarized component has a constant, omnidirectional, gain at the level of -1.24 dBi as a function of elevation angle θ. As expected for the linearly polarized component, this constant value of -1.24 dBi is 3 dB below the peak circularly polarized directivity. The linearly polarized $\hat{\theta}$ component has the same radiation pattern (same peak directivity and same beamwidth) as in Figure 1.50

1.13 Antenna Gain, Realized Gain, and Transmit Power

The antenna directivity discussed in the previous section does not take into account any losses in the antenna and its surroundings. The terms antenna gain and antenna realized gain are used to take into account both the radiation pattern (directivity) as well as certain losses as summarized in Figure 1.55 and is discussed below.

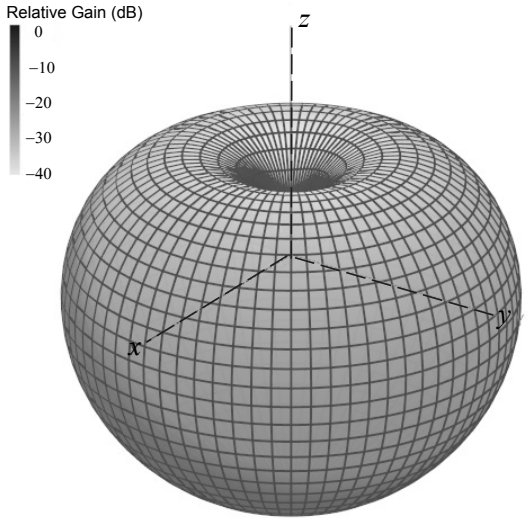

Figure 1.53 Simulated 3D LHCP radiation pattern for crossed-dipole antennas in free space.

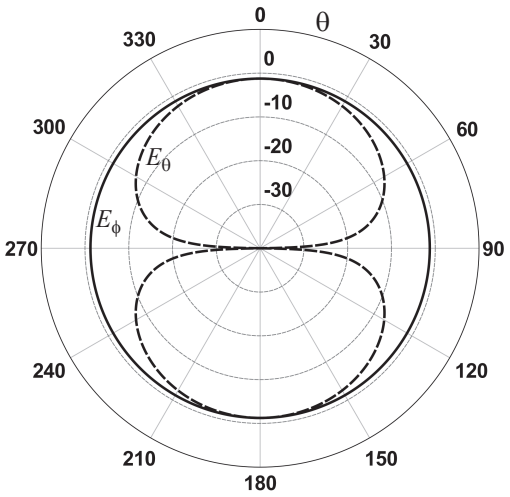

Figure 1.54 Simulated linearly polarized elevation radiation patterns for RHCP crossed-dipole antennas in free space.

Terminology in the literature regarding antenna gain and power can be vague in some instances, so a brief discussion here is appropriate. Transmitter power, transmit power, available power, power accepted by the antenna, input power, power input to the antenna, and power radiated by the antenna are

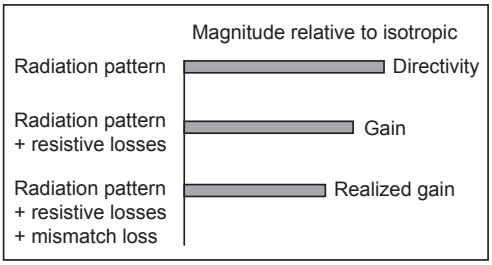

Figure 1.55 Comparisons of the relative magnitude for antenna directivity, gain, and realized gain with respect to an isotropic antenna.

terms found in the literature. The terms directive gain (replaced by the term directivity), power gain, effective gain, gain loss due to impedance mismatch, gain loss due to polarization mismatch, gain loss due to mutual coupling, and gain loss due to power absorbed by the antenna or surrounding structures are found in the literature. In antenna electromagnetic modeling analysis or measurements, it is important to clearly define these terms.

Consider now a transmission line with a transmitter source of a given power level attached at one end of the transmission line. At the other end of this transmission line, which will be the attachment point to the transmitting antenna, a power meter (matched to the transmission line) is attached and registers a power level of P_o watts. Thus, the amount of incident power that is connected to the antenna is accurately known. Now the transmitting antenna element can be mismatched to the transmission line, resulting in reflected power into the transmission line (assumed to be terminated in a resistive load matched to the characteristic impedance of the transmission line) that will be completely absorbed back at the transmitting source location. This reflected power reduces the realized antenna gain and can be quantified and referred to as impedance mismatch loss, transmission mismatch loss, or gain loss. In the case where there are antennas that surround the transmitting antenna (forming an array of antennas), there will be mutual coupling between array elements and, as discussed in Chapter 2, some of the power radiated by the transmit element will be received and consumed (additional power loss or additional gain loss) by the surrounding array elements. The net effect of the gain loss mechanisms will be a reduced transmitted power density (watts per meter squared) at a near-field or far-field position from the array.

The antenna gain, relative to an isotropic radiator with the same input power, can be expressed as

$$G(\theta, \phi) = \frac{4\pi U(\theta, \phi)}{P_{\text{in}}} \tag{1.620}$$

where P_{in} is the input power, that is, the power at the end of the transmission line that will be connected to the antenna. As a result of losses from antenna impedance mismatch and losses attributed to components between the transmitter and the antenna terminals, the power transmitted by the antenna is less than the input power. For electrically small antenna elements, the finite resistive loss of the antenna element itself can significantly reduce both the efficiency and gain of the antenna. The antenna gain in dBi is computed by evaluating $10 \log_{10} G(\theta, \phi)$.

Assuming that the antenna, with input impedance Z_{in}, is connected to a transmission line with characteristic impedance Z_o, the voltage reflection coefficient Γ is given by

$$\Gamma = \frac{Z_{\text{in}} - Z_o}{Z_{\text{in}} + Z_o}. \tag{1.621}$$

The reflection coefficient in dB is computed as

$$\Gamma_{\text{dB}} = 20 \log_{10} \Gamma. \tag{1.622}$$

The reflection coefficient in dB is also referred to in the literature as return loss (a reflection coefficient of zero is the same as a minus infinity dB return loss or a perfect match usually to 50 ohms). In antenna designs, it is often desirable to provide an impedance matching network to improve the return loss [71]. The loss in antenna gain resulting from antenna input impedance mismatch alone is computed from the impedance mismatch efficiency, denoted $\eta_{\text{Z mismatch}}$ (same as transmission mismatch efficiency given by Equation (1.21)),

$$\eta_{\text{Z mismatch}} = 1 - |\Gamma|^2. \tag{1.623}$$

By using Equation (1.623), the mismatch loss ML (or gain loss) in dB as a positive value is computed as

$$\text{ML}_{\text{dB}} = -10 \log_{10} \eta_{\text{Z mismatch}}. \tag{1.624}$$

The radiation loss efficiency factor η_L of an antenna can be calculated as follows [23, pp. 43-48]. The radiation loss efficiency of an antenna is expressed as

$$\eta_L = R_r / R_A \tag{1.625}$$

where R_r is the radiation resistance and

$$R_A = R_r + R_{\text{ohmic}} \tag{1.626}$$

is the total input resistance of the antenna. For example, the ohmic resistance for an electrically short dipole of length L and diameter d is given by

$$R_{\text{ohmic}} = \frac{L R_s}{3\pi d} \tag{1.627}$$

where

$$R_s = \sqrt{\pi f \mu / \sigma} \tag{1.628}$$

is the surface resistance of the dipole, which depends on the frequency f, permeability μ, and electrical conductivity σ of the dipole material. Thus, since the ohmic resistance is inversely proportional to the dipole diameter, the efficiency can be increased by using a larger-diameter dipole.

The realized antenna gain, denoted as G_{realized}, takes account of impedance mismatch and efficiency loss. The realized antenna gain and directivity are related by the following expression

$$G_{\text{realized}}(\theta, \phi) = D(\theta, \phi)\eta_{\text{L}}\eta_{\text{Z mismatch}} \tag{1.629}$$

where η_L is the antenna efficiency loss factor, which includes resistive losses in the antenna. For a 100% efficient (lossless) antenna with $\eta_{\text{L}} = 1$, and with no mismatch loss, the gain is equal to the directivity. For a transmitting antenna, the effective isotropic radiated power (EIRP(θ, ϕ)) is equal to the product of the power incident on the antenna P_o and the realized gain $G_{\text{realized}}(\theta, \phi)$, that is

$$\text{EIRP}(\theta, \phi) = P_o G_{\text{realized}}(\theta, \phi). \tag{1.630}$$

Alternately, if the impedance mismatch loss is included in the power budget, then the transmit power accepted by the antenna is denoted as P_t and then the EIRP is equal to the following product

$$\text{EIRP}(\theta, \phi) = P_t G_t(\theta, \phi) \tag{1.631}$$

where $G_t(\theta, \phi)$ is the gain of the transmit antenna, which includes any resistive losses associated with the antenna and its surroundings.

The far-zone power density P_d (with units of W/m^2) at a distance r from the aperture (one-way path) is given by

$$P_d = \frac{P_t G_t}{4\pi r^2}. \tag{1.632}$$

Based on a receive antenna's maximum effective aperture, denoted A_{em}, the aperture collects incident power density and converts it to an output power. Thus, the received power P_r of an antenna aperture can be expressed as

$$P_r = P_d A_{\text{em}}. \tag{1.633}$$

Furthermore, the receive antenna gain is expressed as

$$G_r = 4\pi A_{\text{em}} / \lambda^2, \tag{1.634}$$

and solving for A_{em} yields

$$A_{\text{em}} = G_r \lambda^2/(4\pi). \tag{1.635}$$

Thus, it follows that

$$P_r = \frac{P_t G_t G_r \lambda^2}{(4\pi r)^2}. \tag{1.636}$$

Equation (1.636) can be rearranged to express the mutual coupling power ratio (P_r/P_t) between two antennas as

$$\frac{P_r}{P_t} = \frac{G_t G_r \lambda^2}{(4\pi r)^2}. \tag{1.637}$$

1.14 Summary

The theory given in this chapter can be used to gain some basic insight into the fundamental radiation properties of antennas. In the case of an array of antennas, the radiation properties of one array antenna element have an effect on the surrounding array antenna elements, and thus the interaction between the array antenna elements must be taken into account in any detailed analysis. Some methods for computing the performance of phased array antennas taking account of mutual coupling effects are discussed in Chapter 2.

References

[1] T.K. Sarkar, R.J. Mailloux, A.A. Oliner, M. Salazar-Palma, D.L. Sengupta, *History of Wireless,* Hoboken, NJ: Wiley, 2006.

[2] C.A. Balanis, *Advanced Engineering Electromagnetics, 2nd ed.* New Jersey: Wiley, 2012.

[3] J.A. Kong, *Electromagnetic Wave Theory.* Cambridge, Mass.: EMW Publishing, 2008.

[4] D.T. Paris and F.K. Hurd, *Basic Electromagnetic Theory.* New York: McGraw-Hill, 1969.

[5] J.A. Stratton, *Electromagnetic Theory.* New York: McGraw-Hill, 1941.

[6] J.D. Kraus, *Electromagnetics.* New York: McGraw-Hill, 1953.

[7] R.F. Harrington, *Time-Harmonic Electromagnetic Fields.* New York: McGraw-Hill, 1961.

[8] W.H. Hayt and J.A. Buck, *Engineering Electromagnetics, 6th ed.* New York: McGraw-Hill, 2001.

[9] C.H. Durney and C.C. Johnson, *Introduction to Modern Electromagnetics*. New York: McGraw-Hill, 1969.

[10] J.D. Kraus and K.R. Carver, *Electromagnetics, 2nd ed.* New York: McGraw-Hill, 1973, pp. 612–613.

[11] D.K. Cheng, *Field and Wave Electromagnetics.* Reading, Mass.: Addison-Wesley, 1983.

[12] S. Ramo, J.R. Whinnery, and T. van Duzer, *Fields and Waves in Communication Electronics.* New York: Wiley, 1984.

[13] M.N.O. Sadiku, *Elements of Electromagnetics, 2nd ed.* New York: Oxford University Press, 1995.

[14] G.S. Smith, *An Introduction to Classical Electromagnetic Radiation.* Cambridge, UK: Cambridge University Press, 1997.

[15] J.D. Kraus and R.J. Marhefka, *Antennas for All Applications, 3rd ed.* New York: McGraw-Hill, 2002.

[16] R.W.P. King, *The Theory of Linear Antennas,* Cambridge, MA: Harvard University Press, 1956.

[17] S.A. Schelkunoff and H.T. Friis, *Antennas: Theory and Practice*. New York: Wiley, 1952.

[18] S. Silver, ed., *Microwave Antenna Theory and Design,* MIT Radiation Lab Series, vol. 12, New York: McGraw-Hill, 1949.

[19] C.H. Walter, *Traveling Wave Antennas*, New York: McGraw-Hill, 1968.

[20] W.L. Weeks, *Antenna Engineering*, New York: McGraw-Hill, 1968.

[21] R.S. Elliott, *Antenna Theory and Design*, New York: Prentice-Hall, 1981.

[22] A.W. Rudge, K. Milne, A.D. Olver, and P. Knight, *The Handbook of Antenna Design, vols. 1 and 2* London: Peter Perigrinus, 1992.

[23] W.L. Stutzman and G.A. Thiele, *Antenna Theory and Design, 2nd ed.* New York: Wiley, 1998.

[24] J. Volakis, ed., *Antenna Engineering Handbook, 4th ed.* New York: McGraw-Hill, 2007.

[25] C.A. Balanis, *Antenna Theory and Design, 3rd ed.* New York: Wiley, 2005.

[26] R.A. Burberry, *VHF and UHF Antennas* London: Peter Peregrinus, 1992.

[27] T.A. Milligan, *Modern Antenna Design, 2nd ed.* Hoboken, NJ: Wiley-IEEE Press, 2005

[28] L.V. Blake and M.W. Long, *Antennas: Fundamentals, Design, Measurement*, Raleigh, NC: SciTech Publishing, 2009.

[29] W. Stutzman, “Bibliography for Antennas: A List of Every English-Language Antenna Book Ever Written," *IEEE Antennas and Propagation Magazine*, vol. 50, no. 4, August 2008, pp. 128–143.

[30] N. Amitay, V. Galindo, and C.P. Wu, *Theory and Analysis of Phased Array Antennas.* New York: Wiley, 1972, ch. 1.

[31] A.A. Oliner and G.H. Knittel, eds., *Phased Array Antennas*. Dedham, Mass.: Artech House, 1972.

[32] R.C. Hansen, ed., *Significant Phased Array Papers*. Dedham, Mass.: Artech House, 1973.

[33] R.J. Mailloux, *Phased Array Handbook, 2nd ed.* Norwood, Mass.: Artech House, 2005.

[34] E. Brookner, ed., *Practical Phased-Array Antenna Systems*. Norwood, Mass.: Artech House, 1991.

[35] R.C. Hansen, *Microwave Scanning Antennas, vol. II: Array Theory and Practice.* Los Altos, Calif.: Peninsula Publishing, 1985.

[36] R.C. Hansen, *Phased Array Antennas, 2nd ed.* New York: Wiley, 2009.

[37] A.K. Bhattacharyya, *Phased Array Antennas.* New York: Wiley, 2006.

[38] T. Jeffrey, *Phased-Array Radar Design: Application of Radar Fundamentals.* Raleigh, North Carolina: Scitech Pub Inc., 2009.

[39] A.J. Fenn, *Adaptive Antennas and Phased Arrays for Radar and Communications.* Norwood, Mass.: Artech House, 2008.

[40] S.P. Skobelev, *Phased Array Antennas with Optimized Element Patterns.* Norwood, Mass.: Artech House, 2011.

[41] H.J. Visser, *Array and Phased Array Antenna Basics.* New York: Wiley, 2005.

[42] R.L. Haupt, *Antenna Arrays: A Computational Approach.* New York: Wiley-IEEE Press, 2010.

[43] D. Ehyale, *Novel Approaches to the Design of Phased Array Antennas: Low Cost, Low Complexity Phased Array Antenna Design.* LAP Lambert Academic Publishing, 2012.

[44] E. Brookner, "Phased-Array Radars," *Scientific American,* vol. 252, no. 2, 1985, pp. 94–102.

[45] A.J. Fenn, D.H. Temme, W.P. Delaney, and W.E. Courtney, "The Development of Phased Array Radar Technology," *Lincoln Laboratory Journal*, vol. 12, no. 2, 2000, pp. 321–340.

[46] R.J. Mailloux, "Phased Array Theory and Technology," *Proc. IEEE*, vol. 70, no. 3, 1982, pp. 246–291.

[47] A.J. Fenn and P.T. Hurst, *Ultrawideband Phased Array Antenna Technology for Sensing and Communications Systems*, Cambridge, MA: The MIT Press, 2015.

[48] P.W. Howells, "Explorations in Fixed and Adaptive Resolution at GE and SURC," *IEEE Trans. Antennas and Propagation*, vol. 24, no. 5, 1976, pp. 575–584.

[49] S.P. Applebaum, "Adaptive Arrays," *IEEE Trans. Antennas and Propagation*, vol. 24, no. 5, 1976, pp. 585–598.

[50] W.F. Gabriel, "Adaptive Arrays – An Introduction," *Proc. IEEE,* vol. 64, 1976, pp. 239–271.

[51] J.T. Mayhan, "Some Techniques for Evaluating the Bandwidth Characteristics of Adaptive Nulling Systems," *IEEE Trans. Antennas and Propagation,* vol. 27, no. 3, 1979, pp. 363–373.

[52] J.T. Mayhan, A.J. Simmons, and W.C. Cummings, "Wide-Band Adaptive Antenna Nulling Using Tapped Delay Lines," *IEEE Trans. Antennas and Propagation,* vol. 29, no. 6, 1981, pp. 923–936.

[53] A.J. Fenn, "Evaluation of Adaptive Phased Array Far-Field Nulling Performance in the Near-Field Region," *IEEE Trans. Antennas and Propagation*, vol. 38, no. 2, 1990, pp. 173–185.

[54] R.A. Monzingo and T.W. Miller, *Introduction to Adaptive Arrays*. New York: Wiley, 1980.

[55] R.T. Compton, Jr., *Adaptive Antennas, Concepts and Performance*. Upper Saddle River, New Jersey: Prentice-Hall, 1988.

[56] M.M. Weiner, *Adaptive Antennas and Receivers*. Boca Raton, Florida: CRC Press, 2006.

[57] S. Chandran, ed., *Adaptive Antenna Arrays: Trends and Applications*. Berlin: Springer-Verlag, 2004.

[58] D.G. Manolakis, V.K. Ingle, and S.M. Kogon, *Statistical and Adaptive Signal Processing: Spectral Estimation, Signal Modeling, Adaptive Filtering, and Array Processing.* Norwood, Mass.: Artech House, 2005.

[59] R. Nitzberg, *Adaptive Signal Processing for Radar*. Norwood, Mass.: Artech House, 1992.

[60] A. Farina, *Antenna-Based Signal Processing Techniques for Radar Systems.* Norwood,

Mass.: Artech House, 1992.

[61] J.E. Hudson, *Adaptive Array Principles*. New York: Peter Peregrinus, 1981.

[62] D.M. Pozar, *Microwave Engineering, 4th ed.*, Hoboken, NJ: Wiley, 2012.

[63] P. H. Smith, "Transmission line calculator," *Electronics*, vol. 12, no. 1, pp. 29–31, Jan. 1939.

[64] P. H. Smith, "An Improved Transmission Line Calculator," *Electronics*, vol. 17, no. 1, pp. 130–133, p. 318, p. 320, p. 322, and pp. 324–325, Jan. 1944.

[65] P. H. Smith, "Electronic Applications of the Smith Chart," – In *Waveguide, Circuit, and Component Analysis*, 2nd ed. Raleigh, NC: SciTech Publishing, 1995.

[66] T. Lee, "The Smith Chart Comes Home," IEEE Microwave Magazine, p. 10, 12, and 25, Nov. 2015, Digital Object Identifier: 10.1109/MMM.2015.2467953, Date of Publication: 14 Oct. 2015.

[67] H.J. Reich, ed., Harvard Radio Research Laboratories, *Very High Frequency Techniques*, New York: Mc-Graw Hill, Vol. 1, Chapter 3, 1947.

[68] R.M. Fano, "Theoretical Limitations on the Broadband Matching of Arbitrary Impedances," Massachusetts Institute of Technology, Research Laboratory of Electronics, Technical Report 41, Jan. 2, 1948.

[69] H.A. Wheeler, "Wideband Impedance Matching," Wheeler Laboratories Report 418, Great Neck, New York, 1950.

[70] V.H. Rumsey, "The Design of Frequency-Compensating Matching Sections," *Proc. IRE*, October 1950, pp. 1191–1196.

[71] R.L. Thomas, *A Practical Introduction to Impedance Matching*, Dedham, MA: Artech House, 1976.

[72] W.N. Caron, *Antenna Impedance Matching*, Newington, CT: American Radio Relay League, 1989.]

[73] G.L. Matthaei, L. Young, E.M.T. Jones, *Microwave Filters, Impedance-Matching Networks, and Coupling Structures*, New York, McGraw-Hill, 1964.

[74] T.R. Cuthbert, *Circuit Design Using Personal Computers*, New York: John Wiley, 1983.

[75] T.R. Cuthbert, *Broadband Direct-Coupled and Matching RF Networks*, Greenwood, Arkansas: TRCPEP Publications, 1999.

[76] C. Bowick, *RF Circuit Design*, Burlington, MA: Newnes, 2008.

[77] R. Mavaddat, *Network Scattering Parameters,* Advanced Series in Circuits and Systems, vol. 2, Singapore, World Scientific Publishing, 1996.

[78] D.A. Frickey, "Conversions Between S, Z, Y, h, ABCD, and T Parameters Which are Valid for Complex Source and Load Impedances," *IEEE Trans. Microwave Theory and Techniques*, vol. 42, no. 2, February 1994, pp. 205-211.

[79] W.F. Egan, *Practical RF System Design*, New York: IEEE, Hoboken, New Jersey: Wiley.

[80] IEEE Standard for Ultrawideband Radar Definitions, IEEE Std 1672-2006, 4 May 2007 (2nd printing, 11 Dec. 2008), doi: 10.1109/IEEESTD.2007.359972.

[81] J.D. Taylor, *Introduction to Ultra-Wideband Radar Systems.* Boca Raton, Florida: CRC Press, 1995.

[82] L. Peters, Jr., J.J. Daniels, and J.D. Young, "Ground Penetrating Radar as a Subsurface Environmental Sensing Tool," *Proc. IEEE*, vol. 82, no. 12, 1994, pp. 1802–1822.

[83] D. Uduwawala et al., "A Deep Parametric Study of Resistor-Loaded Bow-Tie Antennas for Ground-Penetrating Radar Applications Using FDTD," *IEEE Trans Geoscience and Remote Sensing*, vol. 42, no. 4, 2004, pp. 732–742.

[84] M. Kanda, "A Relatively Short Cylindrical Broadband Antenna with Tapered Resistive Loading for Picosecond Pulse Measurements," *IEEE Trans. Antennas and Propagation*, vol. 26, no. 3, 1978, pp. 439–447.

[85] T.P. Montoya and G.S. Smith, "Land Mine Detection Using a Ground Penetrating Radar Based on Resistively Loaded Vee Dipoles," *IEEE Trans. Antennas and Propagation,* vol. 47, no. 12, 1999, pp. 1795–1806.

[86] J.D. Dyson, "The Equiangular Spiral Antenna," *IRE Trans. Antennas and Propagation*, vol. 7, no. 2, 1959, pp. 181–187.

[87] V.H. Rumsey, *Frequency Independent Antennas.* New York: Academic Press, Inc., 1966.

[88] H. Schantz, *The Art and Science of Ultrawideband Antennas*. Norwood, Mass.: Artech House, 2005.

[89] D. Valderas, J.I. Sancho, D. Puente, C. Ling, and X. Chen, *Ultrawideband Antennas, Design and Applications*. London: Imperial College Press, 2011.

[90] T.S. Ralston, G.L. Charvat, and J.E. Peabody, "Real-Time Through-Wall Imaging Using an Ultrawideband Multiple-Input Multiple-Output (MIMO) Phased Array Radar System," *IEEE Int. Symp. on Phased Array Systems and Technology,* 2010, pp. 551–558.

[91] A. Rajagopalan, G. Gupta, A.S. Konanur, B. Hughes, and G. Lazzi, "Increasing Channel Capacity of an Ultrawideband MIMO System Using Vector Antennas," *IEEE Trans. on Antennas and Propagation*, vol. 55, no. 10, 2007, pp. 2880–2887.

[92] C.M. Keller, and D.P. Young, "Ultra-Wideband (UWB) Signal Localization Using a Vehicle-Sized Array," *2005 IEEE International Conference on Ultra-Wideband*, 2005, pp. 290–295.

[93] E.W. Reid, L. Ortiz-Balbuena, A. Ghadiri, and K. Moez, "A 324-Element Vivaldi Antenna Array for Radio Astronomy Instrumentation," *IEEE Trans. Instrumentation and Measurement,* vol. 61, no. 1, 2012, pp. 241–250.

[94] M. Lazebnik, E.L. Madsen, G.R. Frank, and S.C. Hagness, "Tissue-Mimicking Phantom Materials for Narrowband and Ultrawideband Microwave Applications," *Physics in Medicine and Biology*, vol. 50, 2005, pp. 4245–4258.

[95] S. Gabriel, R.W. Lau, and C. Gabriel, "The Dielectric Properties of Biological Tissues:

Part III. Parametric Models for the Dielectric Spectrum of Tissues," *Physics in Medicine and Biology,* vol. 41, 1996, pp. 2271–2293, online http://niremf.ifac.cnr.it/tissprop.

[96] C-K Chou and J. D'Andrea, *IEEE Standard for Safety Levels with Respect to Human Exposure to Radio Frequency Electromagnetic Fields, 3 kHz to 300 GHz*, IEEE Std C95.1-2005. New York: Institute of Electrical and Electronics Engineers, Inc.

[97] J.F. Lehmann, ed., *Therapeutic Heat and Cold, 3rd ed.* Baltimore, Maryland: Williams & Wilkins, 1982.

[98] A.R. von Hippel, *Dielectrics and Waves.* New York: John Wiley, 1954.

[99] A.D. Yaghjian and S.R. Best, Impedance, Bandwidth, and Q of Antennas, IEEE Trans. Antennas and Propagat., vol. 53, no. 4, April 2005, pp. 1298–1324.

[100] C. Cohen-Tannoudji, J. Dupont-Roc, and G. Grynberg, *Photons and Atoms: Introduction to Quantum Electrodynamics*. Weinheim: Wiley-VCH, Verlag GmbH & Co. KGaA, 2004.

[101] C. Cohen-Tannoudji, J. Dupont-Roc, and G. Grynberg, *Atom-Photon Interactions: Basic Processes and Applications*. Weinheim: Wiley-VCH, Verlag GmbH & Co. KGaA, 2004.

[102] J.D. Jackson, *Classical Electrodynamics, 3rd ed.* New York: Wiley, 1999, p. 3.

[103] J.C. Maxwell, *A Treatise on Electricity and Magnetism, vols. 1 and 2*. Oxford, UK: Clarendon Press, 1873.

[104] J.H. Poynting, "On the Transfer of Energy in the Electromagnetic Field," *Philosophical Transactions of the Royal Society of London*, vol. 175, 1884, pp. 343–361.

[105] Y. Zhu and A. Cangellaris, *Multigrid Finite Element Methods for Electromagnetic Field Modeling.* New Jersey: Wiley, 2006.

[106] W.L. Stutzman, *Polarization in Electromagnetic Systems.* Norwood, Mass.: Artech House, 1993.

[107] R.E. Collin, *Foundations for Microwave Engineering.* New York: McGraw-Hill, 1966, pp. 64–143.

[108] P.G. Ciarlet, ed., *Numerical Methods in Electromagnetics, Volume 13: Special Volume (Handbook of Numerical Analysis).* W.H.A. Schilders and E.J.W. ter Maten, guest eds., Chapter 3, *Finite Difference Time Domain Methods,* S.C. Hagness, A. Taflove, and S.D. Gedney, Elsevier B.V., The Netherlands, 2005, pp. 199–314.

[109] C.T. Tai, *Dyadic Green's Functions in Electromagnetic Theory.* London: Intext Educational Publishers, 1971.

[110] C.T. Tai, *Generalized Vector and Dyadic Analysis.* New York: IEEE Press, 1992.

[111] C.T. Tai, "A Survey of the Improper Uses of ∇ in Vector Analysis," Radiation Laboratory, The University of Michigan, Technical Report RL 909, November 1994.

[112] C.T. Tai, "A Historical Study of Vector Analysis," Radiation Laboratory, The University of Michigan, Technical Report RL 915, May 1995.

[113] G. Green, “An Essay on the Application of Mathematical Analysis to the Theories of Electricity and Magnetism," Nottingham, England, printed for the author by T. Wheelhouse, 1828.

[114] D.A. Sanchez-Hernandez, ed., *High Frequency Electromagnetic Dosimetry*, Norwood, MA: Artech House, 2008.

[115] G.W. Hanson and A.B. Yakovlev, *Operator Theory for Electromagnetics, An Introduction*. New York: Springer, 2002.

[116] R. Nevels and J. Jeong, “The Time Domain Green’s Function and Propagator for Maxwell’s equations," *IEEE Trans. Antennas and Propagat.*, vol. 52, no. 11, 2004, pp. 3012–3018.

[117] A.Z. Elsherbeni, P. Nayeri, and C.J. Reddy, *Antenna Analysis and Design Using FEKO Electromagnetic Simulation Software*, SciTech Publishing, 2014.

[118] G. Brown, “The Turnstile Antenna," *Electronics*, 1936.

2

Phased Array Antennas

2.1 Introduction

In Chapter 1, electromagnetic theory for antennas was reviewed in detail. In this chapter, the subject of phased array antennas [1–60] is briefly reviewed. Development of phased array radar technology is described by Fenn et al. [24]. The concept of a phased array and early experiments were presented over 100 years ago in a 1909 Nobel Prize lecture by Braun [54]. A history of phased arrays has been reviewed by Mailloux [55]. Delaney [56] has reviewed the development and deployment of operational phased array radars, with an emphasis on achieving a goal of a solid state phased array. Solid-state phased arrays are now being utilized in many applications as described by Brookner [57]. Herd and Conway [58] have described the evolution of low-cost solid-state phased arrays that utilize high-volume commercial manufacturing and packaging technologies that implement a modern tile array architecture. Millimeter-wave phased arrays have been mass produced for automotive radar systems for collision avoidance [59]. Millimeter-wave phased arrays are being investigated for fifth generation (5G) communications systems for high-data-rate applications [60-62].

This chapter begins with basic phased array theory in Section 2.2. To take into account the simulated effects of array mutual coupling, equivalence principles (Section 2.3), the reciprocity theorem (Section 2.4) and reaction integral equation (Section 2.5) are reviewed, from which the method of moments (Section 2.6) is derived. The method of moments is used in many of the electromagnetic simulations of antennas presented in this book. Section 2.7 provides examples of broadside and endfire linear arrays of Hertzian (short) dipoles. An example of mutual coupling effects on the embedded element pattern in a two-dimensional array of linear dipoles is

shown in Section 2.8. For wide-angle scanning, swept-back dipole antenna elements are used in a number of phased array applications. Swept-back dipole array measurements and simulations are presented in Section 2.9. Simulations of the scanned radiation patterns for a linear array of rectangular waveguides are presented in Section 2.10. Section 2.11 has a summary.

2.2 Phased Array Basics

2.2.1 Introduction

Antenna systems are often required to have apertures with significant radiated power levels, sensitive receive capability, rapid beam scanning, wide bandwidth, and durability. Phased array antennas have been deployed on many ground based systems, automobiles, ships, aircraft, and satellites. Phased array antenna systems with just a few antenna elements or with hundreds or thousands of individual radiating antenna elements can provide electronically controlled beam agility and graceful degradation. Antenna arrays can be used to adaptively suppress interference [63–78], such as jamming, and to suppress radar clutter (background scatter). Antennas that can operate with desired performance characteristics over very wide bandwidths are desirable in many applications. An antenna design that performs well over very wide bandwidths avoids the situation of having to develop multiple, different antenna designs to cover multiple bands spanning a large frequency range.

Figure 2.1 depicts a phased array aperture with multiple antenna elements (represented as dots) that produces a narrow-beam gain radiation pattern that can be electronically scanned over some field of view. In general, the phased array aperture can be composed of radiating and/or receiving antenna elements that are located on a planar or conformal surface. Figure 2.2 shows an N-element two-dimensional planar phased array with a beamforming network that produces a phase coherent combined main

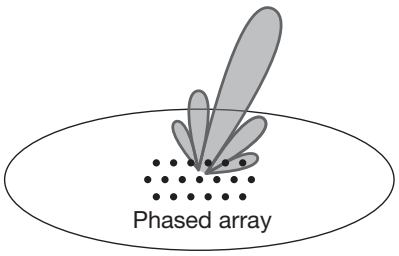

Figure 2.1 Phased array aperture radiating from a general surface that produces an electronically steerable narrow-beam radiation pattern.

channel. In this diagram the antenna array is located on a rectangular ground plane. Depending on required gain, beamwidth, sidelobe levels and other requirements, the antenna elements can be located in a periodic lattice, either rectangular or triangular, or they could be sparsely or randomly positioned on the ground plane. The amplitude and phase of RF signals to and from the antenna elements are electronically adjusted using complex element weighting as $\boldsymbol{W} = (W_1, W_2, \cdots, W_N)^T$, where the superscript T means transpose. The combiner is used to provide a phase coherent summing junction with either uniform amplitude combining or with a fixed taper. The combiner is typically an RF component, although if the element signals are digitized the combiner can be accomplished by digital summation of the data. When the antenna element signals are coherently combined, the resulting radiation pattern will have a main lobe scanned to some desired angle and there will be a number of sidelobes formed away from the main beam. An adaptive beamformer as shown can be added to this architecture if desired for providing adaptive sidelobe cancellation of interference. In this case, M auxiliary antenna element channels are provided with complex adaptive nulling weights denoted as $\boldsymbol{w} = (w_1, w_2, \cdots, w_M)^T$. These auxiliary antenna elements can be separate antennas or they could use signals coupled from the

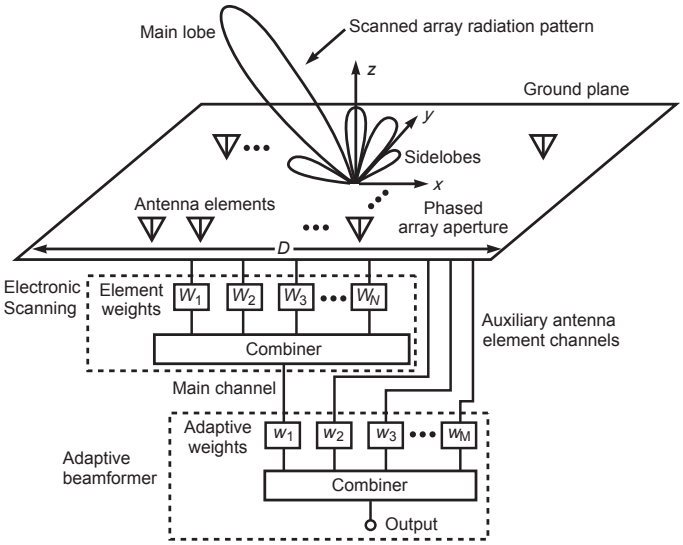

Figure 2.2 Two-dimensional phased array antenna aperture with a beamforming network that electronically scans a narrow-beam radiation pattern. Auxiliary antenna elements and adaptive weights provide adaptive nulling capability.

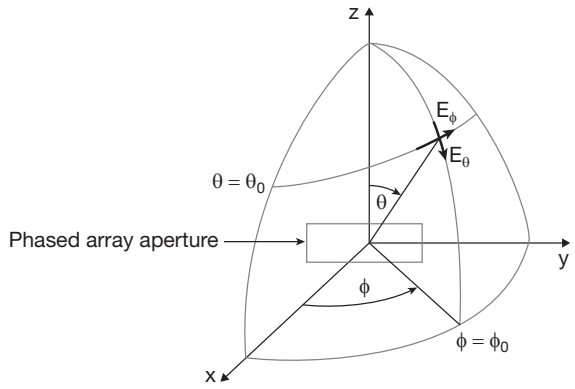

Figure 2.3 Phased array antenna aperture in the spherical coordinate system.

antenna elements used in the phased array aperture.

A sketch of a phased array antenna aperture in spherical coordinates is shown in Figure 2.3. In this diagram, the aperture of the array is oriented parallel to the yz plane. As such, the positive z axis could point to zenith and the angle ϕ could represent azimuth. The angle $\theta = 90^\circ$ would be taken as the horizontal plane, and the angle $90^\circ - \theta$ would then be the elevation angle with respect to the horizon. In the far field, depending on the array element design and antenna orientation, one or both of two orthogonal electric-field components (E_θ, E_ϕ) can be produced, and in the near field, a radial component of the electric field (denoted E_r) can also be generated or received. If the array elements are, for example, linear dipoles oriented in the $\hat{z}$ direction, then only an E_θ far-field component would be transmitted or received. If the linear dipole elements are tilted away from the $\hat{z}$ direction, then in general both E_θ and E_ϕ far-field components will be produced. Besides dipoles, many other types of antennas such as monopoles, waveguides, slots, horns, patches, log periodics, spirals, helix antennas, Yagi-Uda antennas, biconical antennas, reflector antennas, and lenses, have been used in phased array applications [4].

Some of the key parameters that are involved in phased array antenna design are bandwidth, polarization, scan sector, beamwidth, antenna gain, reflection coefficient, and peak and average sidelobe levels. Additional design parameters involve volume, mass, power, thermal/cooling, complexity, and cost for the antenna array system, which need to be addressed for each unique application. Transmit/receive (T/R) modules containing phase shifters to steer the main beam, amplifiers (power amplifiers for transmit and low-noise amplifiers for receive) to provide the desired signal level and noise

figure, and attenuators for generating low sidelobe radiation patterns are used in many phased arrays.

Electronic scanning of the array antenna main beam is effected by means of phase shifters and/or time delays connected to individual array elements or subarrays (groups) of elements. A phased array can be used to transmit or receive a focused electromagnetic wavefront for plane waves or spherical waves as discussed in the next section.

2.2.2 Wavefront Basics

Consider now an electromagnetic wavefront incident on an array of antennas. The source generating the wavefront can be located at close range, producing a spherical wave, or the source could be located sufficiently far from the antenna so that a plane wave is incident upon the array. In this book, we will be dealing primarily with the plane wave, far-field source case, such as for a radar antenna with a target at a range distance of many kilometers. An example of a source producing a spherical wave impinging on an array could be the case of a close-range target in a ground-penetrating radar application or a source of near-field scattering or interference.

The contrast between plane wave incidence and spherical wave incidence [15, 68] is depicted in Figure 2.4. The amount of wavefront dispersion (time delay multiplied by bandwidth) observed by the antenna is a function of the antenna length, angle of incidence, and bandwidth. Dispersion can also be introduced by reflections and other frequency-dependent characteristics within the antenna beamformer or by dispersive materials used in the antenna construction. Wavefront dispersion can cause significant signal distortion unless time-delay weighting across the array antenna is used. Interference wavefront dispersion is an effect that can limit the depth of null (or cancellation) achieved by an adaptive antenna [65–67] To compensate for wavefront dispersion, the adaptive array process can include multiple auxiliary antenna element channels and tapped-delay line weighting. In the case of a pulsed radar system, if the pulse width is narrower than the amount of time delay across the aperture, then to properly transmit or receive the radar waveform, time delay must be provided in the beamformer. Basic time delay or dispersion models for spherical wave incidence and plane wave incidence can be made by considering only the wavefront time delay or dispersion observed by the end points of an array [68].

Consider first a plane wave arriving from infinity and a linear array of length L as shown in Figure 2.4(a). The far-field time delay $\Delta\tau_{FF}$ of the wavefront across the array is given by

$$\Delta\tau_{FF} = \frac{L}{c}\cos\theta_i = \frac{L}{c}\beta_{FF} \tag{2.1}$$

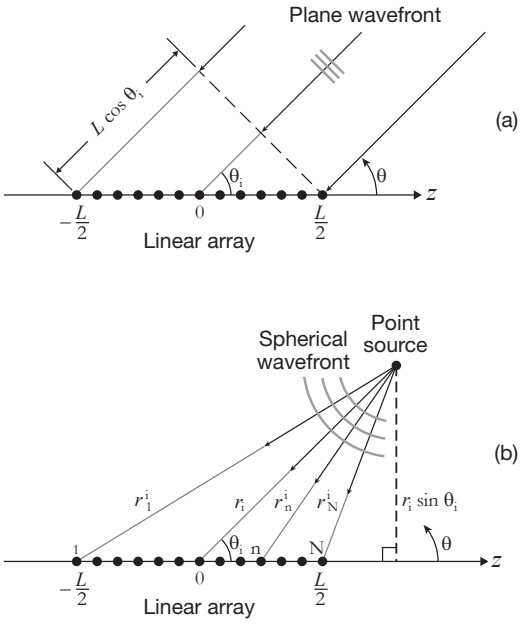

Figure 2.4 Geometry for far-field and near-field wave incidence for a linear array. (a) Plane wavefront, and (b) spherical wavefront.

where

$$\beta_{FF} = \cos\theta_i \tag{2.2}$$

will be referred to as the far-field dispersion multiplier, c is the speed of light, and θ_i is the angle of incidence with respect to the axis of the array. Note that the time delay is maximum for endfire incidence ($\theta_i = 0$) and is zero for broadside incidence ($\theta_i = \pi/2$). The dispersion for this case is denoted γ_{FF} and is computed according to the product of bandwidth and time delay as

$$\gamma_{FF} = B\Delta\tau_{FF} = \frac{BL}{c}\cos\theta_i = \frac{BL}{c}\beta_{FF} \tag{2.3}$$

where B is the waveform bandwidth.

Next, consider the same array and now a point source, at range $r = r_i$ and angle $\theta = \theta_i$, which produces a spherical wavefront as depicted in Figure 2.4(b). The near-field time delay $\Delta\tau_{NF}$ is given by

$$\Delta\tau_{NF} = \frac{L}{c}\beta_{NF} \tag{2.4}$$

where the quantity β_{NF} denotes the near-field dispersion multiplier, which, from the difference between the path lengths r_1^i and r_N^i, is expressed as

$$\beta_{NF} = \sqrt{\alpha^2 + \alpha\,\cos\theta_i + \frac{1}{4}} - \sqrt{\alpha^2 - \alpha\,\cos\theta_i + \frac{1}{4}} \tag{2.5}$$

where

$$\alpha = \frac{F}{L} \tag{2.6}$$

and where F is the focal length of the array such that the source range is equal to the focal distance, that is, $r_i = F$. The near-field dispersion, denoted γ_{NF}, is given by

$$\gamma_{NF} = B\Delta\tau_{NF} = \frac{BL}{c}\beta_{NF} \tag{2.7}$$

where, again, the quantity β_{NF} denotes the near-field time-delay or dispersion multiplier in this case. In comparing Equation (2.3) and Equation (2.7), it is seen that the far-field and near-field dispersions differ only by their respective multipliers β_{FF} and β_{NF}. Figure 2.5 shows a plot of β_{FF} and β_{NF} versus angle of incidence for values of $\alpha = 0.2$ to 2 (i.e., focal lengths $0.2L$ to $2L$). From this figure, it is seen that the near-field dispersion approaches the value of the far-field dispersion for source range distances greater than approximately one aperture diameter ($\alpha \geq 1$). Clearly, at source range distances such that $\alpha \leq 0.5$ (one-half aperture diameter), the near-field dispersion is significantly different from the far-field dispersion. Thus, for this simple dispersion model, it is expected that near-field dispersion will be similar to far-field dispersion at source range distances greater than one aperture diameter.

For a phased array system with a large instantaneous bandwidth, to keep the scanned beam pointing angle fixed, it is necessary to use true time-delay phase shifters. Under far-field conditions, for a linear array with element spacing d and scan angle θ_s as measured from the axis of the array, the electrical phase shift between elements is given by

$$\Delta\Phi_{\text{elements}} = \frac{2\pi}{\lambda} d\cos\theta_s = \frac{2\pi f}{c} d\cos\theta_s. \tag{2.8}$$

To compensate for the linear phase shift versus frequency that occurs from the element spacing and scan angle, the time-delay unit must provide a linear phase shift versus frequency. A time-delay phase shifter can be designed using coaxial lines controlled by diodes. For example a six-bit time-delay phase shifter provides the following phase states for each of the bits: $(0°, 180°)$, $(0°, 90°)$, $(0°, 45°)$, $(0°, 22.5°)$, $(0°, 11.25°)$, and $(0°, 5.63°)$. It is desired to provide an interelement time delay, denoted ΔL as computed below. In a

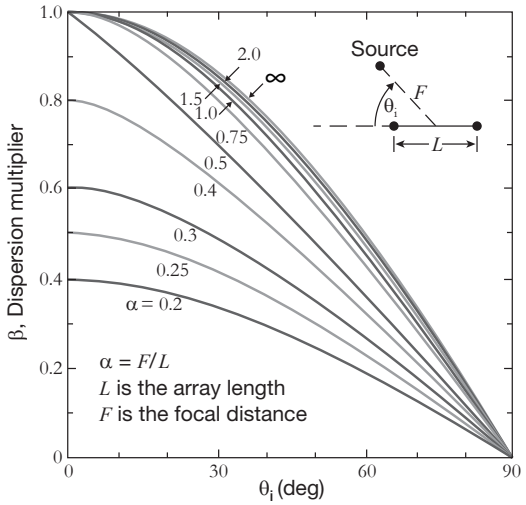

Figure 2.5 Dispersion multiplier as a function of source incidence angle for various source range distances.

coaxial transmission line, the effective electrical phase shift of the line $\Delta\Phi_{\text{line}}$ is expressed in terms of the physical length and the relative dielectric constant ϵ_r of the material filling the coaxial region as

$$\Delta\Phi_{\text{coaxial line}} = \frac{2\pi f}{c}\Delta L_{\text{electrical}} = \frac{2\pi f}{c}\Delta L_{\text{physical}}\sqrt{\epsilon_r}. \tag{2.9}$$

Setting Equation (2.9) equal to Equation (2.8) yields

$$\frac{2\pi f}{c}\Delta L_{\text{physical}}\sqrt{\epsilon_r} = \frac{2\pi f}{c}d\cos\theta_s \tag{2.10}$$

It follows that the required physical length of true-time-delay coaxial line to compensate for the element spacing d and scan angle θ_s from the axis of the linear array is given by

$$\Delta L_{\text{physical}} = \frac{d}{\sqrt{\epsilon_r}}\cos\theta_s. \tag{2.11}$$

The next section describes a number of phased array beamformer architectures.

2.2.3 Beamformer Architectures

Consider Figure 2.6, which shows a linear phased array antenna that generates a radiation main beam at an angle θ_s that can be scanned over a field

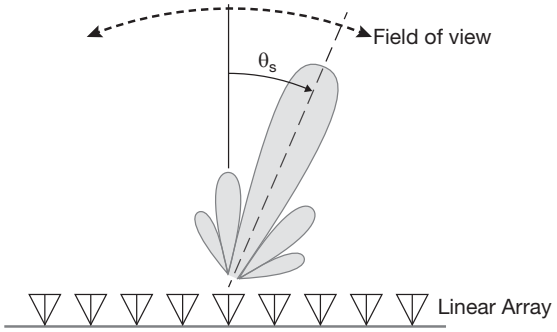

Figure 2.6 Example linear array antenna with the main beam steered to the angle θ_s.

of view. Depending on the spacing in wavelengths between the antenna elements and the phase progression along the array, the scan angle θ_s can vary from 0° (broadside direction) to $\pm 90^\circ$ (endfire direction). The broadside array will typically use one-half wavelength spacing, whereas the endfire array will typically use one-quarter wavelength spacing. The challenge in phased array antenna development is to design the array so that main beam scanning can be achieved, with desired radiation characteristics such as gain, power density on transmit, sensitivity on receive, beamwidth, sidelobe levels, polarization, and reflection coefficient. A block diagram showing an active beamformer arrangement for a transmitting linear phased array antenna is depicted in Figure 2.7. An RF source has its signal divided into a number of paths by using a power divider circuit. Each output port from the power divider is connected to a phase shifter device that applies a linear phase shift from element to element such that the array main beam is scanned to a desired angle. In this transmitting phased array example, prior to the divided and phase-shifted signal reaching each of the antenna radiating elements, amplification is applied such that a desired power level is achieved at each array element. With this beamforming architecture where an RF amplifier is connected to each antenna element, the antenna is referred to as an active electronically scanned array (AESA). If an amplifier at each element is not present, the antenna architecture is referred to then as a passive electronically scanned array (PESA). The phase-steered and amplified RF signal from each antenna element is coherent and additive in the scan angle direction. However, as a consequence of typical one-half-wavelength spacing between the array antenna elements, a portion of the signal from each array element is electromagnetically coupled (curved arrow in Figure 2.7) into the surrounding array elements, and the coupled signal generally becomes stronger/weaker as the distance to the coupled element decreases/increases, respectively. This

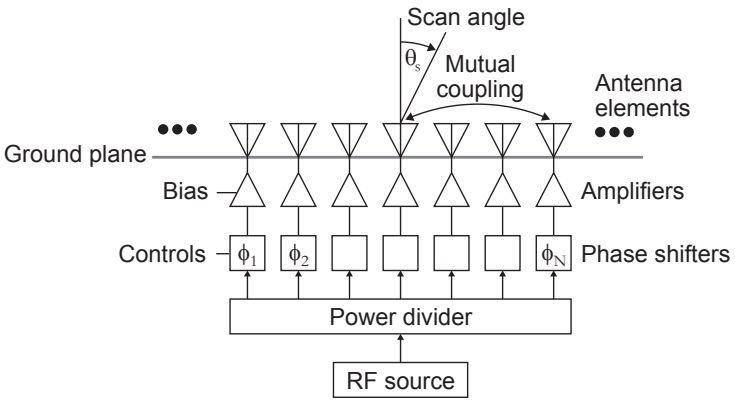

Figure 2.7 Block diagram for a transmitting active electronically scanned array (AESA) antenna. The main beam is steered using phase shifters.

coupled signal is referred to as array mutual coupling, which is a complex quantity.

If phase shifters with constant phase versus frequency are used to steer the main beam, then the main beam pointing angle will be frequency dependent. In a phased array application in which wideband waveforms are involved, time delays with linear phase delay versus frequency need to be used as depicted in Figure 2.8. Time delays can be implemented at intermediate

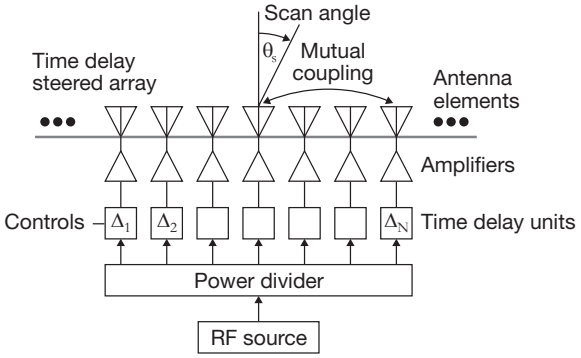

Figure 2.8 Example beamformer for time-delay steered linear array.

frequencies (IF), radio frequencies (RF), or optical frequencies (OF).

The contrast between an active electronically scanned array (AESA) and a passive electronically scanned array (PESA) is shown in Figure 2.9. In Figure 2.9a, a transmit/receive (T/R) module is connected to each antenna

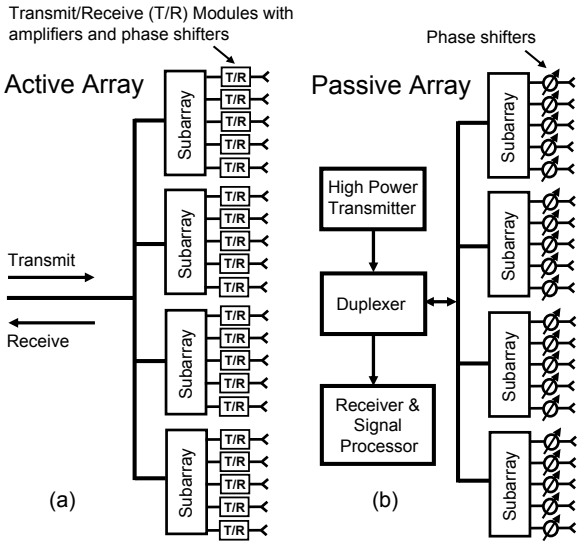

Figure 2.9 Example array beamforming architectures. a) Active electronically scanned array (AESA). b) Passive electronically scanned array (PESA).

element. The T/R module contains amplifiers, phase shifters, and other components including switches, circulators, and filters. In a large phased array aperture with thousands of antenna elements, if a T/R module (or a small percentage of modules) fails to operate properly, the array experiences only a minor degradation in performance. In Figure 2.9b, only a phase shifter is connected to the antenna elements. The PESA requires a high-power transmitter that represents the possibility of a single-point failure. The duplexer can be implemented by either a high-power switch or a circulator and represents another possible single-point failure for a PESA. In Figure 2.9, both types of arrays shown are corporate fed with transmission lines that can be, for example, coaxial cables, microstrip lines, or waveguides. In some phased arrays, to eliminate the RF transmission lines a space-fed beamformer approach is used.

Consider Figure 2.10 that shows two types of space-fed phased array architectures [47, p.13.47], namely, a space-fed lens and a space-fed reflectarray. In Figure 2.10a, a horn antenna generates a spherical wavefront that illuminates a passive lens phased array aperture with phase shifters located between the front and back antenna elements. The phase shifters are calibrated and adjusted to remove the spherical wavefront curvature and generate a flat wavefront to steer the radiation to a desired scan angle. In

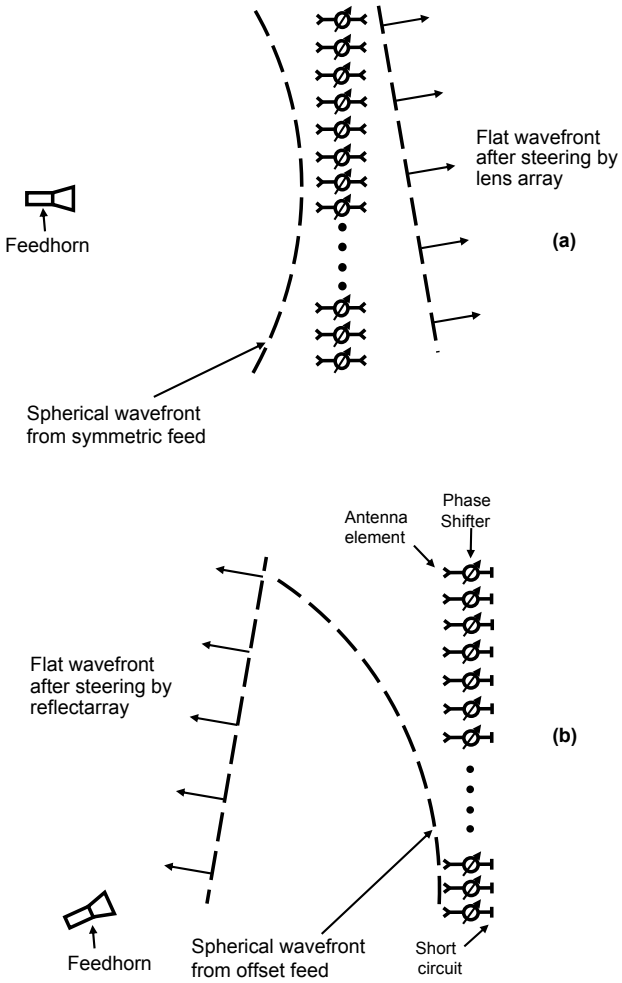

Figure 2.10 Beamforming architectures. a) Space-fed lens array. b) Reflectarray.

Figure 2.10b, the reflect array has a single group of antenna elements facing the feedhorn. In this case, the spherical wavefront illuminates the antenna elements and the received signals pass through a calibrated phase shifter, and then these signals are reflected by a short circuit. The reflected signal passes backward through the phase shifter and the resultant wavefront is now flat and steered to a desired scan angle.

A fully digital beamforming receive array architecture is shown in Figure 2.11. With this digital architecture, the RF signals received by the

antenna elements are downverted to a lower intermediate frequency (IF) (and possibly to a lower baseband frequency) where analog to digital (A/D) converters are used to digitize the received signals. Digital signal processing is used to detect and analyze received signals as well as to provide adaptive nulling to reduce jamming effects. A hybrid analog/digital beamforming phased array architecture is shown in Figure 2.12. In this case, RF phase shifters are used as part of several RF subarrays where the subarray RF output is then downconverted and digitized.

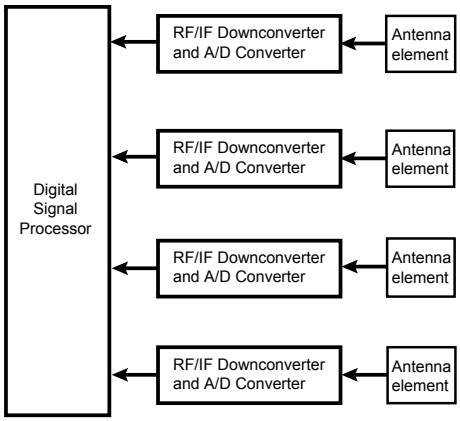

Figure 2.11 Example fully-digital array beamforming architecture.

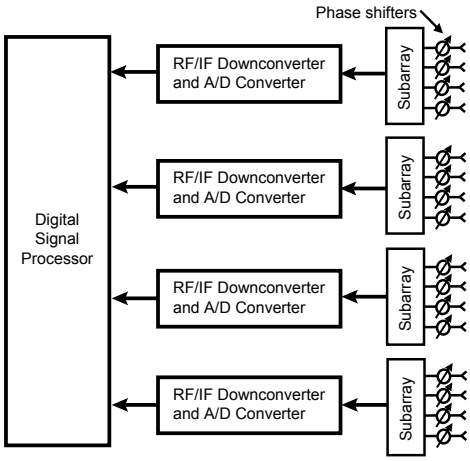

Figure 2.12 Example hybrid analog/digital phased array beamforming architecture.

To achieve a large aperture phased array that can electronically scan a beam over a large field of view, say $\pm 60^{\circ}$, normally a large number (many thousands) of antenna elements is often required. An alternate geometry is to have a smaller phased array feed a single reflector or series of reflectors [82–ref:fenn-richardson-1980], which can provide limited electronic scanning of a few degrees. For example, Figure 2.13 shows an example of an offset Gregorian reflector system with confocal paraboloids and a planar phased array feed, which has been investigated by Fitzgerald in [83]. This dual reflector geometry allows the aperture of the phased array to be magnified by the ratio of the primary to secondary reflector focal lengths. As the phased array scans from broadside, to avoid subreflector spillover the subreflector diameter must be oversized.

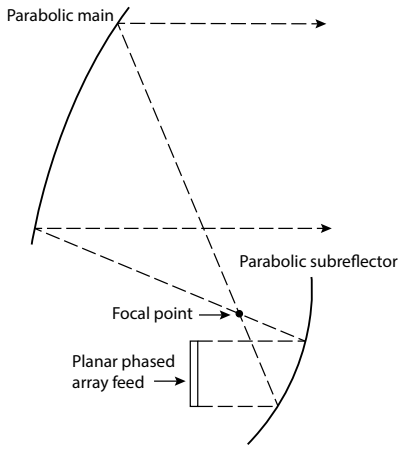

Figure 2.13 Example offset Gregorian reflector system with confocal paraboloids and planar phased array feed. Redrawn from Fitzgerald [83].

In some applications, multiple phase centers are desired for example in displaced phased center antenna (DPCA) designs for radar clutter cancellation [43–47] as in Figure (2.14). In this DPCA architecture, there are two independent beamformers that generate two movable phase centers. The phase center spacing is varied by using attenuators in the receive modules to shut off received signals from groups of antenna elements. In general, the DPCA array will contain a total of N antenna elements that are used to form the receive main channel. In addition to these N elements, a guard band of passively terminated elements can be used to provide impedance matching to the active elements and/or isolation from ground plane edges to improve radiation pattern match between the displaced phase centers. For this two phase center example, the received RF signal output from each of the array antenna

elements is first split into two paths that are weighted and then summed in separate power combiners to form two independent subarray main channels (or moveable phase centers). In each element channel is a transmit/receive module, which has amplitude and phase control. The amplitude control can be used to provide a desired low-sidelobe array illumination function as well as to achieve phase-center displacement. The modules utilize phase shifters, which are used to steer the main beam to a desired angle. Let $\boldsymbol{W}_A = (W_1^A, W_2^A, \cdots, W_N^A)^T$ and $\boldsymbol{W}_B = (W_1^B, W_2^B, \cdots, W_N^B)^T$, where ^{T} is transpose, denote the array element weight vectors (including quantization and random errors) of phase centers A and B, respectively (superscript T means transpose). To effect phase center displacement, a portion of each subarray is turned off by applying a large value of attenuation for a group of antenna elements. This amplitude weighting will essentially move the electrical phase center to the center of gravity for the remaining elements. Thus, there is an effective number of elements actually used in receiving signals in phase centers A and B and are denoted as N_A and N_B, respectively. Let a wavefront (either planar or spherical) due to the jth source (either clutter or jammer), be impressed across the array, which results in a set of array element received voltages denoted as the complex vector $\boldsymbol{v} = v_1^j, v_2^j, \cdots, v_N^j$. The channel covariance matrix $\boldsymbol{R}$ consisting of clutter and jamming signals is formed from the correlation of the received voltage vector as $\boldsymbol{v}^\dagger \boldsymbol{v}$, where † is complex conjugate transpose, from which adaptive array weights (amplitude

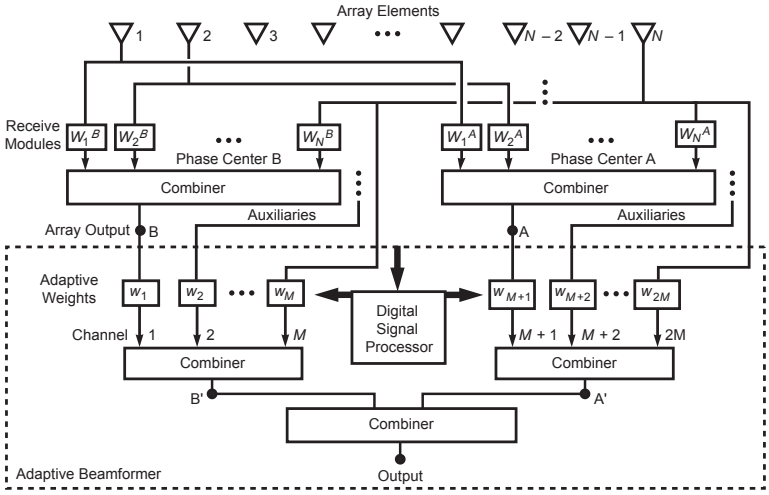

Figure 2.14 Example beamformer design for a displaced phased array antenna with adaptive signal processing to cancel both radar clutter and interference.

and phase) are generated. The number of adaptive channels per phase center is denoted M. For a sidelobe canceller $M = 1 + N_{aux}$ where N_{aux} is the number of auxiliary channels in each phase center. This adaptive system has M degrees of freedom in each phase center and, thus, a total of $2M$ degrees of freedom.

A simplified block diagram for an example transmit/receive (T/R) module is shown in Figure 2.15. By means of switches and proper timing, the phase shifter shown is used for both transmit and receive. In this diagram, the switches are adjusted for the transmit mode. To protect the low noise amplifier (LNA) the combination of a circulator and a switched-in load provides high isolation from the high-power transmit signal. Many different architectures exist for T/R modules, which are designed based on the system requirements. For example, in some radar applications the T/R modules must allow for dual polarization and multiple phase center operation.

Recently, there has been considerable research in the area of multiple-input multiple-output (MIMO) arrays [63-65]. Figure 2.16 shows an artist's concept where a MIMO antenna system uses multiple transmit antennas and multiple receive antennas to help mitigate multipath effects in communications and radar applications.

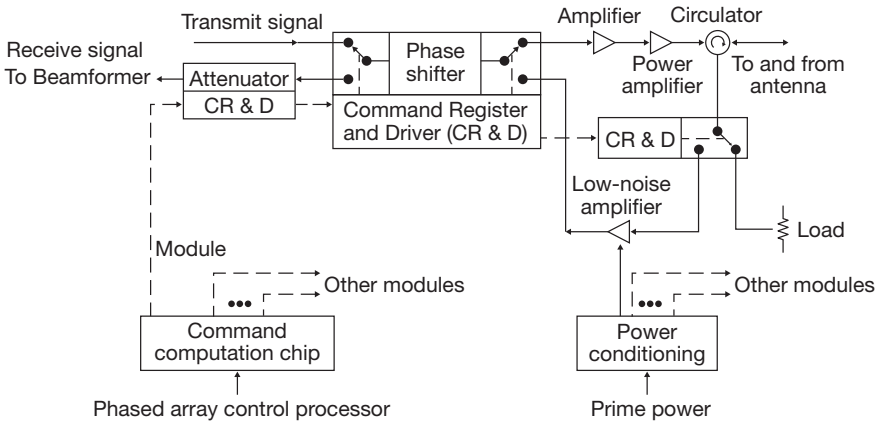

Figure 2.15 Example transmit/receive (T/R) module block diagram.

Now that a number of beamforming architectures have been described, the next section describes basic array theory, which considers phased arrays composed of isotropic antenna elements.

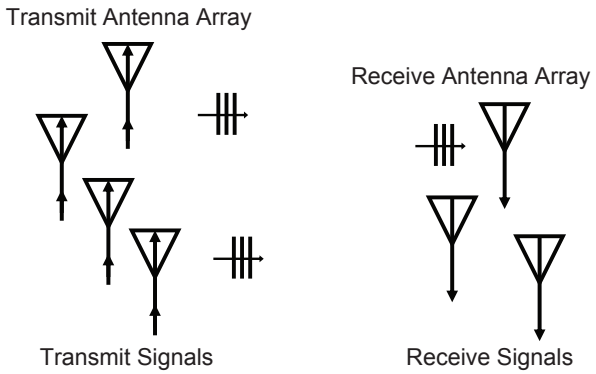

Figure 2.16 Artist's concept of a MIMO array system that consists of multiple transmit antennas and multiple receive antennas.

2.2.4 Arrays of Isotropic Antenna Elements

Consider the case of a two-dimensional N-element phased array of isotropic radiating antenna elements with the $e^{j\omega t}$ time-harmonic dependence of the currents suppressed, where $\omega = 2\pi f$ is the radian frequency, t is time, and f is the frequency. Referring to the geometry in Figures 2.2 and 2.3, the far-field array radiation pattern, or array factor (AF) in this case, in terms of spherical coordinates (θ, ϕ), can be expressed by superposition of the N radiating currents as

$$\mathrm{AF}(\theta, \phi) = \sum_{n=1}^{N} i_n e^{j\Psi_n} \tag{2.12}$$

where i_n is the complex current induced in the nth radiating element, (x_n, y_n, z_n) are the coordinates of the nth array element, and

$$\Psi_n = k \sin\theta (x_n \cos\phi + y_n \sin\phi) + k z_n \cos\theta \tag{2.13}$$

where $k = 2\pi/\lambda$ is the wavenumber with λ denoting the wavelength. In order to electrically scan the main beam to a particular scan angle (θ_s, ϕ_s), the phasing Ψ_{ns} of the element currents is set to be the negative value (phase conjugate) of Ψ_n evaluated at (θ_s, ϕ_s), that is,

$$\Psi_{ns} = -k \sin\theta_s (x_n \cos\phi_s + y_n \sin\phi_s) - k z_n \cos\theta_s. \tag{2.14}$$

The array currents i_n are expressed in complex form as

$$i_n = A_n e^{j\Psi_{ns}} \tag{2.15}$$

where A_n is the current amplitude illumination of the nth array element. Equation (2.15) is general in the sense that amplitude and phase quantization and random errors of the transmit/receive modules can be included. Furthermore, Equations (2.13) and (2.14) allow errors in element positioning $(\Delta x_n, \Delta y_n, \Delta z_n)$ to be taken into account. The array factor for the electrically scanned array can be written as

$$\text{AF}(\theta, \phi) = \sum_{n=1}^{N} A_n e^{j(\Psi_n + \Psi_{ns})}. \tag{2.16}$$

If the current amplitudes are assumed to be uniform with unity amplitude, that is, $A_n = 1$, then when the observation angles (θ, ϕ) are equal to the scan angles (θ_s, ϕ_s), it follows from Equations (2.13) and (2.14) that $\Psi_n + \Psi_{ns} = 0$ and the array factor is evaluated as

$$\text{AF}(\theta_s, \phi_s) = \sum_{n=1}^{N} 1 = N \tag{2.17}$$

That is, for uniform illumination at scan-angle direction (θ_s, ϕ_s) the amplitude of the array factor is equal to the number of array elements.

For a linear array oriented along the x axis, both y_n and z_n are zero. Then with $\phi = 0^\circ$ using Equations (2.13) and (2.14), Equation (2.16) simplifies to

$$\text{AF}(\theta, \theta_s) = \sum_{n=1}^{N} A_n e^{jkx_n(\sin\theta - \sin\theta_s)}. \tag{2.18}$$

It should be noted that for the array factor given by Equation (2.18), since ϕ was set to zero, the angles θ and θ_s are allowed to take on positive and negative values.

A number of phased array illumination functions [5] can be used to control the sidelobe levels and beamwidth of phased array antennas. Some common phased array illumination functions include uniform, binomial, triangular, cosine, Dolph-Chebyshev [89–91], and Taylor [92]. For example, uniformly illuminated arrays are typically used for transmit applications and have a narrow beam with high first sidelobes (on the order of -13 dB relative to the main beam maximum value). Compared to uniform illumination, the binomial illumination has a broader beam with no sidelobes. The Dolph-Chebyshev illumination has low sidelobes at a constant, prescribed, level. The Taylor illumination generates a narrow beam with controlled low sidelobes. Amplitude and phase quantization and random errors in the illumination function can cause the sidelobes to degrade.

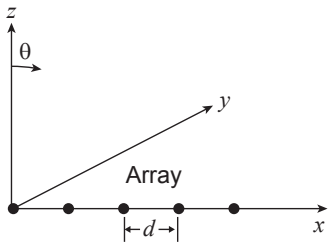

Figure 2.17 Linear array antenna of isotropic elements (point sources) spaced along the x axis.

Consider now a linear array with isotropic elements (point sources) that have spacing d along the x axis as shown in Figure 2.17. For the uniform illumination case $A_n = 1$, let the element position be quantified by $x_n = (n-1)d$ and then let

$$u = kd(\sin\theta - \sin\theta_s). \tag{2.19}$$

Equation (2.18) can now be simplified and then expanded as

$$\mathrm{AF}(u) = \sum_{n=1}^{N} e^{jnu} = 1 + e^{ju} + e^{j2u} + \cdots + e^{j(N-1)u} \tag{2.20}$$

Now multiply both sides of Equation (2.20) by e^{ju} which yields

$$\mathrm{AF}e^{ju} = e^{ju} + e^{j2u} + e^{j3u} + \cdots + e^{jNu} \tag{2.21}$$

Subtracting Equation (2.21) from (2.21) and rearranging yields

$$\mathrm{AF} = \frac{e^{jNu} - 1}{e^{ju} - 1} \tag{2.22}$$

Factoring the exponentials in the numerator and denominator and converting from exponentials to sines yields

$$\mathrm{AF} = e^{j(N-1)u/2}\frac{\sin(Nu/2)}{\sin(u/2)} \tag{2.23}$$

The maximum value of the array factor occurs at the main beam peak, which occurs when the denominator goes to zero, and this condition exists

when $u = 2m\pi$ for $m = 0, \pm 1, \pm 2, \cdots$. Applying L'Hôpital's rule to the ratio of the sine terms in Equation (2.23), evaluated at $u = 2m\pi$, yields the maximum value of N for the array factor, which can be used to normalize AF to unity. Calculated radiation patterns for linear arrays with uniform, Dolph-Chebyshev, and Taylor illumination functions are shown below. Note: the MATLAB Phased Array System Toolbox (http://www.mathworks.com.) provides tapered array illumination functions for one and two-dimensional arrays. For example, the MATLAB statement <taper=chebwin(N,SLLdB)> generates the Dolph-Chebyshev illumination for an N-element linear array with sidelobe levels equal to SLLdB. Similarly, in MATLAB the Taylor illumination statement for N elements is <taper=taylorwin(N,nbar,SLLdB)>, where nbar is a parameter that affects the number of transition sidelobes adjacent to the main beam. A typical value of nbar is equal to five (5) that provides an illumination that is readily implemented in practice.

As an example of the array factor for an ideal uniformly illuminated array, consider an eight-element linear array of isotropic array elements with $\lambda/2$ element spacing, as depicted in Figure 2.18. For this eight-element

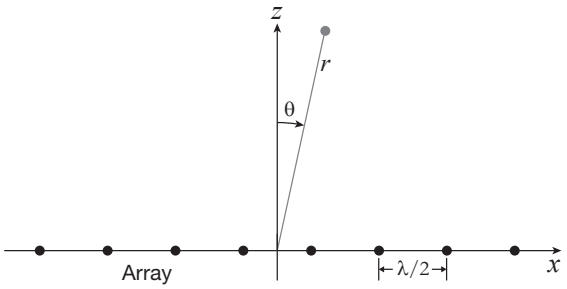

Figure 2.18 Example eight-element linear array antenna with isotropic elements.

array, using Equation (2.18), the array factors for uniform illumination for scan angles of $\theta_s = 0^\circ$ and $\theta_s = 45^\circ$ are shown in Figure 2.19. Next, the normalized array factor magnitude for a larger, 16-element linear array of isotropic antenna elements with uniform amplitude illumination scanned to $\theta = 30^\circ$ is shown in Figure 2.20, and the corresponding phase of the array factor is shown in Figure 2.21. It is observed that the phase alternates between 0° and 180° as the angle varies across the sidelobes. Since the phase center of the array is located at the origin $x = 0$, the far-field phase is flat over the main beam. Note that there are $N - 2$ number of sidelobes for the N element linear array. The uniformly illuminated array has high sidelobe magnitudes, starting with the first sidelobe which is at the -13 dB level. To reduce the sidelobes to a constant level, the Dolph-Chebshev taper for -40 dB uniform

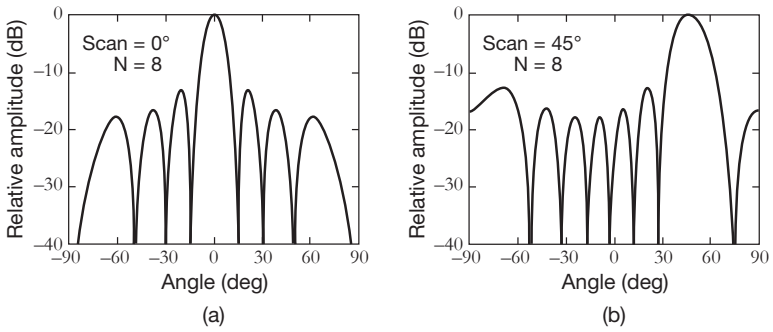

Figure 2.19 Calculated array factor for an eight-element linear array antenna with isotropic elements. (a) Scan angle 0°, and (b) scan angle 45°.

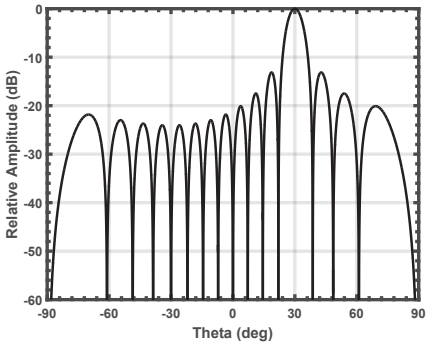

Figure 2.20 Calculated array factor magnitude for a 16-element linear array antenna with isotropic elements. Uniform amplitude illumination with $\theta_s = 30^\circ$.

sidelobes was applied to the 16-element linear array and the radiation pattern is shown in Figure 2.22. In this case, to achieve lower sidelobes with the Dolph-Chebyshev taper, the far-field main beam has broadened compared to the radiation pattern for the uniformly illuminated array in Figure (2.20). Again for a 16-element array, the case of a Taylor taper (-40 dB, nbar=5) is shown in Figure 2.23, which is very similar to the Dolph-Chebyshev pattern except for the first few sidelobe levels. If the array elements are not isotropic radiators, but instead have a radiation pattern that depends on angle, then the array radiation pattern $P(\theta, \phi)$ can be expressed as the product of the array factor and the element radiation pattern (denoted $p_e(\theta, \phi)$) as

$$P(\theta, \phi) = p_e(\theta, \phi)\text{AF} \tag{2.24}$$

where it is assumed that all array elements have the same radiation pattern.

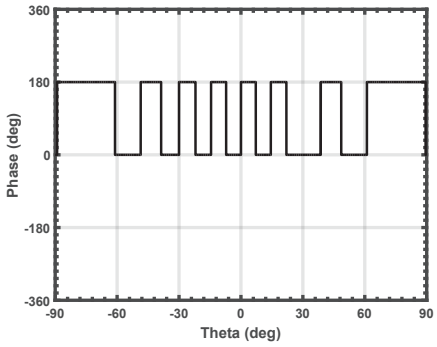

Figure 2.21 Calculated array factor phase for a 16-element linear array antenna with isotropic elements. Uniform amplitude illumination with $\theta_s = 30^\circ$.

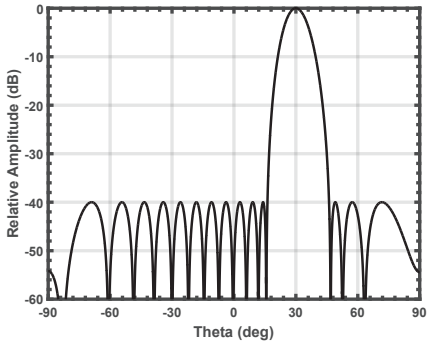

Figure 2.22 Calculated array factor magnitude for an sixteen-element linear array antenna. Dolph-Chebyshev taper (40 dB) with scan angle $\theta_s = 30^\circ$.

2.2.5 Polarized Array Far-Zone Electromagnetic Fields

The previous section considered the far-field radiation for isotropic elements and the theory ignored polarization. In this section, the effect of polarization of the elements is included in the theoretical formulation. In Equation (1.269), the far-field vector current moment $\boldsymbol{f}(\theta, \phi)$ was defined in spherical coordinates in terms of a volume integral of the source current $\boldsymbol{J}(\boldsymbol{r'})$ as

$$\boldsymbol{f}(\theta, \phi) = f_r \hat{\boldsymbol{r}} + f_\theta \hat{\boldsymbol{\theta}} + f_\phi \hat{\boldsymbol{\phi}} = \int_V \boldsymbol{J}(\boldsymbol{r'}) e^{jk\hat{\boldsymbol{r}}\cdot\boldsymbol{r'}} dv', \tag{2.25}$$

Referring generally to Figure 2.2, consider now a two-dimensional periodic array case, in which the array antenna elements are Hertzian (short)

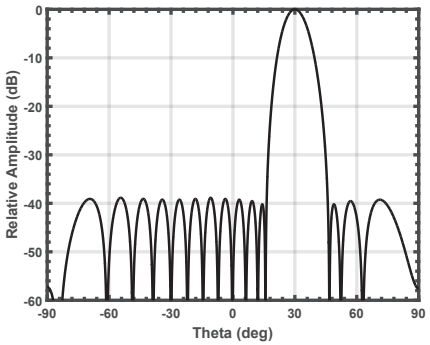

Figure 2.23 Calculated array factor magnitude for an sixteen-element linear array antenna. Taylor taper (40 dB, nbar=5) with scan angle 30°.

electric dipoles of length l and arbitrary polarization $\hat{\boldsymbol{p}}$ that are located in a rectangular lattice parallel to the xy plane at $z = z_o$. Assume that the array has N_x elements in the x direction with interelement spacing d_x and N_y elements in the y direction with interelement spacing d_y. The total number of elements is equal to $N = N_x N_y$. Referring to Equation (2.14), let the electrical phasing of the nth Hertian dipole array element with position (x_n, y_n, z_o) for the scan direction (θ_s, ϕ_s) be given by

$$\Psi_{ns} = -kx_n \sin\theta_s \cos\phi_s - ky_n \sin\theta_s \sin\phi_s - kz_o \cos\theta_s. \tag{2.26}$$

In this case, the current density function $\boldsymbol{J}(\boldsymbol{r}')$ can be expressed in terms of the array element amplitude $A_n = I_n l$ and phase shift Ψ_{ns} as

$$\boldsymbol{J}(\boldsymbol{r}') = \hat{\boldsymbol{p}} \sum_{n=1}^{N} I_n l e^{j\Psi_{ns}} \delta(x' - x_n)\delta(y' - y_n)\delta(z' - z_o). \tag{2.27}$$

The propagation unit vector in terms of the spherical coordinate angles (θ, ϕ) is given by

$$\hat{\boldsymbol{r}} = \hat{\boldsymbol{x}} \sin\theta \cos\phi + \hat{\boldsymbol{y}} \sin\theta \sin\phi + \hat{\boldsymbol{z}} \cos\theta \tag{2.28}$$

and the source vector $\boldsymbol{r}'$ is given by

$$\boldsymbol{r}' = \hat{\boldsymbol{x}} x' + \hat{\boldsymbol{y}} y' + \hat{\boldsymbol{z}} z'. \tag{2.29}$$

The dot product of the propagation direction unit vector and the source vector is equal to

$$\hat{\boldsymbol{r}} \cdot \boldsymbol{r}' = x' \sin\theta \cos\phi + y' \sin\theta \sin\phi + z' \cos\theta \tag{2.30}$$

Substituting Equation (2.27) into Equation (2.25) yields

$$\boldsymbol{f}(\theta,\phi) = \int_V \hat{\boldsymbol{p}} \sum_{n=1}^{N} I_n l e^{j\Psi_{ns}} \delta(x'-x_n)\delta(y'-y_n)\delta(z'-z_o) e^{jk\hat{\boldsymbol{r}}\cdot\boldsymbol{r}'} dv' \tag{2.31}$$

and using Equation (2.30) yields

$$\boldsymbol{f} = \hat{\boldsymbol{p}} \sum_{n=1}^{N} A_n e^{jk[x_n(\sin\theta\cos\phi - \sin\theta_s\cos\phi_s) + y_n(\sin\theta\sin\phi - \sin\theta_s\sin\phi_s) + z_o(\cos\theta - \cos\theta_s)]} \tag{2.32}$$

The far-zone electric and magnetic fields in terms of the far-field vector current moment $\boldsymbol{f}$ are determined from Equations (1.279) and (1.282) as

$$\boldsymbol{E}_{\text{FF}} = -j\omega\mu \frac{e^{-jkr}}{4\pi r}(\hat{\boldsymbol{\theta}} f_\theta + \hat{\boldsymbol{\phi}} f_\phi) \tag{2.33}$$

$$\boldsymbol{H}_{\text{FF}} = -jk \frac{e^{-jkr}}{4\pi r}(\hat{\boldsymbol{\phi}} f_\theta - \hat{\boldsymbol{\theta}} f_\phi). \tag{2.34}$$

The electric and magnetic fields are then computed for elements with a particular polarization $\hat{\boldsymbol{p}}$ by evaluating Equation (2.32) and substituting the result in Equations (2.33) and (2.34), respectively. To obtain the desired spherical components of $\boldsymbol{f}$, the unit vector $\hat{\boldsymbol{p}}$ is dotted into the spherical unit vectors $\hat{\boldsymbol{\theta}}$ and $\hat{\boldsymbol{\phi}}$. In the general case, where the nth element current density has an arbitrary distribution, the volume integral in Equation (2.25) can be evaluated either in closed form or by numerical integration to yield the desired far-field vector current moment $\boldsymbol{f}$, from which the electric and magnetic fields can be computed. When the array is a linear array along the x axis at $z_o = 0$, Equation (2.32) simplifies to

$$\boldsymbol{f}(\theta,\phi,\theta_s) = \hat{\boldsymbol{p}} \sum_{n=1}^{N} A_n e^{jkx_n(\sin\theta\cos\phi - \sin\theta_s)}. \tag{2.35}$$

2.2.6 Array Mutual Coupling Effects

Array mutual coupling, or electromagnetic field coupling between array elements, as depicted in Figure 2.24, is an important effect that can strongly influence the radiation pattern of the individual array elements and the overall array patterns. In this diagram, an input signal is transmitted by one antenna element and this signal is received by the surrounding antenna elements. In a large array with periodic element spacing, each antenna element will have a gain that is related to the element unit cell area. Early developments

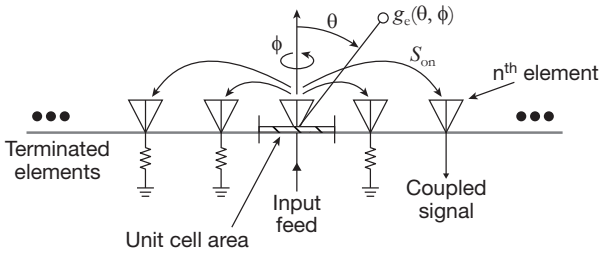

Figure 2.24 Diagram depicting an array with one element driven, with coupling to the surrounding elements.

of phased array radiating-element technology were conducted from 1959 to 1967. Beginning in 1959, there were numerous contributions to the theoretical understanding of phased arrays, particularly the effects of array mutual coupling on the performance of various configurations of dipole and waveguide arrays; for example, the reports and articles by Allen et al. [23–35]. Array mutual coupling is defined as the ratio of the coupled signal voltage in a surrounding array element relative to the input signal voltage in a reference element, when the surrounding elements are terminated in loads matched to the impedance of the transmission line. Letting S_{on} denote the complex mutual coupling between the reference element and the nth array element, the scan reflection coefficient for a planar phased array is calculated as [6, p. 22]

$$\Gamma_o(\theta_s, \phi_s) = \sum_n S_{on} e^{\Psi_{ns}(x_n, y_n, 0)} = \sum_n S_{on} e^{-jk \sin\theta_s (x_n \cos\phi_s + y_n \sin\phi_s)} \tag{2.36}$$

where (x_n, y_n) are the coordinates of the nth array element.

The scanned array impedance mismatch efficiency denoted $\eta_{\text{Z mismatch}}$ is expressed in terms of the reflection coefficient as

$$\eta_{\text{Z mismatch}} = 1 - |\Gamma_o(\theta_s, \phi_s)|^2. \tag{2.37}$$

The scan mismatch loss (ML) in dB can be computed as

$$\text{ML}(\theta_s, \phi_s) = -10 \log_{10} \eta_{\text{Z mismatch}} = -10 \log_{10} \left[1 - |\Gamma_o(\theta_s, \phi_s)|^2\right]. \tag{2.38}$$

When a single antenna element is driven in a passively terminated array (also referred to as an embedded element), the fractional dissipated power (denoted F_p relative to the input power to the element) caused by array mutual coupling is computed as the summation of the magnitude squared of the mutual coupling coefficients, that is [6, p. 22],

$$F_p = \sum_n |S_{on}|^2. \tag{2.39}$$

This fractional dissipated power is the fractional power lost to the terminating loads in the transmission lines connected to the array elements. The array element gain $g_e(\theta, \phi)$ is then the product of the element directivity $D_e(\theta, \phi)$ and the quantity $(1 - F_p)$, that is,

$$g_e(\theta, \phi) = D_e(\theta, \phi)(1 - \sum_n |S_{on}|^2). \tag{2.40}$$

The maximum gain (relative to an isotropic radiator) of an antenna aperture of arbitrary shape is given by the following expression:

$$G_{\text{max}} = 4\pi A_{\text{em}}/\lambda^2 \tag{2.41}$$

where A_{em} is the antenna maximum effective aperture area in square meters and λ is the wavelength in meters. As the frequency increases, the wavelength is reduced according to the following expression,

$$\lambda = c/f \tag{2.42}$$

where c is the speed of light and f is the frequency. Thus, for a fixed aperture dimension in meters, ideally the gain will increase as the frequency increases. However, for a practical antenna aperture, the surface tolerances and, in the case of a phased array, T/R module errors will introduce phase errors and will cause a reduction in antenna gain and an increase in sidelobe levels.

In decibels, the maximum gain of an antenna aperture is given by

$$G_{\text{max, dB}} = 10 \log_{10} G_{\text{max}}. \tag{2.43}$$

The element gain pattern for an infinite array (or very large finite array) is a function of the unit-cell area, the scanned array impedance mismatch efficiency, and the projected aperture [6, pp. 23-25]. The projected aperture will vary as $\cos\theta$, where θ is the angle from broadside. For a general array in the xy plane, the element gain pattern is given by

$$g_e(\theta, \phi) = \frac{4\pi A_e}{\lambda^2} \left[1 - |\Gamma(\theta, \phi)|^2\right] \cos\theta \tag{2.44}$$

where A_e is the unit-cell area occupied by the element. For a rectangular grid array, the element gain pattern is given by

$$g_{er}(\theta, \phi) = \frac{4\pi d_x d_y}{\lambda^2} \left[1 - |\Gamma(\theta, \phi)|^2\right] \cos\theta \tag{2.45}$$

where d_x and d_y are the element spacings in the x and y directions, respectively. For an equilateral-triangle (hexagonal) array lattice, the element gain is expressed as

$$g_{eh}(\theta, \phi) = \frac{2\pi\sqrt{3}b^2}{\lambda^2} \left[1 - |\Gamma(\theta, \phi)|^2\right] \cos\theta \tag{2.46}$$

where b is the side of the equilateral triangle for the element spacing. The scanned radiation pattern, including mutual coupling effects of a large array of thousands of array elements, can be calculated in an approximate manner by first computing the element gain pattern in a large or infinite array and then multiplying it by the array factor given by Equation (2.18).

One of the fundamental challenges in designing a phased array is that significant portions of the microwave field transmitted by one element of the array can be received by the surrounding array antenna elements. This mutual coupling effect, can sometimes lead to surface waves and result in a substantial or total loss of transmitted or received signal in a desired scan direction, which depends on the coherent combination of all of the mutual-coupling signals in the array. This loss of antenna gain is referred to as a blind spot, as is depicted conceptually in Figure 2.25. In this figure, assume

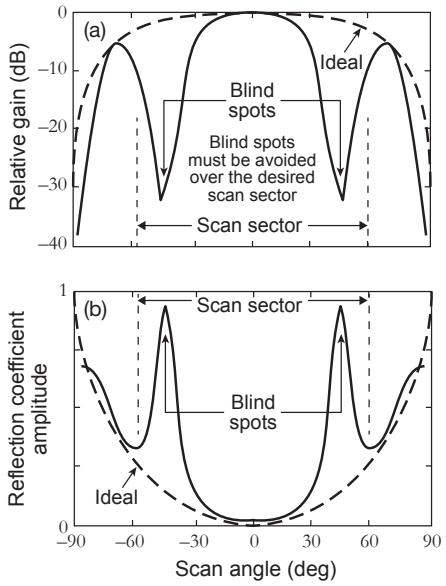

Figure 2.25 Conceptual diagram demonstrating blind spots for a phased array antenna. (a) Element gain pattern and (b) scan reflection coefficient.

that the phased array is designed for maximum gain at broadside (0° scan angle); however, in this artist's concept element gain pattern nulls (minima) are formed at $\pm 45°$. Thus, the full scan sector $\pm 60°$ cannot be covered. The ideal shape of the element gain pattern is a cosine function of the scan angle, when it is assumed that the reflection coefficient amplitude is zero (refer to Equation (2.44) with $|\Gamma| = 0$). When these element gain pattern nulls occur, there will be corresponding peaks occuring in the scan reflection coefficient

amplitude. A phased array blind spot can be described as either a null in the element gain pattern or as a peak tending toward unity in the scanned array reflection coefficient. The amplitudes and phases of the array mutual-coupling signals depend primarily on the type (shape) of the radiating antenna elements, the electrical spacing between the array elements, and the number of surrounding radiating elements. Numerous studies have investigated many different array element designs, taking into account mutual-coupling effects.

In many phased array designs, it is desirable to provide linear-polarized, dual-polarized, or circularly polarized scan coverage with peak gain at broadside and constant gain for any azimuthal (ϕ) angle, as depicted in Figure 2.26.

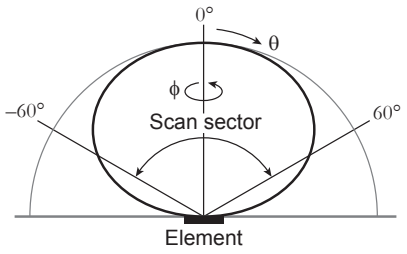

Figure 2.26 Conceptual polar diagram showing an element gain pattern covering a scan sector, with peak radiation at broadside to the plane of the element.

When all of the phase shifters of an array are properly aligned, the array produces a main beam in the desired pointing direction. Generally, the corporate feed (for example, the power divider in Figure 2.7) is designed with minimal crosstalk between channels. However, once the signals have reached the radiating antenna elements, a significant amount of crosstalk in the form of array mutual coupling occurs. As discussed above, the amplitudes and phases of these mutual coupling signals can significantly impact the performance of the phased array. If the array element spacing is around one-half wavelength, substantial amounts of mutual coupling can occur. The mutual coupling amplitude tends to increase as the electrical spacing is reduced. This coupling manifests itself in changes in the element's gain radiation pattern and its scan reflection coefficient. Unless care is taken in the design of the array, undesired blind spots in the scan sector can occur. These blind spots occur at angles where the element gain pattern has a null and the reflection coefficient of the array has a peak close to unity, as was depicted in Figure 2.25. At these blind spots, the transmitted or received signal is significantly reduced in amplitude.

In some applications, it is desirable to place an intentional blind spot or null in directions where it is undesirable to transmit or receive energy [36].

For example, Figure 2.27 shows an example of a broadside-null radiation pattern that could be generated by either a monopole or a uniform-current loop antenna element in an array environment over a ground plane. These types of

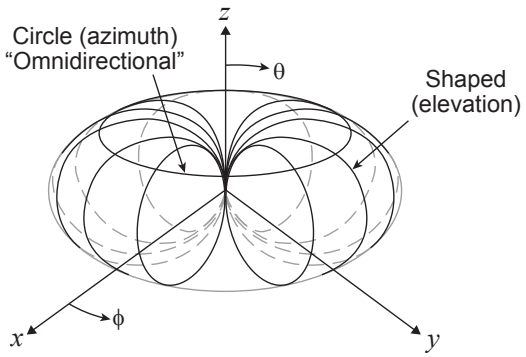

Figure 2.27 Artist depiction of a monopole-type radiation pattern for an element in a phased array antenna.

elements could be useful when broadside radiation is undesirable, such as in reducing broadside clutter and jamming in the case of a spaceborne radar [45, 46]. As the radar beam is steered away from $\theta = 0^\circ$ (broadside) toward $\theta = 60^\circ$, the conventional broadside-peak-type element radiation pattern drops off, but the broadside-null-type element radiation pattern increases to a peak at about $\theta = 45^\circ$ to 50°.

2.2.7 Power Density and Array Gain

The effective isotropic radiated power, denoted EIRP, of an aperture is given by the product of the antenna gain G_{max} and the transmitter power P_t delivered to the antenna as

$$\text{EIRP} = P_t G_t. \tag{2.47}$$

Note that the power transmitted by the antenna is usually less than the power delivered by the generator feeding the antenna. This difference in power is attributed to any RF losses between the generator and the antenna, as well as any mismatch loss resulting from the reflection coefficient at the antenna terminals.

If the overall antenna aperture is assumed to be an array of identical elements, the aperture can be divided into element apertures, which are also referred to as element unit cells (see Figure 2.24). For a large N-element array with an effective aperture A_{em}, the unit cell area is equal to A_{em}/N. If the

embedded element gain patterns are either computed or measured, the array gain can be computed as follows. At range distance r, the embedded-element radiated power density, denoted P_{de}, resulting from the element transmit power (input power to the element) and embedded-element gain is given by [15]

$$P_{de} = \frac{P_{te} g_e(\theta, \phi)}{4\pi r^2} \tag{2.48}$$

and solving for g_e,

$$g_e = 4\pi r^2 \frac{P_{de}}{P_{te}}. \tag{2.49}$$

In the far field, the plane-wave power density of the element is given in terms of the array-element electric field intensity $E_e(\theta, \phi)$ as

$$P_{de} = \frac{|E_e(\theta, \phi)|^2}{120\pi}. \tag{2.50}$$

Substituting Equation (2.50) in Equation (2.49) and simplifying yields

$$g_e(\theta, \phi) = \frac{r^2}{30} \frac{|E_e(\theta, \phi)|^2}{P_{te}}. \tag{2.51}$$

Thus, it follows that

$$|E_e(\theta, \phi)| = \frac{\sqrt{30}}{r} \sqrt{g_e(\theta, \phi)} \sqrt{P_{te}}. \tag{2.52}$$

The element gain pattern, $g_e(\theta, \phi)$ includes the effect of array mutual coupling and mismatch losses.

The transmit power of the nth element is proportional to A_n^2, and using this relation in Equation (2.52) yields

$$|E_{en}(\theta, \phi)| = \frac{\sqrt{30}}{r} \sqrt{g_{en}(\theta, \phi)} A_n. \tag{2.53}$$

To compute the maximum gain of an array at a particular scan angle (θ_s, ϕ_s), by superposition the electric-field contributions for the embedded elements can be summed as

$$E_{\text{array, max}} = \frac{\sqrt{30}}{r} \sum_n \sqrt{g_{en}} A_n. \tag{2.54}$$

Now, following along the lines of Equation (2.51), the array gain can be expressed as

$$G_{\text{array, max}} = \frac{r^2}{30} \frac{|E_{\text{array, max}}|^2}{P_{\text{t, array}}} \tag{2.55}$$

where

$$P_{\text{t, array}} = \sum_{n=1}^{N} A_n^2. \tag{2.56}$$

Substituting Equations (2.54) and (2.56) in Equation (2.55) and simplifying yields

$$G_{\text{array, max}} = \frac{|\sum_{n=1}^{N} \sqrt{g_{en}} A_n|^2}{\sum_{n=1}^{N} A_n^2}. \tag{2.57}$$

For the case of a large array with uniform array illumination (with unity amplitude at each array element), it can be assumed that all of the elements have the same element gain pattern (i.e., $g_{en} = g_e$) and Equation (2.57) reduces to

$$G_{\text{array, max}}(\theta_s, \phi_s) = g_e(\theta_s, \phi_s) N. \tag{2.58}$$

For uniform illumination, the array gain is equal to the element gain times the number of array elements. If the array illumination is not uniform, then a taper efficiency must be included in computing the array gain from the element gain.

To compute the array gain pattern from the element electric field versus angle (θ, ϕ), the element phase pattern $\Psi_{en}(\theta, \phi)$ (either calculated or measured) must be used, that is,

$$E_{en}(\theta, \phi) = |E_{en}(\theta, \phi)| e^{j\Psi_{en}(\theta, \phi)}. \tag{2.59}$$

The array pattern E_{array} is then obtained by the superposition of the individual array element patterns with the desired array amplitude taper and with proper phasing of the array to steer the main beam in a desired direction. Thus,

$$E_{\text{array}}(\theta, \phi) = \sum_{n} E_{en}(\theta, \phi) e^{j\Psi_{ns}} \tag{2.60}$$

or from Equation (2.59)

$$E_{\text{array}}(\theta, \phi) = \sum_{n} |E_{en}(\theta, \phi)| e^{j(\Psi_{en} + \Psi_{ns})} \tag{2.61}$$

and using Equation (2.53) yields

$$E_{\text{array}}(\theta, \phi) = \frac{\sqrt{30}}{r} \sum_{n} \sqrt{g_{en}(\theta, \phi)} A_n e^{j(\Psi_{en} + \Psi_{ns})}. \tag{2.62}$$

The array gain as a function of angle can then be computed from the electric field as

$$G_{\text{array}}(\theta, \phi) = \frac{r^2}{30} \frac{|E_{\text{array}}(\theta, \phi)|^2}{P_{\text{t, array}}}. \tag{2.63}$$

Substituting Equations (2.56) and (2.62) in Equation (2.63) yields the array gain in terms of the element gain and element phase functions and the array illumination, that is,

$$G_{\text{array}}(\theta,\phi) = \frac{|\sum_n \sqrt{g_{en}(\theta,\phi)} A_n e^{j(\Psi_{en}+\Psi_{ns})}|^2}{\sum_n A_n^2}. \tag{2.64}$$

In designing phased array antennas, the maximum electrical spacing d between the elements of a phased array is usually chosen to avoid grating lobes (multiple peaks) according to the following condition [9]

$$\frac{d}{\lambda_h} < \frac{1}{1+\sin|\theta_s|} \tag{2.65}$$

where λ_h is the wavelength at the highest frequency and θ_s is the scan angle from broadside. This equation is readily derived by setting the exponential argument of the array factor in Equation (2.18) equal to -2π and using a positive scan angle and taking the observation angle as the endfire angle -90°, where the grating lobe first occurs, and then solving for d/λ. Typically, the maximum array-element spacing d is more tightly constrained to keep the first null of the endfire grating lobe at the edge of visible space. In practice, the endfire grating lobe should be kept at least one half-power beamwidth away from visible space. For many wide-angle scanning phased arrays, the electrical spacing is often chosen to be close to one-half wavelength for elements on a rectangular or triangular grid.

The next four sections describe methods that are used in computing electromagnetic fields of antennas, including array mutual coupling effects and scattering from obstacles. The discussion begins with a description of electromagnetic field equivalence principles in Section 2.3. In the subsequent section, the reciprocity theorem for antennas is derived. To determine the mutual coupling between an antenna and surrounding antennas in an array or interaction with surrounding structures, a generalized integral equation known as the reaction integral equation is then developed in Section 2.5, which is based on the equivalence principle and the reciprocity theorem for antennas. The reaction integral equation is used in analyzing antennas and phased arrays by the method of moments, which is discussed in Section 2.6.

2.3 Equivalence Principles

To describe the various forms of equivalence principles, assume an antenna with arbitrary impressed electric and magnetic currents, $\boldsymbol{J}_i$ and $\boldsymbol{M}_i$, respectively, in free space (region 1) radiating in the presence of a homogeneous

object (region 2), such as depicted in Figure 2.28(a). For convenience, assume that all currents and fields are time harmonic and the $e^{j\omega t}$ time dependence is suppressed. The surface of the homogeneous object is denoted S and the

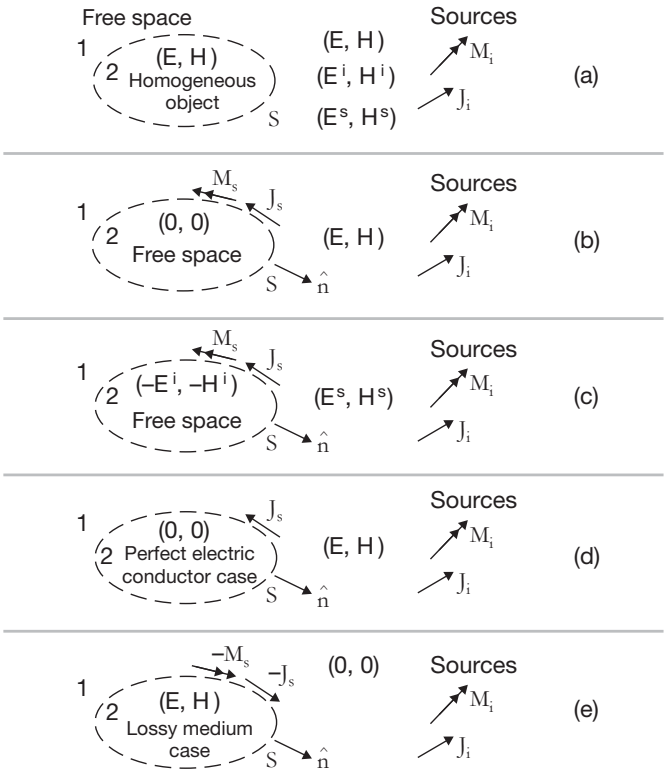

Figure 2.28 Depiction of the surface equivalence principle.

unit normal to the surface is denoted $\hat{\boldsymbol{n}}$, which points from region 2 (internal region) to region 1 (external region). Region 2 is assumed in general to have permittivity ϵ and permeability μ, or the surface of region 2 can be a electric conductor with conductivity σ. These impressed currents ($\boldsymbol{J}_i$ and $\boldsymbol{M}_i$) are assumed to radiate known electric and magnetic fields $\boldsymbol{E}^i$ and $\boldsymbol{H}^i$, respectively, in free space without the homogeneous object present. Also, in the presence of the object, the total electric and magnetic fields generated by the impressed currents are $\boldsymbol{E}$ and $\boldsymbol{H}$, respectively. In the exterior region (region 1), the total electric and magnetic fields are equal to the summation of the incident fields and the fields $\boldsymbol{E}^s$ and $\boldsymbol{H}^s$ scattered by the object. In the interior region (region 2), if the object is not a perfect electric conductor then internal electric and magnetic fields will exist as well.

Equivalent situations can be developed by using surface equivalence principles such as described by Love [94], Schelkunoff [95], Harrington [96], Mautz [97], Arvas [98], and Jakobus [99]. If the electric and magnetic fields are known over the entire surface of a homogeneous object, the object can be replaced by electric and magnetic surface currents radiating in free space, which will produce the correct fields external to the object. For example, if only the fields external to the object are desired, the homogeneous object is equivalently modeled as in Figure 2.28(b) with equivalent electric and magnetic surface currents $\boldsymbol{J}_s$ and $\boldsymbol{M}_s$ placed on the surface S, that is,

$$\boldsymbol{J}_s = \hat{\boldsymbol{n}} \times [\boldsymbol{H}^1 - \boldsymbol{H}^2] \tag{2.66}$$

$$\boldsymbol{M}_s = [\boldsymbol{E}^1 - \boldsymbol{E}^2] \times \hat{\boldsymbol{n}} \tag{2.67}$$

where the superscripts 1 and 2 on $\boldsymbol{E}$ and $\boldsymbol{H}$ indicate the side of S in which the fields are evaluated. In Figure 2.28(c), the same surface currents from Figure 2.37(b) produce the desired scattered fields $\boldsymbol{E}^s$ and $\boldsymbol{H}^s$ in the exterior region and the negative of the incident fields in the interior region.

In the case of a perfect electrically conducting object, the equivalent magnetic surface current is zero ($\boldsymbol{M}_s = 0$), since the total electric field is zero at the surface by the boundary condition. As depicted in Figure 2.28(d), the equivalent electric surface current $\boldsymbol{J}_s$ is assumed to generate scattered fields $\boldsymbol{E}^s$ and $\boldsymbol{H}^s$ as

$$\boldsymbol{E}^s = \boldsymbol{E} - \boldsymbol{E}^i \tag{2.68}$$

$$\boldsymbol{H}^s = \boldsymbol{H} - \boldsymbol{H}^i. \tag{2.69}$$

In the interior region of a perfect conductor, the total vector electric and magnetic fields must be zero; thus, the following relation must hold:

$$\boldsymbol{E}^s = -\boldsymbol{E}^i \tag{2.70}$$

$$\boldsymbol{H}^s = -\boldsymbol{H}^i. \tag{2.71}$$

In this case, where the scatterer is a perfect electric conductor, the total tangential electric field on the outer surface is zero ($\boldsymbol{E}_{\tan} = 0$), and the total tangential magnetic field on the outer surface is equal to the induced current density $\boldsymbol{H}_{\tan} = \boldsymbol{J}_s$. On the outer surface of the perfect conductor, the tangential components of the incident and scattered magnetic fields are equal ($\boldsymbol{H}^s_{\tan} = \boldsymbol{H}^i_{\tan}$). In the technique known as physical optics, the induced electric surface current density is determined from Equation (2.66) as $\boldsymbol{J}_s = 2\hat{\boldsymbol{n}} \times \boldsymbol{H}^i$ [5, pp. 337–338]. The scattered electric field can then be computed from the surface currents $\boldsymbol{J}_s$ over the illuminated region of the surface by using Equation (1.205) as a surface integral. Finally, consider the case where

the object is a homogeneous lossy medium as depicted in Figure 2.28(e). In this case, the negative of the equivalent currents produce the desired fields inside the object in which the dielectric and magnetic properties of the material must be used in computing the internal fields. Now that the necessary equivalence conditions have been described, the next step in developing a method of moments formulation is to derive the reciprocity theorem.

2.4 Reciprocity Theorem

Let there be two sets of electric and magnetic sources $\boldsymbol{J}_a$, $\boldsymbol{M}_a$ and $\boldsymbol{J}_b$, $\boldsymbol{M}_b$, which produce the fields $\boldsymbol{E}_a$, $\boldsymbol{H}_a$ and $\boldsymbol{E}_b$, $\boldsymbol{H}_b$, respectively. The Lorentz reciprocity theorem [5] is derived in the following manner starting with Maxwell's equations in time-harmonic form as:

$$\boldsymbol{\nabla}\times\boldsymbol{E}_a = -\boldsymbol{M}_a - j\omega\mu'\boldsymbol{H}_a \tag{2.72}$$

$$\boldsymbol{\nabla}\times\boldsymbol{H}_a = \boldsymbol{J}_a + j\omega\epsilon'\boldsymbol{E}_a \tag{2.73}$$

$$\boldsymbol{\nabla}\times\boldsymbol{E}_b = -\boldsymbol{M}_b - j\omega\mu'\boldsymbol{H}_b \tag{2.74}$$

$$\boldsymbol{\nabla}\times\boldsymbol{H}_b = \boldsymbol{J}_b + j\omega\epsilon'\boldsymbol{E}_b \tag{2.75}$$

Now, take the divergence of the difference between the vector cross products of the fields from the a and b sources and apply the vector identity

$$\boldsymbol{\nabla}\cdot(\boldsymbol{A}\times\boldsymbol{B}) = \boldsymbol{B}\cdot(\boldsymbol{\nabla}\times\boldsymbol{A}) - \boldsymbol{A}\cdot(\boldsymbol{\nabla}\times\boldsymbol{B}). \tag{2.76}$$

which yields after eliminating the terms involving the dot products of the vector fields

$$-\boldsymbol{\nabla}\cdot(\boldsymbol{E}_a\times\boldsymbol{H}_b - \boldsymbol{E}_b\times\boldsymbol{H}_a) = \boldsymbol{E}_a\cdot\boldsymbol{J}_b - \boldsymbol{H}_a\cdot\boldsymbol{M}_b - \boldsymbol{E}_b\cdot\boldsymbol{J}_a + \boldsymbol{H}_b\cdot\boldsymbol{M}_a \tag{2.77}$$

which is the Lorentz reciprocity theorem in differential form. Now, taking the volume integral of both sides of Equation (2.77) and applying the divergence theorem to the left-hand side yields

$$\int_V \boldsymbol{\nabla}\cdot\boldsymbol{A}dv = \oint_S \boldsymbol{A}\cdot d\boldsymbol{s} \tag{2.78}$$

yields

$$\begin{array}{l} -\oint_S \boldsymbol{\nabla}\cdot(\boldsymbol{E}_a\times\boldsymbol{H}_b - \boldsymbol{E}_b\times\boldsymbol{H}_a)\cdot d\boldsymbol{s} = \\ \int_V(\boldsymbol{E}_a\cdot\boldsymbol{J}_b - \boldsymbol{H}_a\cdot\boldsymbol{M}_b - \boldsymbol{E}_b\cdot\boldsymbol{J}_a + \boldsymbol{H}_b\cdot\boldsymbol{M}_a)dv \end{array} \tag{2.79}$$

which is the integral form of the Lorentz reciprocity theorem.

The integral form of the Lorentz reciprocity theorem in a source-free region is expressed as

$$\iint_S (\boldsymbol{E}_a \times \boldsymbol{H}_b - \boldsymbol{E}_b \times \boldsymbol{H}_a) \cdot d\boldsymbol{s} = 0. \tag{2.80}$$

That is, if the surface S does not enclose sources, the volume integral on the right side of Equation (2.79) is zero. Next, consider the case of a radiating antenna with source currents contained within a finite volume. In this case, if the surface S is allowed to extend to infinity, the antenna radiated fields at infinity in the surface integral are attenuated to zero and now the left side of Equation (2.79) is zero. Thus, the reciprocity theorem for antennas can be expressed as

$$\iiint_V (\boldsymbol{E}_a \cdot \boldsymbol{J}_b - \boldsymbol{H}_a \cdot \boldsymbol{M}_b - \boldsymbol{E}_b \cdot \boldsymbol{J}_a + \boldsymbol{H}_b \cdot \boldsymbol{M}_a) dv = 0 \tag{2.81}$$

where the volume integration extends over all space including the antenna source currents in the constrained finite volume.

2.5 Reaction Integral Equation

The generalized reaction integral equation is derived from the reciprocity theorem for antennas expressed by Equation (2.81). By definition, the reaction of field a on source current b is given by [101, 102, p. 118]

$$< a, b > = \iiint_V (\boldsymbol{E}_a \cdot \boldsymbol{J}_b - \boldsymbol{H}_a \cdot \boldsymbol{M}_b) dv. \tag{2.82}$$

By reciprocity, the reaction of field a on source current b is the same as the reaction of field b on source current a, that is,

$$< a, b > = < b, a > . \tag{2.83}$$

Let a test source with currents $\boldsymbol{J}_m$ and $\boldsymbol{M}_m$ be placed within the scatterer volume, which has now been replaced by the original ambient medium. These currents radiate the fields $\boldsymbol{E}_m$ and $\boldsymbol{H}_m$ in the ambient medium. It is desired to compute the reaction between the test source currents with the total electric and magnetic fields within the volume within the surface S. Since the total electric and magnetic fields are equal to zero within the scatterer, the reaction between the test source and total fields is zero. Thus, we can write

$$\iiint_m \boldsymbol{J}_m \cdot (\boldsymbol{E}^s + \boldsymbol{E}^i) dv = 0 \tag{2.84}$$

$$\iiint_m \boldsymbol{M}_m \cdot (\boldsymbol{H}^s + \boldsymbol{H}^i) dv = 0. \tag{2.85}$$

To be consistent with the minus sign in the reciprocity theorem, the difference between Equations (2.84) and (2.85) is taken, which results in

$$\iiint_m (\boldsymbol{J}_m \cdot \boldsymbol{E}^s - \boldsymbol{M}_m \cdot \boldsymbol{H}^s) dv + \iiint_m (\boldsymbol{J}_m \cdot \boldsymbol{E}^i - \boldsymbol{M}_m \cdot \boldsymbol{H}^i) dv = 0 \tag{2.86}$$

where the volume integration is over the volume of the test source. In terms of surface integrals and surface currents, Equation (2.86) becomes

$$\iint_S (\boldsymbol{J}_{ms} \cdot \boldsymbol{E}^s - \boldsymbol{M}_{ms} \cdot \boldsymbol{H}^s) ds + \iint_S (\boldsymbol{J}_{ms} \cdot \boldsymbol{E}^i - \boldsymbol{M}_{ms} \cdot \boldsymbol{H}^i) ds = 0 \tag{2.87}$$

where $m = 1, 2, 3, \cdots, N$, $\boldsymbol{J}_{ms}$ is the mth electric surface current, and $\boldsymbol{M}_{ms}$ is the mth magnetic surface current. Equation (2.87) is the desired reaction integral equation. The next section shows how Equation (2.87) can be solved using the method of moments.

2.6 Method of Moments

The reaction integral equation expressed by Equation (2.87) can be solved using the method of moments for the vector currents, from which quantities such as the antenna input impedance and gain radiation patterns can be computed. In general, when one is applying the method of moments, each antenna analysis geometry requires special considerations [102–109]. By using the equivalence principle as shown in Figure 2.28, the moment method solution is considerably simplified for antenna problems involving only electric conductors and, thus, only vector electric currents $\boldsymbol{J}$ are assumed nonzero, and $\boldsymbol{M} = 0$.

In the method of moments, the unknown vector electric surface current density $\boldsymbol{J}_s$ is expressed initially as a summation of n surface currents $\boldsymbol{J}_n$ where

$$\boldsymbol{J}_n = i_n B_n \tag{2.88}$$

in which the current coefficients i_n are complex in general and they are the N unknown coefficients to be determined, and there are N vector basis functions $\boldsymbol{b}_n$ (also referred to as expansion or interpolation functions). Thus, the unknown vector surface current density can be expressed as

$$\boldsymbol{J}_s = \sum_{n=1}^{N} \boldsymbol{J}_n = \sum_{n=1}^{N} i_n \boldsymbol{b}_n. \tag{2.89}$$

It is desired to react an mth vector testing current source $\boldsymbol{t}_m$ (also referred to as a vector weighting source) with the radiated field from the nth basis function $\boldsymbol{b}_n$. The electric field from the nth basis function can be expressed as the scattered field $\boldsymbol{E}_n^s(\boldsymbol{J}_n)$, where it is understood that the electric field is determined by an integral operating on the nth electric-current function $\boldsymbol{J}_n$. This integral operation can be expressed as

$$L_{\text{op}}(\boldsymbol{J}_n) = \boldsymbol{E}_n^s(\boldsymbol{J}_n) \tag{2.90}$$

where L_{op} is the integral operator. For example, the electric field $\boldsymbol{E}_n^s(\boldsymbol{J}_n)$ can be determined using a two-step approach in which the integral in Equation (1.197) is evaluated and is then substituted into Equation (1.192). The integral operation on the current is a linear operator, that is, superposition applies and scalar quantities within the integral can be factored out of the integral. It is noted that the total scattered field is given by

$$\boldsymbol{E}^s = \sum_{n=1}^{N} \boldsymbol{E}_n^s(\boldsymbol{J}_n). \tag{2.91}$$

Thus, it follows from Equation (2.87) that

$$\sum_{n=1}^{N} \iint_S \boldsymbol{t}_m \cdot \boldsymbol{E}_n^s(\boldsymbol{J}_n) ds + \iint_S \boldsymbol{t}_m \cdot \boldsymbol{E}^i ds = 0, \tag{2.92}$$

which is the electric-field integral equation (EFIE), which is valid for open and closed surfaces. Using Equations (2.89) and (2.91) and the linearity of the integral operator, it follows that Equation (2.92) can be rewritten as

$$\iint_S \boldsymbol{t}_m \cdot \boldsymbol{E}^i ds = -\sum_{n=1}^{N} i_n \iint_S \boldsymbol{t}_m \cdot \boldsymbol{E}_n^s(\boldsymbol{b}_n) ds \tag{2.93}$$

where the nth complex current coefficient i_n has been factored out of the double integration. The basis functions $\boldsymbol{b}_n$ can be chosen typically to have an overlapping piecewise sinusoidal or triangular amplitude distribution, and these basis functions are known to provide an accurate representation of currents that flow on antennas and surrounding structures. In the case of a piecewise-sinusoidal basis function of arbitrary unit vector orientation $\hat{\boldsymbol{p}}$ along an arbitrary p axis (for example, p could be the z axis), the basis function takes the following form [83, 85],

$$\boldsymbol{b}_n(p) = \hat{\boldsymbol{p}}_n \frac{\sin k(p - p_{n-1})}{\sin k(p_n - p_{n-1})} \qquad p_{n-1} \le p \le p_n \tag{2.94}$$

$$\boldsymbol{b}_n(p) = \hat{\boldsymbol{p}}_n \frac{\sin k(p_{n+1} - p)}{\sin k(p_{n+1} - p_n)} \qquad p_n \leq p \leq p_{n+1} \tag{2.95}$$

where k is the wavenumber. Similarly, triangular basis functions have the following form

$$\boldsymbol{b}_n(p) = \hat{\boldsymbol{p}}_n \frac{p - p_{n-1}}{p_n - p_{n-1}} \qquad p_{n-1} \leq p \leq p_n \tag{2.96}$$

$$\boldsymbol{b}_n(p) = \hat{\boldsymbol{p}}_n \frac{p_{n+1} - p}{p_{n+1} - p_n} \qquad p_n \leq p \leq p_{n+1} \tag{2.97}$$

Figures 2.29 and 2.30 show examples for the case where there are 5 nodes and 3 overlapping (piecewise) sinusoidal and triangular basis functions along the p axis, respectively. The coefficient a_n that multiplies each basis function b_n is determined by solving a set of simultaneous equations as described below.

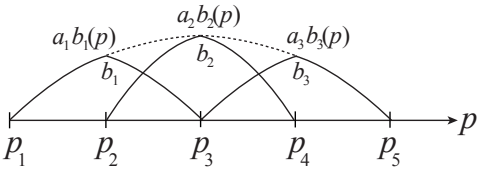

Figure 2.29 Depiction of the piecewise sinusoidal basis functions for the case of 5 nodes.

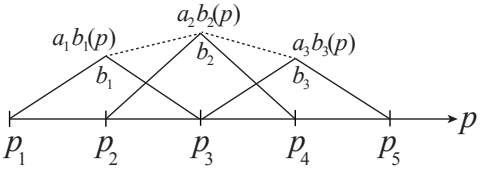

Figure 2.30 Depiction of the piecewise triangular basis functions for the case of 5 nodes.

Now, define the general mth element of the voltage matrix as

$$V_m = \iint_S \boldsymbol{t}_m \cdot \boldsymbol{E}^i ds \tag{2.98}$$

and the general mnth element of the mutual impedance matrix as

$$Z_{mn} = -\iint_S \boldsymbol{t}_m \cdot \boldsymbol{E}_n^s(\boldsymbol{b}_n) ds. \tag{2.99}$$

Note: since the testing and basis functions are typically normalized by dividing by the terminal current, the units of the voltage matrix and impedance matrix are in volts and ohms, respectively. A Galerkin's formulation is obtained by using testing functions $\boldsymbol{t}$ that are equal to the basis functions $\boldsymbol{b}$. It now follows that

$$V_m = \sum_{n=1}^{N} i_n Z_{mn} \quad m = 1, 2, \ldots, N \tag{2.100}$$

where V_m is the voltage excitation and Z_{mn} is the open-circuit mutual impedance between current elements m and n, expressed as the matrix $\boldsymbol{Z}$. These expressions can be combined in terms of the applied voltage excitation vector $\boldsymbol{V}$, the impedance matrix $\boldsymbol{Z}$, and unknown current vector $\boldsymbol{i}$ to give the matrix equation

$$\boldsymbol{V} = \boldsymbol{Z}\boldsymbol{i}; \tag{2.101}$$

that is,

$$\begin{aligned} V_1 = &\quad Z_{11}i_1 + Z_{12}i_2 + \cdots + Z_{1N}i_N \\ V_2 = &\quad Z_{21}i_1 + Z_{22}i_2 + \cdots + Z_{2N}i_N \\ &\quad . \\ &\quad . \\ &\quad . \\ V_N = &\quad Z_{N1}i_1 + Z_{N2}i_2 + \cdots + Z_{NN}i_N. \end{aligned} \tag{2.102}$$

The unknown current coefficients $i_n, n = 1, 2, \ldots, N$ are found by matrix inversion from

$$\boldsymbol{i} = \boldsymbol{Z}^{-1}\boldsymbol{V} \tag{2.103}$$

or by lower-triangular/upper-triangular (LU) matrix decomposition, for example. For phased array antenna analysis, the current responses for multiple beam-steering voltage vectors are readily computed since the impedance matrix inversion or LU decomposition needs to be performed only once for a given antenna geometry.

The voltage source model chosen at the antenna terminals is typically a delta gap generator. This model assumes that the impressed electric field exists only at the antenna element terminals. In this case, the voltage generators can be defined to be one volt in amplitude at the terminals of each array element.

If a general skew-symmetric lattice is assumed for the dipole array as depicted in Figure 2.39, then the required steering phase for an element in the

pth row and qth column of the array is related to the main beam scan direction (θ_s, ϕ_s) by

$$\psi_x = kqd_x \sin\theta_s \cos\phi_s \tag{2.104}$$

$$\psi_y = k(pd_y + q\Delta y) \sin\theta_s \sin\phi_s \tag{2.105}$$

so

$$V_{pq}^g = e^{-j(\psi_x + \psi_y)} \tag{2.106}$$

defines the generator voltages. Note: in Figure 2.31, an artist's concept of an example of three overlapping dashed piecewise triangles, superimposed on the upper right dipole, represent the basis functions that can be used to determine the unknown current coefficients.

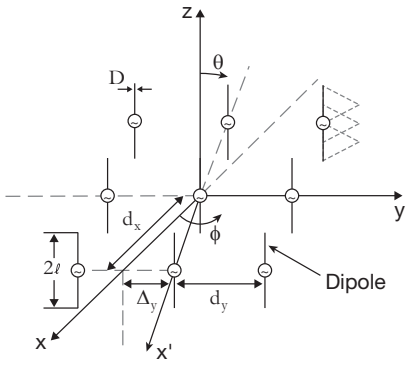

Figure 2.31 Dipole phased array antenna arranged in a two-dimensional skew-symmetric lattice.

In the present form, Equation (2.106) assumes a uniform amplitude excitation. It should be noted, however, that any amplitude taper can be used. To generate low sidelobes, some common array amplitude tapers include Taylor, Chebyshev, cosine, and triangular [5]. The various tapers would be implemented by multiplying the pqth array element terminal voltage of the voltage matrix by the appropriate amplitude coefficient A_{pq}.

The array elements are assumed to be excited by constant incident-power sources. This type of feeding is referred to as free excitation because the complex voltage across the terminals of the array element can vary according to the scan conditions [11]. The equivalent circuit for the mth element port $(m = 1, 2, \ldots, N)$ is shown in Figure 2.32. The effect of the generator (or load) impedance (denoted Z^g) is included in the driven elements in the voltage excitation matrix, that is,

$$V_m = V_m^g - i_m Z^g. \tag{2.107}$$

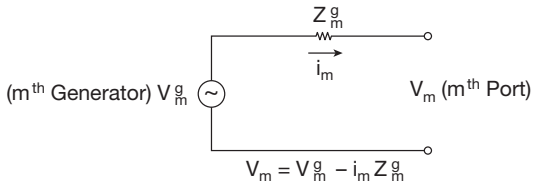

Figure 2.32 Equivalent circuit model for the mth array element port.

For an electrically scanned phased array, all generators are on; hence, every V^g is nonzero. For a single-element excited array, only one voltage generator is nonzero, which can be assumed equal to one volt. For both types of arrays, the value of Z^g can be chosen to be 50 ohms, corresponding to the generator impedance, which is the same as the characteristic impedance of the feedline (usually 50 ohms). The unknown currents $i_n, n = 1, 2, \ldots, N$ are determined from

$$\boldsymbol{i} = [\boldsymbol{Z}']^{-1}\boldsymbol{V}^g \tag{2.108}$$

where

$$\boldsymbol{Z}' = \boldsymbol{Z} + \boldsymbol{I}Z_m^g \tag{2.109}$$

where $\boldsymbol{I}$ represents the identity matrix. The current coefficients i_n determined from the method-of-moments solution are used in the computation of the array radiation patterns. Recent improvements in the speed and reduced memory requirements for moment method analysis has been achieved using the fast multipole method [109, pp. 209–253, 110]

In the case of the mth array element, the input impedance, denoted Z_{in}^m, is computed from

$$Z_{\text{in}}^m = \frac{V_m}{i_m} \tag{2.110}$$

where V_m is the voltage across the terminals of the array antenna element and i_m is the current at the terminals of the mth element determined by the method of moments. Equations (2.18) to (2.20) can be used to determine the radiated fields from the moment method basis functions. The far-zone electric field can be computed from the superposition of the radiated electric fields from the moment-method-determined currents computed from Equation (2.108).

The scanned array reflection coefficient is obtained from the scanned array input impedance by the use of the following equation,

$$\Gamma(\theta_s, \phi_s) = \frac{Z_{\text{in}}(\theta_s, \phi_s) - Z_c}{Z_{\text{in}}(\theta_s, \phi_s) + Z_c} \tag{2.111}$$

where (θ_s, ϕ_s) is the scan direction, and Z_c is the characteristic impedance of the feed line.

2.7 Broadside and Endfire Linear Arrays of Hertzian Dipoles

The radiation pattern of a single z-directed Hertzian dipole in free space was shown in Figure 1.49. Referring now to Figure 2.33, consider two 5-element array cases in which the antenna elements are z-directed Hertzian dipoles where the arrays are designed for either broadside beam direction or endfire beam direction. Figure 2.34 shows the FEKO moment method simulated 3D

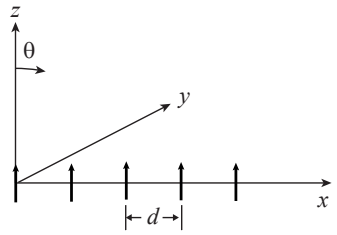

Hertzian Dipole Array

Figure 2.33 Linear array of Hertzian dipole antennas with spacing d along the x axis.

relative gain pattern for a 5-element broadside array of z-directed Hertzian dipoles with $\lambda/2$ element spacing along the x axis, and Figure 2.35 is a polar diagram of the radiation pattern in the xy plane. Figure 2.36 is the moment method simulated 3D relative gain pattern for a 5-element endfire array of z-directed Hertzian dipoles with $\lambda/4$ element spacing along the x axis, and Figure 2.37 is a polar diagram of the radiation pattern in the xy plane.

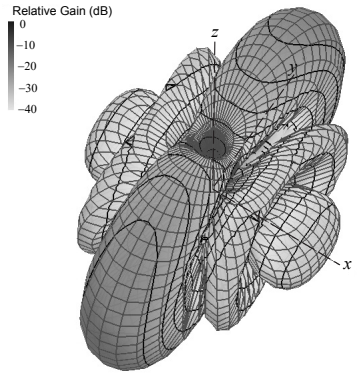

Figure 2.34 Moment method simulated 3D relative gain pattern for a 5-element broadside array of z-directed Hertzian dipoles with $\lambda/2$ element spacing along the x axis.

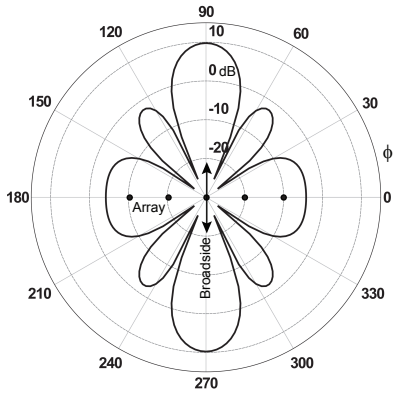

Figure 2.35 Moment method simulated polar absolute gain pattern in the xy plane for a 5-element broadside array of z-directed Hertzian dipoles with $\lambda/2$ element spacing.

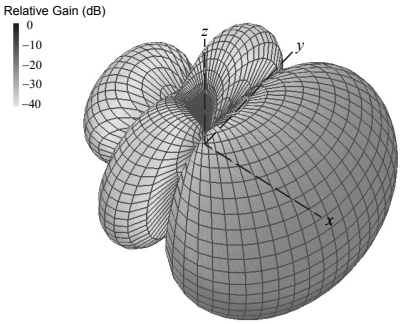

Figure 2.36 Moment method simulated 3D relative gain pattern for a 5-element endfire array of z-directed Hertzian dipoles with $\lambda/4$ element spacing along the x axis.

2.8 Example of 2D Array Mutual Coupling Effects

Consider now a single $\lambda/2$ dipole oriented along the z axis in free space as shown in Figure 2.38. The moment method simulated normalized 3D gain pattern (vertically polarized, θ component) for this dipole antenna is shown in Figure 2.39. To show the effect of array mutual coupling on the element gain pattern, let the same dipole now be embedded in an 11×11 resistively terminated array as depicted in the FEKO model shown in Figure 2.40. Due to array mutual coupling, in Figure 2.41 the moment method simulated normalized gain pattern (vertically polarized, θ component) of the center dipole element now has the peak gain shifted symmetrically upward and

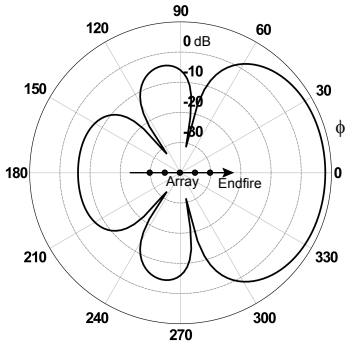

Figure 2.37 Moment method simulated polar absolute gain pattern in the xy plane for a 5-element endfire array of z-directed Hertzian dipoles with $\lambda/4$ element spacing.

downward from the xy plane, and thus has reduced relative gain in the xy plane. There is a natual null in the direction of the z axis, which means the dipole element in this orientation has a natural blind spot.

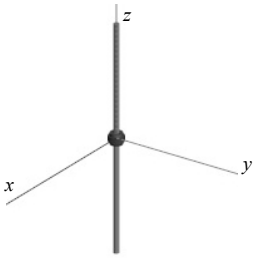

Figure 2.38 Moment method model for a $\lambda/2$ dipole in free space.

2.9 Swept-Back Dipole Array Measurements and Simulations

2.9.1 Introduction

Dipole phased array antennas are commonly used in radar and communications applications, and these elements have been researched extensively in the literature [23–26, 32–34, 48, 111–116]. Linear dipoles can be designed to radiate or receive linear polarization. Crossed-dipoles can operate with dual polarization or circular polarization. Dipoles typically have straight arms that are parallel to a conducting ground plane; however, for wide-angle pattern

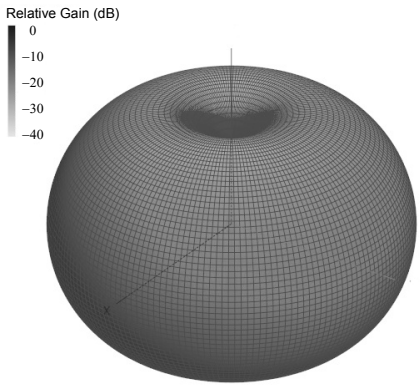

Figure 2.39 Moment method simulated normalized 3D gain pattern (G_θ component) for a single $\lambda/2$ dipole in free space.

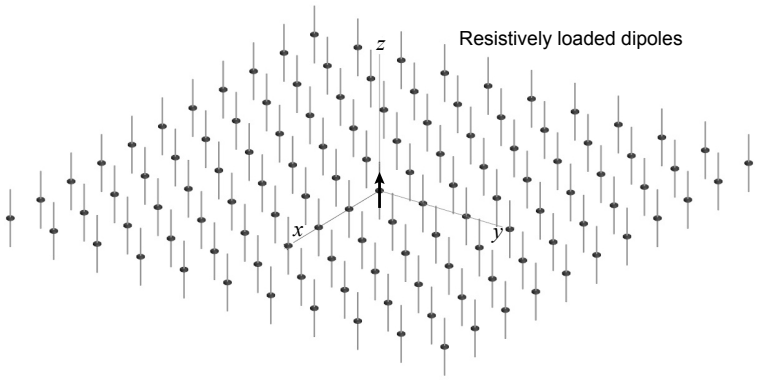

Figure 2.40 Moment method model for an 11 $\times 11$ array of $\lambda/2$ dipoles with the center element driven and the surrounding elements terminated in resistive loads.

coverage for a single element, or wide-angle scanning for an array, the dipole arms can be swept downward toward the ground plane forming a V-shaped antenna [21, 43 p.300,]. The element gain pattern for finite phased arrays of dual-polarized crossed V-dipole (pronounced *Vee* dipole) antennas above a ground plane is addressed in this chapter, both with computer simulation and by measurements. The method of moments is used to compute the center element gain pattern of a finite array of V-dipoles. An experimental 19-element passively terminated planar array is described, and mutual coupling, center element scanned array reflection coefficient, and center-element gain pattern measurements are described here.

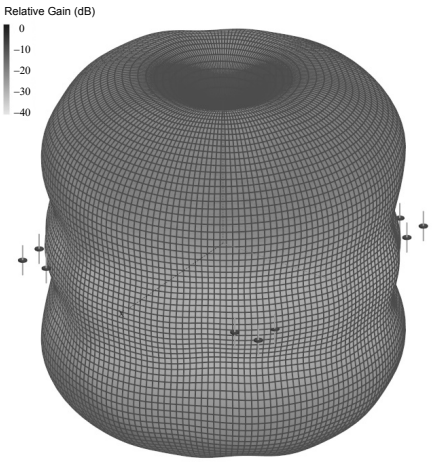

Figure 2.41 Moment method simulated normalized 3D gain pattern (G_θ component) for an 11 $\times 11$ array of $\lambda/2$ dipoles with the center element driven and the surrounding elements terminated in 100Ω resistive loads.

It is known that for certain radiating elements blind spots [1] can occur in large planar phased-array antennas. In phased-array antenna applications, a blind spot is identified with an array element pattern null (minimum) or a scanned array reflection coefficient with amplitude equal to unity. For example, a blind spot has been observed in a balun-fed straight-arm dipole phased array [5, 6]. A center-fed straight dipole with balun is shown in Figure 2.42(a). The dipole has a half length denoted l, with strip width w, and is located a distance h above a conducting ground plane. The balun in this case is a balanced two-wire line that is shorted at the ground plane, which for a one-quarter wavelength transmission line, appears as an open-circuit at the feed terminals to restrict current flow on the balun. When this element is situated in a large phased array with the main beam steered away from broadside, the illumination of the balun from the array elements is not symmetrical, and unbalanced currents can flow on the balun. The presence of induced currents flowing on the balun can radiate and in some cases cancel the primary field of the dipole in a certain direction, creating the blind spot. This effect can be reduced or eliminated by tilting the dipole arms toward the ground plane at an angle α forming a V-shaped element [7-9] (see Figure 2.42(b)).

It can be inferred that the tilted arms of the V-dipole act to reduce the amplitude of currents that flow on the balun stubs. If this inference is true, then it can be assumed that the balun and feedline scattering can be ignored in a theoretical analysis of the element gain pattern.

The radiation pattern of a single V-dipole antenna in free space can be

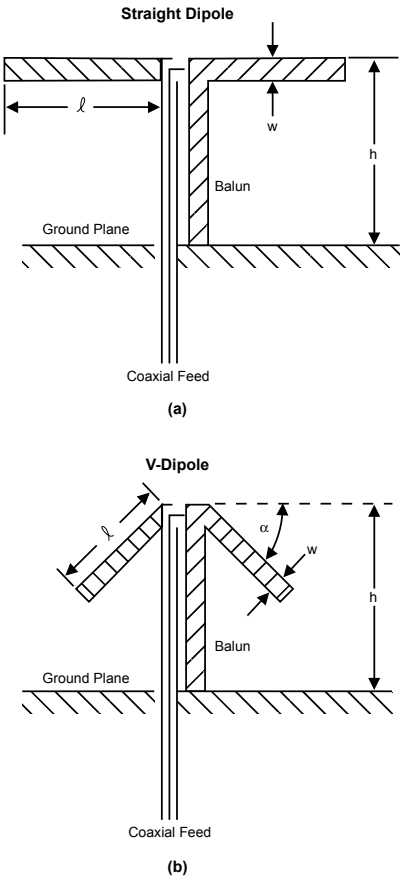

Figure 2.42 Balun-fed dipoles above a ground plane. (a) Straight arm, and (b) V-dipole. © 1988 IEEE [9].

computed as follows. Schelkunoff and Friis have given an expression for the radiation pattern of a dipole arm with sinusoidal current distribution [10]. If it is assumed that the dipole arm is oriented in the z' direction, the radiation field pattern is expressed as

$$E_\theta = \frac{j30i_t}{\sin kl} \frac{e^{jkl\cos\theta'} j\cos\theta' \sin kl - \cos kl}{\sin\theta'} \tag{2.112}$$

where $k = 2\pi/\lambda$, and λ is the wavelength. From the diagram shown in Figure 2.43 for a V-dipole in free space, the pertinent angles θ'_L for the left half dipole and θ'_R for the right half of the V-dipole, in terms of the angles θ and α, are given by

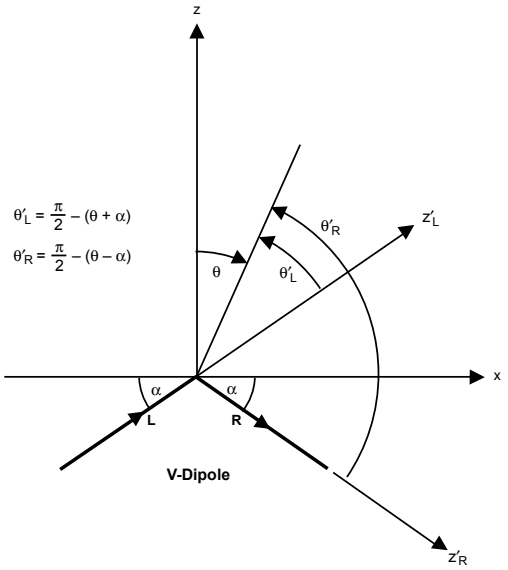

Figure 2.43 V-dipole element in free space.

$$\theta'_L = \frac{\pi}{2} - (\theta + \alpha) \tag{2.113}$$

and

$$\theta'_R = \frac{\pi}{2} - (\theta - \alpha) \tag{2.114}$$

The total electric field due to the left and right halves of the V-dipole antenna is given by

$$E_\theta = E_{\theta_L} + E_{\theta_R} \tag{2.115}$$

Using (2.113) and (2.114) for the left and right halves of the V-dipole in (2.112) can be combined to yield the total E-field for the V-dipole in free space as

$$E_\theta = \frac{j30i_t}{\sin(kl)}\left(\frac{e^{jkl\sin(\theta+\alpha)} - j\sin(\theta+\alpha)\sin(kl) - \cos(kl)}{\cos(\theta+\alpha)}\right.$$
$$\left. + \frac{e^{-jkl\sin(\theta-\alpha)} + j\sin(\theta-\alpha)\sin(kl) - \cos(kl)}{\cos(\theta-\alpha)}\right) \tag{2.116}$$

If the V-dipole is located above a conducting ground plane, the method of images can be used to include an image V-dipole forming a two-element

array in free space, from which the combined primary plus image V-dipole radiation pattern can be determined. The radiation patterns of an array of V-dipole antennas can be computed by using the appropriate array factor.

To include the complete effects of the balun feed and dipole arms a general-purpose moment method solver such as FEKO [12] can be used to compute the V-dipole input impedance and element gain patterns.

Several infinite array analyses for dipole radiators with feedlines have been developed [6, 10, 11]. In [6], straight-arm dipole arrays with feedlines were analyzed in terms of the transverse magnetic (TM) feed region modes. It was shown that the dominant TM mode can go into cut-off, producing a blindspot, prior to the onset of grating lobes. This mode cut-off effect was presented in terms of the propagation constant of the TM mode. The theoretical results presented in [11] indicate the presence of blind spots in the active scan impedance for straight dipole elements with feedlines. For swept-back dipoles with feedlines it was demonstrated that a blind spot does not tend to occur. It is desirable to be able to predict the V-dipole element gain pattern in a finite array, including the effects of mutual coupling. Many phased-array antennas are designed to scan up to about 60° from broadside. The purpose of the next section is to show that over this $\pm 60^\circ$ scan sector embedded element gain pattern simulations are accurate for V-dipole arrays using a simplified method of moments model. Only the current flowing on the dipole arms is included in the moment method model. Balun or feedline effects are not considered here, but the effects of a finite ground plane are included. Crossed dipole elements are useful in generating circular or dual-linear polarization. Dual linearly polarized center-element gain patterns are considered here. Passively terminated arrays are convenient for determining the element gain pattern [5]. In this situation a single element is driven, usually the center element, and the surrounding elements are terminated in resistive loads.

2.9.2 Dipole Element Prototypes

A dipole array element design for straight and V-dipoles is discussed in this section. The desired operating band of interest here is 1.2-1.4 GHz (15.4 percent bandwidth). At the center frequency (1.3 GHz), the dipole terminals are located approximately $\lambda/4$ above the ground plane. Both straight-arm and V-dipole elements were fabricated, for comparing their measured radiation patterns when each element is mounted above a conducting ground plane. A photograph of the crossed straight-arm dipole antenna used in these measurements is shown in Figure 2.44. The dipole arms ($l = 5.461$ cm, $w = 0.356$ cm, $h = 5.588$ cm were etched on a double-sided printed circuit

(PC) board. Two of these PC boards are notched and interleaved, forming the

Figure 2.44 Photograph of a crossed straight-arm dipole antenna.

desired crossed dipole antenna. The crossed dipoles are fed by two separate RG-141 (0.358 cm diameter) coaxial cables (with 50-ohm characteristic impedance), which provide independent orthogonally polarized signals. The balun/feedline is made from a section of RG-141 semi-rigid coaxial cable and a solid brass rod (0.358 cm diameter). Electrical connections at the pair of dipole terminals are facilitated by the use of a double-sided printed circuit board. The balun feedlines (stubs) form a two-wire balanced line with spacing 0.754 cm. For the given line diameter and spacing, the balun characteristic impedance is 165 ohms [14].

The crossed V-dipole element used in these experiments was fabricated in the same manner, but with the arms swept down toward the ground plane at a 45° angle, as shown in Figure 2.45 ($l = 5.461$ cm, $w = 0.356$ cm, $h = 5.588$ cm, $\alpha = 45^\circ$. Nineteen such V-dipoles were fabricated for array testing. The ground plane used for the single element and V-dipole array measurements was a 3.175 mm sheet of aluminum with dimensions 1.22m $\times$ 1.22m square.

2.9.3 Measured and Simulated Results

To compare dipole designs, straight-arm and crossed V-dipole antennas were mounted at the center of a 1.22m square aluminum ground plane, and linearly polarized radiation patterns were measured in an anechoic chamber. The measured E-plane and H-plane patterns are shown in Figures 2.46 and 2.47, respectively.

In the measured E-plane patterns (E_θ component) shown in Figure 2.46, as expected the V-dipole has a wider angular pattern coverage compared to the straight-arm dipole. For angles greater than about 45° from broadside, the E-plane radiation patterns of the straight and V-dipoles differ significantly.

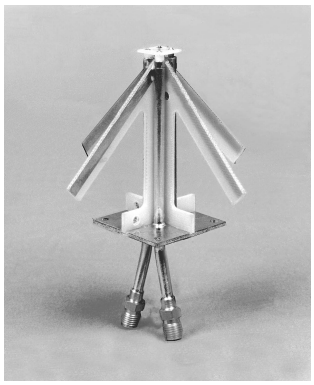

Figure 2.45 Photograph of a crossed V-dipole antenna.

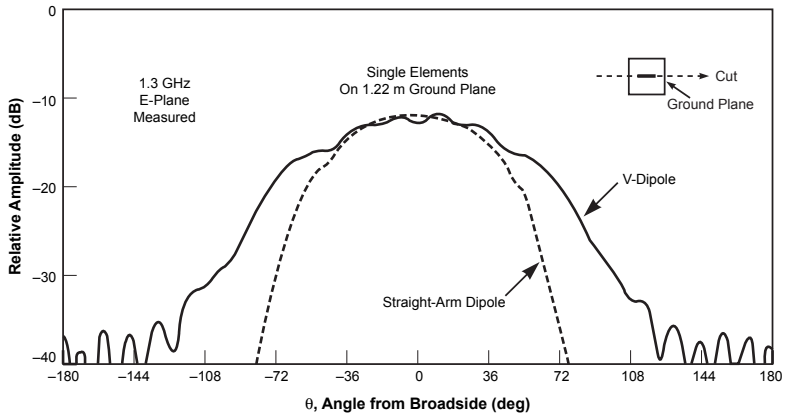

Figure 2.46 Measured E-plane radiation patterns for crossed straight-arm and crossed V-dipole antennas.

For example, at an angle 60° from broadside, the V-dipole gain is about 5 dB higher than the straight dipole gain. This wider pattern coverage should allow wider scanning coverage compared to the straight-arm dipole, which is a motivating factor for tilting the dipole arms. In the measured H-plane patterns (E_ϕ component) shown in Figure 2.47, the radiation patterns of the straight-arm and V-dipole single elements are approximately the same.

A layout for the finite array of 19 V-dipole antenna elements on a 1.22m square ground plane is shown in Figure 2.48. For wide-angle scanning the V-dipole element spacing in the array is chosen as 12.7 cm (corresponding to 0.55λ at the center frequency of 1.3 GHz) on a hexagonal lattice. This lattice spacing allows scanning without the formation of grating lobes in any

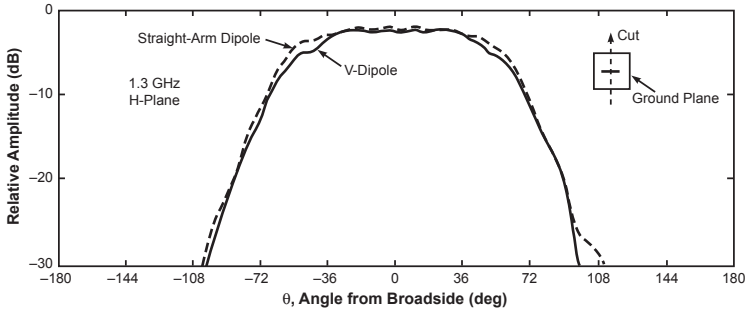

Figure 2.47 Measured H-plane radiation patterns for crossed straight-arm and crossed V-dipole antennas.

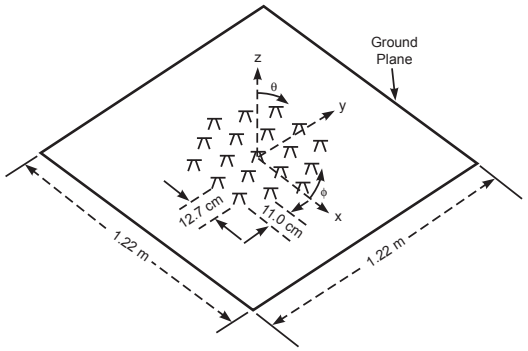

Figure 2.48 Layout for 19-element crossed V-dipole array. © 1988 IEEE [118].

plane out to 60° from broadside. A photograph of the array of 19 V-dipoles is shown in Figure 2.49. For center element gain pattern measurements and moment method simulations, the center element is driven and 50-ohm resistive loads are assumed at the terminals of each surrounding passively terminated dipole element. For array mutual coupling (S parameter) measurements, the center element is driven and all elements except the receive dipole element are terminated in 50-ohm resistive loads. Center element return loss and mutual coupling data were measured for the 19-element V-dipole array, and these data are given in Figure 2.50. At 1.3 GHz (center frequency) the measured return loss ($20 \log_{10} |S_{11}|$) was -8.5 dB. In the E-plane ($\phi = 0^\circ$), the measured coupling to the nearest neighbor was -25.5 dB. In the H-plane, the measured coupling to the nearest neighbor was -19.7 dB. These measured complex mutual coupling data can be summed according to Equation (2.36) to compute the array scan reflection coefficient for the center element versus scan angle in

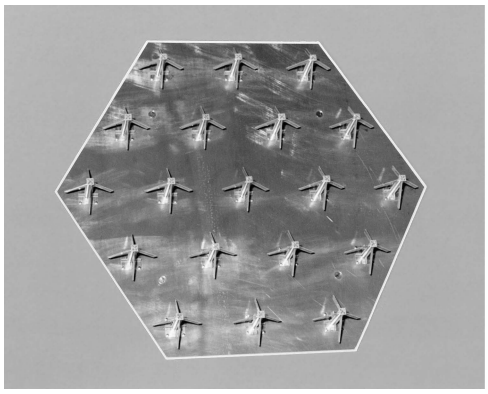

Figure 2.49 Photograph of 19-element crossed V-dipole array.

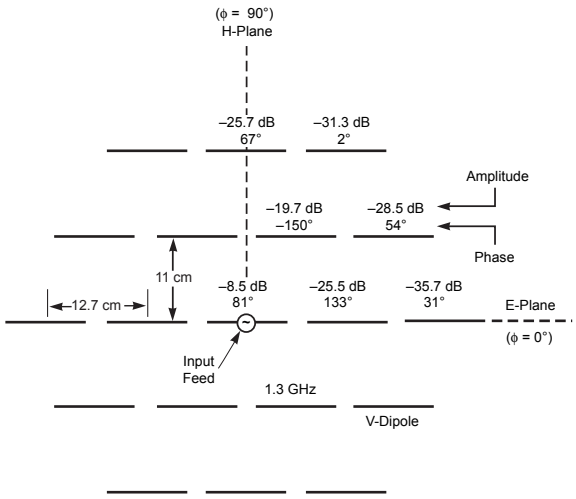

Figure 2.50 Measured return loss and mutual coupling for 19-element crossed V-dipole array.

both E- and H-planes, as depicted in Figure 2.51. Based on these calculations, the array scan mismatch loss ranges from about 0.5 dB to 1 dB over scan angles from 0° to 60°, respectively.

Measured and FEKO moment method simulated center element gain patterns, in the passively terminated array, at 1.2, 1.3, and 1.4 GHz are presented in Figures 2.52 (E-plane) and 2.53 (H-plane). The patterns indicate peak gain (approximately 5 to 6 dBi) occurring in the vicinity of broadside

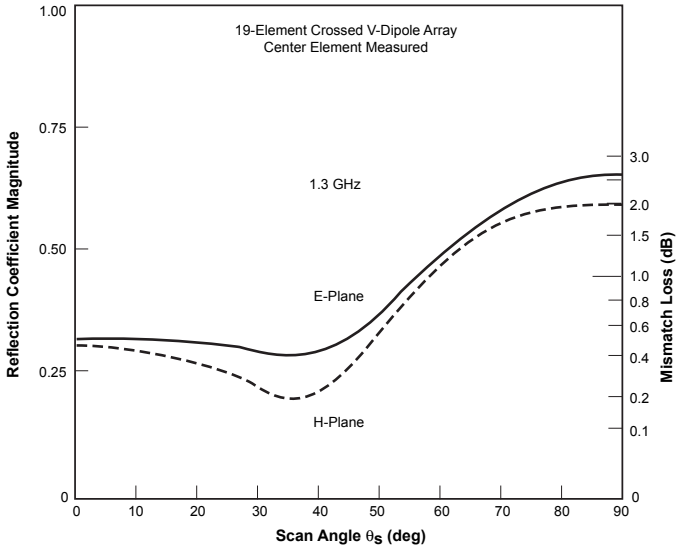

Figure 2.51 Calculated scan reflection coefficient versus scan angle as computed from measured mutual coupling data (Figure 2.49) for the 19-element crossed V-dipole array.

and no more than 4 dB amplitude taper at 60° from broadside. Also, there is no evidence of a blind spot. Over the 15.4% bandwidth shown, the measured and simulated gain patterns are in good agreement.

2.10 Rectangular Waveguide Array Example

Open-ended rectangular or circular waveguide elements are commonly suggested for phased array applications. Single open-ended rectangular and circular waveguide antennas are analyzed in detail in Wolff [119]. The behavior of planar arrays of open-ended rectangular waveguides has been investigated by a number of authors [120–135]. Borgiotti [120] obtained a mutual admittance expression between two identical radiating apertures in the form of a Fourier transform of a function related to the power radiation pattern of the element. Mailloux [121] used the method of moments and a single-mode approximation to the aperture field to analyze the coupling between two closely spaced open-ended waveguide slots. Mailloux [122] also analyzed the coupling between collinear open-ended waveguide slots by expanding the aperture field in a Fourier series. Bird [123] has analyzed the coupling between rectangular waveguides of different sizes. An approximation to the behavior of a finite array of rectangular waveguides was obtained by Amitay, Galindo, and

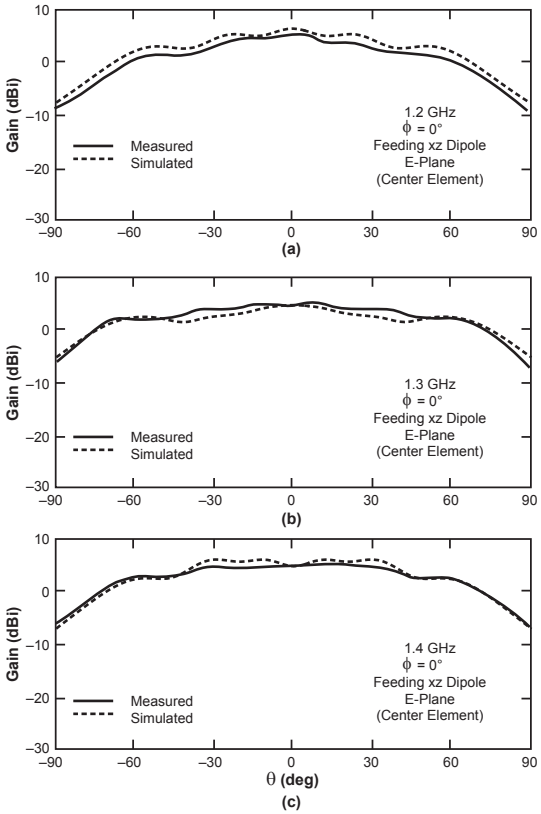

Figure 2.52 Measured and moment method simulated center element gain patterns for 19-element V-dipole array. Feeding xz dipole, E-plane, $\phi = 0^\circ$ cut. (a) 1.2 GHz, (b) 1.3 GHz, and (c) 1.4 GHz.

Wu [6] by using infinite array techniques with finite array excitation. Wu also analyzed a finite array of parallel plate waveguides [124] Cha and Hsiao [125] and Hidayet [126] investigated the reflection coefficients of planar waveguide arrays of size up to 13×13 for a rectangular grid. Hidayet also analyzed a 7×7 planar array arranged in triangular grid. Luzwick and Harrington [127] investigated the coupled power between elements of 7×7 rectangular and triangular grid arrays. Wang [128] investigated the measured E-plane radiation patterns for the center element of a 3×41 array of rectangular waveguides and performed an infinite array analysis of both rectangular and ridged waveguide arrays.

Consider now an example 7-element linear array of rectangular waveguide elements, which is analyzed by the FEKO method of moments solver.

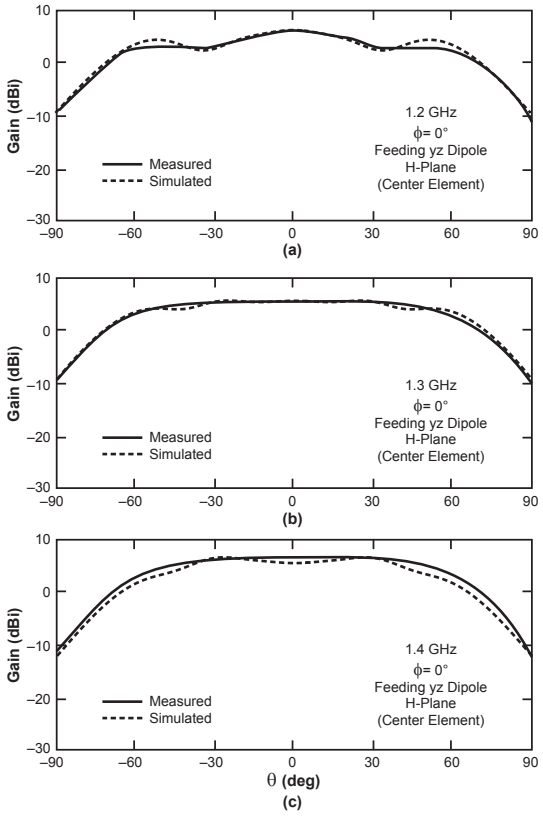

Figure 2.53 Measured and moment method simulated center element gain patterns for 19-element V-dipole array. Feeding yz dipole, H-plane, $\phi = 0^\circ$ cut. (a) 1.2 GHz, (b) 1.3 GHz, and (c) 1.4 GHz.

Figure 2.54 shows the array meshed geometry in which the elements operate at 1.3 GHz and have dimensions a =16.51 cm by b =4.064 cm (6.5 inches by 1.6 inches) are arranged along the y axis with center-to-center spacing 10.922 cm (4.3 inches). The elements radiate through a perfectly conducting rectangular ground plane with dimensions 76.454 cm by 60.96 cm (30.1 inches by 24.0 inches). Each of the seven elements are fed by a rectangular waveguide section 10.16 cm (4.0 cm) long operating in the dominant TE10 mode excitation. The TE10 mode cutoff frequency f_c for these waveguide elements is determined by the following equation

$$f_c = c/(2a) \tag{2.117}$$

where c is the speed of light and a is the waveguide broadwall width.

Substituting $a = 16.51$ cm in Equation (2.117) yields a wavguide cutoff frequency for the TE10 mode equal to 0.908 GHz. The automatically meshed model in Figure 2.54 uses 5278 metallic triangular patches.

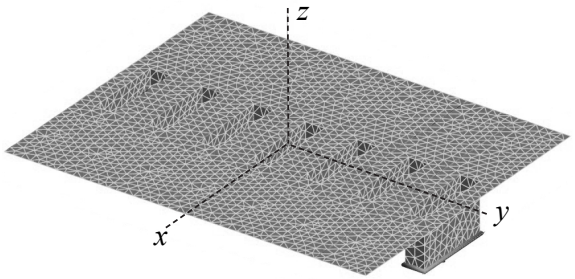

Figure 2.54 Moment method meshed model of a 7-element rectangular waveguide phased array.

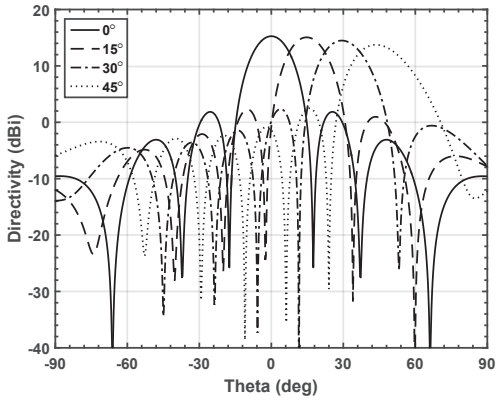

Figure 2.55 Moment method simulated scanned directivity patterns for a 7-element rectangular waveguide phased array.

2.11 Summary

This chapter, together with Chapter 1, has reviewed the important foundation of electromagnetic theory for application to phased array antenna development. In this chapter, basic array theory, the reaction integral equation, method of moments, and infinite-array theory were reviewed in detail to allow the analysis of phased array antennas, including the effects of mutual coupling between the antenna elements. In the following chapters, the practical design

and development of ultrawideband array antennas is described. The method of moments is used in designing and analyzing the performance of these prototype antennas.

References

[1] J.D. Kraus, *Antennas*. New York: McGraw-Hill, 1950.

[2] S.A. Schelkunoff and H.T. Friis, *Antennas: Theory and Practice*. New York: Wiley, 1952.

[3] W.L. Stutzman and G.A. Thiele, *Antenna Theory and Design, 2nd ed.* New York: Wiley, 1998.

[4] J. Volakis, ed., *Antenna Engineering Handbook, 4th ed.* New York: McGraw-Hill, 2007.

[5] C.A. Balanis, *Antenna Theory and Design, 3rd ed.* New York: Wiley, 2005.

[6] N. Amitay, V. Galindo, and C.P. Wu, *Theory and Analysis of Phased Array Antennas.* New York: Wiley, 1972, ch. 1.

[7] A.A. Oliner and G.H. Knittel, eds., *Phased Array Antennas*. Dedham, Mass.: Artech House, 1972.

[8] R.C. Hansen, ed., *Significant Phased Array Papers*. Dedham, Mass.: Artech House, 1973.

[9] R.J. Mailloux, *Phased Array Handbook, 2nd ed.* Norwood, Mass.: Artech House, 2005.

[10] E. Brookner, ed., *Practical Phased-Array Antenna Systems*. Norwood, Mass.: Artech House, 1991.

[11] R.C. Hansen, *Microwave Scanning Antennas, vol. II: Array Theory and Practice.* Los Altos, Calif.: Peninsula Publishing, 1985.

[12] R.C. Hansen, *Phased Array Antennas, 2nd ed.* New York: Wiley, 2009.

[13] A.K. Bhattacharyya, *Phased Array Antennas.* New York: Wiley, 2006.

[14] T. Jeffrey, *Phased-Array Radar Design: Application of Radar Fundamentals.* Raleigh, North Carolina: Scitech Pub Inc., 2009.

[15] A.J. Fenn, *Adaptive Antennas and Phased Arrays for Radar and Communications.* Norwood, Mass.: Artech House, 2008.

[16] D.R. Billetter, *Multifunction Array Radar*. Norwood, Mass.: Artech House, 1989.

[17] S.P. Skobelev, *Phased Array Antennas with Optimized Element Patterns.* Norwood, Mass.: Artech House, 2011.

[18] H.J. Visser, *Array and Phased Array Antenna Basics.* New York: Wiley, 2005.

[19] R.L. Haupt, *Antenna Arrays: A Computational Approach.* New York: Wiley-IEEE Press, 2010.

[20] D. Ehyale, *Novel Approaches to the Design of Phased Array Antennas: Low Cost, Low Complexity Phased Array Antenna Design.* LAP Lambert Academic Publishing, 2012.

[21] E. Brookner, "Phased-Array Radars," *Scientific American,* vol. 252, no. 2, 1985, pp. 94–102.

[22] A.J. Fenn, D.H. Temme, W.P. Delaney, and W.E. Courtney, "The Development of Phased Array Radar Technology," *Lincoln Laboratory Journal*, vol. 12, no. 2, 2000, pp. 321–340.

[23] J.L. Allen, L. Cartledge, W.P. Delaney, and J. Dibartolo, et al., "Phased Array Radar Studies, 1 July 1959 to 1 July 1960," Technical Report 228, MIT Lincoln Laboratory, 12 Aug. 1960, DTIC no. AD-0249470.

[24] J.L. Allen, L. Cartledge, W.P. Delaney, and J. Dibartolo, "Phased Array Radar Studies, 1 July 1960 to 1 July 1961," Technical Report 236, MIT Lincoln Laboratory, 13 Nov. 1961, DTIC no. AD-271724.

[25] J.L. Allen, D.M. Bernella, W.W. Carpenter, and W.P. Delaney, "Phased Array Radar Studies, 1 July 1961 to 1 July 1963," Technical Report 299, MIT Lincoln Laboratory, 20 Feb. 1963, DTIC no. AD-417572.

[26] J.L. Allen, D.M. Bernella, F. Betts, and L. Cartledge, "Phased Array Radar Studies, 1 July 1963 to 1 July 1964," Technical Report 381, MIT Lincoln Laboratory, 31 March 1965, DTIC no. AD-629363.

[27] J.L. Allen, "A Theoretical Limitation on the Formation of Lossless Multiple Beams in Linear Arrays," *IRE Trans. Antennas and Propagation*, vol. 9, no. 4, 1961, pp. 350–352.

[28] W.P. Delaney, "An RF Multiple Beam Forming Technique," Group Report 41G-0012, Lincoln Laboratory, 9 Aug. 1961, DTIC no. AD-262017.

[29] J.L. Allen, "Theory of Array Antennas (with Emphasis on Radar Applications)," Technical Report 323, Lincoln Laboratory, 25 July 1963, DTIC no. AD-422945.

[30] B.L. Diamond, "A Generalized Approach to the Analysis of Infinite Planar Phased Array Antennas," *Proc. IEEE*, vol. 56, no. 11, 1968, pp. 1837–1851.

[31] B.L. Diamond and G.H. Knittel, "A New Procedure for the Design of a Waveguide Element for a Phased-Array Antenna," in *Phased Array Antennas*, A.A. Oliner and G.H. Knittel, eds. Dedham, Mass.: Artech House, 1972, pp. 149–156.

[32] J.L. Allen, "Gain and Impedance Variation in Scanned Dipole Arrays," *IRE Trans. Antennas and Propagation*, vol. 10, no. 5, 1962, pp. 566–572.

[33] J.L. Allen, "On Surface-Wave Coupling Between Elements of Large Arrays," *IEEE Trans. Antennas and Propagation*, vol. 13, no. 4, 1965, pp. 638–639.

[34] J.L. Allen and B.L. Diamond, "Mutual Coupling in Array Antennas," Technical Report 424, Lincoln Laboratory, 4 Oct. 1966, DTIC no. AD-648153.

[35] B.L. Diamond, "Small Arrays – Their Analysis and Their Use for the Design of Array Elements," in *Phased Array Antennas*, A.A. Oliner and G.H. Knittel, eds. Dedham, Mass.: Artech House, 1972, pp. 127–131.

[36] A.J. Fenn, "Theoretical and Experimental Study of Monopole Phased Array Antennas," *IEEE Trans. Antennas and Propagation*, vol. 34, no. 10, 1985, pp. 1118–1126.

[37] J. Butler, and R. Lowe, "Beam-Forming Matrix Simplifies Design of Electronically Scanned Antennas," *Electron. Des.*, vol. 9, 12 Apr. 1961, pp. 170–173.

[38] R.J. Mailloux, "Phased Array Theory and Technology," *Proc. IEEE*, vol. 70, no. 3, 1982, pp. 246–291.

[39] G.N. Tsandoulas, "Unidimensionally Scanned Phased Arrays," *IEEE Trans. Antennas and Propagation*, vol. 28, no. 1, 1980, pp. 86–99.

[40] G.N. Tsandoulas, "Wideband Limitations of Waveguide Arrays," *Microwave J.*, vol. 15, no. 9, 1972, pp. 49–56.

[41] G.N. Tsandoulas and G.H. Knittel, "The Analysis and Design of Dual-Polarization Square-Waveguide Phased Arrays," *IEEE Trans. Antennas and Propagation*, vol. 21, no. 6, 1973, pp. 796–808.

[42] G.H. Knittel, "Relation of Radar Range Resolution and Signal-to-Noise Ratio to Phased-Array Bandwidth, " *IEEE Trans. Antennas and Propagation*, vol. 22, no. 3, 1974, pp. 418–426.

[43] E. Brookner, ed. *Radar Technology*. Norwood, Mass.: Artech House, 1991.

[44] G.W. Stimson, *Introduction to Airborne Radar*. Raleigh, North Carolina: Scitech Publishing, 1998, pp. 546–562.

[45] E.J. Kelly and G.N. Tsandoulas, "A Displaced Phase Center Antenna Concept for Space Based Radar Applications," *IEEE Eascon*, Sept. 1983, pp. 141–148.

[46] G.N. Tsandoulas, "Space-Based Radar," *Science*, 17 July 1987, pp. 257–262.

[47] M.I. Skolnik, ed., *Radar Handbook, 3rd ed.* New York: McGraw-Hill, 2008.

[48] H.K. Schuman, D.R. Pflug, and L.D. Thompson, "Infinite Planar Arrays of Arbitrarily Bent Thin Wire Radiators," *IEEE Trans. Antennas Propagation*, vol. 32, no. 3, 1984, pp. 364–377.

[49] E.D. Sharp, "A Triangular Arrangement of Planar-Array Elements That Reduces the Number Needed," *IRE Trans. Antennas and Propagation*, vol. 9, no. 2, 1961, pp. 126–129.

[50] N.R. Brennecke and W.N. Moule, "Uses of Fences to Optimize Operating Impedance of Phased Arrays Using an Improved Measuring Technique," *IEEE Antennas and Propagation Soc. Int. Symp. Dig.*, 1964, pp. 134–142.

[51] B.A. Munk, *Frequency Selective Surfaces: Theory and Design*. New York: Wiley, 2000.

[52] B.A. Munk, *Finite Antenna Arrays and FSS*. New York: Wiley, 2003.

[53] A.J. Fenn and P.T. Hurst, *Ultrawideband Phased Array Antenna Technology for Sensing and Communications Systems,* MIT Lincoln Laboratory Book Series, Cambridge, MA: The MIT Press, 2015.

[54] K.F. Braun, *Electrical Oscillations and Wireless Telegraphy,* Nobel Prize Lecture, 11

Dec. 1909.

[55] R.J. Mailloux, “A History of Phased Array Antennas," Chapter 17 in *History of Wireless*, T.K. Sarkar, R.J. Mailloux, A.A. Oliner, M. Salazar-Palma, and D.L. Sengupta, eds. New Jersey: Wiley, 2006.

[56] W. Delaney, “From Vision to Reality: 50+ Years of Phased Array Development," *2016 IEEE Int. Symp. on Phased Array Systems and Technology*.

[57] E. Brookner, “Developments and Breakthroughs in Radars and Phased-Arrays," *2016 IEEE Radar Conference*.

[58] J.S. Herd and M.D. Conway, “The Evolution to Modern Phased Array Architectures," *Proc. IEEE* vol. 104, no. 3, March 2016, pp. 519–529.

[59] M. Dudek, I. Nasr; G. Bozsik; M. Hamouda; D. Kissinger; G. Fischer, “System Analysis of a Phased-Array Radar Applying Adaptive Beam-Control for Future Automotive Safety Applications," *IEEE Transactions on Vehicular Technology,* vol. 64, no. 1, 2015, pp. 34 – 47.

[60] G.M. Rebeiz; S.-Y. Kim; O. Inac; W. Shin; O. Gurbuz; Y.-C. Ou; F. Golcuk; T. Kanar; B.-H. Ku, “Millimeter-Wave Large-Scale Phased-Arrays for 5G Systems," 2015 IEEE MTT-S International Microwave Symposium, 2015, pp. 1–3.

[61] M.H. Novak, F.A. Miranda, John L. Volakis, “An Ultra-Wideband Millimeter-Wave Phased Array," 2016 10th European Conference on Antennas and Propagation (EuCAP), 2016 pp. 1 – 3.

[62] M. Agiwal; A. Roy; N. Saxena, “Next Generation 5G Wireless Networks: A Comprehensive Survey," *IEEE Communications Surveys & Tutorials* vol. 18, no. 3, 2016, pp. 1617 – 1655.

[63] P.W. Howells, “Explorations in Fixed and Adaptive Resolution at GE and SURC,” *IEEE Trans. Antennas and Propagation*, vol. 24, no. 5, 1976, pp. 575–584.

[64] S.P. Applebaum, “Adaptive Arrays,” *IEEE Trans. Antennas and Propagation*, vol. 24, no. 5, 1976, pp. 585–598.

[65] W.F. Gabriel, “Adaptive Arrays – An Introduction,” *Proc. IEEE,* vol. 64, 1976, pp. 239–271.

[66] J.T. Mayhan, “Some Techniques for Evaluating the Bandwidth Characteristics of Adaptive Nulling Systems,” *IEEE Trans. Antennas and Propagation,* vol. 27, no. 3, 1979, pp. 363–373.

[67] J.T. Mayhan, A.J. Simmons, and W.C. Cummings, “Wide-Band Adaptive Antenna Nulling Using Tapped Delay Lines,” *IEEE Trans. Antennas and Propagation,* vol. 29, no. 6, 1981, pp. 923–936.

[68] A.J. Fenn, “Evaluation of Adaptive Phased Array Far-Field Nulling Performance in the Near-Field Region,” *IEEE Trans. Antennas and Propagation*, vol. 38, no. 2, 1990, pp. 173–185.

[69] R.A. Monzingo and T.W. Miller, *Introduction to Adaptive Arrays*. New York: Wiley, 1980.

[70] R.T. Compton, Jr., *Adaptive Antennas, Concepts and Performance*. Upper Saddle River, New Jersey: Prentice-Hall, 1988.

[71] M.M. Weiner, *Adaptive Antennas and Receivers*. Boca Raton, Florida: CRC Press, 2006.

[72] S. Chandran, ed., *Adaptive Antenna Arrays: Trends and Applications*. Berlin: Springer-Verlag, 2004.

[73] D.G. Manolakis, V.K. Ingle, and S.M. Kogon, *Statistical and Adaptive Signal Processing: Spectral Estimation, Signal Modeling, Adaptive Filtering, and Array Processing.* Norwood, Mass.: Artech House, 2005.

[74] R. Nitzberg, *Adaptive Signal Processing for Radar*. Norwood, Mass.: Artech House, 1992.

[75] A. Farina, *Antenna-Based Signal Processing Techniques for Radar Systems.* Norwood, Mass.: Artech House, 1992.

[76] J.E. Hudson, *Adaptive Array Principles*. New York: Peter Peregrinus, 1981.

[77] A. J. Fenn; G. A. King, Experimental investigation of an adaptive feedback algorithm for hot spot reduction in radio-frequency phased-array hyperthermia, *IEEE Trans. on Biomedical Eng.* 1996, vol. 43, no. 3, pp. 273 - 280.

[78] A.J. Fenn, *Adaptive Phased Array Thermotherapy for Cancer,* Boston, MA: Artech, 2009.

[79] M. A. Jensen; J. W. Wallace, "A Review of Antennas and Propagation for MIMO Wireless Communications," *IEEE Trans. on Antennas and Propagation,* vol. 52, no. 11, 2004, pp. 2810 – 2824.

[80] F. C. Robey, S. Coutts, D. Weikle, J. C. McHarg and K. Cuomo, "MIMO radar theory and experimental results," *Conference Record of the Thirty-Eighth Asilomar Conference on Signals, Systems and Computers, 2004*, vol. 1, 2004, pp. 300–304.

[81] Y.I. Abramovich, G.J. Frazer, B.A. Johnson, "Principles of Mode-Selective MIMO OTHR," *IEEE Trans. on Aerospace and Electronic Systems,* vol. 49, no. 3, 2013, pp. 1839 - 1868,

[82] C.J. Wilson, Electronically Steerable Field Reflector Techniques, Technical Report No. RADC-TR-64-521, Feb. 1965.

[83] W.D. Fitzgerald, "Limited Electronic Scanning with an Offset-Feed Near-Field Gregorian System," MIT Lincoln Laboratory Technical Report 486, 24 Sept. 1971.

[84] J.A. Martinez-Lorenzo, A. Garcia-Pino, B. Gonzalez-Valdes, and C.M. Rappaport, "Zooming and Scanning Gregorian Confocal Dual Reflector Antennas," *IEEE Trans. on Antennas and Propagat.,* vol. 56, no. 9, 2008, pp. 2910-2919.

[85] A.J. Fenn and R.J. Richardson, "Analysis of an Adaptive Two-Reflector Phased-Array Fed System," *1980 IEEE Antennas and Propagation Society International Symposium Digest,* 2-6 June 1980, pp. 134-137.

[86] Kelly, E.J., and G.N. Tsandoulas, "A Displaced Phase Center Antenna Concept for Space Based Radar Applications," *IEEE Eascon*, September 1983, pp. 141-148.

[87] Tsandoulas, G.N., "Space-Based Radar," *Science*, Vol. 237, July 17, 1987, pp. 257-262.

[88] Fenn, A.J., "Analysis of Phase-Focused Near-Field Testing for Multiphase-Center Adaptive Radar Systems," *IEEE Trans. Antennas Propagat.*, Vol. 40, No. 8, 1992, pp. 878-887.

[89] C. L. Dolph, "A Current Distribution for Broadside Arrays Which Optimizes the Relationship Between Beamwidth and Side Lobe Level," *Proc. IRE,* vol. 31, June 1946, pp. 335–318.

[90] D. Barbiere. "A Method for Calculating the Current Distribution of Tschebyscheff Arrays," *Proc. IRE,* vol. 10, January 1952, pp. 78-82.

[91] A. D. Bresler, "A New Algorithm for Calculating the Current Distributions of Dolph-Chebyshev Arrays," *IEEE Trans. Antennas Propagat.,* vol. AP-28, no. 6, November 1980, pp. 951,952.

[92] T.T. Taylor, "Design of Circular Apertures for Narrow Beamwidth and Low Side Lobes," *IEEE Trans. on Antennas and Propagat.,* vol AP-8, no. 4, January 1960, pp. 17–22.

[93] R.L. Thomas, *A Practical Introduction to Impedance Matching*. Dedham, Mass: Artech House, 1976.

[94] A.E.H. Love, "The Integration of the Equations of Propagation of Electric Waves," *Philosophical Trans.*, Series A197, 1901, pp. 1-45.

[95] S.A. Schelkunoff, "On Diffraction and Radiation of Electromagnetic Waves," *Phys. Rev.*, vol. 56, 1939, pp. 308–316.

[96] R.F. Harrington, *Time-Harmonic Electromagnetic Fields,* New York: McGraw-Hill, 1961.

[97] J.R. Mautz and R.F. Harrington, "Electromagnetic Scattering from a Homogeneous Material Body of Revolution," *Int. J. Electronics and Communications (AEU),* vol. 33, 1979, pp. 71-80.

[98] E. Arvas, A.Rahhal-Arabi, A. Sadigh, S.M. Rao, "Scattering from Multiple Conducting and Dielectric Bodies of Arbitrary Shape," *IEEE Antennas and Propagat. Magazine*, vol. 33, no. 2, 1991, pp. 29-36.

[99] U. Jakobus, "Comparison of Different Techniques for the Treatment of Lossy Dielectric/Magnetic Bodies within the Method of Moments Formulation," *Int. J. Electronics and Communications (AEU),* vol. 54, no. 3, 2000, pp. 163-173.

[100] C.A. Balanis, *Advanced Engineering Electromagnetics, 2nd ed.* New Jersey: Wiley, 2012.

[101] V.H. Rumsey, "Reaction Concept in Electromagnetic Theory," *Physical Review*, vol. 94, 1954, pp. 1483–1491.

[102] R.F. Harrington, *Field Computation by Moment Methods.* New York: Macmillan, 1968.

[103] S. Rao, D. Wilton, and A. Glisson, "Electromagnetic Scattering by Surfaces of Arbitrary

Shape," *IEEE Trans. Antennas and Propagation*, vol. 30, no. 5, 1982, pp. 409–418.

[104] E.H. Newman and K. Kingsley, "An Introduction to the Method of Moments," *Computer Physics Communications,* vol. 68, 1991, pp. 1–18.

[105] J.H. Richmond and N.H. Geary, "Mutual Impedance of Nonplanar-Skew Sinusoidal Dipoles," *IEEE Trans. Antennas and Propagation*, vol. 23, no. 3, 1975, pp. 412–414.

[106] J.H. Richmond, "Radiation and Scattering by Thin-Wire Structures in a Homogeneous Conducting Medium (Computer Program Desc.)," *IEEE Trans. Antennas and Propagation*, vol. 22, no. 2, 1974, p. 365.

[107] K.E. Schmidt, "Mutual Impedance of Nonplanar Skew Dipoles," *IEEE Trans. Antennas and Propagation*, vol. 44, no. 9, 1996, pp. 1298–1299.

[108] N.N. Wang, "Reaction Formulation for Radiation and Scattering from Plates, Corner Reflectors, and Dielectric-Coated Cylinders," The Ohio State University, Project Report 2902-15, Columbus, Ohio, Apr. 1974.

[109] W.C. Gibson, *The Method of Moments in Electromagnetics.* Boca Raton, Florida: Chapman & Hall, 2008.

[110] W.C. Chew, J.M. Jin, E. Michielssen, and J. Song, *Fast and Efficient Algorithms in Computational Electromagnetics*. Norwood, Mass.: Artech House, 2001.

[111] H. Jingjian, Z. Xiaofa, X Shaoyi,W. Weiwei, and Y. Naichang, "Suppression of Cross-Polarization of the Microstrip Integrated Balun-Fed Printed Dipole Antenna," *Int. J. of Antennas and Propagation,* Volume 2014, pp. 1–8.

[112] B. Edward and D. Rees, "A Broadband Printed Dipole with Integrated Balun," *Microwave J.*, vol. 30, no. 5, pp. 339–344, 1987.

[113] R. L. Li, T. Wu, B. Pan, K. Lim, J. Laskar, and M. M. Tentzeris, "Equivalent-Circuit Analysis of a Broadband Printed Dipole with Adjusted Integrated Balun and an Array for Base Station Applications," *IEEE Trans. on Antennas and Propagat.,* vol. 57, no. 7, 2009, pp. 2180–2184.

[114] P. Lindberg, E. Ojefors, Z. Barna, A. Thornell-Pers, and A. Rydberg,"Dual Wideband Printed Dipole Antenna with Integrated Balun," *IET Microwaves, Antennas & Propagation,* vol. 1, no. 3, 2007, pp. 707–711.

[115] M. Scott, "A Printed Dipole for Wide-Scanning Array Application," *Proc. 11th Int. Conf. on Antenna and Propagation,* Manchester, UK, vol. 1, no. 480, 2001, pp. 37–40.

[116] H.-R. Chuang and L.-C. Kuo,"3-D FDTD Design Analysis of a 2.4-GHz Polarization-Diversity Printed Dipole Antenna with Integrated Balun and Polarization-Switching Circuit for WLAN and Wireless Communication Applications," *IEEE Transactions on Microwave Theory and Techniques*, vol. 51, no. 2, 2003, pp. 374–381.

[117] Mayer, E.D., and A. Hessel, "Feed Region Modes in Dipole Phased Arrays," *IEEE Trans. Antennas Propagat.*, Vol. 30, No. 1, 1982, pp. 66-75.

[118] Fenn, A.J., "Element Gain Pattern Prediction for Finite Arrays of V-Dipole Antennas over Ground Plane," *IEEE Trans. Antennas Propagat.*, Vol. 36, No. 11, 1988, pp. 1629-1633.

[119] E.A. Wolff, *Antenna Analysis*, New York: John Wiley, pp.192-208.

[120] G.V. Borgiotti, "A Novel Expression for the Mutual Admittance of Planar Radiating Elements," *IEEE Trans. Antennas Propagat.*, Vol. 16, No. 3, 1968, pp. 329-333.

[121] R.J. Mailloux, "First-Order Solutions for Mutual Coupling Between Waveguides Which Propagate Two Orthogonal Modes," *IEEE Trans. Antennas Propagat.*, Vol. 17, No. 6, 1969, pp. 740-746.

[122] R.J. Mailloux, "Radiation and Near-Field Coupling Between Two Collinear Open-Ended Waveguides," *IEEE Trans. Antennas Propagat.*, Vol. 17, No. 1, 1969, pp. 49-55.

[123] T.S. Bird, "Analysis of Mutual Coupling in Finite Arrays of Different-Sized Rectangular Waveguides," *IEEE Trans. Antennas Propagat.*, Vol. 38, No. 2, 1990, pp. 166–172.

[124] C.P. Wu, "Analysis of Finite Parallel-Plate Waveguide Arrays," *IEEE Trans. Antennas Propagat.*, Vol. 18, No. 3, 1970, pp. 328–334.

[125] A.G. Cha and J.K. Hsiao, "A Matrix Formulation for Large Scale Numerical Computation of the Finite Planar Waveguide Array Problem," *IEEE Trans. Antennas Propagat.,* Vol. AP-22, No. 1, January 1974, pp. 106–108.

[126] M.A. Hidayet, "Finite Phased Array Analysis," Ph.D. dissertation, Univ. Michigan, 1974.

[127] J. Luzwick and R.F. Harrington, "Mutual Coupling Analysis in a Finite Planar Rectangular Waveguide Antenna Array," Dept. Elect. Computer Eng., Syracuse Univ., Tech. Rep., No. 7, June 1978.

[128] S.S. Wang, "Wide-Angle Wide-Band Elements for Phased Arrays," Ph.D. dissertation, Polytechnic Institute of New York, 1975.

[129] J.D. Kraus, *Antennas*, New York: McGraw-Hill, 1950, ch. 4.

[130] R.F. Harrington and J.R. Mautz, "A Generalized Network Formulation for Aperture Problems," Sci.Rep. no. 8 contract F19628-73-C-0047, A.F. Cambridge Res. Lab., Rep. AFCRL-TR-75-0589, November 1975.

[131] A.J. Fenn, "Moment Method Calculation of Reflection Coefficient for Waveguide Elements in a Finite Planar Phased Antenna Array," Ph.D. dissertation, The Ohio State Univ., 1978.

[132] A. J. Fenn, G.A. Thiele, and B.A. Munk, "Moment Method Analysis of Finite Rectangular Waveguide Phased Arrays," *IEEE Trans. Antennas Propagat.*, Vol. 30, No. 4, 1982, pp. 554–564.

[133] B.L. Diamond, "Resonance Phenomena in Waveguide Arrays," *IEEE G-AP Int. Symp. Dig.*, 1967, pp. 110–115.

[134] H. Yavuz and O.M. Buyukdura, "Mutual Coupling Effects of Finite Rectangular Phased Arrays," *IEEE Antennas and Propagat. Soc. Int. Symp. Digest,* 1994, pp. 418–421.

[135] P. Grassi, R. Mittra, A. Monorchio, and G. Manara, "Characterization of Finite Waveguide Arrays Using a New Generalized Scattering Matrix Approach," *IEEE Antennas and Propagat. Symposium Digest*, 2004, pp. 125–128.

[136] A. Pellegrini, A. Monorchio, G. Manara, R. Mittra, “A Hybrid Mode Matching-Finite Element Method and Spectral Decomposition Approach for the Analysis of Large Finite Phased Arrays of Waveguides", *IEEE Trans. on Antennas and Propagat.,* vol. 62, 2014, pp. 2553–2561.

3

Line Transformer Matching of a Dipole Antenna

3.1 Introduction

Dipole antennas are commonly used as single elements, as a feed for reflector antennas, or in arrays for communications and radar applications [1-32]. Crossed dipole antennas can be used for example for dual linearly polarized or circularly polarized applications. The RF performance of an antenna is often quantified by the reflection coefficient (also referred to as return loss) or VSWR at the input port to the antenna. For example, the magnitude of the reflection coefficient of an antenna is a critical design parameter that must be minimized for providing maximum realized antenna gain or efficient power transmission between the antenna and the transmission line connected to the antenna.

Impedance matching is a well established technique for improving the reflection coefficient of antennas over a band of frequencies [33-44]. Dipoles are sometimes fed in a balanced (differential) mode by using a folded balun design [44, 45]. In this chapter, an impedance matching example for a folded balun-fed dipole antenna is described in detail. Besides impedance matching, to provide an increased amount of inherent bandwidth, the dipole arms are designed to be cylindrical tubes rather than thin wires. In Figure 3.1, the tubular dipole arms have length l and diameter d. The folded balun section consists of two vertical tubes with center-to-center spacing s and height H. The balun tubes are assumed to have outer diameter D and they are short circuited to the ground plane, forming a short-circuit stub in parallel with respect to the dipole feed terminals. In this antenna design, the arms are swept-back at a 45° angle to increase the E-plane beamwidth as discussed in

Chapter 2. An electrically conducting feed tab connects the center conductor to the dummy (passive metal tube) portion of the folded balun. The coaxial port connects to an inner conductor of diameter d_1 and a surrounding tube with inner diameter D (an infinitesimal wall thickness is assumed here). The values of d_1 and D are adjusted typically to provide a 50Ω characteristic impedance. In practice, the coaxial port is fed typically with a microwave connector such as type N or SMA depending on RF power handling requirements and operating frequency. The parallel balun tubes form an open-wire transmission line with characteristic impedance given by [44]

$$Z_o = \frac{120}{\sqrt{\epsilon_r}} \cosh^{-1} \frac{s}{D} \tag{3.1}$$

The characteristic impedance of the coaxial feed line is given by [44]

$$Z_o = \frac{138}{\sqrt{\epsilon_r}} \log_{10} \frac{D}{d_1} \tag{3.2}$$

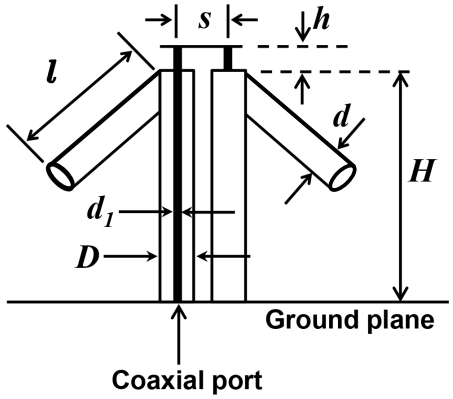

Figure 3.1 Diagram showing a swept-back dipole with coaxial folded balun over a ground plane.

In [33–35], the theory for impedance matching using line transformers, series networks, and parallel networks is provided. This chapter provides a detailed discussion and simulations of a line transformer for providing wideband matching for the input impedance of an example UHF swept-back dipole antenna. In practice, the impedance matching approach discussed here would involve the design of the feeding structure, which in this case would be a stepped coaxial transmission line transformer contained within the balun as depicted in Figure 3.2. In this case, the coaxial feedline

contains an impedance transformer section with an inner conductor with diameter d_2 adjusted for a desired characteristic impedance to match the input impedance of the dipole. Chapter 1 reviewed transmission line theory in detail. The next section (Section 3.2) provides a brief review as it relates to the derivation of the line transformer matching theory (Section 3.3). An application of the line transformer matching theory to designing a wideband swept-back dipole is described along with simulated moment method results in Section 3.4. Section 3.5 describes a comparison between simulated and measured mismatch loss results for a prototype swept-back dipole. Section 3.6 simulates the radiation patterns for the wideband swept-back dipole feeding a parabolic reflector antenna. Section 3.7 has a summary.

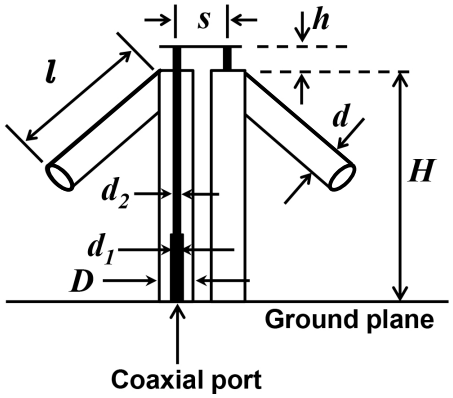

Figure 3.2 Diagram showing a swept-back dipole with line transformer section with a coaxial folded balun over a ground plane.

3.2 Basic Transmission Line Theory

In this section, a brief review of basic transmission line theory is provided as it relates to the line transformer impedance matching theory [33-35]. Referring to Figure 3.3, consider first a length l of transmission line with a characteristic impedance Z_o. Assume that the transmission line's attenuation constant α is equal to zero. The electrical length is given by the quantity βl, where $\beta = 2\pi/\lambda$ is the wavelength-dependent phase propagation constant of the transmission line. Assume that an antenna has a complex load impedance denoted as Z_L. At a distance l along a lossless transmission line with characteristic impedance Z_o and phase propagation constant β, the input

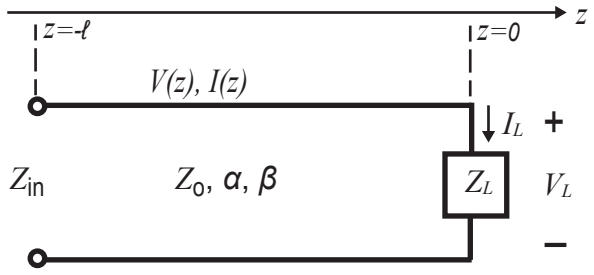

Figure 3.3 Transmission line with characteristic impedance Z_o and length l connected to a load impedance Z_L.

impedance Z_{in} as function of position is then given by

$$Z_{\text{in}} = Z_o \frac{Z_L + jZ_o \tan \beta l}{Z_o + jZ_L \tan \beta l} \tag{3.3}$$

and in terms of its complex conjugate

$$Z_{\text{in}}^* = Z_o \frac{Z_L^* - jZ_o \tan \beta l}{Z_o - jZ_L^* \tan \beta l} \tag{3.4}$$

The input admittance Y_{in} is given by

$$Y_{\text{in}} = 1/Z_{\text{in}} \tag{3.5}$$

Solving Equation (3.3) for Z_L yields

$$Z_L = Z_o \frac{Z_{\text{in}} - jZ_o \tan \beta l}{Z_o - jZ_{\text{in}} \tan \beta l} \tag{3.6}$$

In the case where the load is a short circuit ($Z_L = 0$) or an open circuit ($Z_L = \infty$), respectively, Equation (3.3) reduces to

$$Z_{\text{in}}^{\text{sc}} = jZ_o \tan(\beta l) \tag{3.7}$$

$$Z_{\text{in}}^{\text{oc}} = -jZ_o \frac{1}{\tan(\beta l)} \tag{3.8}$$

The product of Equations (3.7) and 3.8 leads to an expression for the characteristic impedance in terms of the short-circuit and open-circuit input impedances as

$$Z_o = \sqrt{Z_{\text{in}}^{\text{sc}} \times Z_{\text{in}}^{\text{oc}}} \tag{3.9}$$

The reflection coefficient in terms of the load impedance Z_L and transmission line characteristic impedance Z_o is given by

$$\Gamma = \frac{Z_L - Z_o}{Z_L + Z_o} \tag{3.10}$$

and in normalized form in terms of $z_L = Z_L/Z_o$ as

$$\Gamma = \frac{z_L - 1}{z_L + 1} = |\Gamma| e^{j\phi} \tag{3.11}$$

It follows from Equation (3.11) that the normalized load impedance is expressed as

$$z_L = \frac{1 + \Gamma}{1 - \Gamma} \tag{3.12}$$

Rearranging Equation (3.10), the load impedance in terms of the reflection coefficient is given by

$$Z_L = Z_o \frac{1 + \Gamma}{1 - \Gamma} \tag{3.13}$$

The voltage standing wave ratio (VSWR) is expressed as

$$\text{VSWR} = \frac{1 + |\Gamma|}{1 - |\Gamma|} \tag{3.14}$$

Having reviewed some of the fundamental equations that quantify the input impedance, load impedance, reflection coefficient, and VSWR, the next section addresses line transformer impedance matching theory.

3.3 Line Transformer Impedance Matching Theory

In the impedance matching procedure that follows, electromagnetic simulations (or measurements) would be used to determine the input impedance at the antenna terminals of the swept-back crossed dipole antenna depicted in Figure 3.1. The dipole arms and geometry and height of feed terminals with respect to the ground plane are designed based on simple theory and using prior experience, which is discussed later in this chapter. In the electromagnetic field simulations and line transformer calculations that follow, the dipole antenna is fed initially (before matching) with a standard $Z_o = 50\Omega$ coaxial feedline, which is not expected to provide the desired final reflection coefficient magitude or VSWR. A voltage source is located at the input port of the 50-ohm coaxial feedline (located at the ground plane), and the input impedance of the antenna simulated at the ground plane

reference position is determined. (Note: the same approach can be applied for measurements). The next step is to transform the input impedance at the ground plane to the complex load Z_L at the antenna terminals using Equation (3.6). This antenna terminal input impedance (load impedance) becomes the starting value for impedance matching. Next, a series transformer transmission line with derived values of characteristic impedance and length is introduced to improve the reflection coefficient. The input impedance matching technique discussed in this chapter is as follows:

- Plot the antenna load impedance (input impedance) in Cartesian coordinates, where the horizontal axis is resistance and the vertical axis is reactance,
- Define a target maximum allowed VSWR (plotted as a circle) at an input port located on a standard 50-ohm transmission line,
- Draw an outer boundary circle (OBC) encompassing the input impedance data at the antenna terminals and tangent to the target VSWR circle,
- Compute the required characteristic impedance of the line transformer Z_o' using the square root (geometric mean) of the product of the resistance minimum (denoted $R_{\text{min}}^{\text{OBC}}$ and resistance maximum $R_{\text{max}}^{\text{OBC}}$ on the resistance axis intersecting the OBC, that is,

$$Z_o' = \sqrt{R_{\text{min}}^{\text{OBC}} \times R_{\text{max}}^{\text{OBC}}} \tag{3.15}$$

- Compute and plot the family of transformation circles that ensures impedance values versus frequency will transform to within the desired target VSWR (target circle).
- Select a critical frequency in this case where the antenna load impedance intersects the outer boundary circle, and locate the corresponding transformation circle that encompasses the impedance data point at this frequency, From the electrical length βl of the corresponding transformation circle, solve for the transformer critical length $l = l_c$ using $\beta = 2\pi/\lambda$ where λ is the wavelength at the critical frequency.
- Tabulate the electrical line length of the transformer section over the frequency band of interest, and verify that the input impedance at the terminals of the dipole antenna tracks within the series of transformation circles.
- Transform the antenna load impedance to the input impedance and reflection coefficient looking into the line transformer with characteristic impedance Z_o' and critical length l_c.

- Normalize the reflection coefficient data to the final characteristic impedance (50Ω) of the feedline attached to the transformer, and plot as the matched input impedance.

3.3.1 Target Circle for Maximum Allowed VSWR

Consider first a *target circle*, which is also referred to by some authors as a *definition circle* [33-35]. The target circle defines the maximum allow VSWR, and is expressed mathematically and visually in the Cartesian complex impedance coordinate system. Letting $Z_{\text{in}} = R_{\text{in}} + jX_{\text{in}}$, the equation for the target circle is given by

$$(R_{\text{in}} - a)^2 + X_{\text{in}}^2 = b^2 \tag{3.16}$$

where R_{in} is the input resistance, X_{in} is the input reactance, a is the offset of the center of the target circle from the value of zero input resistance, and b is the radius of the circle. The a and b parameters are expressed in terms of the target transmission line characteristic impedance Z_o and the VSWR as

$$a = \frac{Z_o}{2}\left(\text{VSWR} + \frac{1}{\text{VSWR}}\right) \tag{3.17}$$

$$b = \frac{Z_o}{2}\left(\text{VSWR} - \frac{1}{\text{VSWR}}\right) \tag{3.18}$$

and note that

$$a^2 - b^2 = Z_o \tag{3.19}$$

Equation (3.16) is now expanded as

$$R_{\text{in}}^2 - 2aR_{\text{in}} + X_{\text{in}}^2 = b^2 \tag{3.20}$$

Noting for an arbitrary impedance Z that

$$Z = R + jX \tag{3.21}$$

$$Z^* = R - jX \tag{3.22}$$

and

$$Z + Z^* = 2R \tag{3.23}$$

$$Z - Z^* = j2X \tag{3.24}$$

it follows that

$$ZZ^* = R^2 + X^2 \tag{3.25}$$

Using these impedance relations (Equations (3.21) to (3.25)), Equation (3.20) can be expressed as

$$Z_{\text{in}}Z_{\text{in}}^{*} - a(Z_{\text{in}} + Z_{\text{in}}^{*}) = b^2 - a^2 \tag{3.26}$$

Equation (3.26) is the desired expression for the target circle in terms of the input impedance Z_{in} and VSWR matched to the input transmission line. The next section derives a series of transformation circles that will ensure that the terminal impedance of the antenna will be matched to the target VSWR on the input transmission line.

3.3.2 Transformation Circle Derivation

Refer now to Figure 3.4, which shows a line transformer with characteristic impedance Z_o' and an antenna load impedance Z_L. The input impedance Z_{in} at the port defined by nodes 1 and 2 is expressed as,

$$Z_{\text{in}} = Z_o' \frac{Z_L' + jZ_o' \tan\beta l}{Z_o' + jZ_L \tan\beta l} \tag{3.27}$$

and in terms of its complex conjugate

$$Z_{\text{in}}^{*} = Z_o' \frac{Z_L^{*} - jZ_o' \tan\beta l}{Z_o' - jZ_L^{*} \tan\beta l} \tag{3.28}$$

At the port defined by nodes 1 and 2, the input impedance can be normalized

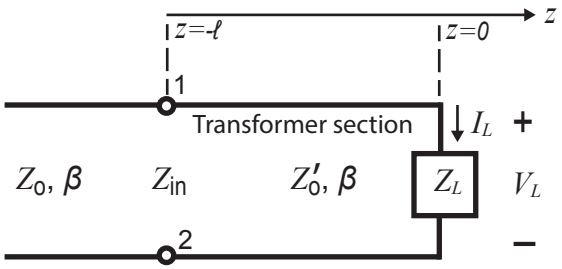

Figure 3.4 Transmission line with characteristic impedance Z_o followed by a transformer section with characteristic impedance Z_o' and length l connected to a load impedance Z_L.

either by Z_o' or by Z_o, depending on which side the input impedance is being computed.

Substituting Equations (3.27 and (3.28) into Equation (3.26) yields

$$\begin{aligned}&\left(Z'_o\frac{Z_L+jZ'_o\tan\beta l}{Z'_o+jZ_L\tan\beta l}\right)\left(Z'_o\frac{Z^*_L-jZ'_o\tan\beta l}{Z'_o-jZ^*_L\tan\beta l}\right)\\&-a\left[\left(Z'_o\frac{Z_L+jZ'_o\tan\beta l}{Z'_o+jZ_L\tan\beta l}\right)+\left(Z'_o\frac{Z^*_L-jZ'_o\tan\beta l}{Z'_o-jZ^*_L\tan\beta l}\right)\right]=b^2-a^2\end{aligned}\tag{3.29}$$

In the book by Reich [33], it is shown that Equation (3.29) can be expressed in the standard form of the equation of a circle center on the resistance axis at R and on the reactance axis at X with radius r as

$$(R_L-R)^2+(X_L-X)^2=r^2\tag{3.30}$$

where

$$R=\frac{a(1+\tan^2\beta l)}{1+\frac{a^2-b^2}{(Z'_o)^2}\tan^2\beta l}\tag{3.31}$$

$$X=\frac{Z_o\tan\beta l\left(\frac{a^2-b^2}{(Z'_o)^2}-1\right)}{1+\frac{a^2-b^2}{(Z'_o)^2}\tan^2\beta l}\tag{3.32}$$

$$r=\frac{b(1+\tan^2\beta l)}{1+\frac{a^2-b^2}{(Z'_o)^2}\tan^2\beta l}\tag{3.33}$$

Equation (3.30) is the desired transformation circle that forms a bilinear transformation to the target circle for a line transformer with characteristic impedance Z'_o and electrical length βl. In other words, load impedance values Z_L that are located within the transformation circle will be transformed to impedance values within the desired target circle with characteristic impedance Z_o. To derive Equations (3.31) to (3.33) it is necessary first to multiply all terms in Equation (3.29) by the expression $(Z'_o+jZ_L\tan\beta l)(Z'_o-jZ^*_L\tan\beta l)$. Next, the relations given by Equations (3.23) to (3.25 are used to express the equation in terms of R_L and X_L. Next, bring all terms involving R_L and X_L to the left side and the remaining terms to the right side. By completing the square for the R_L and X_L terms, and a considerable amount of algebraic manipulations, the desired results Equations (3.31) to (3.33) are obtained.

By referring to Equation (3.19) a further simplification of the transformation Equations (3.31) to (3.33) is achieved, that is, replace a^2-b^2 with Z_o, so that

$$R=\frac{a(1+\tan^2\beta l)}{1+\frac{Z_o}{(Z'_o)^2}\tan^2\beta l}\tag{3.34}$$

$$X = \frac{Z_o \tan \beta l \left(\frac{Z_o}{(Z_o')^2} - 1 \right)}{1 + \frac{Z_o}{(Z_o')^2} \tan^2 \beta l} \tag{3.35}$$

$$r = \frac{b(1 + \tan^2 \beta l)}{1 + \frac{Z_o}{(Z_o')^2} \tan^2 \beta l} \tag{3.36}$$

3.4 Wideband V-Dipole Antenna Simulation

3.4.1 Dipole Design and Moment Method Simulation Model

Consider now a computer simulation model of a wideband dual-polarized crossed dipole antenna with swept-back arms. A V-dipole antenna of this type could be mounted on a small ground plane and could be used in this configuration for example as a wideband gain calibration antenna or as a wideband feed for an instrumentation parabolic reflector antenna. Figure 3.5 shows an example of a linearly polarized swept-back (V-shaped) dipole antenna feeding a reflector antenna.

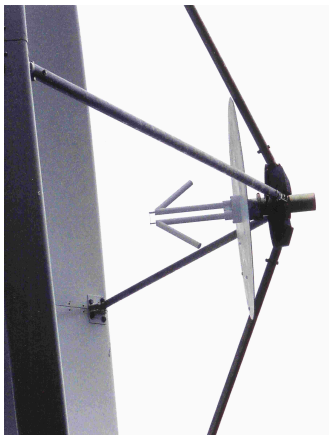

Figure 3.5 Example prototype linearly polarized V-dipole antenna as a feed for a reflector antenna.

A dual-polarized dipole antenna over a ground plane in free space is now designed here for wide bandwidth within a portion of the arbitrarily chosen octave frequency range 400 MHz to 800 MHz. At an assumed center frequency of 600 MHz, the free-space wavelength is 50 cm. For this example, consider a dual-polarized swept-back dipole antenna with folded balun over a perfectly conducting finite ground plane that is modeled with the FEKO moment method solver (www.feko.info) as shown in an isometric view in

Figure 3.6. A side view of the antenna is shown in Figure 3.7. The dipole

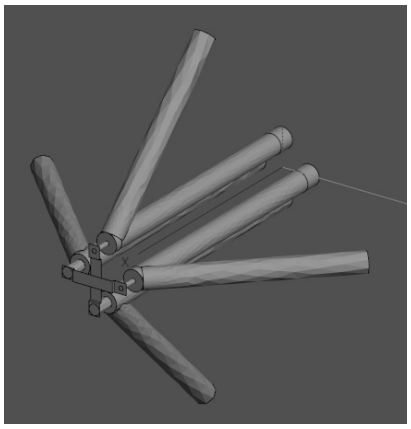

Figure 3.6 Simulation model of a crossed V-dipole antenna. Isometric view.

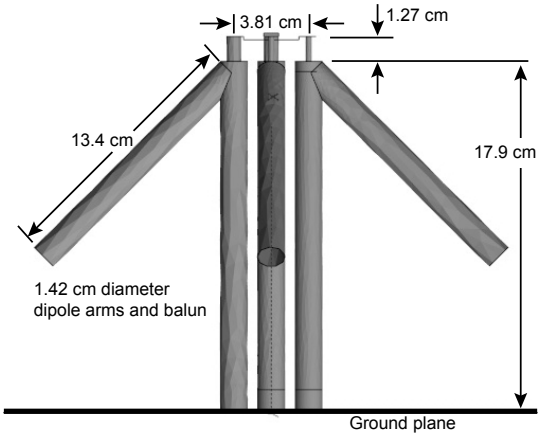

Figure 3.7 Simulation model of a crossed V-dipole antenna. Side view.

arm length was chosen as 13.4 cm, which is 0.268λ at 600 MHz (center frequency). The dipole arms and balun sections are modeled as 1.42 cm

diameter (D in Figure 3.1) perfectly conducting tubes. The dipole height is chosen as 17.9 cm (H in Figure 3.1) so that at the center frequency, the height at the midpoint of the dipole arm is approximately $\lambda/4$ over the ground plane. The square ground plane side dimension was 45.72 cm. The folded balun tubes are spaced 3.81 cm center to center (s in Figure 3.1), which by Equation (3.1) provides a 197Ω characteristic impedance transmission line. The folded balun provides mechanical support of the dipole arms and is short circuited at the ground plane. Electrically, this balun behaves as a purely reactive impedance in parallel with the dipole feed terminals. One of the balun tubes contains a uniform diameter perfectly conducting rod that provides a 50Ω characteristic impedance coaxial transmission line. This coaxial line is connected to the dipole terminals using a crossover connection located 1.27 cm (h in Figure 3.1) above the top of the folded balun. A top view of the antenna is shown in Figure 3.8, where the side length of the ground plane in this example is noted to be 0.46m.

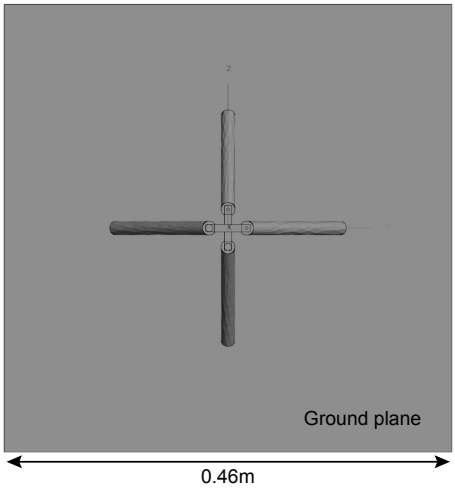

Figure 3.8 Simulation model of a crossed V-dipole antenna. Front view.

3.4.2 Impedance Matching Procedure for the Wideband Dipole

The impedance matching procedure in this example is as follows:

- Plot the dipole antenna load impedance (at the dipole terminals) in Cartesian coordinates, where the horizontal axis is resistance and the vertical axis is reactance,

- Define a target maximum allowed VSWR=2 (plotted as a circle) at an input port located on a standard 50-ohm transmission line,
- Draw an outer boundary circle (OBC) encompassing the antenna load impedance data and tangent to the target VSWR=2 circle at the minimum resistance value,
- Compute the required characteristic impedance of the line transformer Z_o' using the square root (geometric mean) of the product of the resistance minimum (denoted $R_{\text{min}}^{\text{OBC}}$ and resistance maximum $R_{\text{max}}^{\text{OBC}}$ on the resistance axis intersecting the OBC, that is,

$$Z_o' = \sqrt{R_{\text{min}}^{\text{OBC}} \times R_{\text{max}}^{\text{OBC}}} \tag{3.37}$$

- Compute and plot, as an overlay on the impedance data, the transformation circles, from 15° to 165° in 15° steps. Construct additional transformation circles for finer resolution as needed.
- Select a critical frequency in this case where the antenna load impedance intersects the outer boundary circle, and locate the corresponding transformation circle that encompasses the impedance data point at this frequency, From the electrical length βl of the corresponding transformation circle, solve for the transformer critical length $l = l_c$ using $\beta = 2\pi/\lambda$ where λ is the wavelength at the critical frequency.
- Tabulate the electrical line length of the transformer section over the frequency band of interest, and verify that the input impedance at the terminals of the dipole antenna tracks within the series of transformation circles.
- Transform the antenna load impedance to the input impedance and reflection coefficient looking into the line transformer with characteristic impedance Z_o' and critical length l_c.
- Normalize the reflection coefficient data to the final characteristic impedance (50Ω) of the feedline attached to the transformer, and plot as the matched input impedance.

3.4.3 Impedance Matching Simulated Results for the Wideband Dipole

Before matching, the simulated input impedance and reflection coefficient versus frequency at one of the terminals of the crossed dipole, with the other port 50Ω resistively loaded, is shown in Figures 3.9, 3.10 and 3.11. In this moment method simulation, a voltage source was applied at the input port to the 50Ω coaxial feed line at the ground plane, and then the computed input impedance at the ground plane was transformed to the dipole terminals

using Equation (3.6). The input impedance has a first natural resonance at approximately 440 MHz, and is antiresonant at approximately 560 MHz. The antenna has a second natural resonance at approximately 720 MHz. The same simulated input impedance data are plotted in a Smith chart in Figure 3.10. The corresponding reflection coefficient magnitude versus frequency is shown in Figure 3.11. It is observed that the reflection coefficient magnitude in dB has minima occuring near the two natural resonant frequencies. The reflection coefficient magnitude has a peak occuring at the antiresonant frequency as well as large values occuring at the edges of the 400 MHz to 800 MHz band.

Assume now that it is desired to improve the reflection coefficient performance, such that a voltage standing wave ratio (VSWR) ≤ 2 is achieved over a large bandwidth. To start the impedance matching procedure, in Figure 3.12 the complex (real, imaginary) input impedance is plotted as reactance versus resistance. Let the desired upper frequency arbitrarily be chosen as 780 MHz. Then, construct the outer boundary circle (OBC) to encompass the impedance data such that the OBC (solid circle) is tangent to the VSWR=2 circle (dashed circle) where the minimum resistance value is 25Ω, as shown in Figure 3.12. The minimum and maximum resistance values of the outer boundary circle are 25Ω and 260.5Ω, respectively. Then from Equation (3.37) the required line transformer has a characteristic impedance

$$Z_o' = \sqrt{25\Omega \times 260.5\Omega} = 80.7\Omega \tag{3.38}$$

which is rounded here to $Z_o' = 81\Omega$.

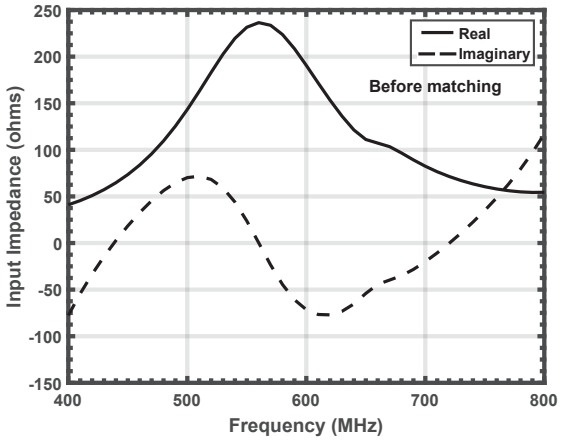

Figure 3.9 Simulated input impedance versus frequency at the terminals of a crossed V-dipole antenna before matching.

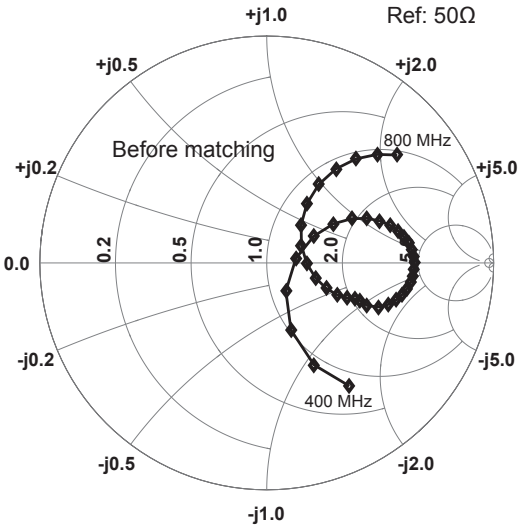

Figure 3.10 Simulated input impedance (Smith chart) at the terminals of a crossed V-dipole antenna before matching.

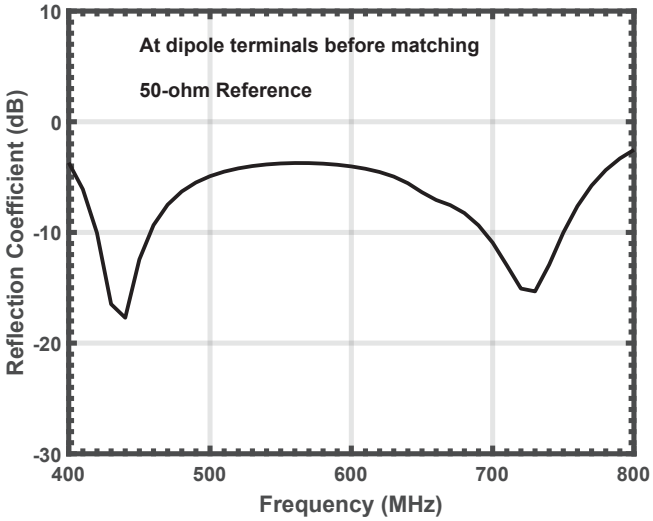

Figure 3.11 Simulated reflection coefficient magnitude in decibels versus frequency at the terminals of a crossed V-dipole antenna before matching.

Having determined the line transformer characteristic impedance $Z'_o = 81\Omega$, the next step is to construct the corresponding series of transformation circles (refer to Equations (3.29 and 3.34 to 3.36)) from 15° to 165°, which are shown in Figure 3.13. The input impedance data at the dipole terminals are then overlayed with the transformation circles in Figure 3.14. To determine the required length (l) of the impedance-matching line transformer, it is necessary to select the so-called critical frequency, in this case where the upper frequency (780 MHz) load impedance intersects with one of the transformation circles. The impedance data at 780 MHz is at the edge of the $\beta l = 120°$ circle. Since $\beta = 2\pi/\lambda$, then $l = 12.7$ cm is the length of the line transformer to be considered. Table 3.1 shows the electrical length of the 81Ω line transformer at several frequencies. Comparing these electrical lengths with the transformation circles and data shown in Figure 3.14, it is observed that the impedance data points fall within, or lay just outside, transformation

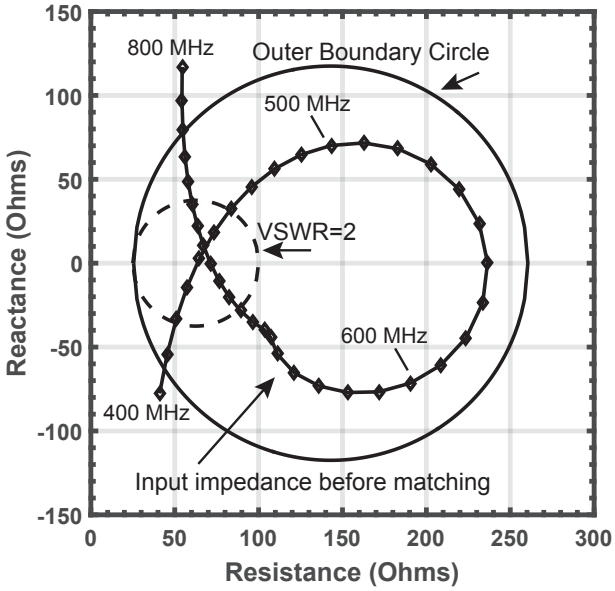

Figure 3.12 Simulated input impedance (solid curve with diamond markers) at the terminals of a UHF crossed V-dipole antenna fed with a 50-ohm coaxial transmission line in a folded balun arrangement. The target circle (dashed curve) corresponds to a VSWR=2 on a 50-ohm characteristic impedance line. An outer boundary circule has been constructed to define the region of the input impedance that will be impedance matched to the target circle region.

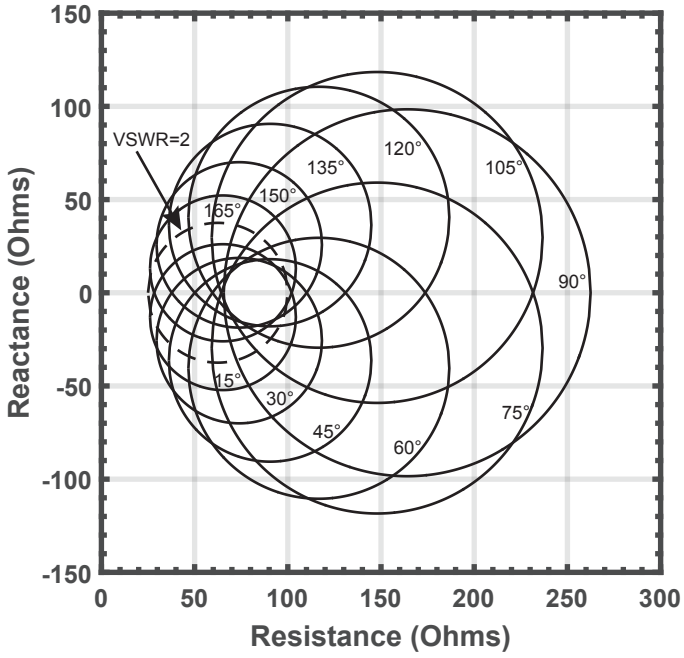

Figure 3.13 The family of transformation circles for a line transformer of 81-ohm characteristic impedance for electrical lengths 15° to 165°. The target circle (dashed curve) corresponds to a VSWR=2.

circles that impedance match to the target VSWR=2 circle (dashed circle). That is, as the complex input impedance varies with frequency as shown in Figure 3.14, the data approximately track within the diameter of one of the transformation circles.

Having determined the desired parameters of the line transformer, that is, characteristic impedance $Z_o' = 80.7\Omega$ and line length $l = 12.7$ cm, Equation (3.3) can be used to compute the dipole antenna input impedance at the end of the line transformer. Figure 3.15 shows the before and after impedance matching results where it is observed that the impedance-matched data generally fall within the target VSWR=2 circle, except (as expected) at the band edges. The simulated VSWR before and after matching is shown in Figure 3.16. The target VSWR=2 has generally been achieved over a wide bandwidth as desired. Note that the VSWR increases to just under 2.2 in the vicinity of 480 MHz. Due to impedance matching, the overall improvement in VSWR is observed to be significant, by about a factor of two over the middle portion of the frequency range. The simulated reflection coefficient magnitude before and after matching is shown in Figure 3.17, and

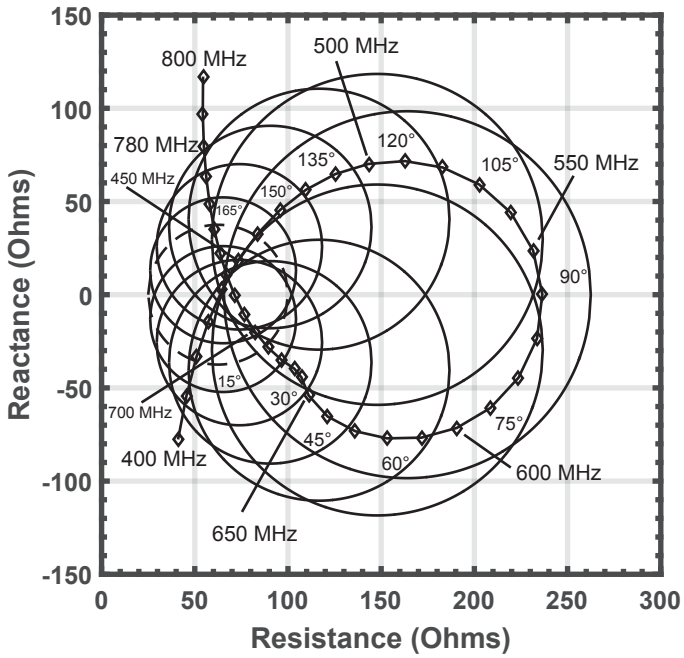

Figure 3.14 Simulated input impedance (solid curve with diamond markers) at the terminals of a UHF crossed V-dipole antenna fed with a 50-ohm coaxial transmission line in a folded balun arrangement. The target constant VSWR=2 circle is shown as a dashed curve. The impedance transformation circles from 15° to 165° are shown

the corresponding transmission mismatch loss is shown in Figure 3.18. The transmission mismatch loss before matching has a maximum value of about 2.4 dB occuring near 560 MHz. After impedance matching the mismatch loss is less than about 0.6 dB from 420 MHz to 780 MHz – due to impedance matching the realized gain would be within 0.6 dB of the ideal antenna directivity with no mismatch loss. For example, with the 81-ohm coaxial line transformer section simulated in FEKO, at the center frequency of 600 MHz the simulated boresight directivity of the swept-back dipole over ground plane was 6.45 dBi and the realized gain was 6.0 dBi – for this case the simulated mismatch loss was 0.45 dB. Prior to matching with the line transformer section, for the constant 50-ohm coaxial feed at 600 MHz the simulated boresight directivity was 6.45 dBi, but the realized gain was only 4.27 dBi due to the mismatch loss being 2.18 dB. Thus, with the line transformer design, at the center frequency the swept-back dipole realized gain increased

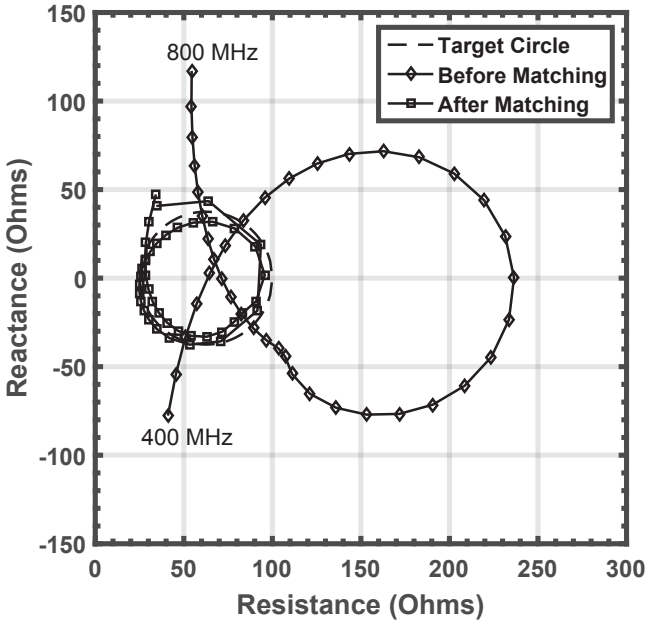

Figure 3.15 Simulated input impedance of a UHF crossed V-dipole antenna before and after impedance matching with an 81-ohm series line transformer.

by 1.75 dB compared to the case where the coaxial feedline had a constant 50-ohm characteristic impedance.

3.5 Comparison with Measurements

A dual-polarized swept-back dipole prototype was fabricated using metal tubing based on the dimensions shown in Figure 3.7. The prototype dipole used a stepped coaxial center conductor matching section to implement the 81-ohm series line transformer. The prototype antenna reflection coefficient was measured and was converted to mismatch loss referenced to 50 ohms. A comparison of the simulated and measured mismatch loss over the 400 MHz to 800 MHz band is shown in Figure 3.19 and good agreement is evident.

3.6 Swept-Back Dipole Feeding a Parabolic Reflector

In this section, a simulation of the swept-back dipole (designed in Section 3.4) feeding a 4.57m diameter parabolic reflector with focal distance to diameter

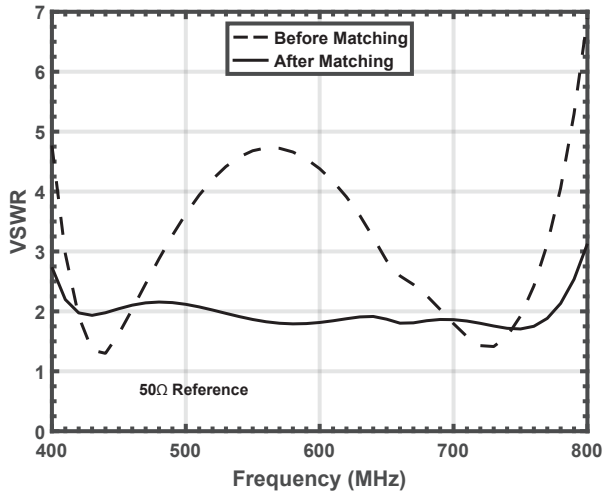

Figure 3.16 Simulated VSWR for a UHF crossed V-dipole antenna before and after impedance matching with an 81-ohm series line transformer. The reference impedance is 50 ohms. The target VSWR was 2.0.

Table 3.1
Line transformer electrical length βl as a function of frequency to match the input impedance to achieve the target VSWR<2 for a crossed V-dipole antenna. The critical frequency is taken as 780 MHz where the electrical length of the line transformer is 120°.

Frequency	Electrical length of line transfomer (βl)
420 MHz	65°
450 MHz	69°
500 MHz	77°
550 MHz	85°
600 MHz	92°
650 MHz	100°
700 MHz	108°
750 MHz	115°
780 MHz	120°

ratio (f/D) equal to 0.4 is described. In this simulation the dipole was assumed to be linearly polarized similar to the dipole shown in the photograph in Figure 3.5. Figure 3.20 shows the simulated dipole/reflector model. In this

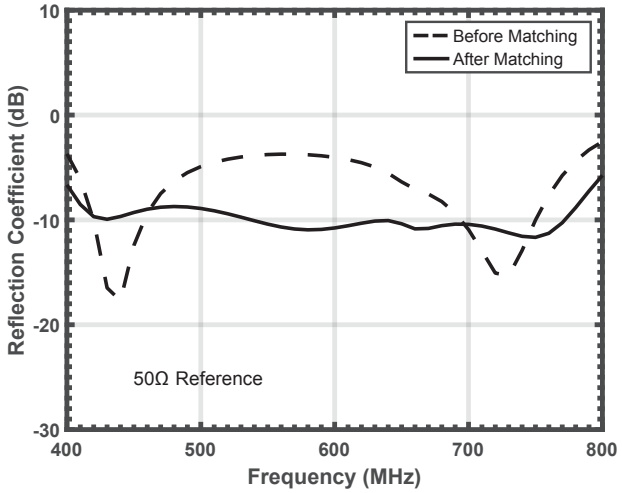

Figure 3.17 Simulated reflection coefficient magnitude for a UHF crossed V-dipole antenna before and after impedance matching with an 81-ohm series line transformer. The reference impedance is 50 ohms.

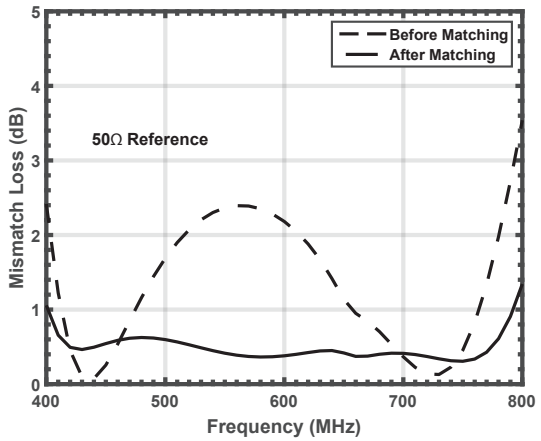

Figure 3.18 Simulated transmission mismatch loss for a UHF crossed V-dipole antenna before and after impedance matching with an 81-ohm series line transformer. The reference impedance is 50 ohms.

case, the angle from the focal point of the reflector to the rim of the reflector

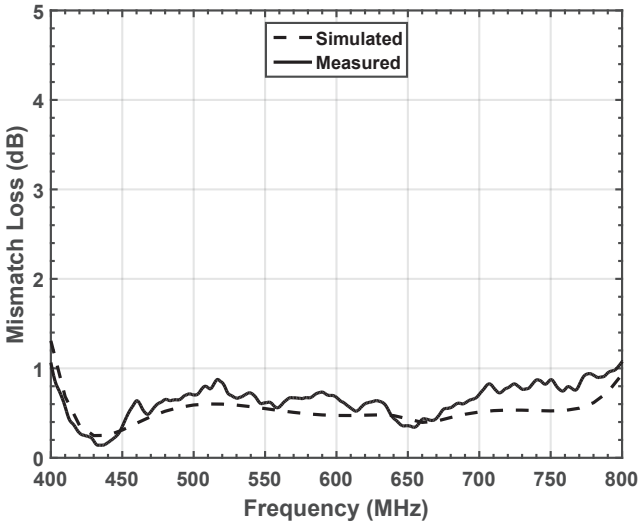

Figure 3.19 Comparison of simulated and measured mismatch loss for a UHF crossed V-dipole antenna before and after impedance matching with an 81-ohm series line transformer. The reference impedance is 50 ohms.

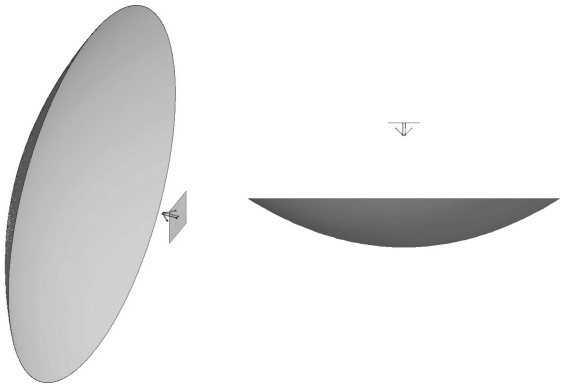

Figure 3.20 Parabolic reflector fed with a V-dipole antenna at the focal point.

is 64°. The method of moments simulated wideband swept-back dipole far-zone E-plane and H-plane directivity patterns are shown in Figures 3.21 and 3.22, respectively, and wide-angle coverage is observed. The FEKO physical optics solver was used to compute the far-field E-plane and H-plane radiation patterns of the reflector antenna (Figures 3.23 and 3.24). The simulated reflector peak directivity is 24.7 dBi, 27.4 dBi, and 28.6 dBi at 420 MHz,

600 MHz, 780 MHz, respectively. Wideband performance is observed with this type of dipole feed.

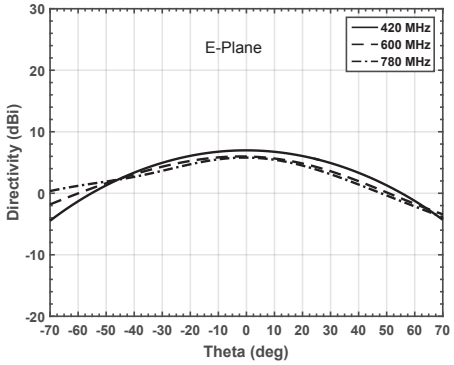

Figure 3.21 Simulated wideband V-dipole E-plane directivity patterns.

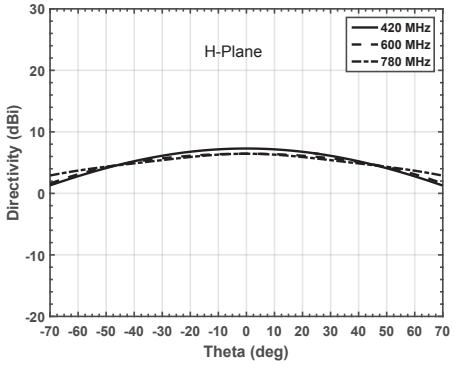

Figure 3.22 Simulated wideband V-dipole H-plane directivity patterns.

3.7 Summary

This chapter has reviewed the line transformer theory and method for impedance matching a complex antenna load to a target VSWR over a wide band of frequencies. The input impedance of an example UHF crossed swept-back dipole antenna was simulated using the method of moments. The line transformer impedance matching method was applied to the simulated antenna and a wide-band match was achieved. This impedance matching technique can be applied readily to other antennas. This type of dipole

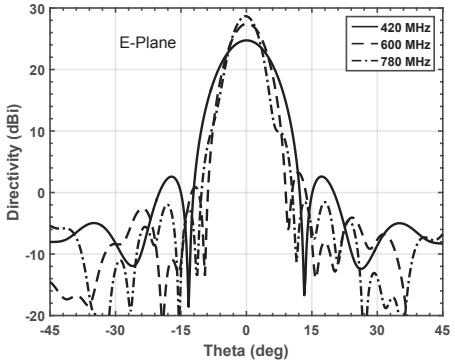

Figure 3.23 Simulated E-plane directivity patterns for wideband V-dipole feeding a parabolic reflector.

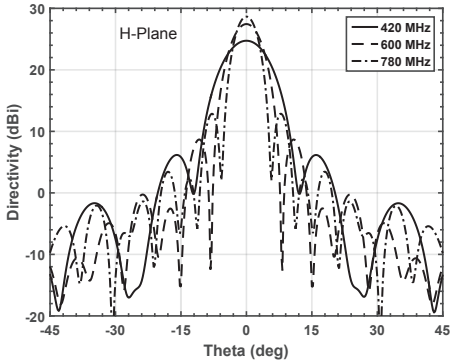

Figure 3.24 Simulated H-plane directivity patterns for wideband V-dipole feeding a parabolic reflector.

antenna has wide-angle pattern coverage and was shown to provide wideband performance as a feed for a parabolic reflector antenna.

References

[1] Allen, J., "Gain and Impedance Variation in Scanned Dipole Arrays," *IEEE Trans. Antennas and Propagat.*, Vol. 10, No. 5, 1962, pp. 566-572.

[2] Hansen, R.C., (ed.), *Microwave Scanning Antennas, Vol. 2*, Los Altos, CA: Peninsula Publishing, 1985, pp. 162-170, 301-308.

[3] Hansen, R.C., *Phased Array Antennas*, New York: Wiley, 1998, pp. 273-303.

[4] Kraus, J.D., *Antennas,* 2nd ed., New York: McGraw-Hill, 1988, pp. 435-496.

[5] Mailloux, R.J., "Phased Array Theory and Technology," *Proc. IEEE*, Vol. 70, No. 3, 1982, pp. 246-291.

[6] Mayer, E.D., and A. Hessel, "Feed Region Modes in Dipole Phased Arrays," *IEEE Trans. Antennas Propagat.*, Vol. 30, No. 1, 1982, pp. 66-75.

[7] Stark, L., "Comparison of Array Element Types," in *Phased Array Antennas (Proc. 1970 Phased Array Antenna Symp.)*, A.A. Oliner and G.H. Knittel, (eds.), Dedham, MA: Artech House, 1972, pp. 51-66.

[8] Knittel, G.H., (Brookner, E., ed.), Chapter 21 in *Radar Technology*, Dedham, MA: Artech House, 1977, pp. 289-301.

[9] Fenn, A.J., "Element Gain Pattern Prediction for Finite Arrays of V-Dipole Antennas over Ground Plane," *IEEE Trans. Antennas Propagat.*, Vol. 36, No. 11, 1988, pp. 1629-1633.

[10] Schelkunoff, S.A., and H.T. Friis, *Antennas: Theory and Practice*, New York: Wiley, 1952, pp. 499-502.

[11] Schuman, H.K, D. R. Pflug, and L. D. Thompson, "Infinite Planar Arrays of Arbitrarily Bent Thin Wire Radiators," *IEEE Trans. Antennas Propagat.*, Vol. 32, No. 4, 1984, pp. 364-377.

[12] E. Brookner, B. Porter, K. Chang, Y.-C. Chang, D. Zwillinger, B. Considine, T. Sikina Demonstration of accurate prediction of PAVE PAWS embedded element gain, 2010 IEEE International Symposium on Phased Array Systems and Technology, pp. 417 - 422.

[13] Jasik, H., *Antenna Engineering Handbook,* New York: McGraw-Hill, 1961, p. 30-3.

[14] J.D. Kraus, *Antennas*. New York: McGraw-Hill, 1950.

[15] W.L. Stutzman and G.A. Thiele, *Antenna Theory and Design, 2nd ed.* New York: Wiley, 1998.

[16] J. Volakis, ed., *Antenna Engineering Handbook, 4th ed.* New York: McGraw-Hill, 2007.

[17] C.A. Balanis, *Antenna Theory and Design, 3rd ed.* New York: Wiley, 2005.

[18] A.J. Fenn, *Adaptive Antennas and Phased Arrays for Radar and Communications.* Norwood, Mass.: Artech House, 2008.

[19] E. Brookner, "Phased-Array Radars," *Scientific American,* vol. 252, no. 2, 1985, pp. 94–102.

[20] A.J. Fenn, D.H. Temme, W.P. Delaney, and W.E. Courtney, "The Development of Phased Array Radar Technology," *Lincoln Laboratory Journal*, vol. 12, no. 2, 2000, pp. 321–340.

[21] J.L. Allen, L. Cartledge, W.P. Delaney, and J. Dibartolo, et al., "Phased Array Radar Studies, 1 July 1959 to 1 July 1960," Technical Report 228, MIT Lincoln Laboratory, 12 Aug. 1960, DTIC no. AD-0249470.

[22] J.L. Allen, L. Cartledge, W.P. Delaney, and J. Dibartolo, "Phased Array Radar Studies, 1 July 1960 to 1 July 1961," Technical Report 236, MIT Lincoln Laboratory, 13 Nov. 1961, DTIC no. AD-271724.

[23] J.L. Allen, D.M. Bernella, W.W. Carpenter, and W.P. Delaney, "Phased Array Radar Studies, 1 July 1961 to 1 July 1963," Technical Report 299, MIT Lincoln Laboratory, 20 Feb. 1963, DTIC no. AD-417572.

[24] J.L. Allen, D.M. Bernella, F. Betts, and L. Cartledge, "Phased Array Radar Studies, 1 July 1963 to 1 July 1964,' Technical Report 381, MIT Lincoln Laboratory, 31 March 1965, DTIC no. AD-629363.

[25] R.J. Mailloux, "Phased Array Theory and Technology," *Proc. IEEE*, vol. 70, no. 3, 1982, pp. 246–291.

[26] J.L. Allen, "Gain and Impedance Variation in Scanned Dipole Arrays," *IRE Trans. Antennas and Propagation*, vol. 10, no. 5, 1962, pp. 566–572.

[27] J.L. Allen and W.P. Delaney, "On the Effect of Mutual Coupling on Unequally Spaced Dipole Arrays," *IRE Trans. Antennas and Propagation,* vol. 10, no. 6, 1962, pp. 784–785.

[28] J.L. Allen, "On Array Element Impedance Variation with Spacing," *IRE Trans. Antennas and Propagation*, vol. 12, no. 3, 1964, pp. 371–372.

[29] J.L. Allen, "On Surface-Wave Coupling Between Elements of Large Arrays," *IEEE Trans. Antennas and Propagation*, vol. 13, no. 4, 1965, pp. 638–639.

[30] H.K. Schuman, D.R. Pflug, and L.D. Thompson, "Infinite Planar Arrays of Arbitrarily Bent Thin Wire Radiators," *IEEE Trans. Antennas Propagation*, vol. 32, no. 3, 1984, pp. 364–377.

[31] A.J. Fenn, P.T. Hurst, J.D. Krieger, J.S. Sandora, and L.I. Parad, "Ultrawideband VHF/UHF Dipole Array Antenna," 2010 IEEE International Symposium on Phased Array Systems and Technology, Waltham-Boston, Mass., 2010, pp. 79–82.

[32] K.E. Schmidt, "Mutual Impedance of Nonplanar Skew Dipoles," *IEEE Trans. Antennas and Propagation*, vol. 44, no. 9, 1996, pp. 1298–1299.

[33] H.J. Reich, ed., Harvard Radio Research Laboratories, *Very High Frequency Techniques*, New York: Mc-Graw Hill, Vol. 1, Chapter 3, 1947.

[34] R.L. Thomas, *A Practical Introduction to Impedance Matching*, Dedham, MA: Artech House, 1976.

[35] W.N. Caron, *Antenna Impedance Matching*, Newington, CT: American Radio Relay League, 1989.]

[36] R.M. Fano, "Theoretical Limitations on the Broadband Matching of Arbitrary Impedances," Massachusetts Institute of Technology, Research Laboratory of Electronics, Technical Report 41, Jan. 2, 1948.

[37] H.A. Wheeler, "Wideband Impedance Matching," Wheeler Laboratories Report 418, Great Neck, New York, 1950.

[38] V.H. Rumsey, "The Design of Frequency-Compensating Matching Sections," *Proc. IRE*, October 1950, pp. 1191–1196.

[39] G.L. Matthaei, L. Young, E.M.T. Jones, *Microwave Filters, Impedance-Matching Networks, and Coupling Structures*, New York, McGraw-Hill, 1964.

[40] T.R. Cuthbert, *Circuit Design Using Personal Computers*, New York: John Wiley, 1983.

[41] T.R. Cuthbert, *Broadband Direct-Coupled and Matching RF Networks*, Greenwood, Arkansas: TRCPEP Publications, 1999.

[42] C. Bowick, *RF Circuit Design*, Burlington, MA: Newnes, 2008.

[43] B.A. Munk, *Finite Antenna Arrays and FSS,* Hoboken, New Jersey: John Wiley, 2003.

[44] H. Jasik, *Antenna Engineering Handbook*, New York: McGraw Hill, 1961.

[45] T.A. Milligan, *Modern Antenna Design, 2nd ed.* Hoboken, NJ: John Wiley, 2005, pp. 252-253.